Optical fibre based cantilever for sensing applications

Jun Li

A dissertation submitted for the degree of Doctor of Philosophy

Heriot-Watt University

School of Engineering and Physical Sciences

May 2014

Abstract

The project investigated in this thesis is concerned with application of using optical fibre cantilever sensors for various applications where traditional electrical sensors cannot survive or work. These applications include micro-machined optical fibre-top cantilever sensor for high temperature and pH measurement, ferrule-top measurement to monitor real-time biomolecule binding process and optical fibre side cantilever sensor for acceleration measurement. In addition, a further investigation of optical fibre diaphragm sensor used for prostate stiffness measurement is also presented based on the same interrogation technique.

First of all, interferometry to monitor the cantilever deflection will be investigated to avoid issues associated with intensity based systems while retaining high measurement resolution.

Secondly, different manufacture techniques of cantilevers compatible with silica optical fibres (laser machining with ns/ps laser, FIB machining) is proposed for deflection measurement. This includes temperature/pH sensing, biological binding monitoring multicore fibres for multi-measurand sensors and optically activated sensors for acceleration measurements.

The use of optical fibre offers a route to miniaturise sensor configuration to allow measurement of real-time bending of micro-cantilevers which can be transferred to cantilever surface energy change by Stoney's equation. By investigating this small energy change, behaviour of real-time biomolecule binding can be monitored. A number of techniques and applications are investigated in the thesis.

Dedication

To my parents for their love and endless support to me without any reasons!

To my wife for her great patience and understanding during my 42 months of PhD. Life!

Acknowledgements

Firstly, I would like to thank my supervisor Dr W N MacPherson for his kind and patient reply to my every question during my PhD life. His wide experience in the field of optical fibre sensors has been useful knowledge throughout my academic life.

Secondly, I would like to thank my second supervisor Prof D P Hand for giving me the opportunity to join the applied optics and photonics research group in 2010.

Then, I would like to thank Dr R R J Maier and Dr W Shu for their helpful suggestion and discussion on my project.

I would also like to thank Dr J N Sun and Mrs M M Millar for his support and helpful discussion with FIB work.

Thanks should also give to Dr R Fowler and Miss Y X Zhou for the collaboration work on food pathogen detection experiments.

I would like to thank my colleagues within the AOP group, especially Mr F Albri, who provided many helpful suggestions on cantilever fabrication. They have made my vast majority of time at Heriot-Watt an enjoyable experience.

Finally, I would like to thank Scottish Universities Physics Alliance provision of a studentship and Renishaw plc. partial provided the funding for me.

ACADEMIC REGISTRY
Research Thesis Submission

Name:	JunLi		
School/PGI:	EPS		
Version: *(i.e. First, Resubmission, Final)*	Final	Degree Sought (Award **and** Subject area)	PhD

Declaration

In accordance with the appropriate regulations I hereby submit my thesis and I declare that:

1) the thesis embodies the results of my own work and has been composed by myself
2) where appropriate, I have made acknowledgement of the work of others and have made reference to work carried out in collaboration with other persons
3) the thesis is the correct version of the thesis for submission and is the same version as any electronic versions submitted*.
4) my thesis for the award referred to, deposited in the Heriot-Watt University Library, should be made available for loan or photocopying and be available via the Institutional Repository, subject to such conditions as the Librarian may require
5) I understand that as a student of the University I am required to abide by the Regulations of the University and to conform to its discipline.

* *Please note that it is the responsibility of the candidate to ensure that the correct version of the thesis is submitted.*

Signature of Candidate:	Jun Li.	Date:	23-06-2014

Submission

Submitted By *(name in capitals)*:	JUN LI
Signature of Individual Submitting:	JunLi
Date Submitted:	24-06-2014

For Completion in the Student Service Centre (SSC)

Received in the SSC by *(name in capitals)*:			
Method of Submission *(Handed in to SSC; posted through internal/external mail)*:			
E-thesis Submitted ***(mandatory for final theses)***			
Signature:		Date:	

Table of Contents

List of Publications

Journal

1. J Li, F Albri, R R J Maier, W N MacPherson, and D P Hand, "Fabrication optical fibre-top cantilever sensor for temperature sensing", *Measurement Science and Technology*,vol.25, pp.035206, 2014.
   http://iopscience.iop.org/0957-0233/25/3/035206
2. J N Sun, J Li, R R J Maier, D P Hand, W N MacPherson, M K Miller, J M Ritchie and X Luo, "Fabrication of a side aligned optical fibre interferometer by focused ion beam machining", *Journal of Micromechanic and Microengineering*, vol.23 pp.105005, 2013.
   http://iopscience.iop.org/0960-1317/23/10/105005
3. F Albri, J Li, R R J Maier, W N MacPherson and D P Hand, "Laser machining of sensing components on the end of optical fibres", *Journal of Micromechanic and Microengineering*, vol.23, pp.045021,2013.
   http://iopscience.iop.org/0960-1317/23/4/045021/article

Conference Proceedings

1. J Li, Y X Zhou, R Folwer, R R J Maier, D P Hand and W N MacPherson, "Optical fibre cantilever sensor for biological application", *Proceedings of 23rd international conference on Optical Fibre Sensing*, vol.9157, 2 June, Santander, Spain, 2014. (accepted for poster presentation)
2. J Li, J N Sun, M M Miliar, J M Ritchie, X Luo, R R J Maier, D P Hand, and W N MacPherson, "Focussed ion beam machining of an in-fibre 45˚ mirror for fibre end sensors", *Proceeding of SPIE 8794, Fifth European Workshop on Optical Fibre Sensors*, vol.8794, pp.847904 , 20 May 2013.(accepted for poster presentation)
3. J Li, F Albri, R R J Maier, W N MacPherson, and D P Hand, "Fabrication of a micro-cantilever sensor on a single mode fibre by picoseconds laser", *Proceedings of 22nd International Conference on Optical Fibre Sensing*, vol.8421, pp.84211G, Beijing, China, 15-19 October, 2012. (accepted for oral presentation)
4. J Li, F Albri, R R J Maier, W N MacPherson, and D P Hand, "Optical fibre cantilever sensors fabricated using ps-laser machining", *Photon-12*, Durham, UK, 3-6 September, 2012. (accepted for poster presentation)
5. J Li, F Albri, R R J Maier, W N MacPherson, and D P Hand, "Micro-machined optical fibre cantilever as sensor elements", Proceeding of SPIE vol.8428, pp.842816-842827, 2012. (accepted for oral presentation)
6. J Li, F Albri, R R J Maier, W N MacPherson, and D P Hand, "Carving Fabry-Perot interferometer at the end of an optical fibre", *The 11th international OSA Network of Students Conference*, Paris, France, 22-25 February, 2012. (accepted for oral presentation)
7. J Li, F Albri, R R J Maier, W N MacPherson, and D P Hand, "Advanced Micro-machining Technique for Fabrication of Optical Fibre Cantilever Sensor", Oral presentation, *The 10th international OSA Network of Students Conference* Southampton, UK, 10-12 August, 2011. (accepted for oral presentation)

8. F Albri, J Li, R R J Maier, W N MacPherson, D P Hand, "Picosecond Laser Machining of Fibre Based Sensing Devices", *The International Congress on Applications of Lasers & Electro-Optics*, Paper M1003, Orlando, USA, October 23-27, 2011.
9. F Albri, J Li, R R J Maier, W N MacPherson, D P Hand, "Picosecond Laser Machining of Optical Fibre Based Cantilever Sensors", *13th International Symposium on Laser Precision Microfabrication*, Washington, DC, USA, June 12-15, 2012.

Awards

1. SPIE best paper presented at 5th EU workshop on optical fibre sensors, Krakow, PL(05/2013)
2. Runner-up prize for best poster at Photon12, Durham, UK(09/2012)
3. Best pitch prize of Enterprise summer school Heriot-Watt University, UK(07/2012)
4. Travel grant for excellent postgraduates, Opto Co. Ltd., Pairs (02/2012)
5. 1st Research prize of Engineering and Physical Science, Heriot-Watt University, UK (10/2011)
6. Scottish Universities Physics Alliance Prize Studentship, UK (05/2010)

Chapter 1

Introduction

Sensors are all around us. They are vital in the modern world, from controlling industrial processes, healthcare, transportation, and in personal electronics. Almost all aspects of our everyday life depend upon sensors. The majority of these are based upon electronic principles, however, there is an increasing need for sensors to fill niche applications where electrical sensors are unsuitable. This may be because of the operating environment conditions, the need for high resolution, or the ability to measure something in a completely new way. In this thesis the motivation for developing optical fibre cantilever sensors is driven by the need for miniaturised sensor elements that offer measurement capability not currently available using traditional techniques. This is applied to a range of physical and bio-sensing applications, to demonstrate the potential of the sensors developed.

1.1 Motivation

A sensor usually refers to a device that measures some environmental parameter and converts it into a signal which can be read by a person or by monitoring equipment. Many sensors are based on an electrical principle for ease of subsequent data handling. They are common in everyday life e.g. measuring room temperature, video camera capture, car speed, etc. Sensors need to be designed to have a negligible effect on the parameter being measured; making the sensor smaller often improves this and may introduce other advantages. Technological progress allows more sensors to be manufactured on a microscopic scale commonly by exploiting Microelectromechanical systems (MEMS) technology [1.1]. In many cases, a micro-sensor reaches a significantly higher sensitivity compared with macroscopic approaches. With the development of MEMS sensors, researchers and engineers have expanded the use of

these sensors to more advanced and challenging areas such as lab-on-a-chip biosensors [1.2], high sensitive accelerometers [1.3], and chemical sensor [1.4] for example.

However, there are cases where the electrical sensor cannot meet the application requirements, for example due to high magnetic fields or, explosive environments. In such cases, optical sensors have been developed because of their high sensitivity and performance in harsh environments [1.5]. For instance, Fibre Bragg Grating (FBG) sensors are widely used for strain and temperature monitoring where the miniature senor dimensions, light weight and multiplexing capability offer advantage over alternative techniques [1.6]. A schematic diagram of the coupling principle of FBG is illustrated in Figure 1.1. The FBG is fabricated by using holographic interference or a phase mask to expose a short length of photosensitive fibre to a periodic distribution of UV light. The refractive index of the fibre is permanently altered according to the intensity of UV light. The resulting structure reflects a 'single' wavelength of light depending upon the grating pitch which shifts in response to variations in temperature and/or strain.

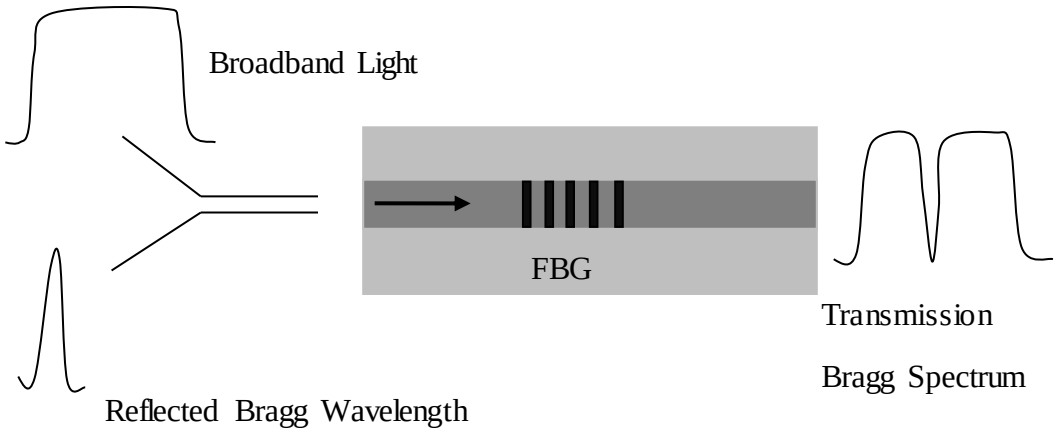

Figure 1.1 General coupling principle of FBG. Light from a broadband source is coupled into an optical fibre. Both the transmission and the reflection spectrum of the FBG are shown.

Alternatively interferometry offers a route to accurate measurements. For example Fabry-Perot (FP) sensors have been demonstrated for high sensitivity measurement [1.7]. FP cavity can be formed using reflective splices or thin optical coatings, offering a miniature point sensor on the scale of the fibre.

In this thesis interferometers based upon micro-cantilevers are developed as an alternative to electrical sensors for acceleration and displacement measurement as well for bio sensing of small interaction volumes in space constrained environments.

Micro-cantilever sensors, as shown in Figure 1.2, offer a promising and highly sensitive approach to "label-free" detection of bio-molecules without the need for fluorescent or radioactive labeling. The underlying principle is to directly translate molecular interactions, e.g. binding between antibody-antigen, on one side of a cantilever surface into mechanical bending, which can be precisely detected using optical methods that are routinely used for atomic force microscopy (AFM). However, conventional AFM techniques involve bulky optical beam detection systems that are unsuitable for some applications.

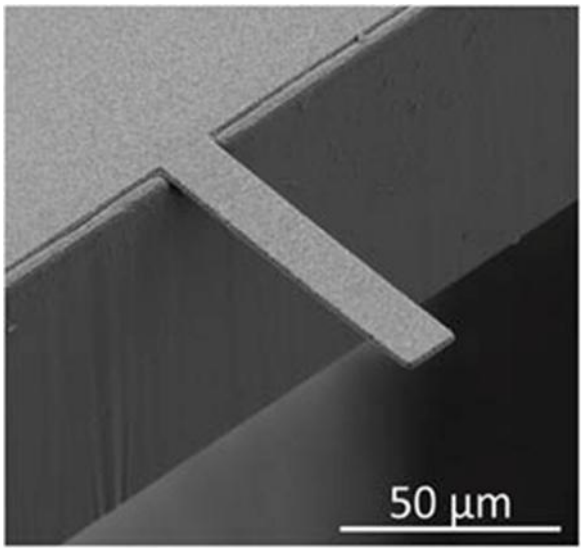

Figure 1.2 A typical Micro-cantilever under SEM ([1.8]).

The work presented in this thesis is concerned with the design, fabrication and application of optical fibre based cantilever sensors for various applications. This includes micro-machined optical fibre-top cantilever sensors for high temperature and pH measurements, ferrule-top sensors to monitor real-time bio-molecular binding process, and optical fibre-side cantilever sensors for multi axis acceleration

measurement. To realize this requires development of suitable interrogation techniques, as well as novel fabrication processes, and cantilever 'activation':

1. Development of cantilever interrogation scheme

Interferometry is used to monitor the cantilever position. This approach avoids issues associated with intensity based systems while retaining high measurement resolution. Initial modelling explores the designs of the optical system – including the cavity optical design (cantilever reflectivity and cavity length) and the optical interrogation systems. These are validated experimentally using broadband and swept wavelength interrogation approaches.

2. Manufacture of cantilevers compatible with optical fibres

Novel manufacturing routes based upon Picosecond laser processing and/or Focussed Ion Beam milling will be used to fabricate sensor components with appropriate resolution. Three areas will be investigated in this thesis:

(i) Fabrication of cantilevers directly onto silica optical fibre using ps-laser machining (manufacturing sketch is shown in Figure 1.3). While this may result in lower sensitivity cantilevers (due to fused silica mechanical properties) and higher fabrication costs the benefits of a single material (all-silica) cantilever and addressing system with in-built optical alignment and minimum overall dimension is of potential interest. This approach is successfully demonstrated for a number of sensing applications.

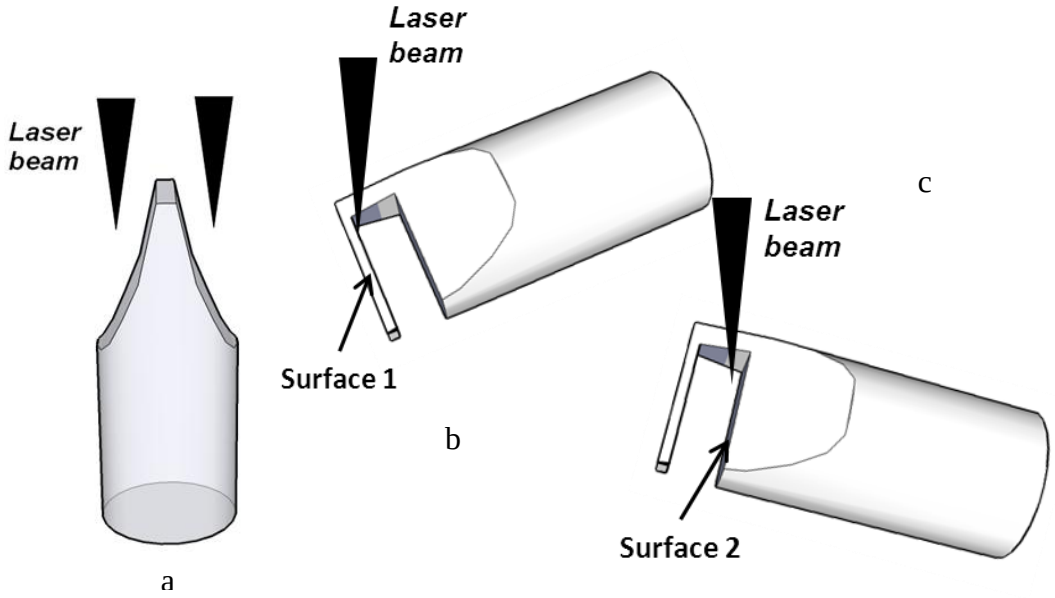

Figure 1.3 General manufacturing steps for optical fibre-top cantilever: (a) Laser machining to form a ridge, (b) Laser micro-machining of surface 1, (c) Laser micro-machining of surface 2.

(ii) Fabrication of sensor elements that can then be attached to a conventional optical fibre ferrule. This has been successfully demonstrated for bio-sensing.

(iii) Fabrication of in-fibre 45˚ mirror to allow for side mounted cantilevers. The 45˚ micro turning mirror is fabricated by FIB/laser dual process. This will offer the possibility to machine longer cantilevers onto the side of the fibre thereby demonstrating higher sensitivity. This is applied for low g multi-axes acceleration measurement with micro-machined optical fibre side cantilevers.

1.2 Summary of Chapters

Chapter 2 comprises a comprehensive review of conventional methods for fabrication and interrogation of micro-cantilever sensors. These are reviewed and then compared to the approach developed and investigated in this thesis.

Chapter 3 introduces the essential theory of the operation principle of the optical fibre cantilever demodulation system. One approach developed uses a low cost light source and spectrometer to acquire the spectral information. A bespoke LabView software program based on FFT algorithm is developed to determine the cantilever cavity length. The measured cavity length is calibrated using a Reinishaw ML10 position sensor

(accuracy ~1nm) which reveals a resolution of around ±15nm. By the use of a phase recover algorithm this error can be further reduced to ~2nm.

Chapter 4 explores the design and manufacture techniques of optical fibre-top cantilevers. The use of optical fibres opens a route to miniaturise the sensor configuration and allow measurement of real-time bending of micro-cantilevers in order to enable various sensing applications. Two different applications, temperature and pH sensing, will be discussed. The work from this chapter is published in IOP Journal of Measurement Science and Technology [1.9].

Chapter 5 describes the Focussed Ion Beam experimental work conducted to fabricate in-fibre 45˚mirrors. These are micro-machined on both single mode fibre (SMF-28) and Multi Core Fibre (MCF). For reliable results the resulting mirror must be at least 25µm by 25µm in size. The machined angle is then verified using white light intereferometry to be 45˚±0.01˚ with an optical surface finish. The in-fibre micro-mirror provided a new route for deflection and displacement sensing parallel to the direction of optical fibres in a space restricted environment. Three potential applications are demonstrated: MCF three-axis displacement measurement, MCF two-axis acceleration measurement and an optical fibre side cantilever for acceleration measurement.

Chapter 6 investigates ferrule-top cantilever biosensor fabricated onto the end of an optical FC/PC ferrule. The fabrication offers potentially low cost scalable production suitable for industrial applications. Proof-of-concept binding experiments between biotin and streptavidin are also studied. The use of the cantilever biosensor for food pathogen detection has also been demonstrated. Food pathogen of less than 10^5cfu/ml was successfully detected in 'real-time' (within 30 minutes) which allows the development of a new generation of micro-cantilever biosensors with even higher sensitivities and opens a new transfer route for clinic application with potentially low-cost fabrication process.

Chapter 7 presents an optical finger sensor for prostate tissue stiffness measurement. An optical finger with 45˚ polished optical fibre as a key sensing element is employed to address the issues brought by conventional electrical gauge. The sensor can offer a much higher sensitivity and resolution with a small size compared with electrical gauge. The technology can be potentially used to develop methods of reliably diagnosing prostate cancer for clinic purpose.

Chapter 8 makes a conclusion of the thesis and discusses potential application areas for optical fibre cantilever sensors. An assessment of the optical fibre cantilever sensors designed in the thesis is presented and suggestions for future direction are noted.

References

[1.1] M Tanaka, "An industrial and applied review of new MEMS devices features", *Microelectronic Engineering*, vol. 84, pp.1341–1344, 2007.

[1.2] J Y Yoon, "Introduction to Biosensors", *Springer*, pp. 225-256, 2013.

[1.3] J Wu, "A low-noise low-offset capacitive sensing amplifier for a 50-μg/√Hz monolithic CMOS MEMS accelerometer", *IEEE Journal of Solid-State Circuits*, vol. 39, pp.722-730, 2004.

[1.4] S Semancik, R E Cavicchi, M C Wheeler, J E Tiffany, G E Poirier, R M Walton, J S Suehle, B Panchapakesan, and D L DeVoe, "Microhotplate platforms for chemical sensor research", *Sensors and Actuators B: Chemical*, vol. 77, pp. 579-591, 2001.

[1.5] J Xu, "A novel temperature-insensitive optical fiber pressure sensor for harsh environments" , *IEEE Photonics Technology Letters* , vol.17, pp. 870 - 872, 2005.

[1.6] X W Shu, Y Liu, D H Zhao, B Gwandu, F Floreani, L Zhang, and I Bennion, "Dependence of temperature and strain coefficients on fiber grating type and its application to simultaneous temperature and strain measurement," *Optics Letters*, vol. 27, pp.701-703, 2002.

[1.7] A D Kersey, D A Jackson, and M Corke, "A simple fibre Fabry-Perot sensor," *Optics Communications*, vol. 45, pp.71-74, 1983.

[1.8] M Suter, O Ergeneman, J Zürcher, S Schmid, A Camenzind, B J Nelson and C Hierold, "Superparamagnetic photocurable nanocomposite for the fabrication of microcantilevers," *Journal of Micromechanics and Microengineering*, vol. 21, pp. 025023-025032, 2011.

[1.9] J Li, F Albri, J N Sun, M M Miliar, R R J Maier, D P Hand and W N MacPherson, "Fabricating optical fibre-top cantilevers for temperature sensing," *Measurement Science and Technology*, vol. 25, pp.035206-035214, 2014.

Chapter 2

Literature Review and Background

Cantilever based sensors show great promise for a wide range of sensing applications. The premise of this thesis is that incorporating cantilever structures onto the end of optical fibres will offer additional flexibility in their application and deployment. In this chapter sensors are briefly considered before concentrating on optical fibre sensors and cantilever sensors. A background review of conventional micro-fabrication and interrogation techniques for micro-cantilever sensors is presented. This develops into a more detailed discussion of micro-cantilever sensors, with the general sensing technologies introduced to give the reader an overall feel for potential applications of these sensors.

Conventional electronic sensors are unsuitable for some niche sensing application, for example in restricted spaces and harsh environments such as regions of high Electrical and Magnetic Interference (EMI) or chemical corrosion. Optical sensors offer a route to solve these issues. After a brief introduction to optical fibre sensor concepts, an overview of cantilever sensors is considered. Both electronic and bulk optics approaches of cantilever interrogation structure are discussed. These methods have been developed during recent years and some are becoming established commercially. However, they are either prone to EMI or too bulky (free space optics) to be used for some applications. Therefore, optical fibre sensors are proposed to address these issues.

2.1 Introduction

The initial motivation of using micro-cantilever sensors is to monitor biological binding processes. The sensor may prove useful for new drug discovery and early diseases diagnosis. Using optical fibre sensing technology, high precision measurements can be achieved in a miniaturised sensor by combining the sensing and interrogation as a single element. In this case, the fibre plays a role as a touch-and-tell device with a fast measurement response. In the following section, general sensor technologies will be

introduced, followed by the application of sensors for biological binding measurements. Conventional biosensor technologies have some drawbacks and the micro-cantilever sensor is introduced as an alternative route to explore biological binding. Different fabrication techniques to create the cantilever structure are investigated. The use of the cantilever structure proposed in this thesis is further extended to other applications, such as all optical fibre cantilever accelerometer, pH sensor and temperature sensor. The last part of the chapter will focus on typical interrogation techniques that could be used to monitor deflection of cantilever sensors.

2.1.1 Sensor Overview

Sensors are vital to allow us to understand the world around us. There have been many important developments in sensing, often driven by industrial and technological demand, such as conventional temperature and mechanical sensors and micron scale semiconductor sensors. Here sensors related to bio- and pH sensing (biosensors), and displacement, movement, acceleration (accelerometers) are considered as they form the main topic in this thesis.

A biosensor is normally an analytical device to detect analyte, combining a biological component with a physicochemical detector. The bio-elements of interest e.g. tissue, microorganisms, receptors, enzymes, antibodies, etc., are measured by a biologically derived material that interacts (binds or recognises) the analyte under study. The interaction signal of the analyte with the biological element is often transformed into an electrical signal and analysed. The main requirements for a biosensor approach to be useful for commercial applications are the identification of a target analyte, availability of a suitable biological recognition element, fast response and the potential for portable detection systems. The applications of the biosensor can be various, such as glucose monitoring in diabetes patients or detection of pathogens [2.1].

One commercial biosensor (the 'immune' sensor) utilises the very specific binding between antibody and antigen [2.2]. The specific nature of the antibody-antigen interaction can result in a physicochemical change and can be measured by the sensor probe. Such a biosensor is very useful as it can monitor medical health related targets

which is significant to human well-being. It is also useful for drug discovery and evaluation of biological activity of new compounds.

One common immune sensor is caller Enzyme Labelled Immune Sorbent Assay (ELISA), which has become a very popular and effective clinical tool [2.2]. The detailed comparison of using ELISA sensor and the optical fibre cantilever sensors developed in this thesis will be discussed in Chapter 6. Another popular immune sensor is based on fluorescence, in which the antibodies are labelled with a fluorescent reagent without affecting its biological activity. The fluorescent intensity measured is related to the amount of antigen present in a processed sample. This technique has been used in the rapid detection of foodborne pathogens [2.4]. However, the technology usually involves a time-consuming multi-step process to identify the target bioanalyte. Therefore although there are many well developed biosensor technologies, there is scope for fast, miniaturised, label free sensing technologies.

Inertia sensors are another widely used sensor. One application of inertia sensors is the measurement of acceleration. This is commonly measured by applying a force on a 'test mass' and the acceleration can be calculated by Newton's second law. Single and multi-axis accelerometers are available to detect direction of the movement, and they can be used to measure orientation (via acceleration due to gravity), directional acceleration, vibration, shock, etc. For example, micro-machined accelerometers [2.5] are widely used in video game controllers and smartphones to detect the position of the device or provide for game input. Besides these cheap commercial accelerometers, there is also a demand for acceleration measurement in harsh industrial and research environments where there are greater demands on EMI immunity, and inherent safety. For this purpose the concept for a multi-axis optical fibre accelerometer is designed and manufactured to demonstrate the potential of fibre based micro-cantilevers in such applications.

2.1.2 Optical fibre sensors

Optical fibre sensors have applications where conventional electronic sensors are not suitable due to their size, mass, EMI sensitivity, etc. Optical sensors have been

developed to address these issues. Optical fibres can be used as sensors for various measurement requirements, where the parameter of interest interacts with some property of the guided light. Intensity, phase, polarization, or wavelength information can be modulated by external perturbations on an optical fibre.

There are many different types of optical fibre sensor. For instance, temperature and strain are often measured by using a Fibre Bragg Grating (FBG) sensor. In the simplest case the FBG reflects a 'single' wavelength: the Bragg wavelength. Shifts in this wavelength can be measured to determine temperature and strain effects that act on the FBG [2.6]. The sensor can be easily multiplexed to create sensing networks. Therefore it has been applied for many applications such as downhole temperature and pressure measurement in oil wells [2.7], and aerospace structure health monitoring [2.8].

Electrical voltage can be detected by nonlinear optical effects in specially-doped fibres, which alter the polarization of light as a function of voltage or electrical field [2.9]. Angle measurement sensors can be based on the Sagnac effect (an effect in interferometer which optical phase change is sensitive to rotation) with a resolution of ~0.1 °/h [2.10]. These applications show the capability of optical fibre sensors to accomplish a sensing task where traditional electrical sensors cannot easily be used.

The recent development of microstructured fibres [2.11] has made it possible to develop various micro/nano sensors. An example of this sensor is found in the photonic crystal fibre sensor (fibre structure shown in Figure 2.1).

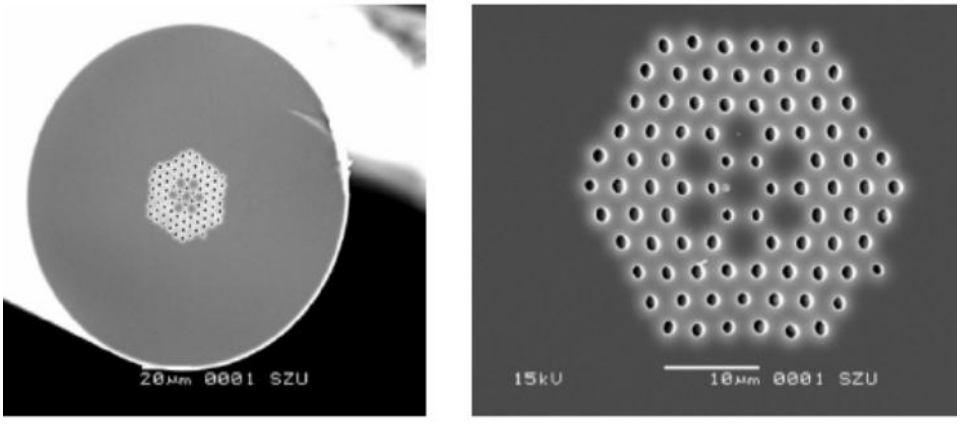

Figure 2.1 An overview of photonic crystal fibre (left) and the detailed microstructure (right) under SEM ([2.11]).

The large surface area offered by accessing the holes has led to the potential for biochemical sensing [2.12]. Here a layer of biomolecules was immobilized onto the sides of the holes of the photonic crystal fibre. By observing the shift in the resonant wavelength of a long-period grating formed in the fibre, the thickness of the layer is measured and the thickness of biomolecule can be determined [2.13].

2.1.3 Cantilever Sensors

In the macro-world, a cantilever usually refers to a beam or overhanging architectural element that is supported at only one end. A common example is the swimming pool diving board, whereas in the micro-world, micro-fabricated cantilevers are one of the most elementary and successful example of miniaturised sensors. A suitably activated free-standing beam can detect changes in the chemical, biological, and physical properties of the surroundings [2.14]. One of the most successful examples of the cantilever sensor is atomic force microscope (AFM) [2.15] which is able to image a surface profile with (sub-)nanometer resolution by measuring the force between a sharp tip of a suspended cantilever and the surface. In terms of micro-cantilever sensors, a mechanism to change the surface stress will cause the cantilever to deflect or change its resonant frequency.

Micro-cantilevers have been widely employed for physical, chemical and biological sensing [2.16][2.17][2.18][2.19]. They have also seen applications in the field of medicine, specifically for the screening of diseases, blood glucose monitoring and detection of chemical and biological analytes [2.20][2.21][2.22][2.22]. These sensors have several advantages over conventional analytical techniques because of their high sensitivity, low cost, simple operation, small sample volumes (μl) and quick response. The technology is promising to be used for miniaturised and high sensitive biosensors, due to its ability of high throughput analysis of analytes and sensitive detection.

2.2 Cantilever beam theory

It is important to understand the mechanical properties of the cantilever beam before it can be used as a sensor. In this section, cantilever beam theory for determining the deflection resulting from an applied force will be considered.

Figure 2.2 Simple cantilever (A-B) subject to deflection υ at point B due to force F applied onto the -x direction.

Consider a cantilever beam with an applied force F at the free end in the x direction. The deflection υ is the displacement in the x direction (as shown in Figure 2.2). The angle of rotation θ of the axis (also called slope) is the angle between the x axis and the tangent to the deflection curve. ds is a small movement along the deflection direction. v is the cantilever deflection. The curvature k can be expressed by:

$$k = \frac{1}{\rho} = \frac{d\theta}{ds} \tag{2.1}$$

$$\frac{dv}{dx} = \tan\theta \tag{2.2}$$

Suppose that the radius of the curvature is ρ, then we have the following relationship:

$$\rho d\theta = ds \tag{2.3}$$

For small θ, $ds \cong dx$, $\cos\theta \cong 1$, then we have:

$$k = \frac{d\theta}{ds} = \frac{d^2v}{dx^2} \tag{2.4}$$

If the material of the beam is assumed to be linear elastic, then we have:

$$k = \frac{1}{\rho} = \frac{M}{EI} \tag{2.5}$$

M is the moment, E is the Young's Modulus, and I is the moment of the inertia of the cantilever beam respectively. Then the differential equation of curve is obtained:

$$\frac{d\theta}{ds} = \frac{d^2v}{dx^2} = \frac{M}{EI} \tag{2.6}$$

The above equations can be written in a simple form:

$$EI\frac{d^2v}{dx^2} = M \tag{2.7}$$

These equations are valid only when Hooke's law applies and when the slope and the deflection are very small. Most of the cantilever deflection measurements for chemical and biological applications discussed in this thesis are based on this assumption, since the maximum deflection is usually < μm, which is still 'small' compared to typical 10's-100's μm cantilever dimensions.

2.3 Cantilever sensors: Operation principle

Generally speaking, micro-cantilever sensors can be operated in two different ways: bending mode [2.24] and dynamic mode [2.25]. Figure 2.3 illustrates these operating principles. In the static mode, interactions on the cantilever surface are translated into a cantilever bending as a result of changes in the surface stress – this may be due to molecular interactions for example where interactions on only one side of a micro-cantilever surface will induce a surface stress change resulting in cantilever deflection. The relationship between the bending and the surface stress change can be written using Stoney's equation [2.26]:

$$\Delta z = \frac{3(1-\nu)L^2}{Et^2}\Delta\sigma \tag{2.8}$$

Here Δz is the amplitude of cantilever bending, shown in Figure 2.3. $\Delta\sigma$ is the surface stress change, v is the Poisson's ratio, E is the Young's modulus, and L and t are the length and the thickness of the cantilever respectively. It is clear from equation 2.8 that, for a given cantilever with fixed mechanical (v and E) and geometrical (L and t) values, the cantilever bending is proportional to surface stress. This means the performance or the sensitivity of the sensor is determined by the mechanical and geometrical properties of the cantilever itself. For example, the sensitivity of the sensor or the bending response to a given biochemical reaction or surface stress is proportional to the square of cantilever length (L^2), and inversely proportional to both the Young's modulus *(E)* and the square of cantilever thickness (t^2). Consequently, increasing the cantilever length, reducing the Young's modulus (making softer cantilevers, e.g. using polymers), and fabricating thinner cantilevers will lead to higher sensitivity.

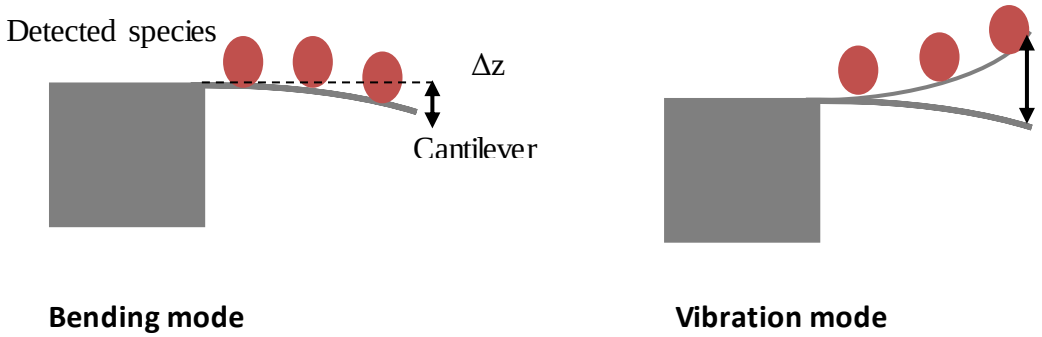

Figure 2.3 Two operating modes for a micro-cantilever sensor: Bending mode and vibration mode.

In vibration mode operation a change in the resonant frequency of the cantilever is monitored. The resonance frequency f_{res} for a simple rectangular cantilever can be expressed as [2.27]:

$$f_{res} = \frac{0.162\sqrt{E}h^3W}{\sqrt{\rho}l^2} \tag{2.9}$$

Where ρ is the mass density, l is the cantilever length; h and W denote the height and the width of the cantilever respectively. The moment of inertia for a rectangular cantilever can be written as [2.27]:

$$I = \frac{Wh^3}{l^3} \tag{2.10}$$

Alternatively a simpler expression for the resonance frequency can be written as a function of the spring constant as [2.27] :

$$f_{res} = \frac{0.32\sqrt{k}}{\sqrt{m}} \tag{2.11}$$

Where mass, $m=\rho hlW$ and k is spring constant of the cantilever. The relation shows that the resonance frequency increases as a function of increasing spring constant and of decreasing cantilever mass. Therefore a change in cantilever mass will affect the system resonant frequency. In this thesis, only the bending mode will be investigated for sensor applications as vibration mode will have damping issues when operating at liquid environment.

In order to use the micro-cantilever concept as a sensing device, it is necessary to review fabrication techniques for micron-scale devices. The most commonly and widely used micro-fabrication techniques is optical lithography. It is suitable for mass production and low cost due to high volume output, thus this is the first fabrication technology discussed. Alternative techniques that allow greater flexibility in 3 dimensional fabrications are then introduced, in particular Focussed Ion Beam (FIB) milling and laser micro-machining, both of which provide a fabrication route for cantilever sensors in this thesis.

2.4 Fabrication techniques for micro-cantilevers

2.4.1 Optical lithography

Optical lithography (or photolithography) is a process used in micro-fabrication to selectively remove parts of a thin film or the bulk of a substrate. It uses light to transfer a geometric pattern from a photo mask to a light-sensitive chemical

"photoresist", (or "resist,") on the substrate [2.28]. A series of chemical treatments then engraves the exposed pattern into the material underneath the photoresist. Optical lithography shares some fundamental principles with photography in that the pattern in the resist is created by exposure to light, either using a projected image or an optical mask. The procedure is comparable to a high precision version of the method used to make printed circuit boards. It is used because it affords exact control over the shape and size of the objects it creates [2.29], and because it can create patterns over a large surface simultaneously. The main disadvantages are that photolithography requires a very flat substrate on the order of ~nm, therefore, limited its application for rough surfaces. The requirement for ultra-smooth surfaces also means that it requires extremely clean operating conditions to achieve a high yield.

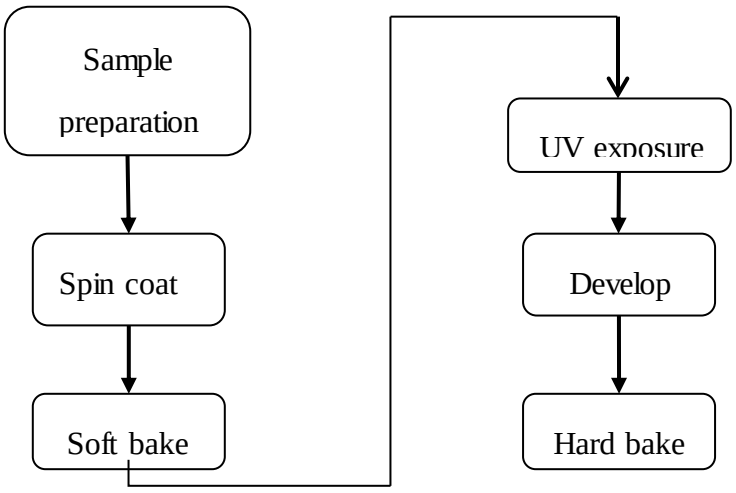

Figure 2.4 Schematic process of photolithography process.

The standard fabrication procedure of optical lithography usually follows several steps (illustrated in Figure 2.4). The first step is called wafer preparation, which the wafer is first heated up to drive off any moisture that may be present on the surface. Then the wafer is covered with photoresist by spin coating. The spin coating process typically can last for several seconds. The aim is to create a uniform thin layer of several nanometers across the surface. The photoresist-coated wafer is then prebaked to drive off excess photoresist solvent. After prebaking, the photoresist is exposed to a pattern of intense ultraviolet light to allow the photoresist to be removed by a special solution,

called a "developer". During the exposure process, the resist undergoes a chemical reaction. Depending on the chemical composition of resist, the resist can react in one of two ways when light interacts with the surface. The action of light on a positive resist causes it to become polymerized where it has been exposed to the light while a negative resist exposure to UV-light causes the resist to decompose. To further harden and remove any residue of the developer, the wafer undergoes a post-bake (hard bake) process. During this process, the resist temperature can be controlled to cause a plastic flow in the resist which can be desirable for tailoring sidewall angles. Optical lithography has become a standard and popularly used technology in semiconductor industry.

2.4.2 Top-down approach to fabricate fibre-top cantilevers

Photolithography has also been applied to form micron scale features onto the end of optical fibres. Low mass gold fiber-top cantilevers have been fabricated via photolithography by top-down micromachining techniques [2.30]. The work presented in the paper also showed potential for using fiber-top sensors for remote detection of biochemical substances after the gold coating layer is activated with bio molecules.

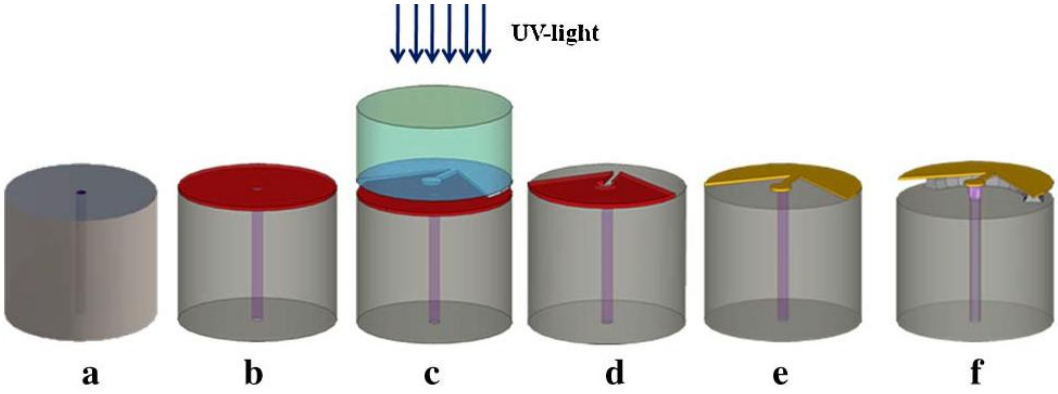

Figure 2.5 Top-down approach to fabricate fibre-top cantilever (from [2.30]).

The detailed fabrication process is illustrated in Figure 2.5. A standard single-mode optical fibre with a cleaved end (Figure 2.5 (a)) is dipped in positive photoresist. The thin, flat photoresist layer that remains attached at the end of the dipping step is then hardened by keeping the fiber at 105 °C for 10 minutes (Figure 2.5 (b)) and exposed to UV light via a patterned mask fibre (Figure 2.5 (c),(d)). After removal of the exposed

photoresist areas (resist development), a thin chromium-gold bilayer is evaporated onto the surface. The remaining photoresist film and the top deposited metal are then rinsed and removed with methanol (Figure 2.5 (e)), leaving a chromium-gold pattern that has the shape of the cantilever. Finally, the fiber tip was chemically etched to remove a few micrometers of silicon dioxide from all the areas that are not protected by the chromium-gold bilayer. The final released cantilever can be found in Figure 2.5(f).

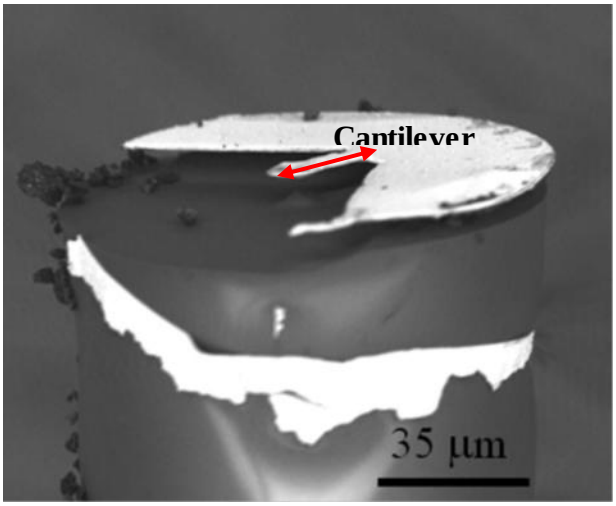

Figure 2.6 Scanning electron micrograph of a fiber-top cantilever fabricated with a top-down approach (from [2.30]).

Figure 2.6 shows the SEM image of the resultant cantilever fabricated in [2.30]. It consists of a metallic structure machined out of a 350nm thick metallic layer (30nm chromium plus 320nm gold) that was deposited on top of an optical fiber. Similar steps can be followed to produce cantilevers of different dimensions and materials. This technique opens a route for developing a new platform of all-optical user-friendly biochemical detectors. The disadvantage of this technique is that it involves several complex fabrication steps, and furthermore, the thin cantilever is fragile and easy to break off.

2.4.3 Focused Ion Beam (FIB) milling

Another fabrication technique that can be used to manufacture 3 dimensional micro-cantilever structures is called Focused Ion Beam (FIB) milling. This is a widely used technique in the semiconductor and materials science fields for micromachining, deposition, and ablation of materials [2.31][2.32][2.33][2.34]. FIB typically uses a

Gallium ion beam to scan the surface of a sample in a similar way to an electron beam in a scanning electron microscope (SEM).

The choice of the source for machining is very important. Ga ions are used in FIB for various reasons. Ga has a low melting temperature and hence it is a very convenient material to construct a compact ion gun with limited heating requirement. The Ga can be contained in a small volume so the gun has longer life-time. Although other materials such as Ar (gas) in theory can be used, the brightness of such a gun would be far lower and an Ar focused beam of the same size would not be very intense. Note that whatever material is chosen, it needs to be ionized before beam formation and then accelerated. Figure 2.7 shows a few examples of FIB machined structure under SEM view. Figure 2.7 (a) and (b) show the trial machining results on an optical fibre by FIB in our group, while Figure 2.7 (c) demonstrated the FIB machined structure on silica surface [2.33].

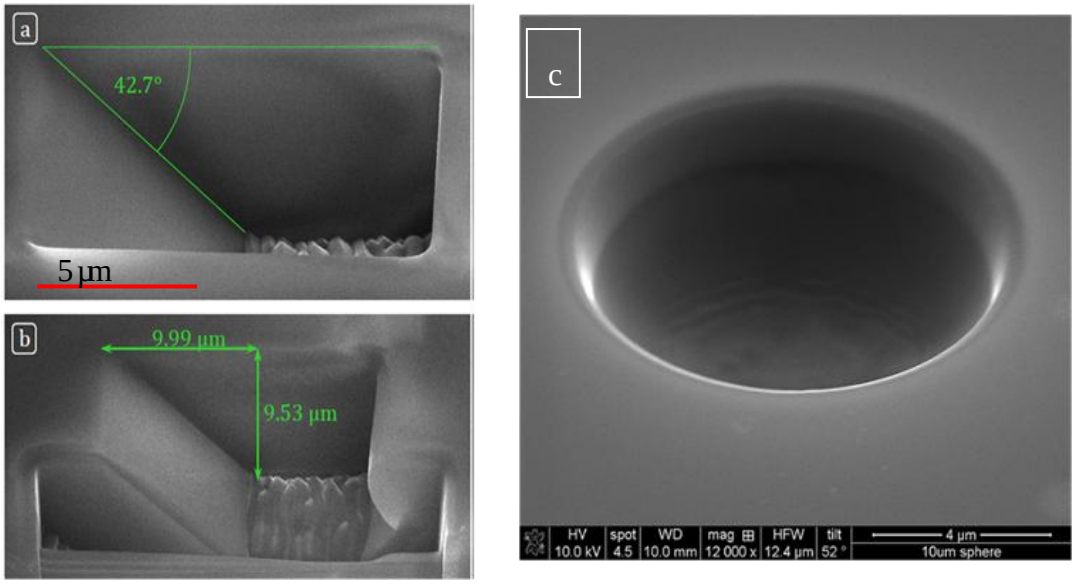

Figure 2.7 (a) SEM view of FIB machined structure, (b) SEM view of 45˚ mirror machined by FIB onto an optical fibre, (c) SEM view of micro hole machined by FIB (from [2.33]).

The most important characteristics of FIB and the subsequent interaction with sample are:

- Ions are larger than electrons. Therefore they can easily penetrate individual atoms of the sample. Interaction of ions with sample often results in atomic

ionization and breaking of chemical bonds of the substrate atoms. The process is how secondary electrons and change of chemical state are created.

- Ions are heavier than electrons. In this case, ions can gain a high momentum. For the same energy, the momentum of the ion is much larger than electron. Once an electron collides with an atom, it can penetrate the electron cloud and reach the nucleus of the atom. As the electron mass is low compared to the mass of the sample atoms, the sample atom will hardly move at all. On the other hand, when the ion hits an atom, its mass is comparable to the mass of the sample atom and as a result, a large amount of momentum will be transferred.
- Ions are positive and electrons are negative. The particles leave the sample when irradiated with neutral atoms, positive and negative ions and electrons. On average a completely isolating sample such as glass will charge up positively because of the incoming positive ion and the outgoing negative secondary electrons.

FIB [2.36] has been shown capable of machining sensing structures on fibre end tips. FIB is highly suitable for micro-fabrication due to its small spot size and stable operating condition [2.37]. It has been demonstrated for fabrication of two-dimensional (2D) structures on optical fibres with nm feature size [2.38]. The approach has been extensively used in a number of fibre-based applications, including modification of waveguide properties [2.39], micromachining of a micro-notch cavity on the fibre tip for interferometric sensing [2.40], and caving of the fibre-top cantilever for atomic force microscopy [2.39].

The idea of FIB machining micro-cantilever onto the end of optical fibres was first proposed by Iannuzzi *et al* [2.39]. Their initial aim is to use the sensor for atomic force microscopy and other physical and chemical research. The fibre-top cantilever relies on the ability to measure the cantilever deflection with nanometer accuracy.

Figure 2.8 shows the profile of the micro-machined fibre top cantilever fabricated by using FIB milling. The advantages of this structure are that the cantilever and the fibre is a single pre-aligned component. In addition, it is convenient to read out the bending

signal of the cantilever in space constrained environment. However, one of the major disadvantages is that the fabrication process of the fibre-top cantilever is very complicated and time-consuming by using FIB and this adds to the manufacturing cost.

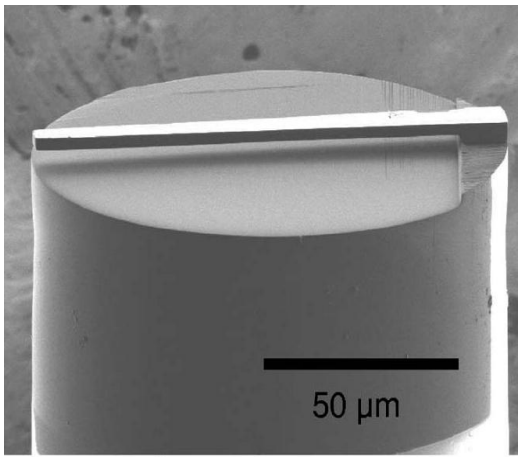

Figure 2.8 SEM view of the fibre-top cantilever machined by FIB (from [2.39]).

2.4.4 Laser micro-machining

FIB milling offers excellent machining resolution, but is slow for 'large' structures. Laser micromachining offers an alternative fabrication route to produce micron scale structures. The technology is widely reported in recent years [2.40] [2.41] [2.42] [2.43]. Normally, laser micro-machining uses a focused optical beam to selectively remove material from a substrate creating a desired feature. Unlike mechanical machining techniques, laser machining induces low heat deposition to the work piece. The technology is capable of rapid replication of microstructures with a high degree of robustness, high throughput, wide range of compatible materials, and 'low-cost' manufacturing. These features make laser micro-machining an ideal candidate for fabrication of micro-cantilever structures.

Laser micro-machining can be divided into various regimes, nanosecond, picosecond and femtosecond, according to the pulse width of the laser. The mechanism of material removal during laser micro-machining includes different stages such as melting, vaporization, and chemical degradation (chemical bonds are broken which causes the materials to degrade) depending on how the laser energy interacts with the material. When a high energy density laser beam is focussed onto the work surface, energy is absorbed and the surface is heated. As a result, molten, vaporized or chemically

changed states are formed. The comparison between long pulse and short pulse laser machining process is shown in Figure 2.9.

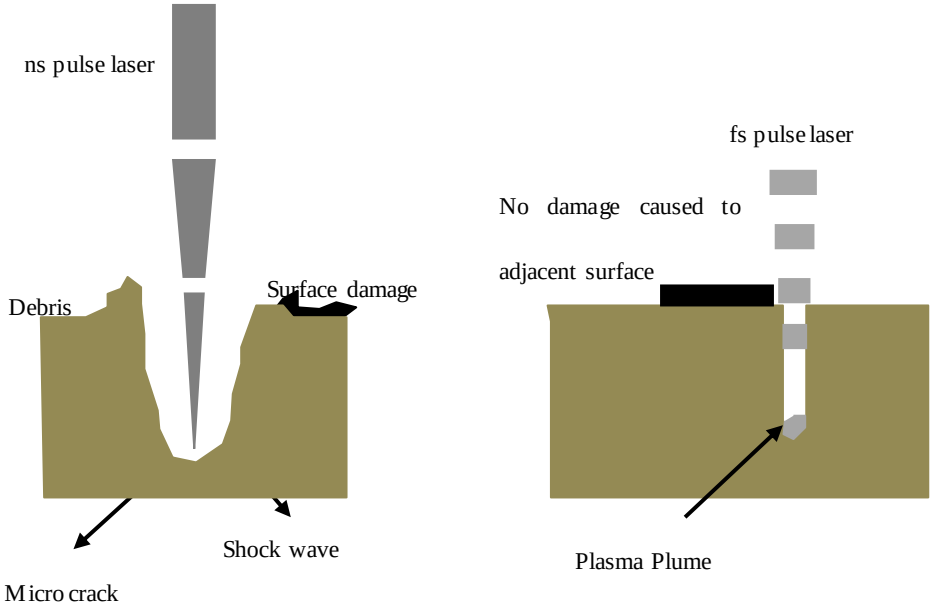

Figure 2.9 Laser machining effect on the same substrate by using ns pulses (left) and fs pulses (right) (adapted from [2.43]).

For a nanosecond laser pulse, material is removed by thermal ablation and local heating to the near boiling point. Figure 2.9 shows that as the laser pulses interaction time with material becomes shorter, the laser energy doesn't transfer to lattice when interacting with electronic lattice thus no shock wave and micro cracks will be produced during the machining. Furthermore, the heat affected zone is quite different in each case: for longer ns laser pulses, heat is transferred to surrounding material, making the machined hole bigger, whilst for fs laser pulses, the heat affect zone is so small that the surface roughness of the machined surface is much better compared with ns laser pulses. The phenomenon observed shows that longer pulses can deliver more energy and a larger machining area at a high speed, however, the machined material can be easily melted, damaging the surrounding areas. In contrast, short-pulsed laser shows promising manufacturing advantages due to a small heat affected zone and better surface roughness.

Although femtosecond lasers offer new and promising ways to micro-machine almost any solid material, they do have a few drawbacks for industrial applications. First of

all, fs-laser machining is a slow process. Usually, the interaction of laser beam with the sample is to modify the refractive index change rather than ablation. Secondly, the system contains many more optical components than longer pulse length lasers which might influence the stability of operation by environmental conditions like temperature, vibrations, etc. However, on the other hand, fs-lasers can be used for high quality applications which are not achievable by traditional laser micro-machining. Table 2.1 shows the basic property of lasers with different pulse width.

Table 2.1 Comparison of different laser micromachining techniques.

	Damage to material	*Precision*	*Heat affect zone*	*Processing speed*	*Cost*
ns	*High*	*Low*	*Large*	*Fast*	*Low*
ps	*Low*	*High*	*Small*	*Fast*	*Medium*
fs	*Very low*	*Very high*	*Very small*	*Slow*	*High*

To summarise the different pulse widths used for laser micromachining, the choice strongly depends on the application. In terms of machining big metal sheets, nanosecond pulse or longer pulse duration/Continuous Wave (CW) lasers remain the best choice, since they can deliver very high average power of up to tens of kilowatts while maintaining a high machining speed. In terms of small feature size, picosecond and femtosecond laser might be ideal candidates because of their low heat affected zone and small spot size.

In micro-cantilever machining, silica, polymer and silica oxide are the commonly used materials due to their optical and mechanical properties over other materials. With different ultrashort pulse, different feature sizes can be machined to meet the best application performance. For the purpose of micro-cantilever bending measurement, polymer materials would be a good choice because of its low Young's modulus and mechanical characteristics. However, a trade-off between high sensitivity and laser machined surface quality must be considered before it can be used for practical application.

One of the most important parameters used for evaluating the machined surface quality is called surface roughness which is the arithmetic mean roughness (R_a). It is assumed that a roughness profile has been filtered from the raw profile data and the mean line has been calculated. The roughness profile contains n ordered, equally spaced points along the trace, and y_i is the vertical distance from the mean line to the i^{th} data point. Height is assumed to be positive in the up direction, away from the bulk material. Then R_a can be defined as:

$$R_a = \frac{1}{n}\sum_{i=1}^{n}|y_i| \tag{2.12}$$

Generally speaking, laser machining is capable of generating a surface roughness of $R_a \le 0.3\mu m$ in stainless steel, $R_a \approx 0.9\mu m$ in Alumina and $R_a \approx 0.434\mu m$ in dielectrics [2.45]. When a laser process is used for micro polishing, the average surface roughness can be decreased from $R_a = 0.112\mu m$ to $R_a = 0.015\mu m$ [2.45] by optimizing the processing parameters such as pulse energy and scanning speed.

Surface roughness of machined materials is one of the most important factors that affect its application. By using ultrashort (up to 10 ps) laser pulses, many materials can be machined to very high precision. The ability to machine such a wide range of materials is very different from that of conventional longer pulse lasers. The interaction between laser and material is independent of the linear absorption properties of the material and is applicable to materials which would otherwise be transparent to the laser wavelength. Machining down to micron scale precision with small damage to the remaining material is achieved by ablating material faster than heat transferring time.

Petkov *et al.* [2.46] employed four different laser milling systems with different pulse durations by ablating a field with dimensions of 1 by 1mm in order to investigate the relationship between laser pulse widths and surface roughness. The characteristics of the laser sources employed in this experimental study are shown in Table 2.2.

Table 2.2 laser source characteristic ([2.47]).

Laser source	*Laser process parameter*	*Surface roughness (R_a)(μm)*
fs-laser	*Power:20mW* *Scanning speed:100mm/min* *Fluence:0.25J/cm^2*	*0.35*
ps-laser	*Power:100mW* *Scanning speed:100mm/s* *Fluence:0.25J/cm^2*	*0.29*
ns-laser	*Power:10W* *Scanning speed:100mm/s* *Fluence:2J/cm^2*	*0.86*
ms-laser	*Power:5.2W* *Scanning speed:305mm/s* *Fluence:1.8J/cm^2*	*2.18*

From the above table, it is clearly that when applying ultra-short pulses, significant improvements of surface roughness can be achieved by using ps and fs pulse lasers, whereas a marginally better surface quality was achieved when performing laser milling with a ps-laser source compared to a fs-laser. This might due to the non-linear effects that usually happen for processing materials in the fs regimes, as well as the specific machining materials with the laser wavelength used for machining.

In order to investigate ps-laser machined surface roughness, an AFM was used to measure the surface quality of a machined optical fibre end facet. Figure 2.10 shows preliminary measurement results. Surface roughness of the selected area is approximate 200nm, which indicates that ps-laser is a good choice to improve the surface finish as also shown in Table 2.2 from the previous research (detailed discussion will be presented in Chapter 4).

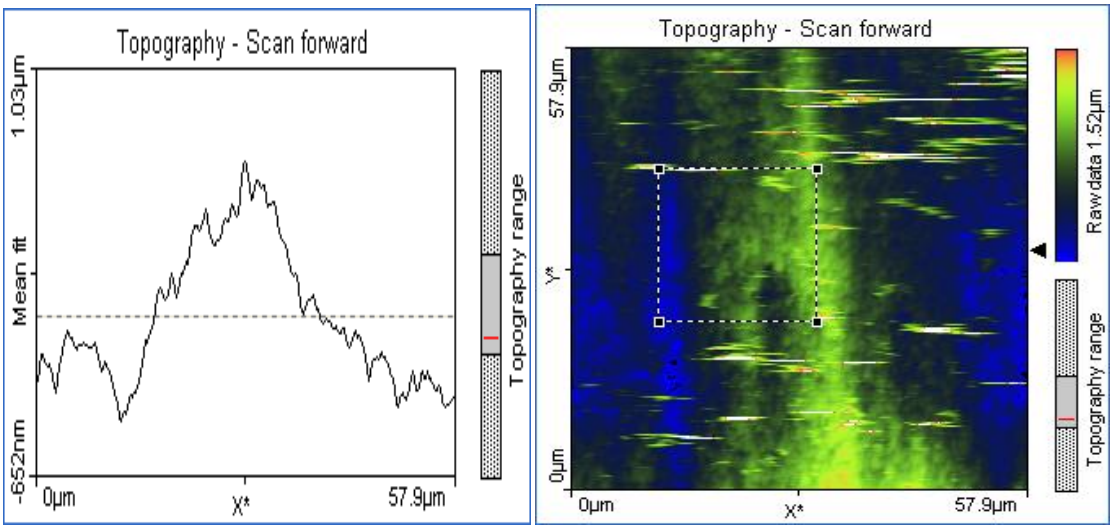

Figure 2.10 AFM scanned results of a ps-laser machined optical fibre end surface.

Existing studies show that a trade-off between the surface finish and the material removal rate is usually found. For high surface quality with small material removal area, ultrashort pulsed laser might be a good candidate. Therefore, the optimum laser parameters used for micromachining need to be investigated for each specific application.

2.4.5 Fs-laser plus HF etching

Another technique to produce micron scale components is a two-step procedure based on femtosecond laser irradiation and HF wet etching (see Figure 2.11). Typically a fs-laser with 250 kHz repetition rate, 800 nm wavelength and 0.1μJ pulse energy is focused onto the substrate using a microscope objective. The pattern used to machine the structure is constructed by moving a three-axis stage under the microscope objective at a speed of 0.1 mm/s. After exposure, the fiber is then immersed into a low-concentration HF aqueous solution for 30 minutes. The patterned areas are quickly etched away while the rest of the (undamaged) glass was etched at a much slower rate. This approach has been used to fabricate cantilever structures as shown in Figure 2.12. The roughness of the machined surfaces is much larger compared with FIB milled samples in this case, which could cause problems when optically interrogating the system.

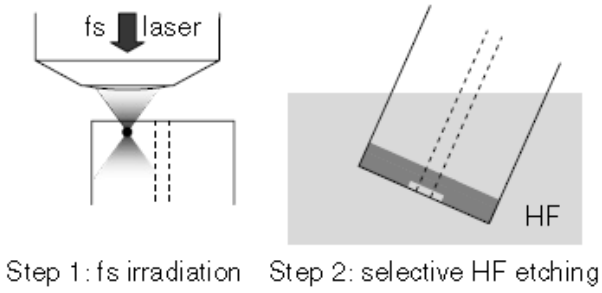

Figure 2.11 Fabrication procedure of fibre-top cantilever by fs-laser machining and HF etching ([2.48]).

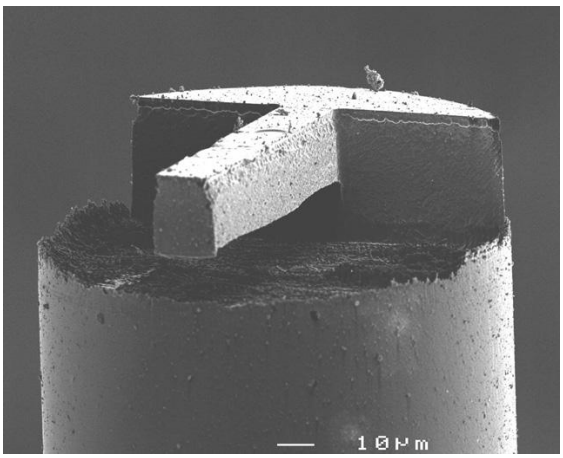

Figure 2.12 Fibre-top cantilever machined by femtosecond laser under SEM ([2.48]).

The whole manufacturing time by using this technique is ~90 minutes. It has potential for mass production, since the laser processing time can be optimized to be on the order of 1 minute with the aid of automatic setup alignment. Furthermore, multiple fibres can be laser machined and wet etched simultaneously. However, the surface finish by using this technique is not optimum for optical interrogation.

2.4.6 Ferrule-top micromachined micro-cantilever

FIB milling provides sufficient machining resolution however it is not suitable for cost-effective mass production due to its slow machining process. On the other hand, laser machining technique doesn't quite achieve sufficient resolution for most of the applications where fibre-top sensors may be used. An all-optical micro-machined device obtained by carving a rectangular mechanical beam out of the end of a ferruled optical fibre is proposed [2.50]. The device offers the advantage of a much lower production cost. A standard single-mode optical fibre is inserted and glued into a cylindrical ferrule made out of glass. The outer diameter of the ferrule is typically 1.8

mm. The diameter of the hole along the axis of the cylinder is 127μm. The ferrule is machined by a ps-laser to form a rectangular cantilever at the tip with mm dimension [2.50] . Figure 2.14 shows the side view of machined structure and also a 3D model of cantilever indicating the optimum machined result.

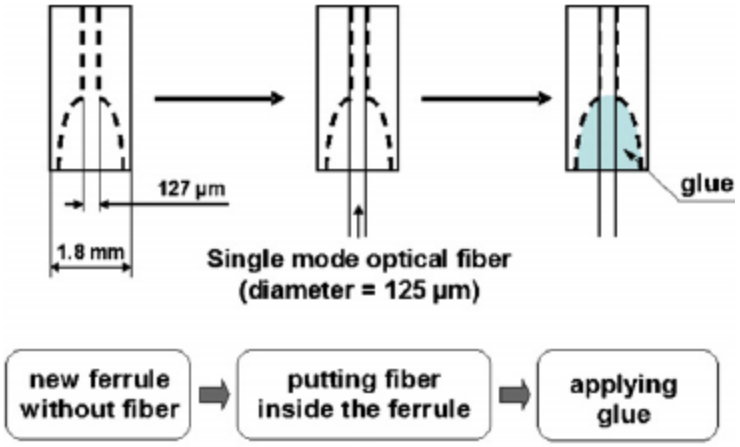

Figure 2.13 Fabrication process of ferruled fibre cantilever ([2.50]).

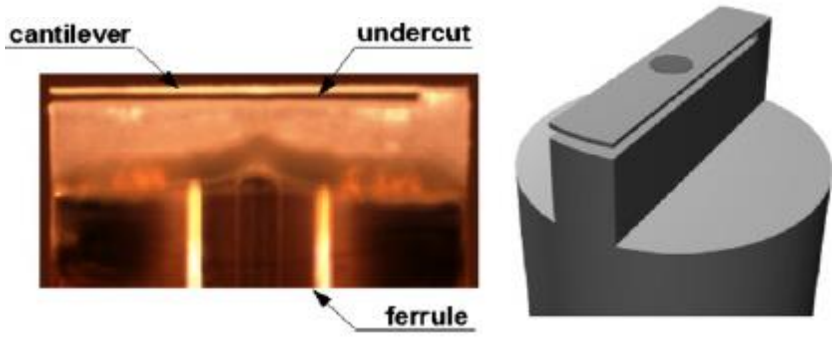

Figure 2.14 Microscope image (side view) and 3D model of the cantilever ([2.50]).

This new ferrule top optical fibre cantilever does have the same spring constant as the conventional micro-cantilever because of the dimension. In addition, the fabrication process presented here is very reproducible, thus making it a cost-effective way for industry application. However, the increased dimension compared with fibre-top cantilever limits the application of the sensor in space constrained environment.

2.4.7 Application of cantilever sensor: Casmir force measurement

By using the similar fabrication techniques to fabricate the ferrule-top cantilever, a Casimir force sensor is demonstrated by Iannuzzi *et al.* [2.51]. The sensor can be used to measure the gradient of the Casimir force between a gold-coated sphere and a

gold-coated plate by using the similar experiments achieved by AFM. The fabrication process and the resulting cantilever structure are illustrated in Figure 2.15. An optical fibre is inserted into the ferrule and machined to a rectangular cantilever structure. The detailed machining process can be found in the previous section.

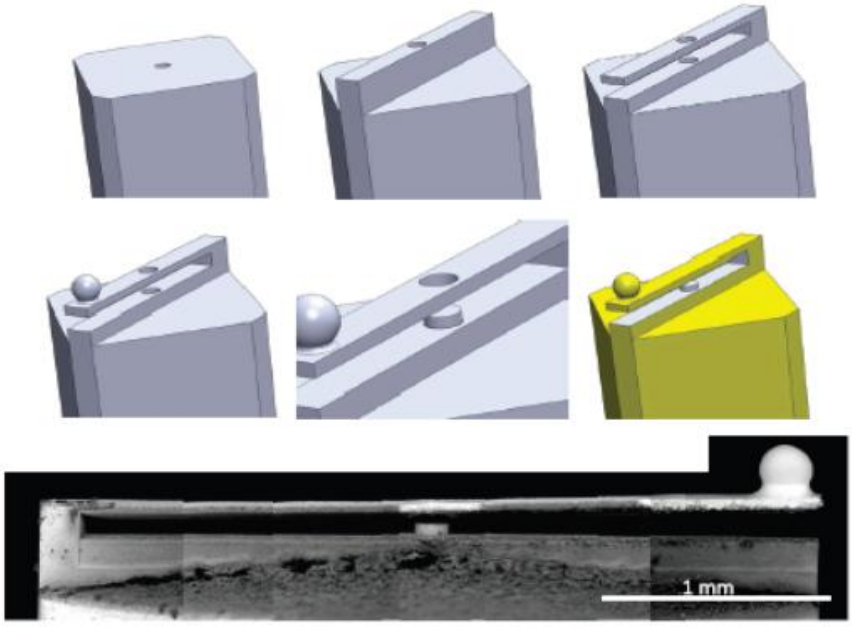

Figure 2.15 Fabrication steps for Casimir force measurement by ferrule-top cantilever, above: fabrication steps, below: side view of resultant ferrule-top cantilever structure ([2.51]).

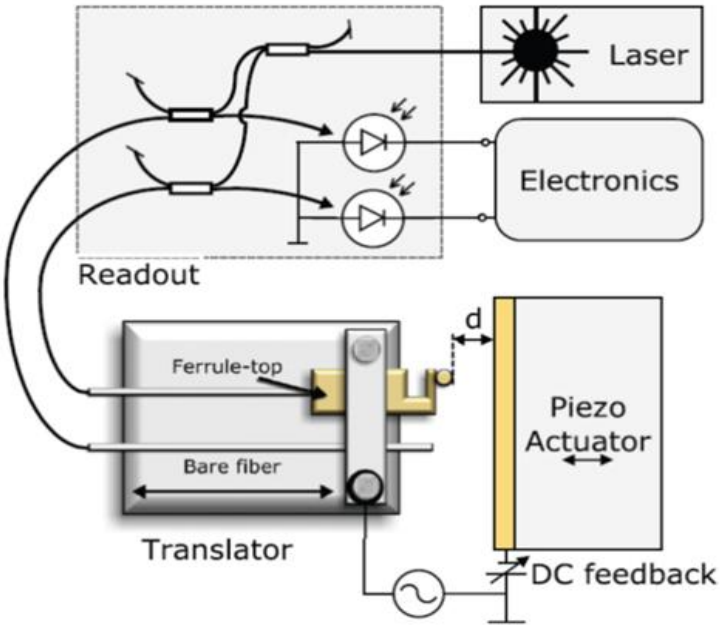

Figure 2.16 Sketch of experimental setup used to measure the Casimir force ([2.51]).

The Casimir force is measured between a plate and a sphere attached to the ferrule-top cantilever as shown in Figure 2.16. A laser is coupled into both the fibre and the cantilever. The detected optical signal is transformed to an electronic signal and processed for later use. The plate is attached to a piezoelectric stage for fine tuning the separation between the two interacting surface. Casimir force measurements are carried out following a method similar to that described in [2.51].

The benefit of this sensing design is that the sensor does not involve any electronics on the sensing head. Therefore, allowing future studies of the Casimir effect in engineering regardless of the measurement environments. A minor disadvantage is that the interrogation method mentioned in [2.52] needs to bring the measuring distance to quadrature point of Fabry-Perot (FP) spectrum, and precisely tune the laser wavelength to the quadrature point, in which case optical intensity fluctuation might be an issue.

2.4.8 Build up techniques (laser additive manufacturing)

Laser Additive Manufacturing (LAM) refers to a process by which a digital 3D model is used to build up a component in layers by depositing material. LAM overcomes the limits imposed by conventional production techniques. It is more flexible than traditional machining since AM builds up components layer by layer using materials which are available in fine powder form thereby is it possible to modify the internal structure of components.

With LAM, three-dimensional micro-photonic structures can be fabricated directly onto the end face of an optical fibre using the cross-linkable resist SU-8. A fabrication process developed in [2.53] can be described as follows: mount (Figure 2.17A) an optical fibre to be affixed and positioned within a vacuum-baked SU-8 resin at a targeted depth, then transferred onto a three-axis nano-positioner for laser machining. Micro-optical structures can be fabricated onto the end of a single-mode fibre by dipping the fibre into the resin. The resin mold was then transferred to a hot plate heated and cooled down to form the final structure. The whole process can be found in Figure 2.17.

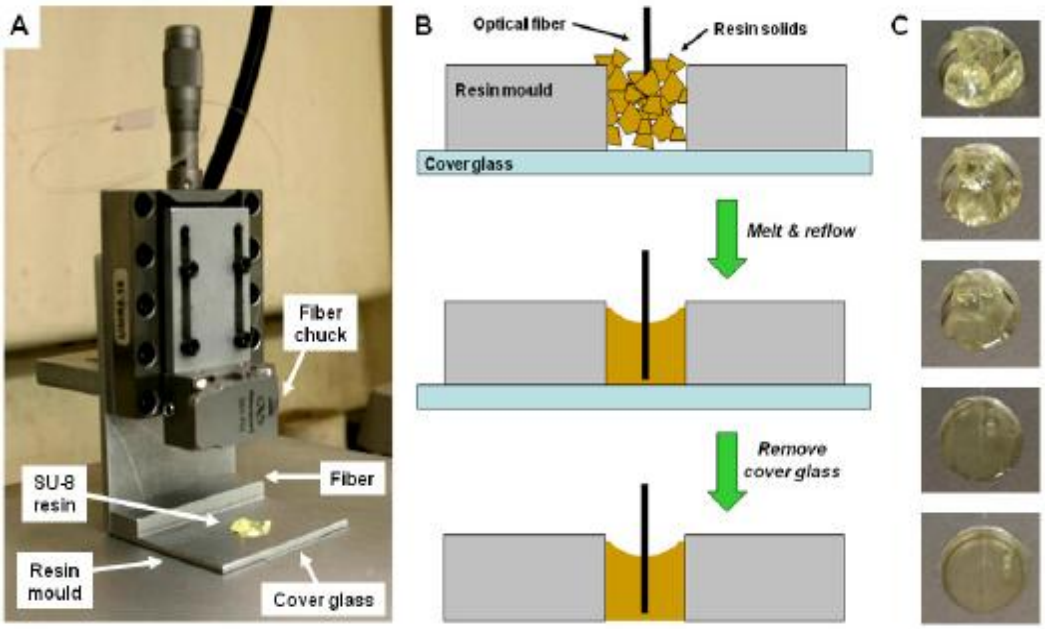

Figure 2.17 Fabrication procedures to create three dimensional structure onto the end facet of an optical fibre [2.53].

The next step is to photo-pattern micro-optic devices, using a computer program to control the exposed pattern. After that, samples are baked to cross-linking temperature. Then structure is cooled down and cleaned, leaving a free-standing micro-structure remained on the substrate. The SEM images of different micro-structures created on the end of an optical fiber by in SU-8 resin are shown in Figure 2.18.

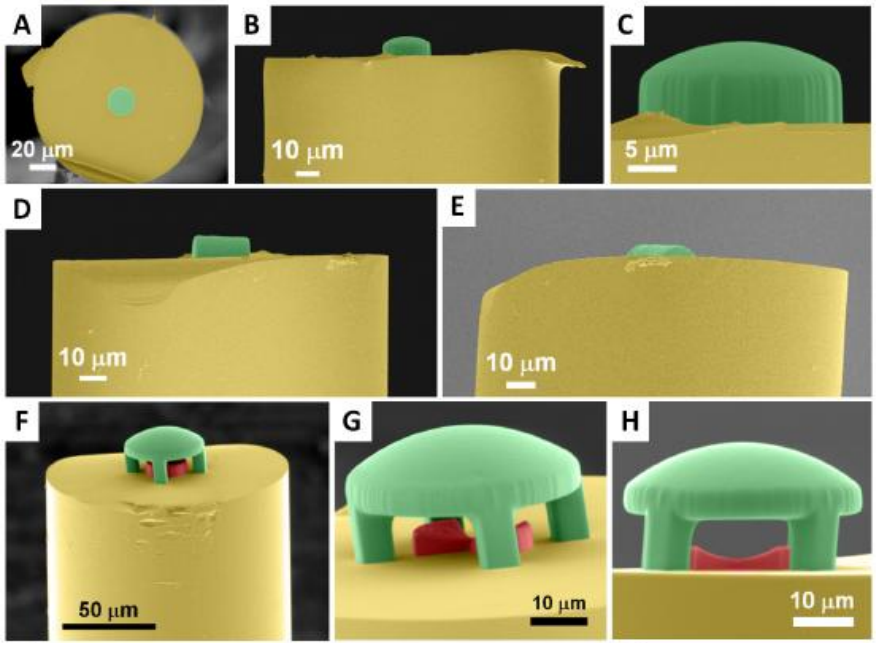

Figure 2.18 (A C) Plano-convex lens having radius of curvature R = + 18.3μm viewed (A) down the fiber axis and (B, C) from the side. (D, E) Cylindrical lens having R = +15.7μm. (F) - (H) Compound micro-optic system consisting of a suspended plano-convex lens [2.53].

This fabrication method can be used to create new micro-optical structures with a high degree of undercut and complex shape directly onto an optical fibre. Similar techniques could be employed to build up micro-cantilevers on top of an optical fibre. However, at the moment, most of the materials to be fabricated are polymer resins, which limit further applications of silicon and metals based micro-devices.

2.4.9 Summary

Other fabrication techniques which can be used to manufacture a micro-cantilever include EDM (Electro Discharge Machining) [2.54] and LIGA [2.55] (Lithographie, Galvanoformung, Abformung). In many cases, several technologies can be combined together to fabricate a single sensor. Below is a table of major techniques that can be used to machine micro-cantilever structure. It summarises the advantages and disadvantages of the major fabrication technologies (Table 2.3).

Table 2.3 Summary of advantages and disadvantages of major micro-machining technologies.

	Advantage	*Disadvantage*
Optical lithography	*High precision (Extreme Ultra Violet up to 26nm)* *Mass production* *Suitable for industry, repeatable*	*Resolution is confined by diffraction limit, multi-step process, time-consuming*
LIGA	*High precision* *Machine complicated structure* *High aspect ratio*	*High cost* *Not compatible with standard integrated circuit fabrication*
EDM	*Ability to machine almost all conductive materials of any hardness* *Small feature size* *Less debris*	*Slow material removal rate* *Difficult to be repeatable* *High power consumption* *Not suitable for dielectric*
FIB	*High precision* *Optical surface finish*	*Not suitable for narrow line cut* *Slow processing rate* *Sample need to be conductive*
Laser micromachining	*Fast and easy* *Cost-effective* *High material remove rate*	*Relatively low repeatability* *Thermal damage* *Contamination on the surface*

2.5 Interrogation techniques for micro-cantilever

2.5.1 Piezoresistive method

Several interrogation techniques have been proposed to measure cantilever deflection or resonant vibration. One popular method is to use piezoresistive materials as the sensing element [2.56]. Piezoresistive materials allow a straightforward way to convert bending signal, i.e. surface strain of micro-cantilever to an electrical output. The principle uses the resistivity changes of piezoresistive elements to allow measurement of differential surface stress. A piezoresistive material is embedded near the top surface of the cantilever to record the stress change occurring at the surface of the cantilever. As the micro-cantilever deflects, it suffers a stress change that will apply strain to the piezoresistor, thereby causing a change in resistance that can be measured by electronic means. The piezoresistor material in the beam must be put as close to one surface of the cantilever as possible for maximum sensitivity. The relative change in resistance as function of applied strain can be written as:

$$\frac{\Delta R}{R} = K_l K_t \delta \tag{2.12}$$

where K denotes the gauge factor, which is a material parameter. R is the resistance and ΔR is the change of resistance. L and t refers to the longitudinal, the transversal part of the gauge factor and δ is the strain in the material. The sensitivity of a piezoresistor varies proportionally to the thickness t and the radius of curvature. The gauge factor is proportional to Young's Modulus E, which is the intrinsic characteristic of material. The gauge factor can also be calculated directly by straining the cantilevers and measuring the resistance change.

$$K\delta = \frac{\Delta R}{R} \tag{2.13}$$

K is the total gauge factor. The piezoresistive cantilever beam can be used as an arm of the wheatstone bridge circuit as shown in Figure 2.19.

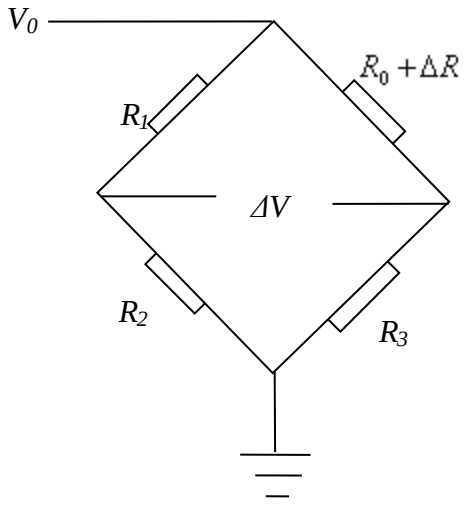

Figure 2.19 The Wheatstone bridge circuit used for the piezoresistive micro-cantilever. V_0 is the input voltage while ΔV is the output voltage change. R_1, R_2, R_3 and $R_0 + \Delta R$ are the resistance in each arm.

The resistance of the variable resistance arm $R_0 + \Delta R$ in the above figure can be determined by using the common Voltage divider formula [2.57]:

$$\Delta V = V_0 \left\{ \frac{R_2}{R_1 + R_2} - \frac{R_3}{R_0 + \Delta R + R_3} \right\} \tag{2.14}$$

$$R_0 + \Delta R = R_3 \left\{ \frac{V_0 (R_1 + R_2)}{R_2 V_0 - \Delta V (R_1 + R_2)} - 1 \right\} \tag{2.15}$$

By detecting the voltage change ΔV (due to a resistance change whenever the cantilever is subjected to a deflection), the mechanical stress of the cantilever can be deduced.

The advantage of the piezoresistive method is that the readout system can be integrated easily while the disadvantage is that the electric readout current is affect by changes in ambient temperature. Furthermore, the electrical method can be sensitive to electronic noise pickup, particularly in an electromagnetic environment.

2.5.2 Optical Beam deflection measurement technique

As a result of the drawbacks of electronic interrogation techniques, researchers started to find other possible approaches to address the issues. An optical read-out method was developed to measure the bending signal. The most widely used technique is

called the optical beam deflection method [2.58]. The technology uses a Position Sensitive Detector (PSD) to measure the position of a cantilever surface with a reflected beam. The position of the beam spot on the PSD encodes the surface stress induced deflection of the cantilever. The technology is highly sensitive with a deflection measurement resolution usually up to ~nm. However, it usually needs precise alignment, while the measurement equipment is usually bulky and complicated thus limits its application.

The optical beam deflection method is a popular way to detect the bending information by using a PSD. The main sensing configuration is shown in Figure 2.20. A diode laser beam with low power is introduced; therefore, it does not affect the biomolecular coating on the surface of the micro-cantilever. The laser beam falls on the cantilever and reflects from the gold coated cantilever top surface. The PSD receives the light reflected from the cantilever surface. When the cantilever is at zero position, i.e. it is not coated with any molecule, the laser beam would fall on a particular region on the PSD, when the cantilever deflects, the position of the beam changes, which in turn, will fall on another location on the PSD. The position information will be converted to electrical signal and then converted to cantilever deflection.

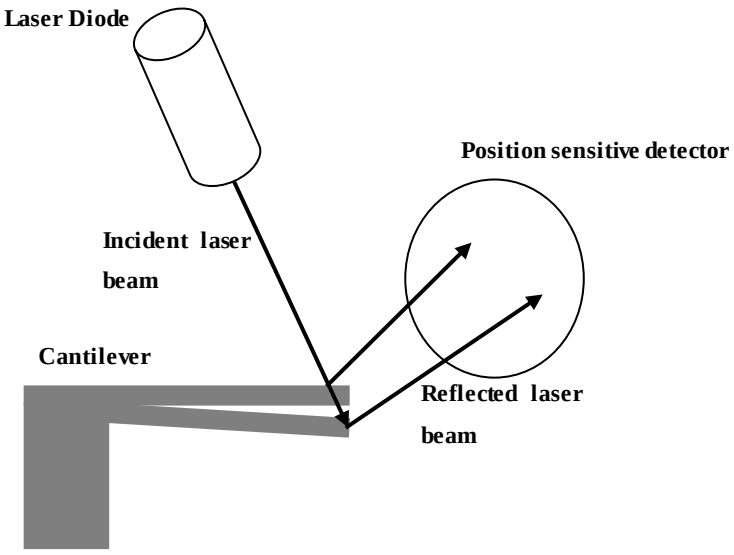

Figure 2.20 Schematic diagram of an optical beam deflection system.

The advantage of this detection system is that it is capable of detecting deflection in the sub-nanometer range. However, the presence of the focused laser beam in a liquid cell environment can result in additional thermal management issues giving rise to extraneous readings. Secondly, the alignment system is expensive and involves great precision, which can ultimately raise the cost of the whole detection system.

To address these problems, an interferometer readout method is proposed by creating a Fabry Perot cavity onto the end of an optical fibre. The benefit of such a device is that it does not require any mechanical alignment procedure. In addition, nm detection resolution can be achieved as a result of the high sensitivity of the interferometry technique [2.59]. The idea can be further expanded to micro-cantilever arrays, where the deflection measurement range is improved to sub-nanometer [2.60].

2.5.3 Interferometic method

The limitations of the traditional optical beam deflection methods can be overcome by using the interferometric arrangement. Normally an optical fibre is set a few microns away from the free end of the micro-cantilever to measure deflection in the range of 0.01 Å [2.61]. Examples of this include a Fabry-Perot interferometer that is set up to reliably read out the bending of micro-cantilever arrays in liquid and gaseous environments [2.62]. Interferometric methods are highly sensitive while providing a direct and absolute measurement of displacement. However, the positioning of the fibres sometimes remains a difficult task.

2.5.4 Optical intensity based interrogation

An alternative route to interferometry is to use an intensity based measurement approach. An example of this is presented by Su and Elliot [2.63] who demonstrated a low-cost, high-sensitivity, all-fibre micro-cantilever sensor, fibre-to-tip micro-cantilever sensor (FTMS) (Figure 2.21). In their design, an nm size fibre tip serves as both micro-cantilever and miniaturized light probe. A sub-nanometer displacement of the fibre-top cantilever is achieved by measuring the light intensity that it receives from an aligned single-mode fibre (SMF). An estimated resolution of 2 Å could be

implemented to detect very small vibration signal and opens new methods for inexpensive fibre-optic micro-cantilever sensing. However the design is susceptible to any other intensity variation for the whole optical system.

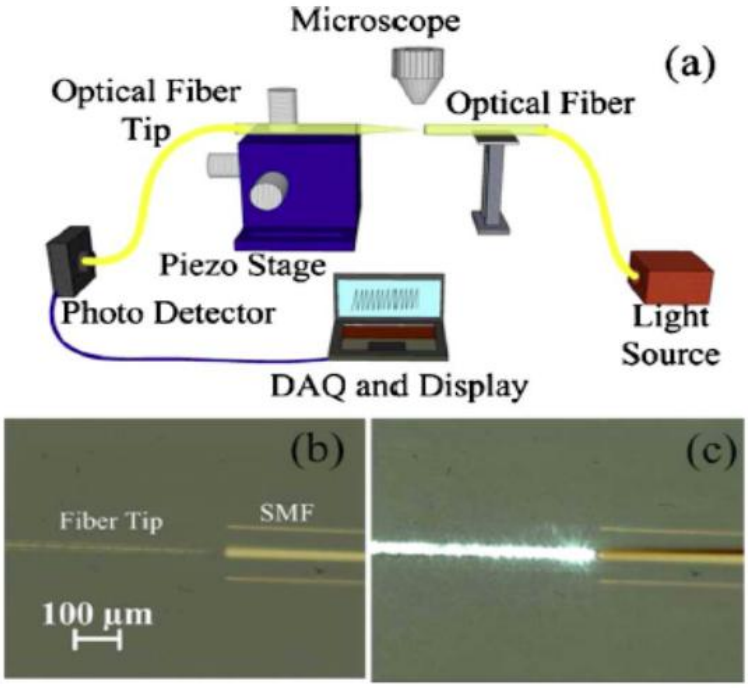

Figure 2.21 Experimental setup of fibre tip cantilever: (a) experiment set-up, (b) Microscopic view of aligned fibre tip with SMF, (c) Microscopic image when transmitting light from SMF to a tapered optical fibre [2.63].

In summary, micro-cantilever interrogation techniques can be categorized mainly as either electronic or optical readout methods. Electronic readout is not always compatible with the environment where measurements must be performed. Furthermore, the fabrication often involves complicated and expensive processes. On the other hand, optical fibre techniques can easily combine the sensing probe and interrogation as a single element. They can also survive in harsh environment. However, the technology generally requires an inconvenient alignment procedure that can represent a major technical challenge for applications beyond standard experiments.

2.6 Interferometer interrogation techniques

In this section, the basic idea of interferometer interrogation techniques will be briefly reviewed. Detailed discussion of interferometer interrogation techniques will be covered in Chapter 3.

2.6.1 Free spectral range detection method

Most commonly the absolute cavity length is determined using a white-light interferometer (WLI). Here a broadband source (BBS) is injected into the optical cavity (in our case the fibre-optic FP sensor). The absolute cavity length can be obtained by measuring the peak wavelengths spacing between two adjacent peaks. Suppose λ_1, λ_2 are two adjacent peak wavelengths (see Figure 2.22). According to the interference theory, we have:

$$\frac{4\pi}{\lambda_1} L = (2m_1 - 1)\pi \tag{2.16}$$

$$\frac{4\pi}{\lambda_2} L = (2m_2 - 1)\pi \tag{2.17}$$

where L is the absolute cavity length, m_1 and m_2 are the two neighbouring fringe numbers and have the following relationship:

$$m_1 = m_2 + 1 \tag{2.18}$$

In this case, L can be derived by the following equation:

$$L = \frac{\lambda_1 \lambda_2}{2n(\lambda_2 - \lambda_1)} \tag{2.19}$$

where n is the refractive index of measured material. From equation 2.19 we know that the FP cavity length can be calculated by reading the adjacent peak wavelengths. The advantage of the peak-to-peak method is that the output sensing signal is in wavelength, thus it's not affected by intensity fluctuations due to optical source fluctuation and changes in connecting fibre losses, connectors, etc. In addition, the interrogation doesn't involve complicated mathematical calculation. However, the peak-to-peak algorithm has some drawbacks. First of all, the resolution of the algorithm is determined by the resolution of optical spectrum analyser (i.e. the means of determining the peak wavelengths). Secondly, the spectral profile of the broad band source is typically not flat. Therefore, the actual peak wavelength position of interfered signal

will deviate from the real position and add an error on the measured cavity length. A modified algorithm is proposed by Zhang *et al.* to reduce the effect of light source profile [2.64]. The algorithm is demonstrated to have improved the demodulation accuracy significantly.

Another way to solve this problem is to make use of more of the available data using the Fast Fourier Transformation (FFT) algorithm which will be discussed in the following section.

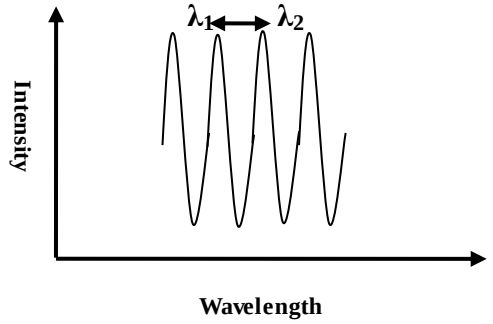

Figure 2.22 Schematic diagram of Peak-to-Peak method to determine the cavity length. λ_1, λ_2 are two adjacent peak wavelengths of a Fabry-Perot spectrum.

2.6.2 Fast Fourier Transformation interrogation method

The FFT algorithm was first proposed by the Cooley and Tukey in 1965 [2.65]. The algorithm soon gained wide application in signal analysis, image processing and many computation science fields. In the optic fibre sensor field, the FFT has been employed for interrogation of FP cavities [2.66]. When a WLI is considered, the output signal can be treated as two beam interference. Thus the intensity of interfered signal *I* can be expressed by the following equation:

$$I = C + V\cos(2\pi \cdot 2L\frac{1}{\lambda} + \pi) \qquad (2.20)$$

Where *C* is a constant value, *V* is the visibility of the fringes and *L* is the measured FP cavity length. From equation 2.20 we know that the spacing between each fringe will decrease as measured cavity length increases. The real cavity length of FP by calculating the FFT peak frequency can be written as:

$$\frac{1}{\lambda} = \frac{v}{c} \tag{2.21}$$

where v is the frequency of the light beam, c is the speed of light. From equation 2.20 and equation 2.21 we have:

$$I = C + A\cos(2\pi \cdot 2L\frac{v}{c} + \pi) \tag{2.22}$$

Assuming that v is an independent variable, by using FFT, the frequency f_L of the above function can be derived:

$$f_L = \frac{2L}{c} \tag{2.23}$$

So the cavity length L can be easily derived from the above equation:

$$L = \frac{cf_L}{2} \tag{2.24}$$

Compared with the peak-to-peak method, the FFT interrogation algorithm greatly reduces the *DC* noise, at the same time there is no signal distortion due to the spectrum fluctuation. By increasing the FFT sampling number, the calculated FFT frequency peak will be more accurate and this will reduce the measurement error of the cavity length.

2.6.3 Discrete Gap Transformation Algorithm

The Discrete Gap Transformation (DGT) algorithm was first proposed by Musa in 1997 [2.69]. The algorithm calculates the cavity length by transforming the wavelength information into frequency domain. The optical intensity signal in frequency domain can be written as:

$$I(L) = \int_{-\infty}^{+\infty} I^{(r)}(v)\exp(j\frac{4\pi L}{c} + \pi)dv \tag{2.25}$$

Where $I(L)$ is optical intensity related with cavity length and $I^{(r)}(v)$ is the optical intensity as a function of v. Combining with equation 2.21, we have:

$$I(L) = \int_{-\infty}^{+\infty} I^{(r)}(\frac{c}{\lambda}) \exp(j\frac{4\pi L}{\lambda} + \pi) d(\frac{c}{\lambda}) \qquad (2.26)$$

Using discrete value to replace L and λ:

$$I(L_m) = \sum_{n=1}^{N} I^{(r)}(n) \exp(j\frac{4\pi L_m}{\lambda_n} + \pi) \qquad (2.27)$$

L_m is the transformation cavity length of FP , $I^{(r)}(n)$ is the interfered spectrum intensity in accordance with λ_n, which is the n^{th} wavelength of the whole spectrum. If we square the absolute value of the intensity signals:

$$\left|I(L_m)\right|^2 = \left|\sum_{n=1}^{N} I^{(r)}(n) \cos(j\frac{4\pi L_m}{\lambda_n} + \pi)\right|^2 + \left|\sum_{n=1}^{N} I^{(r)}(n) \sin(j\frac{4\pi L_m}{\lambda_n} + \pi)\right|^2 \qquad (2.28)$$

The above equation will generate a maximum value when $L_m = L$, here L is the real cavity length. DGT realizes the direct transfer from wavelength to cavity length. Therefore it's more straightforward than the FFT algorithm. In addition, DGT doesn't require a rigorous sampling process, thus reduces much of the error produced by an FFT. However, the drawback of the DGT is obvious. There is no fast algorithm with DGT, which means that it will take longer to calculate, therefore, it's not suitable for practical use.

2.7 Summary and discussion

The optical fibre cantilever sensors reviewed in this chapter were initially designed to investigate real time biological binding process that can be used for new drug discovery and food pathogen detection. Conventional biosensors are capable of detecting the binding between each bio-molecule, however, they usually need several days and multi-steps processes. Furthermore, in some cases, the sensitivity of the sensor doesn't meet the application requirement. Therefore, a sensor which can monitor the binding process with a shorter response time and high sensitivity while keeping the process simple and easy would be ideal. Because of the advantages of optical fibre sensor, these requirements have become practical: investigating the possibility of making a

cantilever onto a single mode optical fibre. In this case, measurement can be finished by detecting the binding induced deflection that applied onto the cantilever surface. The design of cantilever structures onto an optical fibre has brought the challenge of fabricating this small element with good optical and mechanical proprieties. For this purpose, different fabrication techniques for making micro-cantilever structures are reviewed. Optical lithography is a useful technique for semiconductor industrial mass production, however, within the dimension of a standard single mode optical fibre, it is difficult to produce cantilevers with good mechanical properties for bioanlyte binding. Previous studies have shown that FIB techniques to manufacture small feature size with optical surface finish are possible. Some of them have demonstrated the possibility of using this technique to produce a single cantilever device onto optical fibres, however, the process is slow and expensive thus makes it unsuitable for mass production. Therefore, it is necessary to investigate new fabrication techniques that can not only address the previous issues but are also potentially suitable for industrial mass production.

It is important to investigate interrogation techniques for optical fibre cantilever sensors, since this will determine the suitable resolution for the cantilever deflection measurement. To assess the techniques, both electronic and optical interrogation approaches are reviewed in this chapter. Traditional electronic approaches using piezoresist are capable of high sensitivity measurement, but are generally not suitable for operation in a liquid environment. Optical beam deflection approach is a good candidate to solve this problem. With a cheap laser diode sending a beam onto the reflecting cantilever surface, the beam can be detected and processed by a PSD with nm deflection resolution. However, the alignment of the laser beam with respect to the cantilever surface makes the system time-consuming to construct. In addition, the whole system is bulky compared with an optical fibre, which sometimes is less competitive for commercial sensor requirements. With this motivation, the approach of combining cantilever structures with interrogation by an optical fibre is proposed in this thesis to meet the sensing requirement for bioanalyte binding. Based on this

structure, temperature and pH sensing is explored. To further extend the sensing capability, multi-axis cantilever accelerometer is also design and manufactured for sensing in a space constrained environment.

2.8 Conclusion

In conclusion, the general concept of sensing was introduced in this chapter and followed by the discussion of a more advanced biosensor and fibre optic sensor. For the purpose of finding the presence of specified bioanalyte and the interaction between different biomolecule, optical fibre cantilever sensors are proposed as a micro-mechanical transducer to transfer biological energy into mechanical force.

In the following chapters, interrogation techniques together with different applications of optical fibre cantilever sensors, e.g. biomolecule binding, chemical sensing and acceleration measurement will be investigated. The detailed design and fabrication techniques of optical fibre cantilever sensors developed in this thesis for this range of applications will be described. Proof-of-concept demonstration of optical fibre cantilever based sensors will be presented for temperature, acceleration, pH and biological binding measurement.

References

[2.1] M Pohanka, P Skladal, and M Kroca, "Biosensors for biological warfare agent detection", *Defence Science Joural,* vol. 57, pp.185-93, 2007.

[2.2] Y Liu, Z H Qin, X F Wu, and H Jiang, "Immune-biosensor for aflatoxin B_1 based bio-electrocatalytic reaction on micro-comb electrode", *Biochemical Engineering Journal*, vol. 32, pp.211-217, 2006.

[2.3] E Engvall and P Perlmann, "Enzyme-linked immunosorbent assay (ELISA) quantitative assay of immunoglobulin G", *Immunochemistry* vol.8, pp.871-874, 1971.

[2.4] H C Chen and T C Chang, "Rapid detection of Vibrio parahaemolyticus in oysters by immunofluorescence microscopy", *International Journal of Food Microbiology,* vol. 29, pp. 311-319, 1996.

[2.5] A G Krause, M Winger, T D Blasius, Q Lin, and O Painter, "A microchip optomechanical accelerometer", *Nature Photonics* , vol. 6, pp.768-772, 2012.

[2.6] Y J Rao, "Recent progress in applications of in-fibre Bragg grating sensors", *Optics and Lasers in Engineering*, vol.31, pp.297-324, 1983.

[2.7] P M Nellen, P Maurona, A Frank, U Sennhauser, K Bohnert, P Pequignot, P Bodor and H Brändle, "Reliability of fiber Bragg grating based sensors for downhole applications", *Sensors and Actuators A: Physical,* vol.103, pp.364–376, 2003.

[2.8] P D Foote, "Fiber Bragg Grating strain sensors for aerospace smart material", *Proceeding of Second European Conference on Smart Structures and Materials*, vol.2361, 1994.

[2.9] B Lee, "Review of the present status of optical fiber sensors", *Optical Fiber Technology*, vol.9, pp.57-59, 2003.

[2.10] B Culshaw, "The optical fibre Sagnac interferometer: an overview of its principles and applications," *Measurement Science of Technology,* vol.17, 2006.

[2.11] J C Knight, "Photonic crystal fibres", *Nature* , vol.424, pp.847-851, 2003.

[2.12] H F Wei, H W Chen, S P Chen, P G Yan, T Liu, L Guo, Y Lei, Z L Chen, J Li, and X B Zhang, "A compact seven-core photonic crystal fiber supercontinuum source with 42.3 W output power", *Laser Physics Letters,* vol.10, pp.045101-045108, 2013.

[2.13] L Rindorf, J B Jensen, M Dufva, L H Pedersen, P E Høiby, and O B L Rindorf, "Photonic crystal fiber long-period gratings for biochemical sensing", *Optics Express*, vol.14, pp.8224-8231, 2006.

[2.14] E Shi, J L Yang, T Ono and Masayoshi, "Mechanical behavior of ultrathin microcantilever", *Sensors and Actuators A: Physical,* vol. 88, pp.102-107, 2000.

[2.15] G Binnig, C F Quate, and C Gerber, "Atomic force microscope", *Physics. Review Letters,* vol. 56, pp. 930-933, 1986.

[2.16] W Xiang and C Lee, "Nanophotonics sensor based on microcantilever for chemical analysis", *IEEE Journal of selected topics in Quantum Electronics*, vol. 15, pp.1323-1326, 2009.

[2.17] D Iannuzzi, S Deladi, V J Gadgil, R G P Sanders, H Schreuders and M C Elwenspoek, "Monolithic fiber-top sensor for critical environments and standard applications", *Applied Physics Letters,* vol. 88, pp.053501-053503, 2006.

[2.18] R Bashira, J Z Hilt, O Elibol and A Gupta, "Micromechanical cantilever as an ultrasensitive pH microsensor", *Applied Physics Letters,* vol.81, pp.3091-3093, 2002.

[2.19] R Raiteri, and M Grattarola, "Micromechanical cantilever-based biosensors", *Sensors and Actuators B,* vol.79, pp.115-126, 2001.

[2.20] M Su, S Y Li, and V P Dravid, "Microcantilever resonance-based DNA detection with nanoparticle", *Applied Physics Letter,* vol. 82, pp.3562-3564, 2003.

[2.21] J H Pei, F Tian, and T Thundat, "Glucose Biosensor Based on the Microcantilever", *Analytical Chemical,* vol. 76, pp. 292-297, 2004.

[2.22] J J Gooding, "Biosensor technology for detecting biological warfare agents: Recent progress and future trends", *Analytica Chimica Acta,* vol.559, pp.137-151, 2006.

[2.23] P Li and X X Li, "A single-sided micromachined piezoresistive SiO2 cantilever sensor for ultra-sensitive detection of gaseous chemicals", *Journal of Micromechanics and Microengineering,* vol.16, pp.2539-2551, 2006.

[2.24] N V Lavrik, "Cantilever transducers as a platform for chemical and biological sensors", *Review of Scientific Instrument ,* vol. 75, pp. 2229-2238, 2004.

[2.25] T Thundat, R J Warmick, G Y Chen, and D P Allison, "Thermal and ambient-induced deflections of scanning force microscope cantilevers", *Applied Physics Letters,* vol. 64, pp.2894-2896, 1994.

[2.26] Stoney G G , "The Tension of Metallic Films Deposited by Electrolysis," *Proceeding of Royal Society,* London, 1909.

[2.27] S K Vashist, "A Review of Microcantilevers for Sensing Applications", *Journal of Nanotechnology,* vol.3, pp.1-18, 2007.

[2.28] A N Boto, "Quantum Interferometric Optical Lithography: Exploiting Entanglement to Beat the Diffraction Limit", *Physics Review Letters,* vol. 85, pp.2733-2736, 2000.

[2.29] F H Dill, "Optical lithography", *IEEE Transactions on Electron Devices,* vol. 22, pp.440-444, 1975.

[2.30] K B Gavan, J H Rector, K Heeck, D Chavan, G Gruca, T H Oosterkamp, and D Iannuzzi, "Top-down approach to fiber-top cantilevers", *Optics Letters,* vol.36, pp. 2898-2900, 2011.

[2.31] J Melngailis, "Focused ion beam technology and applications", *Journal of Vacuum Science & Technology B: Microelectronics and Nanometer Structures ,* vol. 5, pp. 469-495, 1987.

[2.32] S Reyntjens and R Puers, "A review of focused ion beam applications in microsystem technology", *Journal of Micromechanics and Microengineering,* vol. 11,pp.287-293, 2001.

[2.33] J Sun, X Luo, J Ritchie, and T Hrncir, "A predictive divergence compensation approach for the fabrication of three-dimensional microstructures using focused ion beam machining", *Proceedings of the Institution of Mechanical Engineers, Part B: Journal of Engineering Manufacture,* vol. 12, 2011.

[2.34] S Deladi, D Iannuzzi, V J Gadgil, H Schreuders, and M C Elwenspoek, "Carving fiber-top optomechanical transducers from an optical fiber", *Journal of Micromechanics and Microengineering,* vol.16, pp. 886-895, 2006.

[2.35] C A Volkert and A M Minor, "Focused Ion Beam Microscopy and Micromachining", *MRS bulletin,* vol.32, pp.389-399, 2007.

[2.36] C Martelli, P Olivero, J Canning, N Groothoff, B Gibson, and S Huntington, "Micromachining structured optical fibers using focused ion beam milling", *Optics Letters,* vol.32, pp. 1575-1577, 2007.

[2.37] M V Bibra, J Canning, and A Roberts, "Mode profile modification of H^+ ion beam irradiated waveguides using UV processing", *Journal of Non-Crystalline Solids,* vol.239, pp.121-125, 1998.

[2.38] J L Kou, J Feng, Q J Wang, F Xu and Y Q Lu, "Microfiber-probe-based ultrasmall interferometric sensor", *Optics Letters,* vol.35, pp. 2308-2310, 2010.

[2.39] D Iannuzzi, K Heeck, M Slaman, S de Man, J H Rector, H Schreuders, J W Berenschot, V J Gadgil, R G P Sanders, M C Elwenspoek, and S Deladi, "Fibre-top cantilevers: design, fabrication and applications", *Measurement Science and Technology,* vol.18, pp.3247-3252, 2007.

[2.40] J Jandeleit, A Horn, R Weichenhain, E W Kreutz, R Poprawe, "Fundamental investigations of micromachining by nano- and picosecond laser radiation", *Applied Surface Science,* vol.97, pp. 885-891, 1998.

[2.41] R R Gattass and E Mazur, "Femtosecond laser micromachining in transparent materials", *Nature Photonics,* vol.2, pp. 219-225, 2008.

[2.42] X Liu, D Du, and G Mourou, "Laser ablation and micromachining with ultrashort laser pulses", *IEEE Journal of Quantum Electronics,* vol.33, pp.1706-1716, 2002.

[2.43] A K Dubey and V Yadava, "Laser beam machining—A review", *International Journal of Machine Tools & Manufacture,* vol. 48, pp.609-628, 2008.

[2.44] M R H Knowles, G Rutterford, D Karnakis, T Dobrev, P Petkov, and S Dimov, "Laser mirco-milling of ceramics, dielectrics and metals using nanosecond and pico-second lasers", *Proceedings of International Conference,* vol.6457, pp.645711-645723, 2006.

[2.45] T L Perry, D Werschmoeller, N A Duffie, X Li, and F E Pfefferkorn, "Examination of Selective Pulsed Laser Micropolishing on Microfabricated Nickel Samples Using Spatial Frequency Analysis", *Journal of Manufacturing Science and Engineering,* vol.131, pp.3075847-3075862, 2009.

[2.46] P V Petkov, S S Dimov, R M Minev, and D T Pham, "Laser milling: pulse duration effects on surface integrity", *Proceeding of Institute of Mechanical Engineering Part B: Journal of Engineering Manufacture,* vol.222,pp.35-45 , 2008.

[2.47] T Dobrev, D T Pham, and S S Dimov, "Techniques for improving surface quality after laser milling", *Proceeding of Institute of Mechanical Engineering Part B:*

Journal of Engineering Manufacture, Special issue paper, vol.222, pp.55-65, 2008.

[2.48] A A Said, M Dugan, S de Man and D Iannuzzi, "Carving fiber-top cantilevers with femtosecond laser micromachining", *Journal of Micromechanics and Microengineering,* vol. 18, pp. 035005-035012 , 2008.

[2.49] G Gruca, S de Man, M Slaman, J H Rector and D Iannuzzi, "Ferrule-top micromachined devices: design,fabrication, performance", *Measurement Science and Technology,* vol. 21, pp.094033-094045, 2010.

[2.50] P Zuurbier, S de Man, G Gruca, K Heeck and D Iannuzzi, "Measurement of the Casimir force with a ferrule-top sensor", *New Journal of Physics,* vol.13, pp.023027-023033, 2011.

[2.51] S de Man, K Heeck, and D Iannuzzi , "No anomalous scaling in electrostatic calibrations for Casimir force measurements", *Physics Review A,* vol.79, pp.024102-024104, 2009.

[2.52] J Thaysen, "Cantilever-based bio-chemical sensor integrated in a microliquid handling system**",** *IEEE International Conference on Micro Electro Mechanical Systems*", 2001

[2.53] H E Williams, D J Freppon, S M Kuebler, R C Rumpf, and M A Melino "Fabrication of three-dimensional micro-photonic structures on the tip of optical fibers using SU-8", *Optics Express*, vol.19, pp. 22910-22922 ,2011.

[2.54] T Masaki and R Matsushita, "Micro electro-discharge machining and its application", *Proceedings, An Investigation of Micro Structures, IEEE Sensors, Actuators, Machines and Robots*, pp.21-26, 1990.

[2.55] J Hruby, "LIGA Technologies and Applications", Cambridge University Press, vol.26, pp.337-340, 2001.

[2.56] S C Seel and C V Thompson, "Piezoresistive Microcantilevers for in-situ Stress Measurements During Thing Film Deposition", *Review of Scientific Instrument,* vol.76, pp.075103-075116, 2005.

[2.57] C Herrick, "Basic Electronics Math", Newnes, 1996.

[2.58] C A J Putman, B G D Grooth, N F V Hulst and J Greve, "A detailed analysis of the optical beam deflection technique for use in atomic force microscopy", *Journal of Applied Physics,* vol. 72, pp.6-12, 2009.

[2.59] D Iannuzzi, S Deladi, V J Gadgil, R G P Sanders, H Schreuders and M C Elwenspoek, "Monolithic fiber-top sensor for critical environments and standard applications", *Applied Physics Letters*, vol. 88, pp.053501-053503, 2006.

[2.60] S Fernando, "Extending the deflection measurement range of interferometric microcantilever arrays", *Journal of Microelectromechanical system*, vol.18, pp.480-487, 2009.

[2.61] S Manalis, S Minne, A Atalar, and C Quate, "Interdigital cantilevers for atomic force microscopy", *Applied Physics Letters*, vol. 69, pp.3944-3946, 1996.

[2.62] J Wehrmeister, A Fuß, F Saurenbach, R Berger and Mark Helm, "Readout of micromechnical cantilever sensor arrays by Fabry-Perot interferometry," *Review of Scientific Instrument*, vol. 78, pp.104105-104112, 2007.

[2.63] L Su and S R Elliott, "All-fiber microcantilever sensor monitored by a low-cost fiber-to-tip structure with subnanometer resolution", *Optics Letters*, vol.35, pp.1212-1214, 2010.

[2.64] W T Zhang, J Y Dai, B C Sun, Y L Du, "Study on Demodulation Algorithm of Fibre-optic Fabry-Perot Sensors based on spectrum adjusting", *Proceeding of SPIE*, vol.6830, 2008.

[2.65] J W Cooley, P A W Lewis, and P D Welch, "Historical notes on the fast Fourier transform", *Proceeding of IEEE*, vol.55, pp.1675-1677, 1967.

[2.66] Y Jiang, "Fourier Transform White-Light Interferometry for the Measurement of Fiber-Optic Extrinsic Fabry–Pérot Interferometric Sensors", *Photoincs Technology Letters*, vol. 20, pp.75-77, 2008.

[2.67] K B Gavan, J H Rector, K Heeck, D Chavan, G Gruca, T H Oosterkamp, and D Iannuzzi, "Top-down approach to fiber-top cantilevers", *Optics Letters*, vol.36, pp.2898-2900, 2011.

[2.68] D H Zhao, X F Chen, K M Zhou, L Zhang, I Bennion, W N MacPherson, J S Barton, and J D C Jones, "Bend sensors with direction recognition based on long-period gratings written in D-shaped fiber", *Applied Optics*, vol.43, pp.5425-5428, 2004.

[2.69] M A Farahani and T Gogolla , "Spontaneous Raman Scattering in Optical Fibers with Modulated Probe Light for Distributed Temperature Raman Remote Sensing", *Journal of Lightwave Technology*, vol.17, pp.1379-1391, 1999.

[2.70] S M Musa, "Real-Time Signal Processing and Hardware Development for a Wavelength Modulated Optical Fiber Sensor System", *PhD thesis*, Virginia Polytechnic Institute and State University, 1997.

Chapter 3

Cavity length measurement

In this thesis it is proposed to use interferometry to monitor the deflection of the cantilever. The optical cavity is formed between the cantilever and the end face of an optical fibre. In order to interrogate the deflection signal the cavity length between the cantilever surface and fibre end surface needs to be determined. The cavity length will change as the cantilever deflects. By monitoring the cavity length change, physical or chemical sensing parameters can be demodulated depending upon the means of sensitising the cantilever.

In this chapter, the fundamental principle of the Fabry-Perot (FP) interferometer, which is used for micro-cantilever interrogation, will be introduced first. Most of this is based on well-known FP interferometry, therefore it is important to review FP theory before moving on to the implementation and development for the particular application to cantilever sensors.

3.1 Optical Interferometry

In this thesis, an interferometer refers to an optical system that makes use of the principle of interfering light waves. Combining waves with the same frequency, the resulting pattern modulated by the phase difference between these waves can be divided to: waves that are in phase undergo constructive interference while waves that are out of phase undergo destructive interference. By using interfermetery method, precise measurements of very small distances and thicknesses can be measured, including surface roughness in optical devices such as mirrors. There are many different types of optical interferometer including Mach-Zehnder interferometer [3.1], Sagnac interferometer [3.2], Michelson interferometer [3.3], and Twman-Green interferometer [3.4].

A simple case of optical Michelson interferometer is shown in Figure 3.1. A single incoming beam from a coherent light source is split into two identical beams by a beam splitter (a partially reflecting mirror). Each of these beams travels a different route, and recombined before arriving at a detector. The path difference, which is the difference in the distance traveled by each beam, creates a phase difference $\Delta\varphi$ between the two beams. The observed intensity I is a function related to this phase difference and is given by [3.5]:

$$I = I_1 + I_2 + 2\sqrt{I_1 I_2}\cos\frac{4\pi n\Delta L}{\lambda} \tag{3.1}$$

I_1 and I_2 are the intensity of the two interfered arm respectively. ΔL is the optical path difference, n is the refractive index and λ is the wavelength of the light. In this case, the interference can be recorded by the photodetector (PD) (shown in Figure 3.1). Assuming a typical 633nm He-Ne laser system, the phase change can be calculated by equation 3.1. In the air environment, a phase change of 2π equals to 316.5nm displacement of M_1. The same principle can also be applied for fibre optics [3.6].

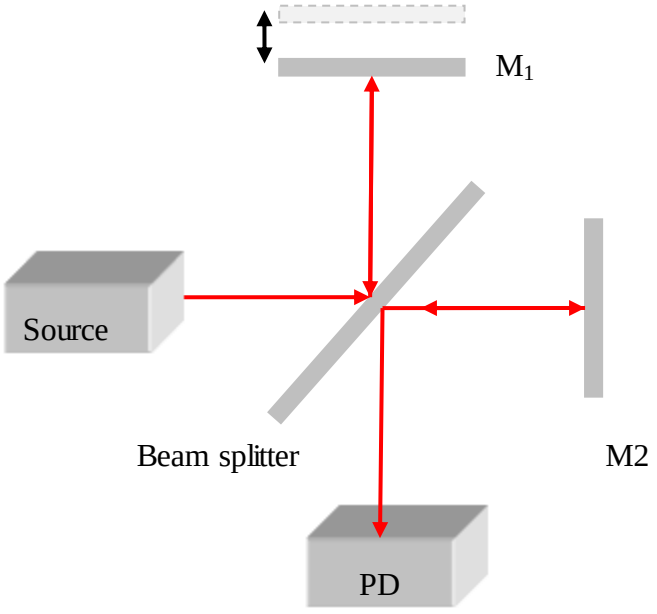

Figure 3.1 Basic set-up of an interferometer. Source refers to a laser, M_1 is the moving mirror and M_2 is a fixed mirror respectively. Interferogram of the two beams are detected by a photodector (PD).

3.2 The Fabry-Perot Interferometer

The micro-cantilever optical fibre sensor proposed in this thesis will essentially operate as an Fabry-Perot interferometric cavity formed between two reflective surfaces. This arrangement will be practical for an optical fibre cantilever sensor. The first cavity reflective interface can be defined by the end face of an optical fibre, the second by a reflecting portion itself.

The cavity length can be determined by analysis of the peak positions in the reflection spectrum or by FFT analysis of the reflection spectrum [3.7]. However before starting to investigate micro-cantilevers for sensing applications, it is helpful to first get an understanding on the origin of the interference effect that can be used for cantilever deflection measurement.

3.2.1 Theoretical analysis of the FP interferometer

In general the FP interferometer makes use of multiple reflections between two closely spaced partially reflecting surfaces. Part of the light is transmitted at each interface, resulting in multiple beams which can interfere with each other. A schematic diagram of an FP intereferometer in optical fibre is shown in Figure 3.2.

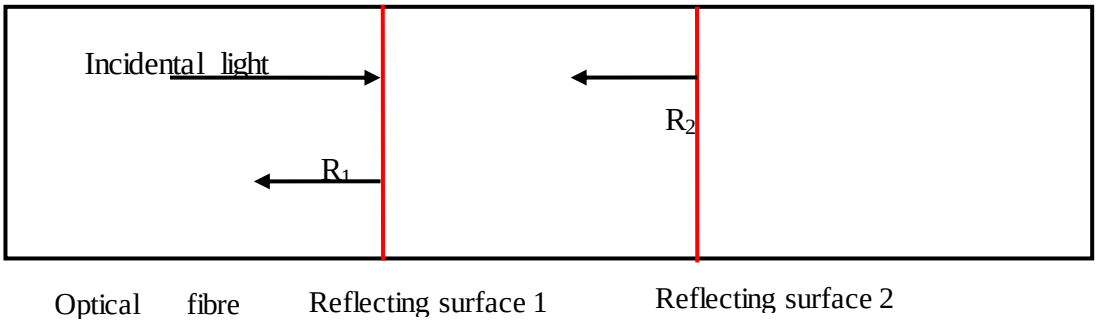

Figure 3.2 Schematic diagram of an FP interferometer.

Considering an FP interferometer formed in a standard optical fibre, assuming a low-coherence light source, such as (S)LEDs and halogen lamp as a broadband source suitable for illuminating an extrinsic FP interferometer (EFPI) formed by two reflecting surfaces. Analysis of the reflected (or transmitted) spectrum will result in fringes with a spacing that is characteristic of the cavity length. Now, consider each reflecting

surface to be 'low' reflectivity (few percent) then the low finesse two beam assumptions can be made, i.e. ignore higher order reflections inside the cavity.

Assuming that the optical intensity I of the light source at wavelength λ is approximated by a Gaussian function [3.8] with the following equation:

$$I_0(\lambda) = I_0 f(\lambda) = \frac{I_0}{(2\pi)^{1/2}\Delta\lambda} \exp[-(\lambda - \lambda_0)^2 / (2\Delta\lambda)^2] \qquad (3.2)$$

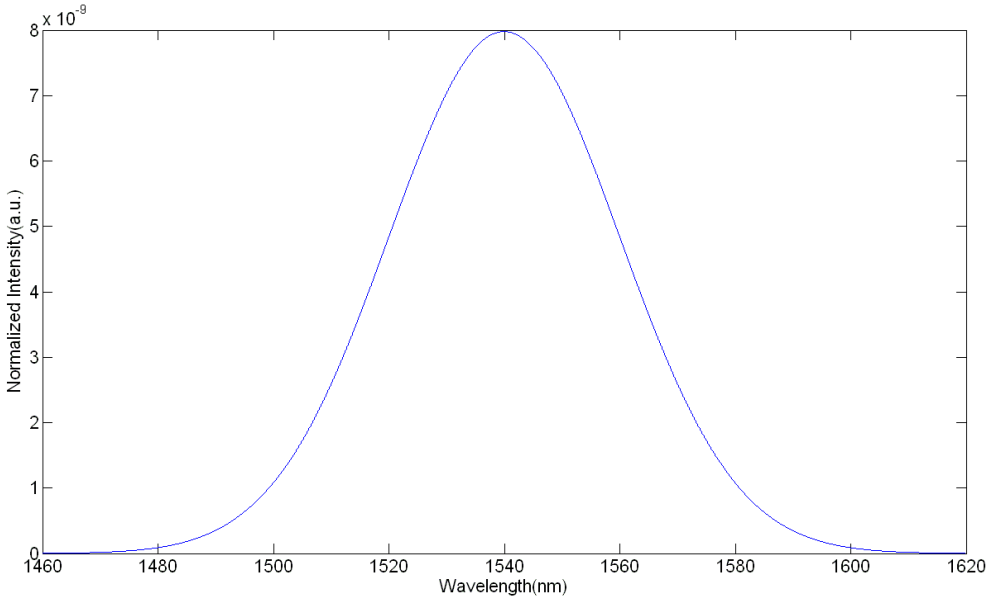

Figure 3.3 Example of a model spectrum of Gaussian light source spectrum.

and $f(\lambda)$ is the spectral distribution of light source:

$$f(\lambda) = \frac{1}{(2\pi)^{1/2}\Delta\lambda} \exp[-(\lambda - \lambda_0)^2 / (2\Delta\lambda)^2] \qquad (3.3)$$

where λ_0 is the central wavelength, and $\Delta\lambda = \Delta\lambda_{FWHM} / (8\ln 2)^{1/2}$. I_0 is the output power at λ_0. A typical model spectrum is shown in Figure 3.3. Then, in the two beam case, the reflected intensity I_r is given by [3.8] :

$$I_r(\lambda) = \alpha I_0 f(\lambda) = \frac{R_1 + \eta^2 R_2 - 2\eta\sqrt{R_1 R_2}\cos(\frac{4\pi n_0 L}{\lambda})}{1 + \eta^2 R_1 R_2 - 2\eta\sqrt{R_1 R_2}\cos(\frac{4\pi n_0 L}{\lambda})} \qquad (3.4)$$

Here η is the coupling coefficient. α is a normalised constant. R_1 and R_2 are the reflectivities of the Fabry-Perot surfaces respectively. n_0 is the refractive index and L is the Fabry-Perot cavity length. If a free space cavity is considered then the coupling

coefficient will depend on the cavity length due to the divergence of the free space beam which can be written as:

$$\eta = \frac{1}{1+[\frac{2\lambda_0 L}{2\pi n_0 w^2}]^2} \tag{3.5}$$

w is the light beam diameter in the fibre. In this case, the total reflecting intensity I received by spectrometer is:

$$\begin{aligned} I &= \int_{\lambda_0-BW/2}^{\lambda_0+BW/2} I_r f(\lambda) d\lambda \\ &= \frac{\alpha I_0}{(2\pi)^{1/2}\Delta\lambda} \int_{\lambda_0-BW/2}^{\lambda_0+BW/2} \frac{R_1+\eta^2 R_2 - 2\eta\sqrt{R_1 R_2}\cos(\frac{4\pi n_0 L}{\lambda})}{1+\eta^2 R_1 R_2 - 2\eta\sqrt{R_1 R_2}\cos(\frac{4\pi n_0 L}{\lambda})} \frac{1}{(2\pi)^{1/2}\Delta\lambda} \exp[-(\lambda-\lambda_0)^2/(2\Delta\lambda)^2] d\lambda \end{aligned} \tag{3.6}$$

where BW is the $FWHM$ spectrum width and $\Delta\lambda$ is the source spectrum width. equation 3.6 is the standard expression for most FP systems. This equation represents most of the key factors in the optical system, such as the cavity length, source central wavelength and bandwidth, reflectance of surfaces, and optical loss. In terms of a cantilever interrogation system, an important parameter we need to mention is fringe visibility. A high visibility usually means a good optical system. The fringe visibility γ is defined with the following equation in [3.9] :

$$\gamma = \frac{I_{\max} - I_{\min}}{I_{\max} + I_{\min}} \tag{3.7}$$

Where I_{min} and I_{max} are the minimum and maximum intensities of the optical interference, respectively. This can be rewritten in terms of our system parameters:

$$\gamma = \frac{4\eta\sqrt{R_1 R_2}(1-R_1)(1-\eta^2 R_2)}{(R_1+\eta^2 R_2)(1+\eta^2 R_1 R_2) - 4\eta^2 R_1 R_2} \tag{3.8}$$

It is clear that the cantilever sensor's visibility relies on the surface reflectivity, the coupling coefficient and the cavity length. Higher fringe visibility normally means

higher performance in terms of sensitivity and this will help improve the accuracy when demodulating the cavity length.

In this thesis, the cantilever is either machined by laser or fabricated by attaching an additional polymer layer, thus the surface reflectivity are usually smaller than Fresnel reflection for a fibre to air interface. The cavity length between the fibre end surface and cantilever surface will also affect the visibility of the sensor. The direction of the incident beam needs to be aligned accurately with respect to the interfered surface to maintain high finesse interference. This is particularly important with highly reflecting surfaces where small misalignments may lead to poor visibility. Therefore, low reflectivity partially scattering surface can give an improved tolerance to the reflected angle and may be preferable despite the lower reflected intensity coupled back into the fibre.

There is also a trade-off regarding the nominal cavity length. A large cavity length may lead to lower reflected power while a small cavity length may be difficult to analyse accurately since the reflection spectrum will contains fewer fringes over a given interrogation wavelength range. Overall, it is important to find the optimum cavity length and surface reflectance to achieve optimum visibility and this is considered in the following sections.

3.2.2 Effect of surface reflectance on FP interferogram

Following the equation 3.8 in section 3.1.1, the effect of surface reflectance on the visibility of the interferogram can be determined as a function of cavity length. For a low-finesse interferometer, the sensor with higher reflectance interfaces has higher return intensity. However, this doesn't necessarily mean a better visibility. In some situations a low-finesse interferometer can achieve better visibility with two weak reflectors rather than that with higher reflectance.

Figure 3.4 shows the modeled visibility due to different surface reflectivities based on equation 3.8. In this thesis, R_1 is the reflectivity of a micro-machined surface (or

cantilever surface), and is normally smaller than an ideal 4% Fresnel reflection. R_2 is the cleaved optical fibre facet with a standard Fresnel reflectivity of 4% between the fibre to air interface. Three most commonly used cases are plotted in Figure 3.4 and from the figure, sensor visibility is potentially greater than 90% for all three cases when the cavity length is smaller than 40 μm. As the cavity length increased, the visibility drops quickly due to beam divergence. In practical operation, cavity lengths around 10 μm are usually chosen because at this point, enough fringes can be used to determine the cavity length accurately while maintaining a high visibility. In addition, a short cavity length is more stable to environmental noise; therefore, improve the overall performance of the sensor.

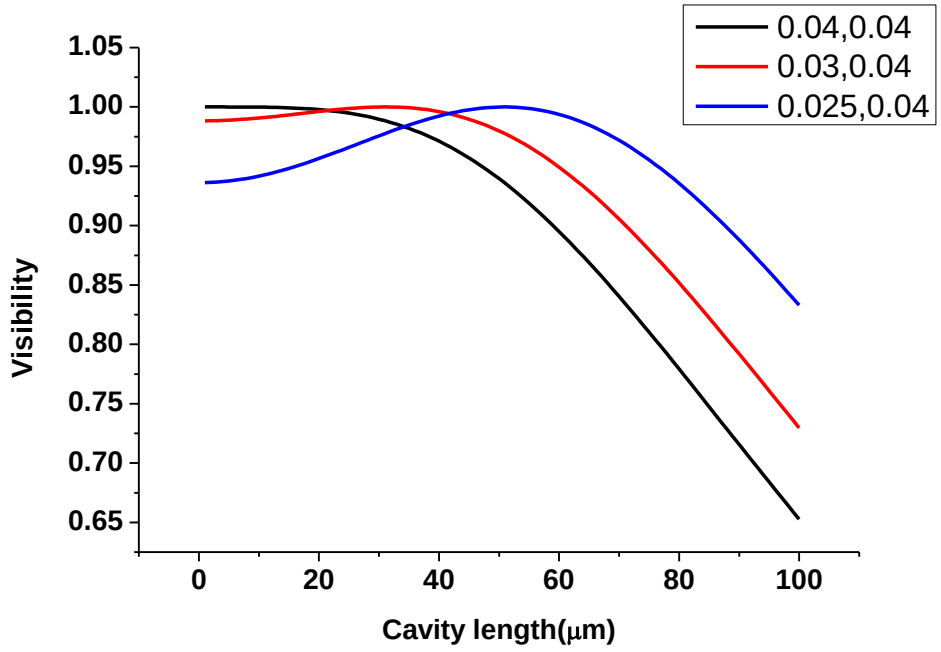

Figure 3.4 Modelled cavity length versus visibility as reflectivities change. Black line: both surface reflectivity are 0.04, Red line: surface reflectivities are 0.03 and 0.04, Blue line: surface reflectivities are 0.025 and 0.04.

3.3 Broadband illumination interrogation scheme

The typical interrogation scheme requires broadband illumination (SLED or lamp), a means of delivering the light to the sensor and returning the reflected signal to a spectrometer.

3.3.1 Ocean Optics Spectrometer

The Ocean Optics S2000 Spectrometer (Ocean Optics, Co. Ltd) [3.10] includes the linear CCD-array optical detector, plus a diffraction grating to disperse the spectrum across the array. The result is a compact, flexible system, with no moving parts, that's easily integrated as an OEM component. It interfaces to computer and other embedded controllers through USB 2.0 or RS-232 communications. The S2000 spectrometer used incorporates a high-sensitivity 2048-element CCD array. The S2000 is a microcontroller-controlled spectrometer, thus all operating parameters are implemented through software interfacing to the unit.

A broadband light source and a microscope objective are used to couple light into the optical fibre. In our case, the fibre used is a HP 780 optical fibre (Thorlabs, USA). Compared with standard 1550nm, the shorter wavelength may provide more sensitivity as phase changes which can be seen in equation 3.1. This will in turn provide a higher sensitivity for the cavity length measurement. Furthermore, the CCD is silicon based detector, therefore, it cannot work at longer wavelengths. The useful spectrum of the BBS (halogen lamp) is from 304nm to 1024nm. The benefit of using a lamp as a light source is that the inteferogram can be viewed over a very broad range of wavelengths and this is a cost-effective solution for industry applications. The BBS provides more spectral information; therefore, more fringes can be used to demodulate the cavity length by using FFT algorithm. The more fringes it contains, the more accurate the FFT peak will be. Unfortunately the optical power delivered into the fibre by a lamp is low, so care is needed in setting up the system to maximize light coupled into the fibres.

3.3.2 Optical fibre cantilever sensor interrogation arrangement

The experimental set-up for optical fibre cantilever interrogation is shown in Figure 3.5, where a bulb lamp is used as a Broad Band Source (BBS) and an Ocean Optics spectrometer (S2000) is employed to measure the reflected interferogram. Light is coupled to the cantilever via a 780nm 2×2 coupler. Index matching gel is applied to

the unused coupler arm to avoid any reflected light from this fibre. A typical example for the measured interferogram is shown in Figure 3.6.

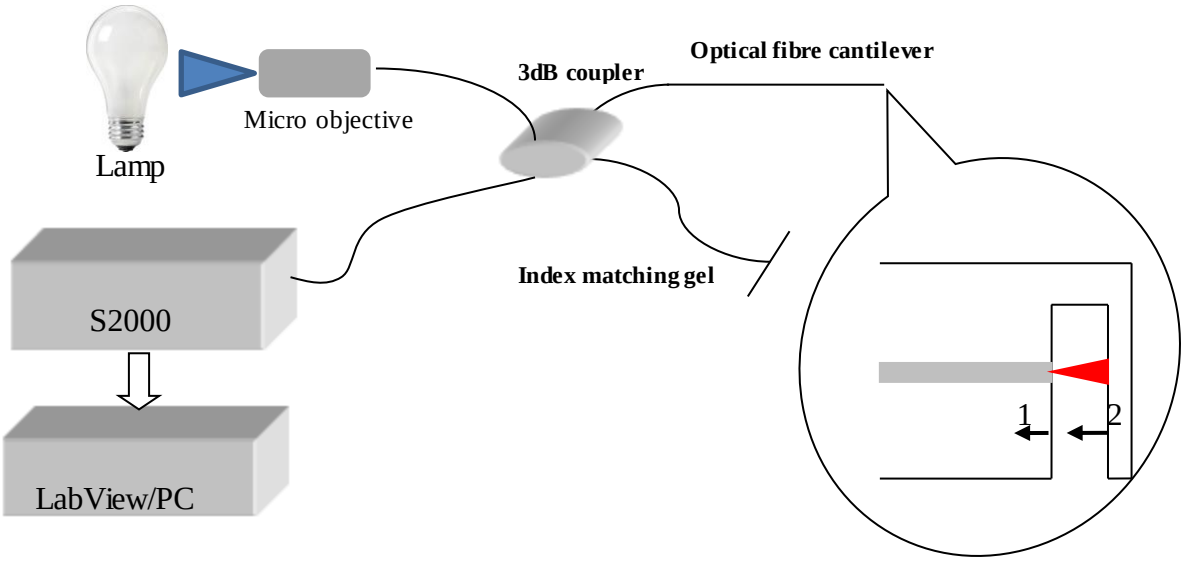

Figure 3.5 Experiment set-up of an optical fibre sensor interrogation system. Light from a bulb lamp is coupled into the fibre via a micro objective lens. The zoomed in part shows that 1 and 2 are the two interfered surfaces for a fibre-top cantilever.

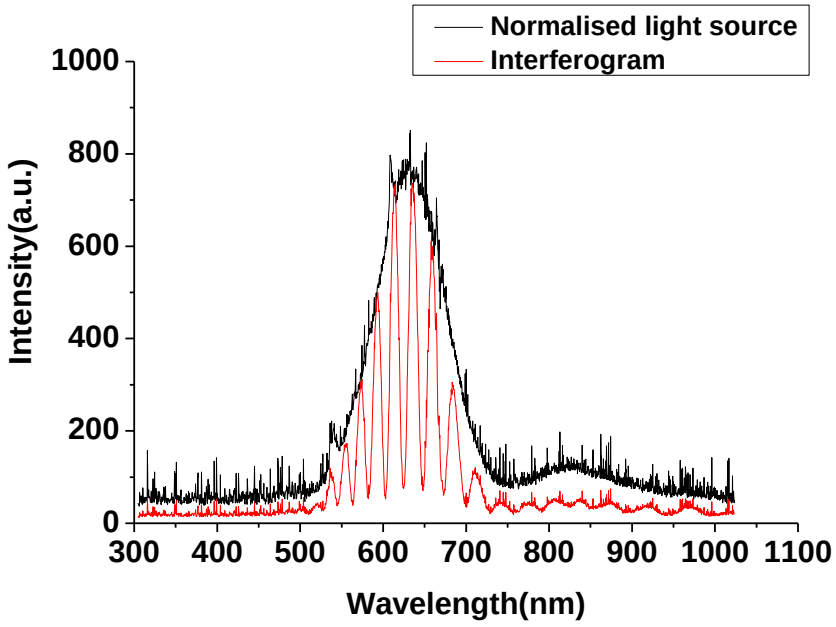

Figure 3.6 Interferogram from a 54.5μm cavity length found between two reflected surfaces with normlised light source spectrum.

As the surface reflectivity is low in this case, a low finesse interference assumption is used. For a two beam interference, the final intensity I_R can be expressed as:

$$I_R = I_0[1 + V\cos(\frac{4\pi nL}{\lambda} + \varphi_0)] \quad (3.9)$$

where I_0 is the input light intensity, V is the visibility, n is the refractive index, λ is the wavelength and φ_0 is the initial phase. The cavity length can be obtained by analyzing this reflection spectrum, either by analysing the position of the peaks of the interferogram (i.e. a measure of the free spectral range) or by converting to the optical frequency domain and using FFT to find the dominant frequency associated with the free spectral range which determines the cavity length.

3.4 FFT cavity length demodulation technique

3.4.1 LabView introduction

In chapter two, the FFT algorithm was introduced as a means to analyse an interferogram produced by FPI. Here the focus is on the software implementation of the FFT technique using LabView. With flexible software design, it is easy to use LabView to develop an interface between hardware and the host computer. It's also a powerful and effective tool to perform real time monitoring task. In this thesis the cantilever cavity length is calculated and then real-time deflection is recorded/displayed by bespoke LabView program.

3.4.2 Cavity length determination by LabView/FFT

In terms of demodulating cavity length of an FP cavity, the FFT is an efficient method to extract fringes per spectral unit. Although it's simple to implement, special care still needs to be paid to provide reliable pre-processing steps reducing the error and accurately transferring the data for final cavity length measurement. LabView software is used here to determine cavity length and can be summarized with the following steps as shown in Figure 3.7.

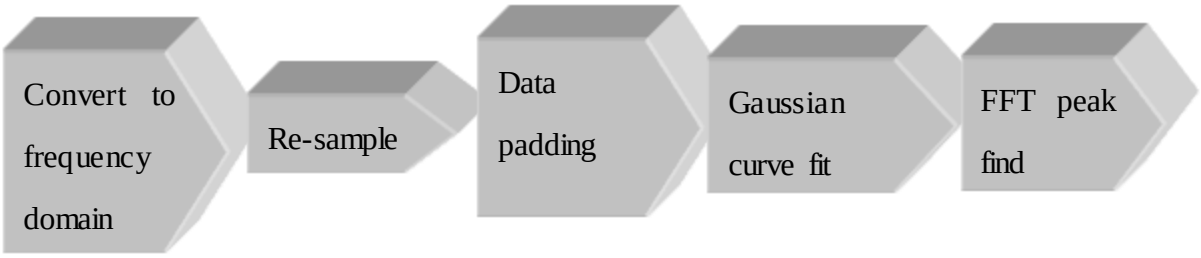

Figure 3.7 Schematic diagram of cavity length determination procedure.

Spectral information is first converted to the frequency domain. This is the prerequisite for an FFT transform. The original data are recorded in the wavelength domain and it should be noted that the frequency interval between each data point is not uniformly spaced, since $\frac{1}{\lambda}$ will reduce the interval gradually. Therefore, in order to reconstruct the interferogram in the frequency domain, it's necessary to resample the signal with a suitable sampling rate for the FFT process later. Data padding is used to add sufficient data points to find the FFT peak with an improved accuracy. After this process, a Gaussian curve is used to fit the experimental data by a least-square-mean algorithm to find the dominant frequency of interest. The detailed LabView code for each step is shown from Figure 3.8 to Figure 3.11.

In Figure 3.8 the source spectrum is acquired and pre-processed. The dash rectangular box shows a flexible way to select a range of wavelength of source spectrum and filter the spectrum noise when necessary.

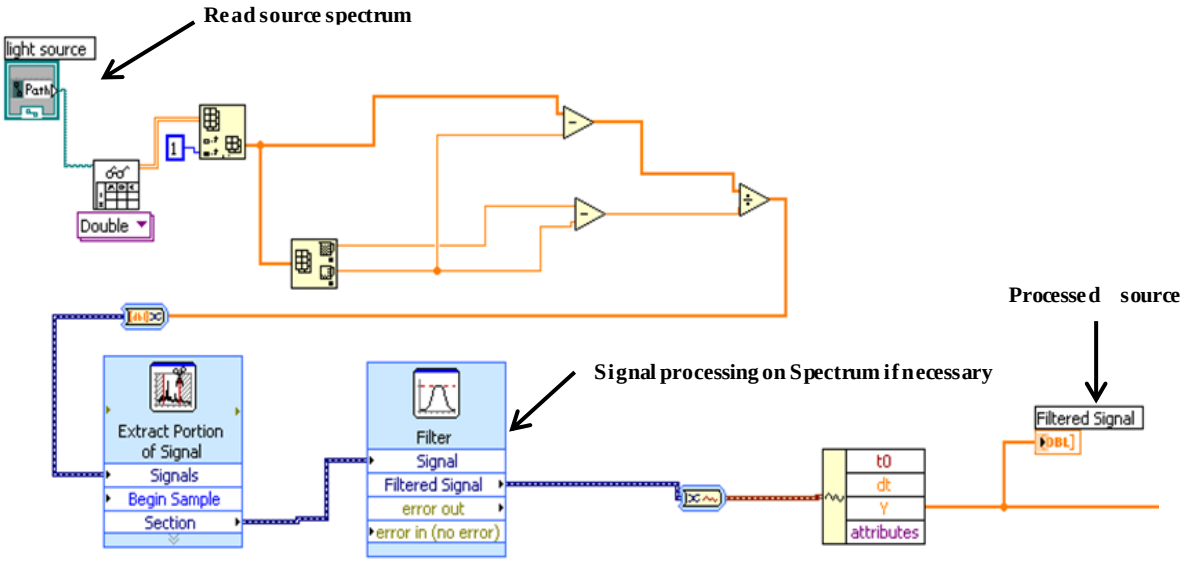

Figure 3.8 LabView VI to normalise the light source spectrum. Saved light source data are read and divided to wavelength and intensity information and processed by LabView VI.

Figure 3.9 shows the LabView algorithm used to normalise the interferogram signal. The Pre-processed source spectrum from the previous step is directly used for normalisation and preparation of the signal for the next step: changing wavelength information to frequency domain. This step is shown in Figure 3.10 where the data is resampled. In our case, a second-order polynomial function was used to fit the resampled data. Resampling spacing will also affect the accuracy of the final cavity length. When reducing the sampling spacing, the error made by curve fitting will reduce and thus the original spectrum is well reconstructed.

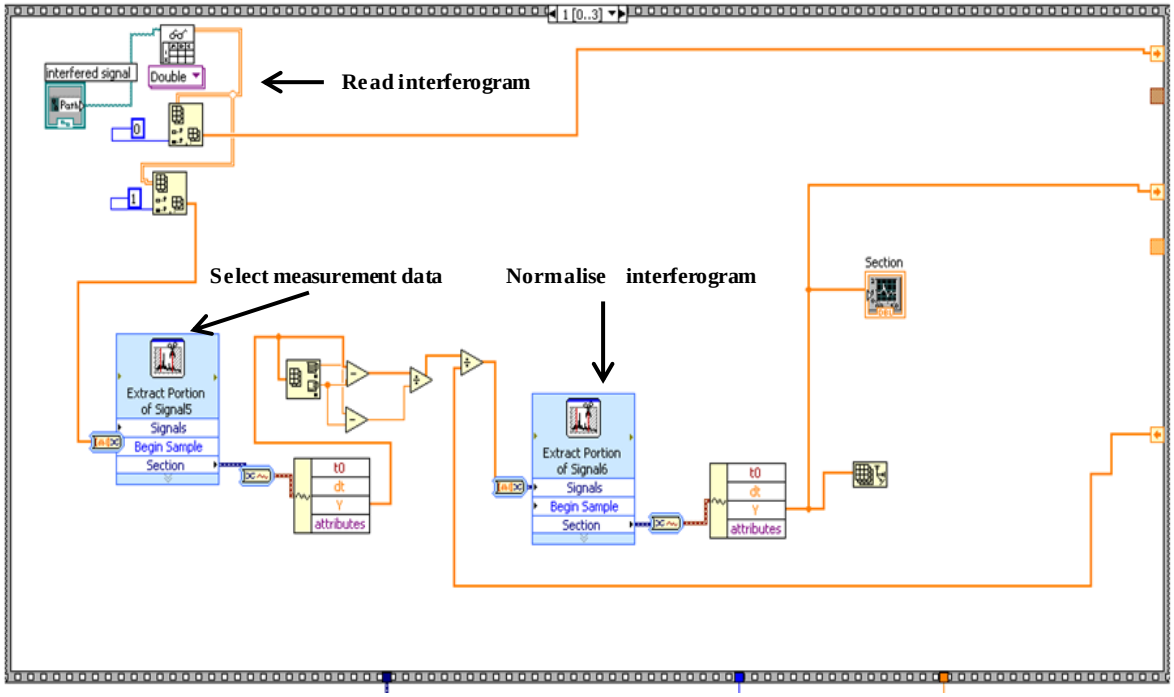

Figure 3.9 LabView VI to normalise interferogram. A block of read VI is used to acquire measured data and processed by Extract Portion of System VI. Data are then normalized and programmed for next step shown in Figure 3.10.

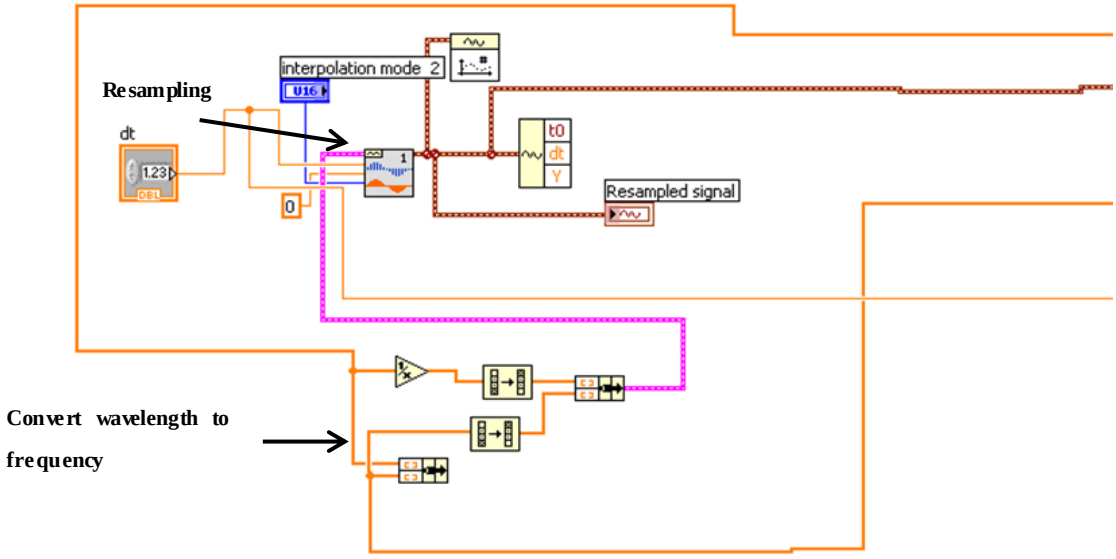

Figure 3.10 Resampling and pre-FFT VI. Wavelength spectrum is converted to frequency and a resampling VI is used to interpolate data points before using FFT to find the peak position.

The final step is to use the FFT algorithm to calculate the peak frequency position and determine the cavity length. The LabView code for this step is shown in Figure 3.11. Here, an extract portion VI (Virtual Instrument block used in LabView) is used to select

the sampling data for the FFT and a peak detection VI with several detection algorithms is used to determine the FFT peak position. A polynomial fit is used to fit the curve and calculate the peak position and convert this peak to the cavity length.

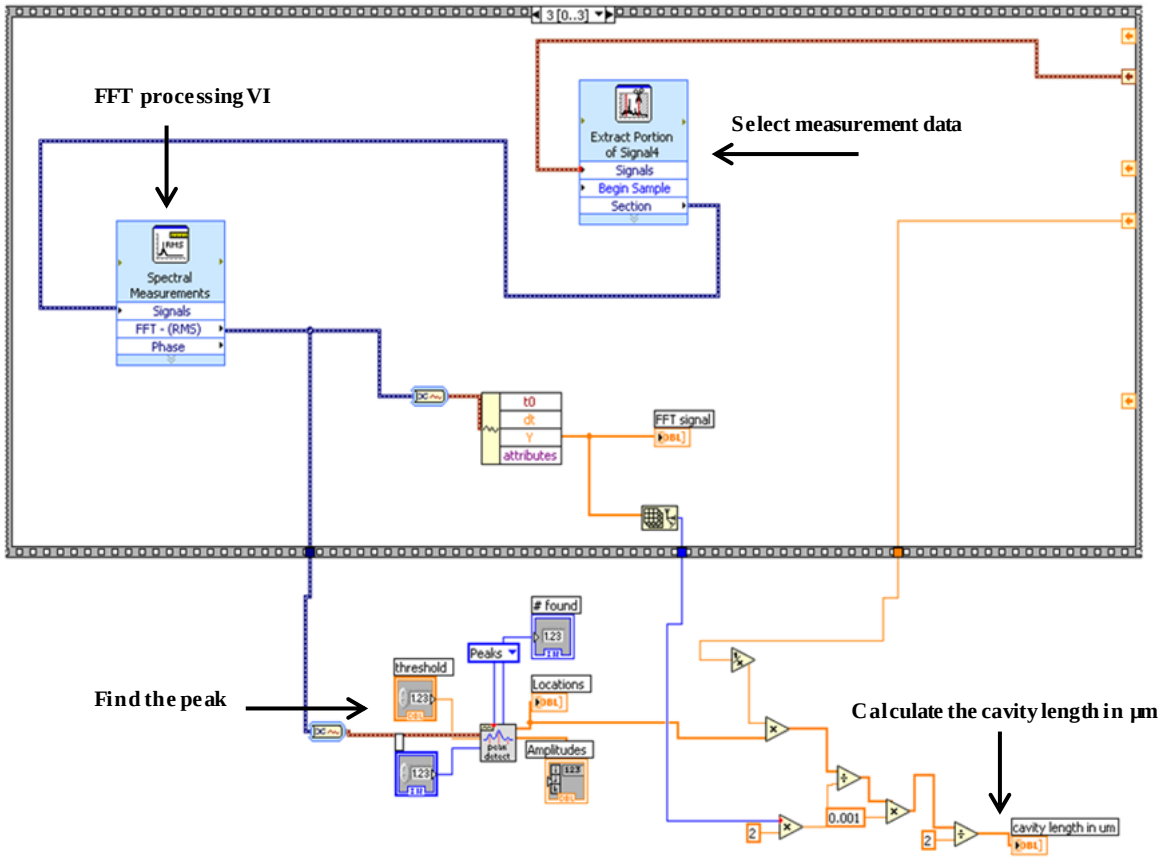

Figure 3.11 LabView VI of FFT calculation and cavity length determination. The resampled data is employed for FFT and a peak finder VI is used to determine the peak position and convert it to cavity length in µm.

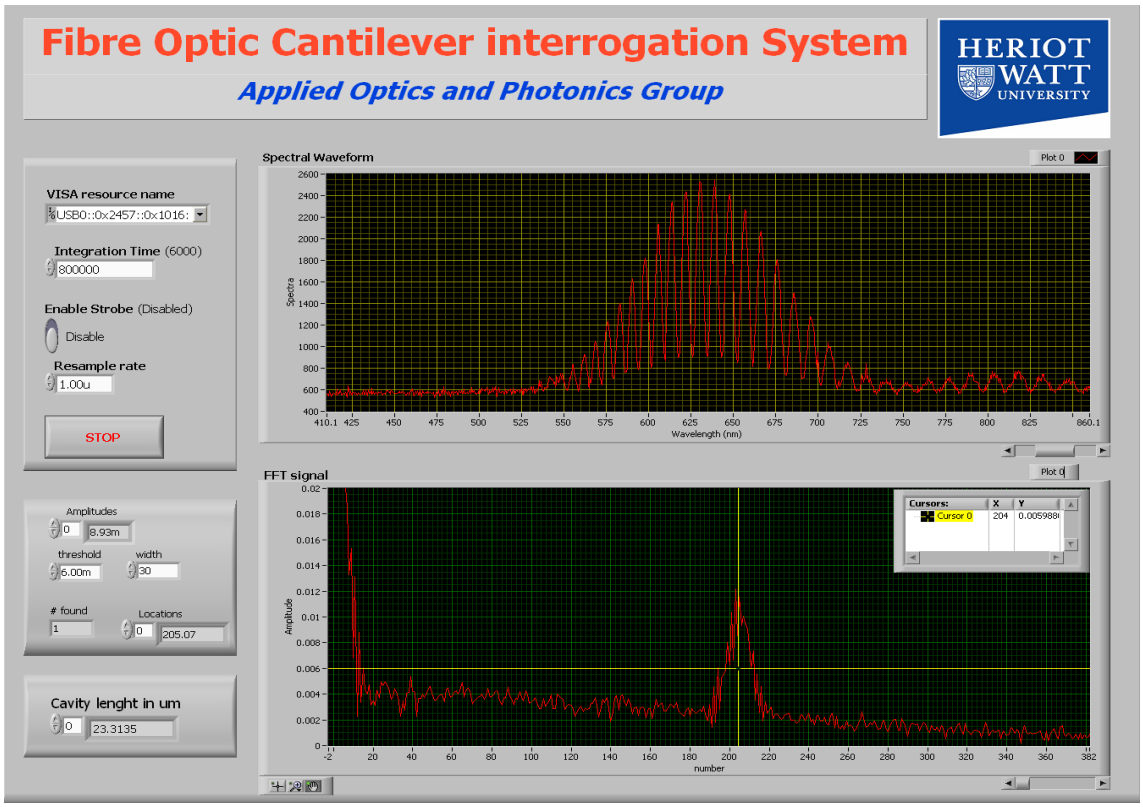

Figure 3.12 LabView software panel of cantilever interrogation system. The spectra are shown in both wavelength and frequency domain. Cavity length can be calculated using FFT and displayed in the left side of the panel.

The bespoke interrogation software for real-time interrogation is shown in Figure 3.12. Both the wavelength and frequency domain signals are clearly exhibited. At the left side of the panel, cavity length in μm is displayed with several adjustable parameters. In a practical application, a user friendly interface is necessary to allow a customer to view useful information and the function on front panel can be extended according to customer's needs.

3.4.3 Discussion of FFT algorithm errors

The first potential error in determining the cavity length is due to the data sampling rate. As the maximum detectable frequency is defined by Nyquist frequency, a correctly measured frequency must be sampled at least twice the maximum frequency of the signal. Failure to meet this condition will lead to aliasing, in which case low frequencies are observed due to the too coarse sampling of data. In a real case, the Nyquist theory is only used as a guide, much more data is necessary for a reliable FFT analysis. Error also exists after converting wavelength data to frequency domain for

resampling process. As these discrete data in frequent domain are not evenly spaced, interpolation is usually necessary by add sampling data to obtain an equal sampling interval between each data. The frequency of the FFT can be defined as:

$$\Delta \boldsymbol{f} = \frac{\boldsymbol{f_s}}{\boldsymbol{N}} \tag{3.10}$$

Where f_s is the Nyquist frequency and N is the sampling number. From equation (3.10) the cavity length information can be extracted from FFT peak position. Once the FFT analysis is finished, the peak frequency which corresponds to the Free Spectral Range (FSR) [3.9] can be extracted. To gain maximum accuracy from the peak data, a function, e.g. Gaussian function is fitted to the data to determine the peak value. The accuracy of this stage can be greatly affected by the number of data points within the FFT spike. For a typical interferogram with 2000 data points the FFT peak will contain 8-10 data points (shown in Figure 3.13), thus the peak position of the fit will greatly influenced by individual points.

One option to increase the number of data points is zero-padding the data after re-sampling but pre-FFT. To do this, zero value data points are added to the original interferogram data. In this way, the sampling interval of the FFT over the region of interest is greatly reduced and the number of data points within the FFT peak is increased. This can give a much more accurate peak position. The method is effective but does increase the computational power and time required for the process. From Figure 3.14, by using zero-padding, the interval of sampling data is reduced, therefore, the number of data points contained in the FFT frequency spike is increased. This offers more information to fit a Gaussian curve and therefore, gives a more reliable result to determine the peak position. It should be noted that, the fitted curve after FFT is not an ideal Gaussian shape shown in Figure 3.14. This is because that surface finish of cantilevers used here is not as good as a mirror, thus more noise will be contained in the interferogram.

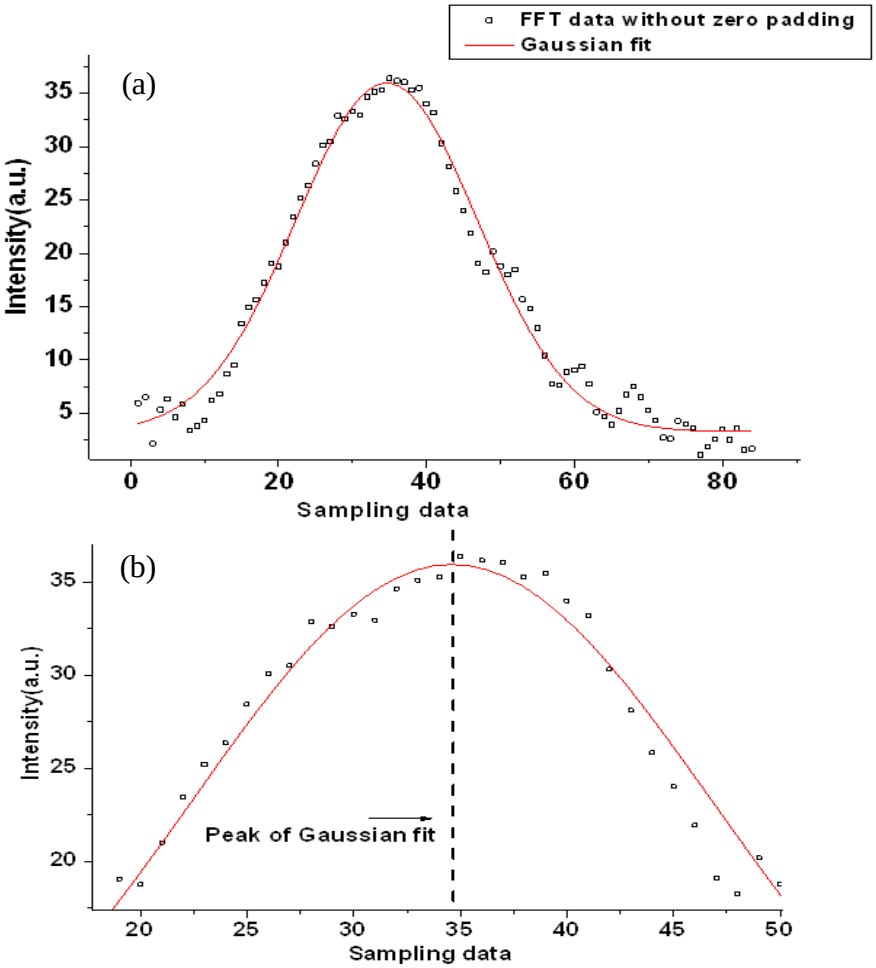

Figure 3.13 (a) FFT intensity versus sampling data without zero-padding with Gaussian fit. (b) Zoomed in area of Gaussian fitted FFT peak position.

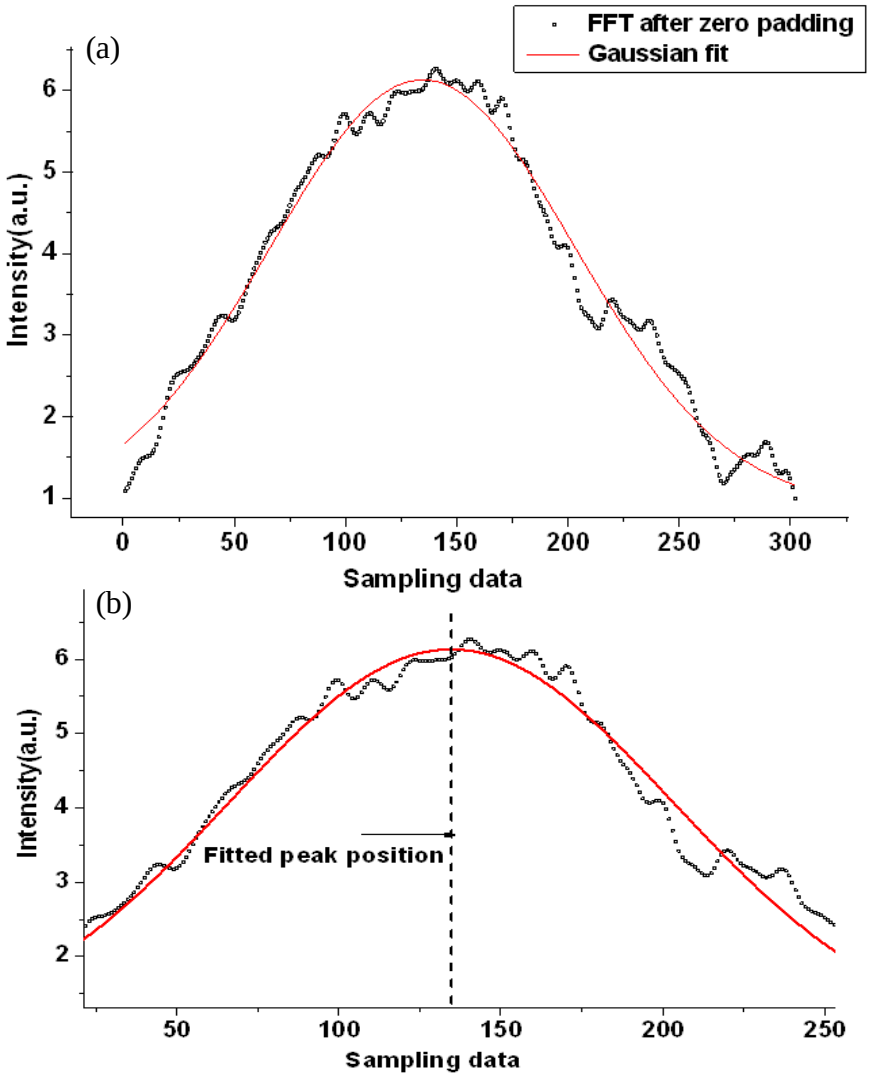

Figure 3.14 (a) FFT intensity versus sampling data after zero-padding with Gaussian fit. (b) Zoomed in area of Gaussian fitted FFT peak position.

The FFT algorithm only considers the periodicity of the interferogram in the spectral domain and ignores the phase information contained in the spectral signal. Therefore, the cavity length error can be further reduced by considering the exact interferogram phase. In the later section, a new algorithm to recover the phase information in the spectrum signal and improve the overall system performance will be investigated.

3.4.4 Evaluating cavity length interrogation system performance

To evaluate the cantilever interrogation software performance, a cleaved optical fibre and a mirror are employed to build a simple FPI. Both the fibre and the mirror are mounted onto an optical bench to avoid mechanical movement. The temperature drift

during the experiment was less than 1 ˚C, measured by a thermocouple. Fringes were then recorded and analysed by the interrogation system. The software monitored the gap length between the fibre and the mirror surface. Figure 3.15 shows the absolute cavity length over a 1000 second period. The maximum cavity length deviation is 18.5nm and the calculated r.m.s. error is ±8nm. This demonstrated the possibility of using low-cost lamp source and S2000 spectrometer to achieve a nanometer displacement measurement.

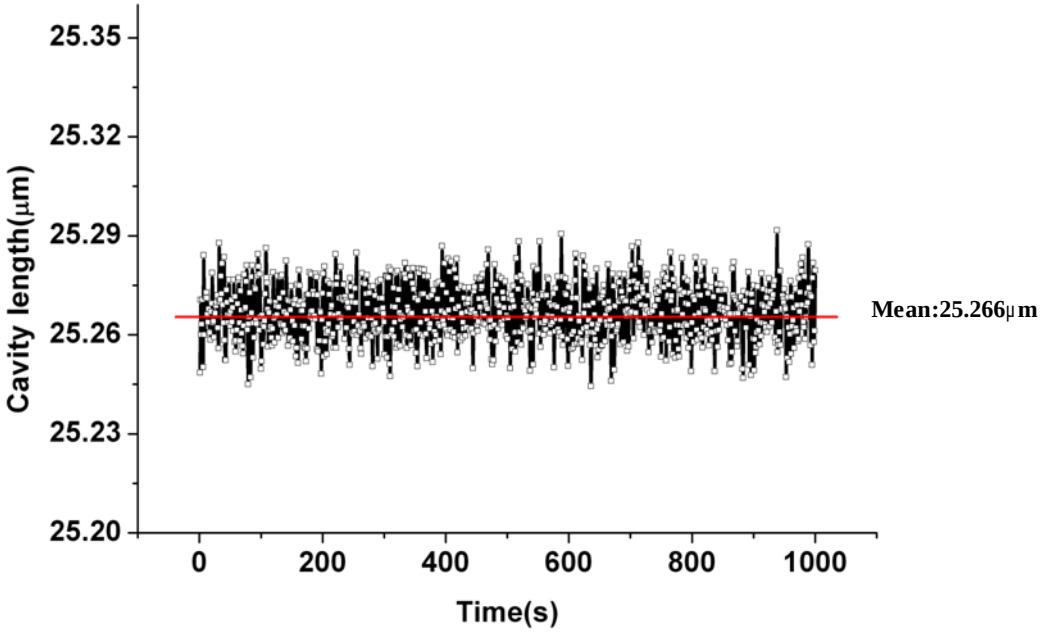

Figure 3.15 Cavity length fluctuation over 1000s period

To assess the dynamic response of the system, the following experiment was set up to monitor the gap length between the fibre and mirror (shown in Figure 3.16). A cleaved optical fibre was mounted onto a translation stage with a moving mirror used to approach the fibre at a constant speed. The movement of the actuator was controlled using a piezoelectric driven translation stage. For calibration purpose, a Renishaw ML10 position sensor with a resolution of 1nm was used to monitor the position of the piezoelectric translation stage. Figure 3.17 shows the demodulated cavity length change by optical fibre cantilever sensor interrogation system over a movement range up to 4.5 μm monitored by Renishaw ML10 displacement sensor. A linear fit is used to

find the relation between cavity length measured by ML10 and the interrogation system developed here. The residual error of the cavity length change can be seen in the insert in Figure 3.17. The maximum error shown is 60nm with a calculated r.m.s. error of ~23nm. The large error might due to the vibration of accelerate and decelerate the translation stage from one position to another. According to the specification, the transition stage has a repeatability of ±40nm, which will lead to the instability of the measured cavity length.

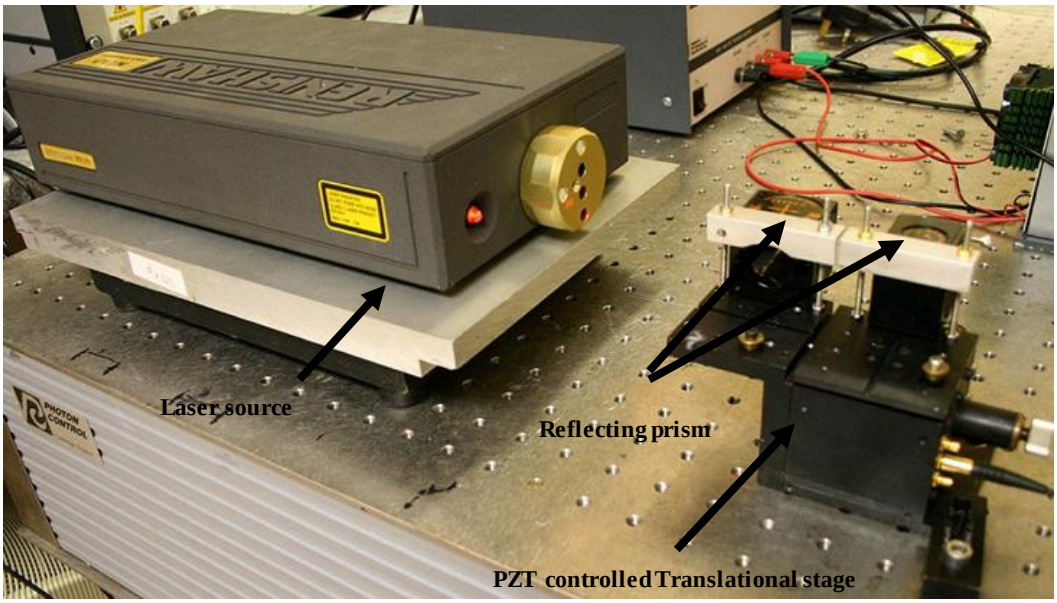

Figure 3.16 Experimental set-up of ML10 position sensor used to calibrate the optical fibre interrogation system developed in the thesis.

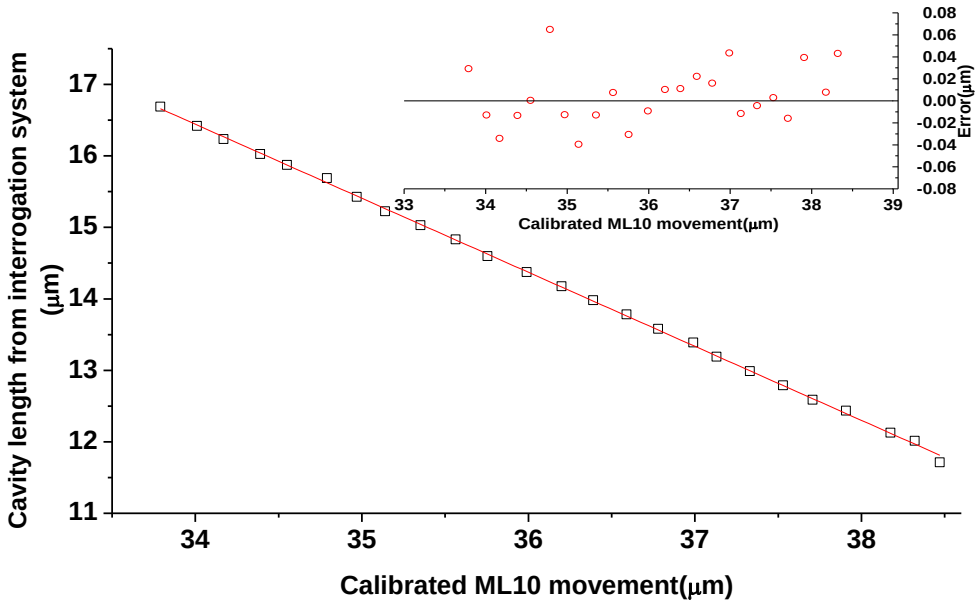

Figure 3.17 Movement of Renishaw ML10 displacement sensor versus cavity length change acquired by optical fibre cantilever sensor interrogation system. The calibrated ML10 movement is from 33.75 μm to 38.5 μm. The insert displays the cavity length residual error over a measurement range of ~4.5 μm.

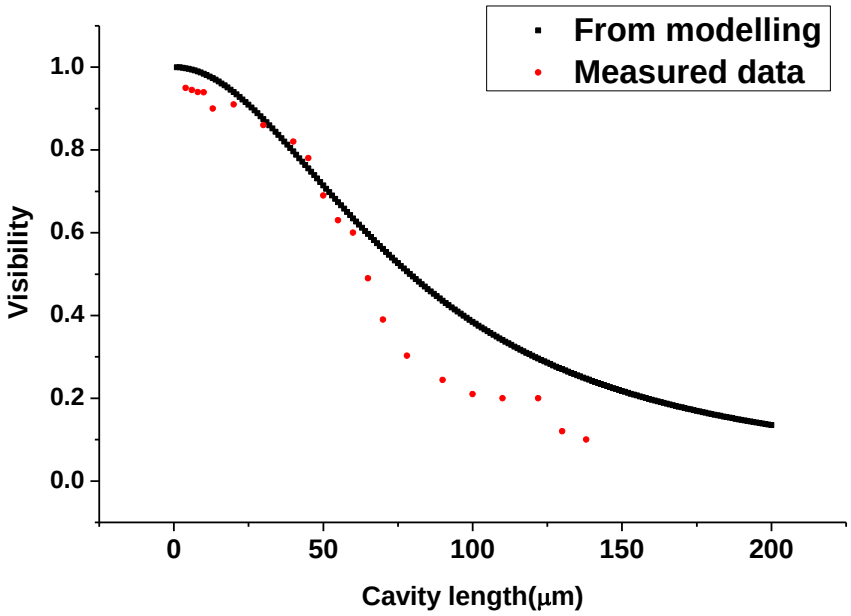

Figure 3.18 Modeling and measured cavity length change versus interferogram visibility.

The minimum detectable cavity length is determined by the spectral width of light source, in our case, the *FWHM* is ~100nm. By using the equation below, the minimum cavity length d is calculated to be ~3 μm.

$$d = \frac{\lambda^2}{2n\Delta\lambda} \tag{3.11}$$

where λ is the central wavelength, Δλ is *FWHM* of the light source and *n* is refractive index. Figure 3.18 plots the fringe visibility changes versus cavity length changes for both theoretical modelling and measured data. In the short cavity length region (cavity length <50μm), the measured visibility matches with the modelling results. It can be seen that the fringe visibility is higher than 0.6 in this region. As the cavity length increases, measured visibility drops more quickly than the model result. When the cavity length is approaching 132 μm, the fringe visibility drops down even more quickly and the fringes disappeared when the cavity length is larger than 132 μm. It is assumed that at this point the intensity of light coupled back into the fibre is too low to produce measurable interference using the S2000. This is probably because that when increasing the cavity length, the returned power from the fibre facet is much higher than from the mirror surface. Therefore the intensity of the two interfered beams is unbalanced, making it more difficult to observe the fringes against the background intensity. Therefore, in this case, fringes disappeared and only the reflected spectrum from the optical fibre end facet is observed as shown in Figure 3.19 below.

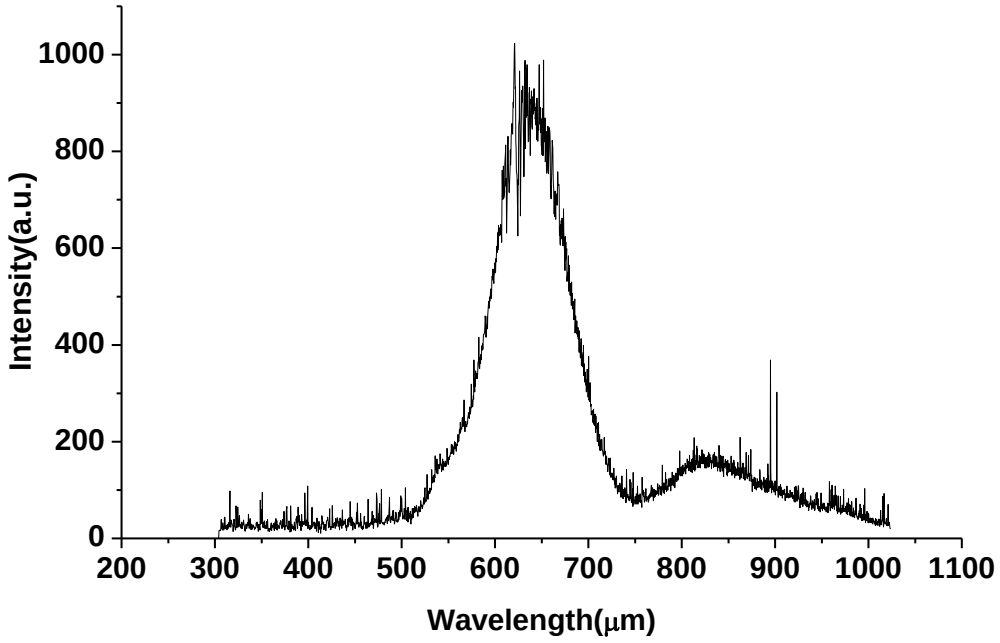

Figure 3.19 Spectrum of a 133μm cavity length between the optical fibre and the mirror. Interferogram disappears, only the reflection spectrum of optical fibre end facet is observed.

3.5 Phase recovery algorithm

3.5.1 Concept of phase recovery

The spectral domain technique [3.11] used here is a common way to determine the cavity length from an interferogram. For precise measurement, the accuracy and sensitivity usually depend on the parameters of the sensor itself and on spectral signal processing. Here we propose an additional phase recovery method to improve the accuracy of cavity length measurement.

We know that when transferring the interferogram to the optical frequency domain by FFT, only the real part intensity information is used. If the imaginary phase information can be used to recover the signal, more information can be acquired to determine the cavity accurately. This can further stabilize the cavity length and improve the resolution of readout system. An example of normal FP spectra in both wavelength and frequency domain is shown in Figure 3.20. Detailed discussion of FFT algorithm can be found in Chapter 2.

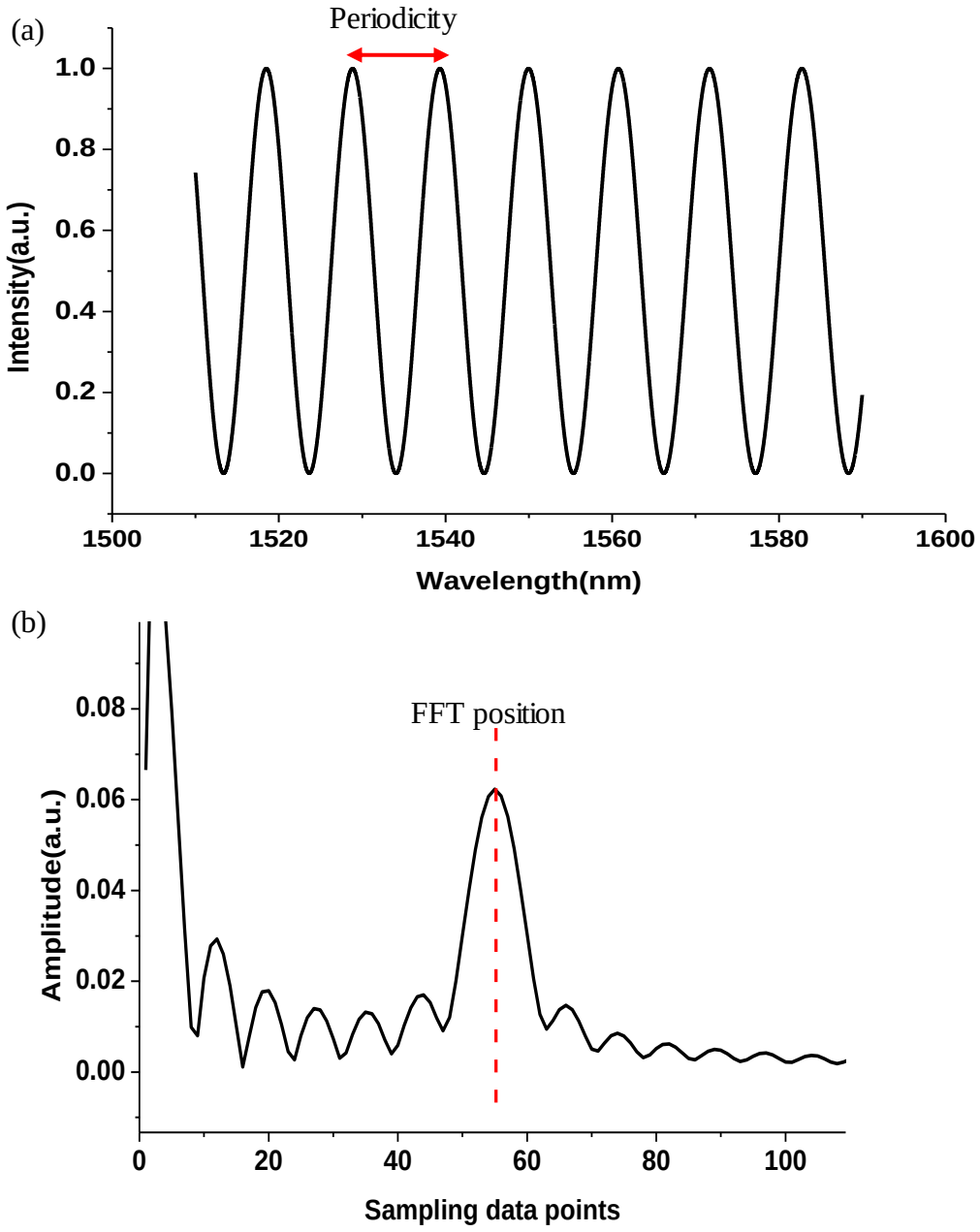

Figure 3.20 (a) Spectrum from a normal FP interferometer and (b) Spectrum after using FFT displayed in frequency domain. The FFT peak position is related with cavity length information in wavelength domain.

3.5.2 Cavity length recovery and analysis

By using the FFT method, it is possible to recover the cavity length from the FFT peak frequency position; however, when this length is used to regenerate the cavity length there is often a discrepancy between this new model interferogram and the real data in the wavelength domain. For high sensitivity measurement this discrepancy may lead to a significant error. The aim of phase recovery is to minimise the measurement error

by assessing the least mean square error between the modeled and the measured interferogram, and varying the recovered cavity length until the model and experimental data match.

First, the cavity length *L* obtained from the FFT analysis is used to reproduce a model FP interference fringe. A small wavelength shift is evident between the measured and modeled spectrum, which is shown in Figure 3.21(a). A least-mean-square algorithm is used to find the minimum error position between the modeled and measured cavity length for small variations in the cavity. Figure 3.21 (b) shows that the least square mean error between the model and experimental spectrum is found at a wavelength shift of 51nm. This means that in order to get an accurate cavity length, the experimental cavity length in Figure 3.21(a) needs to shift by 51nm. From Figure 3.21(c), the modeled spectrum based on this revised cavity length after using the phase recovery algorithm is closer to the experimental spectrum. Figure 3.21(d) shows the improvement for a cavity length error before and after applying the phase recovery algorithm; here the absolute cavity length fluctuation is reduced by nearly ten times. The maximum cavity length deviation after phase recovery algorithm is within 2~3nm, whereas the r.m.s. error is 0.87nm, based on data in Figure 3.21(d). This means the cavity length error produced by FFT algorithm could be reduced to nanometer range by using phase information contained in the interferograms.

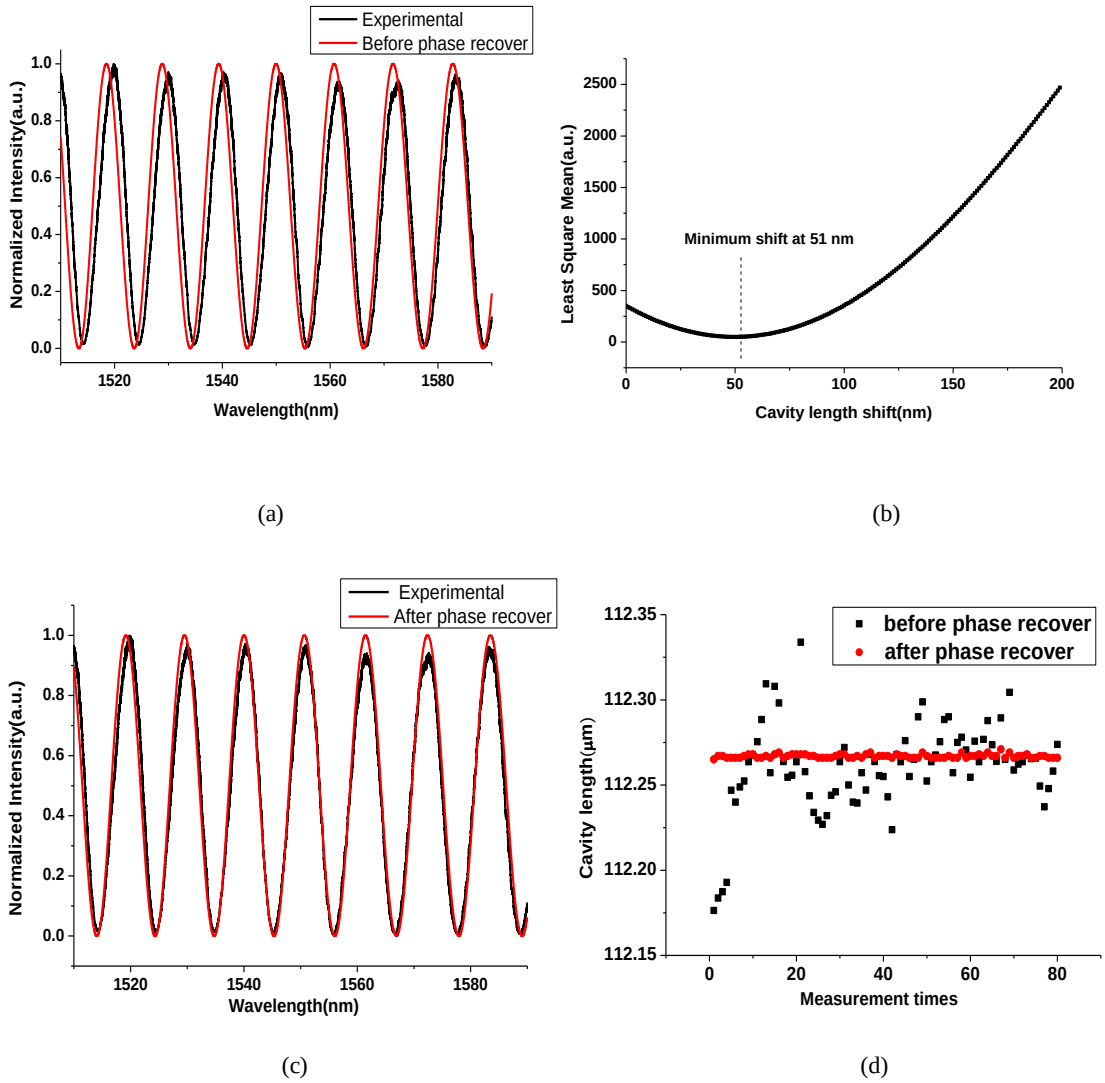

Figure 3.21 (a) Experimental spectrum and model based on starting cavity length recovered from FFT algorithm. (b) Plot of least mean squares fit between experimental and modeled data versus a small shift in cavity length around the FFT value. (c) Comparison between model and experimental after phase recover process applied, (d) Noise measurement over 80 scans for a stabilized cavity length before and after phase recovery algorithm.

A nano-stepper is employed to vary the cavity length up to 20 μm with 500nm intervals. The cavity length change versus residual error is plotted in Figure 3.22. The error before phase recovery is around ±20nm while after phase recovery this reduced to ±10nm over the whole measurement range. The error is still larger than we previously demonstrated for a static cavity length. The repeatability of the nanostepper is ±20nm, with a resolution of 10nm. We assume that this might be the contribution of the error after phase recover.

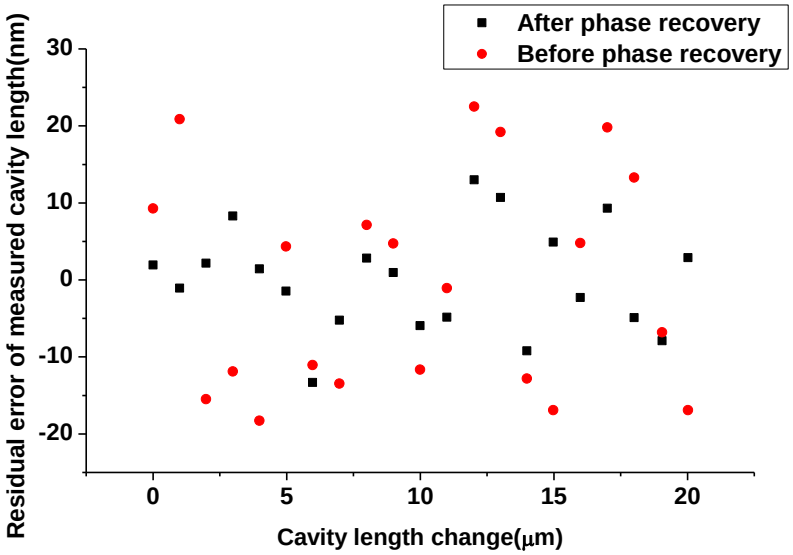

Figure 3.22 Residual error of at different cavity length between two reflected surfaces. Red dots show the residual error before phase recover with a maximum error ~20nm while black squares represent data after phase recovery with an improved error of ~12nm.

3.6 Evaluation of FPI based interrogation system

In this section, the FP based interrogation system has been employed to demodulate the cavity length which is associated with cantilever deflection. A number of interrogation techniques have been discussed in Chapter 2. These include an optical beam deflection technique, an optical intensity based technique and an FSR fringe counting technique. The optical beam deflection technique tends to have a high sensitivity in terms of the deflection measurement. However, the drawback of this technique is obvious that it usually involves time consuming alignment of the laser beam before detection. The high sensitivity of this technique is determined by the noise level and resolution of the PSD. Another issue with optical beam deflection technique is that the position of the laser beam needs to be accurately determined in order to calculate the deflection of the cantilever. A small fraction of misalignment may lead to a deflection error. In terms of optical intensity based interrogation, it is measuring the proportion of light which can be coupled to the fibre from the deflection cantilever. Therefore, it can be easily disturbed by the environment. A tiny vibration of the cantilever may lead to a fluctuation of received power. In addition, the sensitivity of the system is lower than both optical beam deflection and interferometry technique.

The FPI based interrogation system was investigated in this chapter. Compared with other techniques, it has a number of advantages for practical applications. First of all, a highly sensitive interferometry technique was employed to improve the sensitivity of the deflection measurement. In our system a short wavelength (centered around 780nm) is used to offer improved resolution compared with operation at longer wavelengths. Secondly, an FFT algorithm was used to determine the cavity length by finding the peak position in the frequency domain. In practice, the interferogram of a cantilever sensor is a superimposition of all FP cavities and because the surface of the FP is not always as good as an optical mirror, fringes can be quite complicated. In this case, it's impossible to count the fringes and calculate the cavity length. By transferring the spectral information to the frequency domain, the FSR can be determined. The third advantage of spectral based FPI we used here is that by using a wide spectral range commercial lamp, the number of fringes within the spectrum is maximised. The more fringes use, the more accurate the FFT analysis will be.

By building up the cantilever interrogation system and software, the overall performance of the system has been evaluated. This was done first by simulating the FPI to find the suitable operation cavity length range and then validating the system with a commercial Reinishaw ML10 nanoposition sensor. The final r.m.s. resolution of the interrogation system was proved to be ±15nm. The additional noise may come from light source spectrum fluctuations as well as the algorithm used to determine the cavity length. The phase recovery algorithm further improved the system resolution to a few nm, which is approaching the resolution achievable using the S2000 spectrometer. This error is quite close to the high sensitive optical beam deflection technique. From the experiment, it seemed that using the FSR to determine the rough cavity length and tuning the interferogram by the Least Square Mean (LSM) position can improve the system resolution nearly ten times. The system is capable of measuring bending of the cantilever in practice, however, since spectral information is acquired and averaged for a few ms to reduce the system noise, high speed vibration measurement is impossible using this system. However, lower speed deflection measurement is acceptable for

biomedical application, where measurement of cantilever bending needs to be more precise to monitor bio-molecular binding process, but would be unsuitable for any high speed dynamic system.

A number of methods can be used to further improve the resolution and stability of the interrogation system. A wider bandwidth light source can be used to improve the accuracy of FFT peak fitting which thus improves the accuracy of cavity length measurement. Another approach is to compensate for the system noise by introducing a reference cantilever.

3.7 Conclusion

In this chapter, FPI theory was introduced, which is essential to understand the operational principle of the optical fibre cantilever demodulation system. The surface finish is also discussed to help optimise the fringe visibility. After that the basic experimental set-up for a standard optical fibre cantilever interrogation system is described. The system can offer potential robust and low cost interrogation for industrial application. An FFT algorithm is used to determine the cavity length and this is essential for cantilever bending measurements talked about in the later chapters. The measured cavity length error calibrated by a Reinishaw ML10 position sensor is around ±15nm and after using the phase recover algorithm, this error can be further reduced to ~2 nm in a stable air flow environment. This provides a suitable interrogation system for testing a wide range of fibre based cantilever sensors.

References

[3.1] L Zehnder, "Ein neuer Interferenzrefraktor," *Zeitschrift für Instrumentenkunde*, vol.11, pp.275–285, 1891.

[3.2] B Kevin, "The Sagnac Effect", MathPages, Retrieved 15 February, http://mathpages.com/rr/s2-07/2-07.htm, 2013.

[3.3] P Hariharan, "Basics of Interferometry", Second Edition, Elsevier, 2007.

[3.4] D Malacara, "Twyman–Green Interferometer", Optical *Shop Testing*, pp.46. doi:10.1002/9780470135976, ch2, 2007.

[3.5] P Hariharan, "Optical interferometry", Second edition, Academic Press, Sydney, 2003.

[3.6] M J Ahmed, "Optical fiber interferometer", US patent 4772083 A, 1988.

[3.7] Y Jiang, "Fourier Transform White-Light Interferometry for the Measurement of Fiber-Optic Extrinsic Fabry–Pérot Interferometric Sensors", *Photonics Technology Letters*, vol.20, pp.15-18, 2008.

[3.8] Y N Ning, "Fiber-optic interferometric systems using low-coherence light sources", *Sensor and Actuators A*, vol.30, pp.180-192, 1992.

[3.9] M Born and E Wolf, "*Principles of Optics"*, Pergamon, Elmsford, NY, 1975.

[3.10] Ocean Optics, [Online], Available: http://www.oceanoptics.com/Products/spectrometers.asp.

[3.11] Y J Rao and D A Jakon, "Recent progress in fiber optic low-coherence interferometry", *Measurement Science and Technology*, vol.17, pp. 981-999, 1996.

Chapter 4

Micro-machined Fibre-top cantilever sensor for physical and chemical applications

In this chapter, the design and manufacture of micro-cantilevers onto the end of optical fibres are explored. The use of optical fibres offers a route to miniaturise the sensor configuration and allow measurement of real-time bending of micro-cantilevers in order to enable various sensing applications, including temperature sensing, chemical sensing and biomedical applications. Design and manufacture of micro-cantilevers for temperature and pH sensing will be investigated in this chapter.

4.1 Fabricating a fibre-top cantilever

As discussed in Chapter 2, laser micro-machining is one promising route to fabricate micro-devices. Larger dimension ferrule-top cantilevers have been demonstrated by Iannuazzi's group in 2007 [4.1], however, direct fabrication of cantilevers on optical fibres with reduced processing times for low-cost and mass production is still challenging. Here the combination of FIB and ps-laser laser machining is used to manufacture optical fibre tip cantilevers, which can be used for temperature and pH sensing. Before we start to investigate sensing applications of micro-cantilevers, it's helpful to have a general introduction of ps-laser and FIB milling systems used in this thesis.

4.1.1 Introduction to ps-laser machining

The ps-laser machining system is shown in Figure 4.1. This is a Trumicro 5x50 laser system, with an output pulse width of 6 ps, and a maximum repetition rate of 400 kHz. The laser beam is first expanded by a telescope (to allow for beam diagnostics) and is then reflected by two 45˚ steering mirrors into the scan head. Inside the scan head, the beam is focused by an objective lens onto the work stage. The structure inside the

laser scan head is presented in Figure 4.2, where two butterfly mirrors scan two orthogonal directions and provide the ability to move the beam in 2 dimensions.

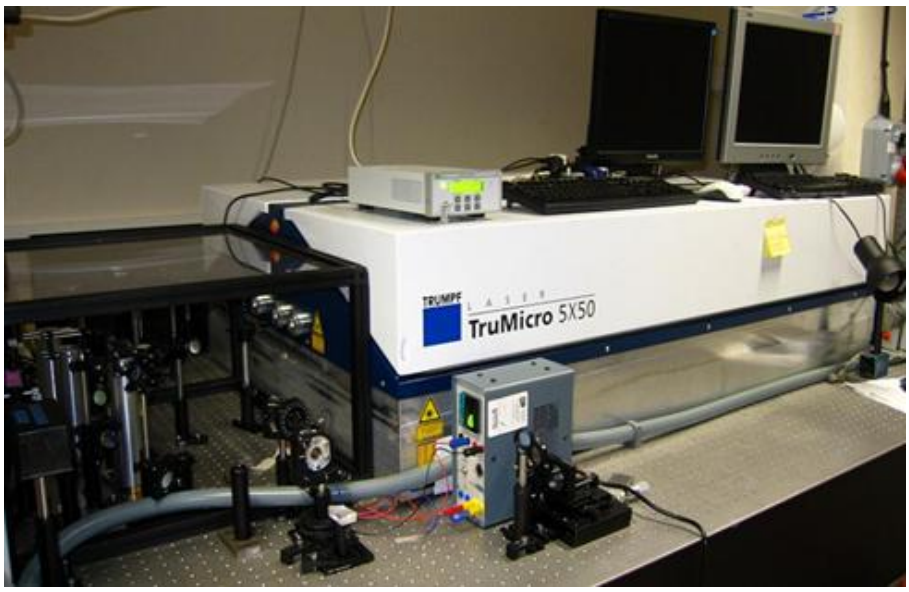

Figure 4.1 TruMicrops-laser ps-laser machining system set-up

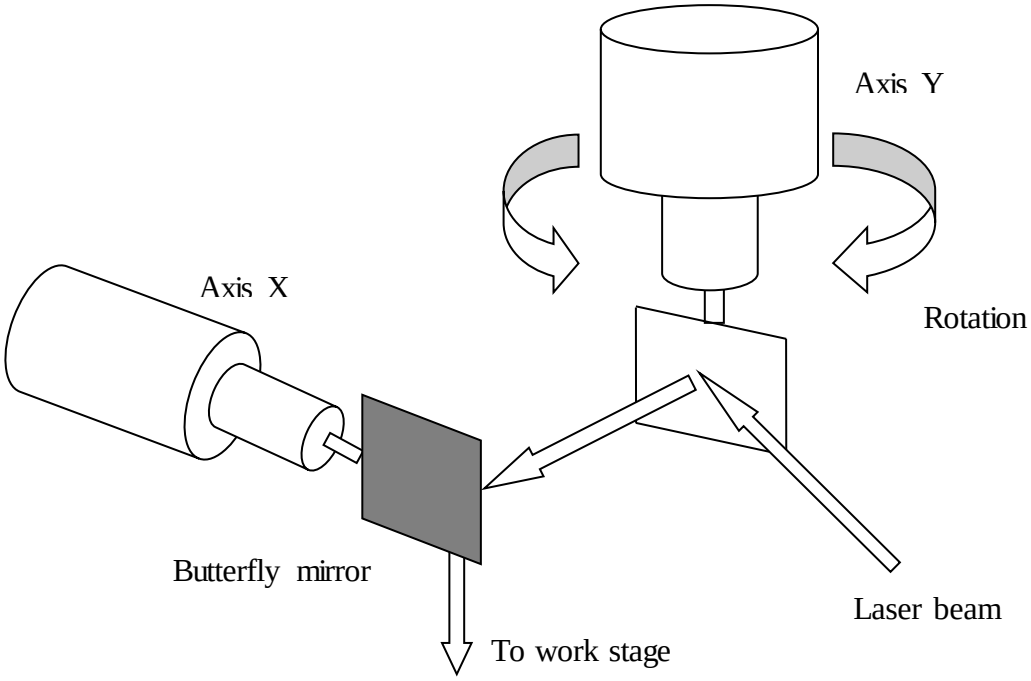

Figure 4.2 Beam inside the laser scan head

The work stage is a precise computerised three dimensional stage, with travel in X, Y, and Z directions. The minimum travelling distance for each direction is 0.1 μm. It

should be noted here that any obstacles along the travelling range can stop the movement of the stages unexpectedly and cause an error that can lead to misalignment of the stages. In the ps-laser fabrication experiments discussed throughout this thesis the 343nm emission wavelength is selected as our working wavelength, due to the transparency of fused silica in this region. In this case, most of the energy will be transferred from radiation into material machining via two-photon absorption [4.2].

One of the important parameters in laser machining is the Depth of Focus (*DOF*) which refers to the distance over which the focused beam has approximately the same intensity. It is defined as the distance over which the focal spot size changes by ±5% using the current set-up, the minimum spot size of the ps-laser system is ~10 μm. Thus we can calculate the *DOF* by the following equation [4.3]:

$$DOF = \pm 0.08\pi \frac{D_0^2}{M^2 \lambda} \tag{4.1}$$

Here D_0 is the diameter of laser spot size, M is the laser quality factor, and λ is the incident laser wavelength. For our system the *DOF* is approximately 100 μm, which means that when machining, we require better than 100μm alignment in the beam divergent direction. This is the same scale as the fibre diameter, which makes it easy to remove material within this scale. The longer the *DOF*, the more straightforward it is to find the focal distance of the laser beam, and thus makes it much easier to remove material. In addition, a longer *DOF* will keep the workpiece in a machining region despite small changes in focus, or movement of the workpiece. However, a longer *DOF* will lead to larger focusing spot size, and this in turn affects the minimum machined feature size. Therefore, there is always a compromise between *DOF* and the minimum beam spot size.

In terms of material removal from optical fibres, the laser will stop machining at a certain depth or even fail to remove any material if the wrong focal distance is used. Determining the correct focal distance with tens of micrometers *DOF* is crucial before starting.

Usually, the focal distance is determined by the Numerical Aperture of the focusing lens. Theoretically, the focal distance can be calculated using Gaussian beam propagation theory. However, the actual beam presented to the focusing lens might not be a perfect Gaussian distribution, and any deviation of the transmitting laser beam from the centre of the lenses will lead to an additional error.

4.1.2 Fabrication process

Part of the laser machining of micro-cantilevers is a collaboration wok with F Albri, a former PhD student in Applied Optics and Photonics Groups. The machining process combines rapid manufacturing afforded by the ps-laser machining process with the optical quality offered by FIB for key parts of the cantilever structures.

In this work, up to 10 fibres can be machined in close succession. With suitable system developments the number of machined fibres could be vastly increased (hundreds). The laser processing is performed using 6ps pulses with energy of 10 μJ per pulse and a focused spot of ~10μm diameter. The beam is focused on the work piece via a galvanometer (galvo) scan head to quickly and accurately move the focused spot across the fibre. In this case, the work stage doesn't have to move at all. Machining accuracy is therefore dependant on the stability of the butterfly mirrors in the galvo scan head. Another issue found during the experiment is that the repeatability of the work stage during alignment will affect the machining process. Even a very small position error will lead to failure of the machining. In our experiments the laser beam is translated at up to 100 mm/s with a pulse repetition rate of 40 kHz which is optimised to be the best machining parameters. A microscope objective is used for detailed process monitoring. Detailed laser micro-machining work can be found in Frank's thesis.

The detailed machining process is illustrated in Figure 4.3. First, the fibres were cleaved, cleaned and then mounted in a V-groove holder. Then the laser beam ablated the top cleaved surface of the fibre and removes material to form a ridge. The fibre was then rotated to allow the cantilever to be fabricated from this ridge by removing a section beneath it, shown in Figure 4.3(b). It should be noted that at this stage it is important to control the alignment of the machined surface, which will form the

reflective surface of the cavity associated with laser cutting process. A rotation mount allows the fibre to be aligned appropriately to compensate for the tapering angle caused by laser beam. The resulting cantilever is shown in Figure 4.3(d), which is 110µm long, 18µm wide and 8µm thick. These dimensions are approaching the limitation of our fabrication process primarily due to errors in mechanical alignment and laser positioning.

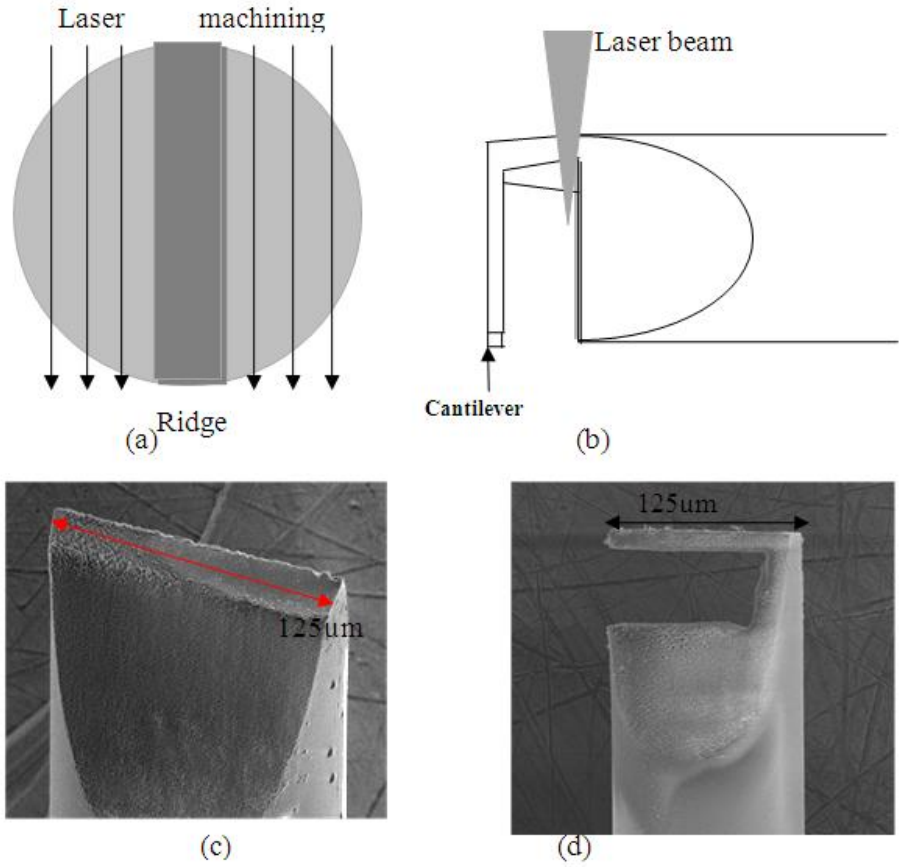

Figure 4.3 Outline laser machining process to form fibre tip cantilever, (a) ps-laser machines a ridge onto cleaved fibre (top view), (b) ps-laser under-cuts to form free standing cantilever (side view), (c) SEM view of machined ridge, (d) SEM view of ps-laser machined cantilever.

The FIB milling process is used to make cantilevers thinner in order to improve the mechanical sensitivity. After the laser machining process, the machined cantilever was coated with a 20nm gold layer in order to reduce electrostatic charge accumulation during the FIB process. FIB machining was then carried out on a dual-beam FIB system (FEI Quanta 3D FEG). The fibres with cantilevers remained on the same

mounting block used in the laser processing to avoid any misalignment during transit between machining stations. The stage can tilt in the electron-ion beam plane from -15˚ to +75˚with a minimum of 0.1º increments. The prepared cantilever was aligned horizontally on the stage. The stage was tilted to 52.0˚ at the eccentric height to ensure correct alignment relative to the ion beam axis. The SEM was placed to the fibre side for real-time monitoring of the fabrication process.

The milling process starts with a beam acceleration voltage of 30keV and a current of 15nA. A narrow rectangular scanning pattern of 110 µm long and 2 µm wide is used to thin the cantilever as shown in Figure 4.4(a). The pattern is aligned with the ion beam, first milling a parallel cut with respect to the cantilever. The cut is not all the way through the cantilever, instead a small connection is left with the main part. This approach of forming a temporary 'shield' between the cantilever and the fibre core is used to mitigate against material re-deposition onto the cantilever bottom surface during polishing of the core surface. Then a second cut around the hinge vertical to the cantilever is used to release the 'shield' thus forming the final cantilever. Due to gravity these materials will fall off automatically after the second cut.

The benefit of using the laser/FIB dual process is that the polishing time is reduced down to less than 20 minutes for cantilevers of these dimensions after ps-laser machining, a significant reduction in FIB machining compared with forming the complete structure using FIB. In order to verify the surface finish of the final polished cantilever, an AFM is used to investigate the surface quality. Figure 4.4(c) shows the topography of the inner cantilever surface. The surface roughness R_a of FIB machined surface is measured to be in the nm range. This FIB step is important to control the amount of optical scatter to provide high quality interferograms for measuring cantilever deflection as discussed in the previous chapter.

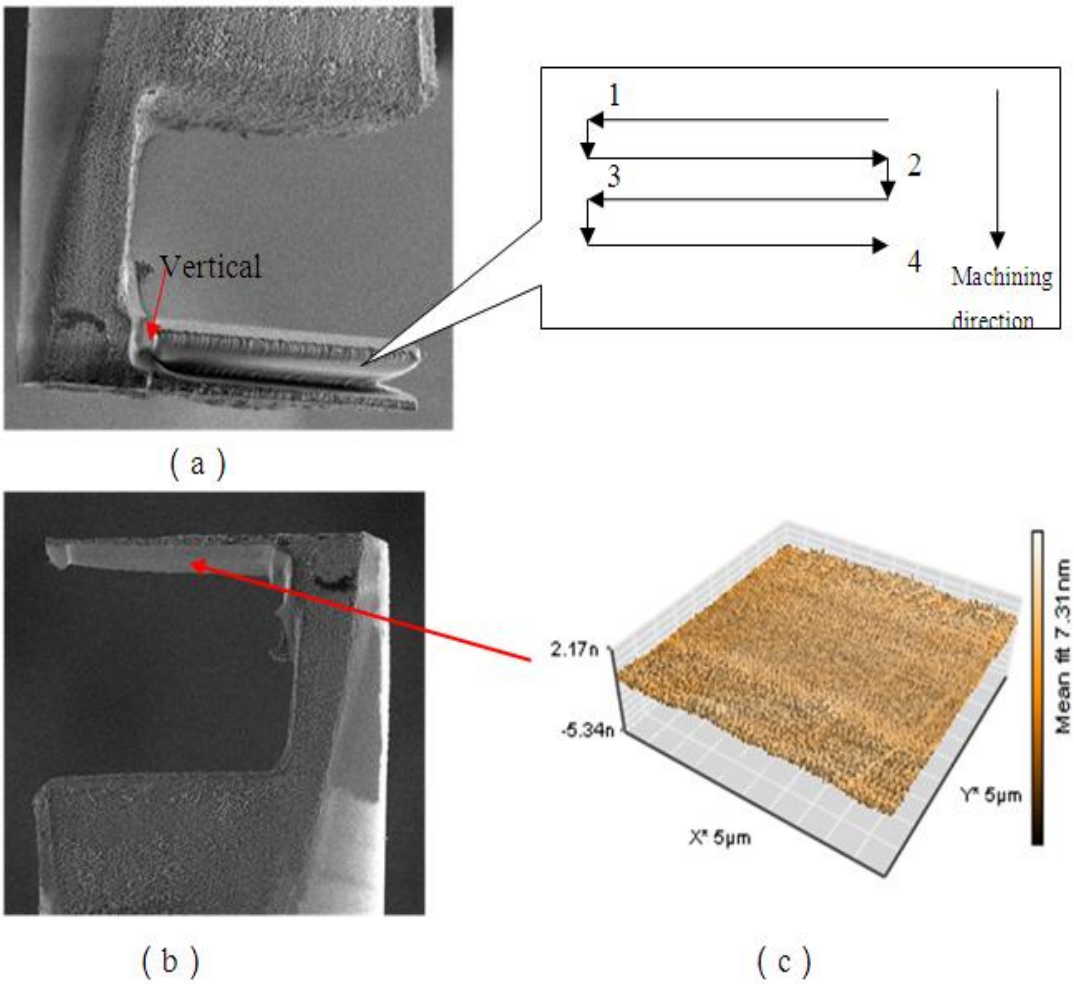

Figure 4.4 (a) SEM view of an optical fibre cantilever during FIB machining. The zoomed in part shows the direction of laser scanning beam applied on the optical fibre. (b) Final machined optical fibre cantilever under SEM view. (c) AFM measured surface roughness of bottom cantilever surface as indicated by the red arrow.

4.1.3 Surface finish study

The surface quality using ps-laser alone is sufficient to carve out a basic cantilever structure but this is still too rough to offer the required reflectivity to form an optical cavity. For this purpose, post processing of optical features using FIB is essential to achieve an optical surface finish. The combination of ps-laser machining and FIB has delivered a cantilever structure that we can use for temperature and pH sensing, depending on the dimension required for individual applications. The overall sensing performance is mostly affected by the machined surface finish and cantilever dimension. Ideally, laser machining without the involvement of FIB or other process would be advantageous, and will lead to fast and low-cost manufacturing. However, this is limited

by the capability of laser machined feature size, in this case, 6-8 µm. Thus it's important to understand the relationship between machining principles and surface finishes in order to create a practical cantilever for sensing applications.

To understand ps-laser machined surface finish, a Corning SMF-28 single mode standard telecommunication optical fibre is used with a cladding diameter of 125 µm, and core diameter of 9 µm. The main material of the fibre is fused silica: a noncrystalline (glass) form of silicon dioxide (quartz, sand). Typical of glasses, it lacks long range order in its atomic structure. The advantages of the fused silica when used for sensing applications is that it has very good chemical inertness, low thermal expansion, while having good UV transparency and low dielectric loss. Figure 4.5 shows the transmission spectrum of fused silica.

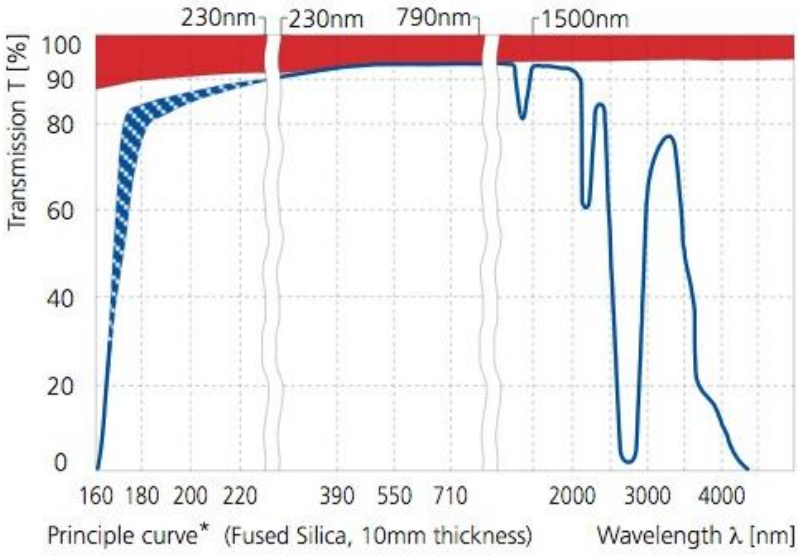

Figure 4.5 Transmission spectrum of fused silica [4.3].

In order to achieve the best surface finish, different laser parameters have been tested whilst machining. These include laser power, repetition rate, scanning speed and machining direction. The fibre is clamped into a V groove mount perpendicular to the cutting direction. First of all, 40 kHz repetition rate, 100mm/s scanning speed and an average laser power of ~6W are used to cut a SMF-28 single mode fibre. The fibre is

cut 200 times all the way through. The schematic laser cutting process is shown in Figure 4.6.

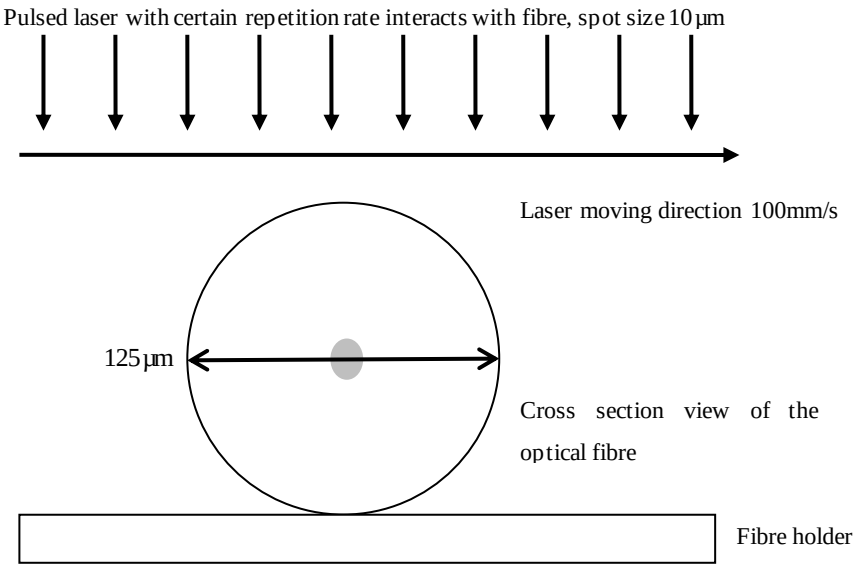

Figure 4.6 Schematic view of ps-laser cutting of a SMF-28 single mode fibre.

The actual laser movement while cutting is shown in Figure 4.7. A straight line of 400 µm is used to cut the cleaved fibre in order to make sure that the laser beam covers the whole cross section of the fibre. The same parameters are used to cut the fibre and the surface finish of the cross section is investigated later. Here, 40 kHz repetition rate equals to a 25 µs pulse interval. As the scanning speed of laser is 100mm/s and the spot size of the laser is 10 µm, here is a 2.5 µm spot overlap. The effect of this overlap can smooth the cutting surface by giving extra thermal energy to the surface, reducing roughness.

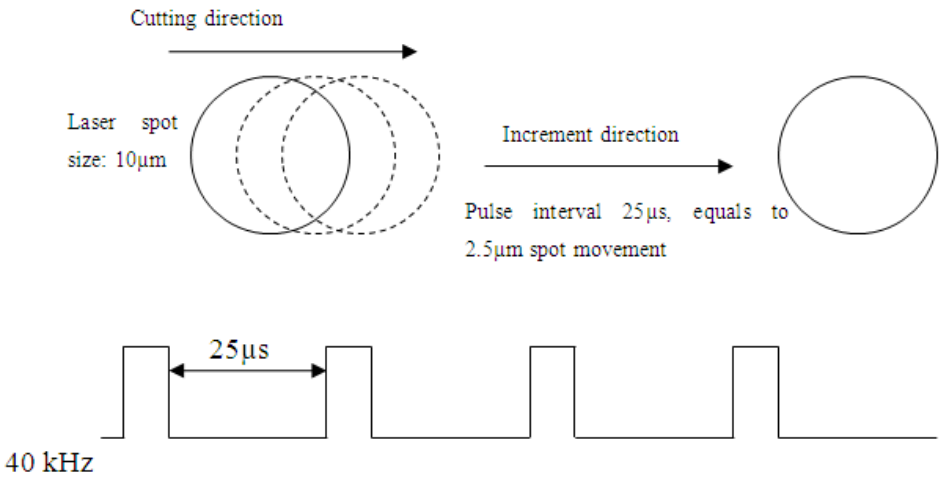

Figure 4.7 Schematic diagram of laser movement when cutting.

Figure 4.8 shows the surface roughness of a ps-laser cut fibre compared with a cleaved fibre measured by AFM. The calculated surface roughness R_a of ps-laser cut fibre end surface is 423.293nm whereas a cleaved fibre end surface is only 18.269nm, which is much smoother than the ps-laser cut fibre end facet. Figure 4.9 shows the microscopy view of a ps cut fibre end facet. A post fabrication process which use high voltage fusion splicing technique can be used to improve the surface quality [4.5] by melting the surface and cooled down. As a result of the surface tension, the surface finish tends to be smoother.

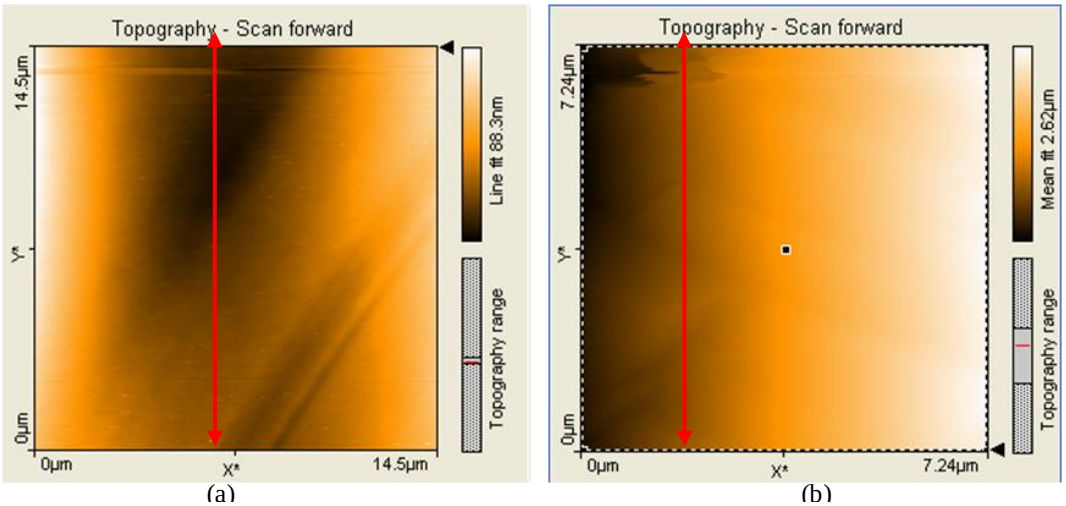

Figure 4.8 (a) A manually cleaved SMF-28 fibre measured by AFM, R_a: 18.269nm. (b) ps-laser cut fibre end facet measured by AFM, R_a: 423.293nm.

Figure 4.9 The ps-laser machined SMF-28 fibre viewed by a light microscope.

The machined surface roughness indicates the surface quality that the ps-laser can achieve. The quality of the surface finish is crucial for interrogation, since an FPI will be created including at least one of the laser machined surfaces. In this case, an optical quality surface down to ~nm with high reflectance would be required to achieve a high visibility for signal read-out. The laser parameters to cut the fibre are based upon the best surface roughness we achieved. Usually R_a is calculated to be several hundred nanometers and this number seems to approach the ps-laser machining limitation of fused silica with our experimental set-up. Previous procedures usually involve expensive and slow FIB milling process, which has been demonstrated to be unsuitable for mass production (see Chapter 2). On the other hand, ps-laser machining can provide fast material removal rate which is a potentially low-cost, fast process suitable for industrial mass production. The fabrication techniques developed in this chapter combine the merits of the two technologies. That is: first use ps-laser to machine cantilever structures onto the end of an optical fibre then polishes the optical surfaces by FIB milling. This approach can give us an optical surface finish for interrogation while reducing the total fabrication time.

4.2 Mechanical response of micro-machined cantilever

To test the behaviour of the cantilever as a micro-displacement sensor, the cantilever is mounted onto a translation stage. A second fibre is used as an actuator approaching the cantilever tip to apply a linear deflection. A schematic view of optical fibre tip cantilever calibration set-up is shown in Figure 4.10. The movement of the actuator is controlled using a piezoelectric driven translation stage. For calibration purposes, a Renishaw ML10 position sensor with a resolution of 1 nm is used to monitor the position of piezoelectric translation stage. By using similar interrogation technique discussed in Chapter 3, experimental data is acquired and processed.

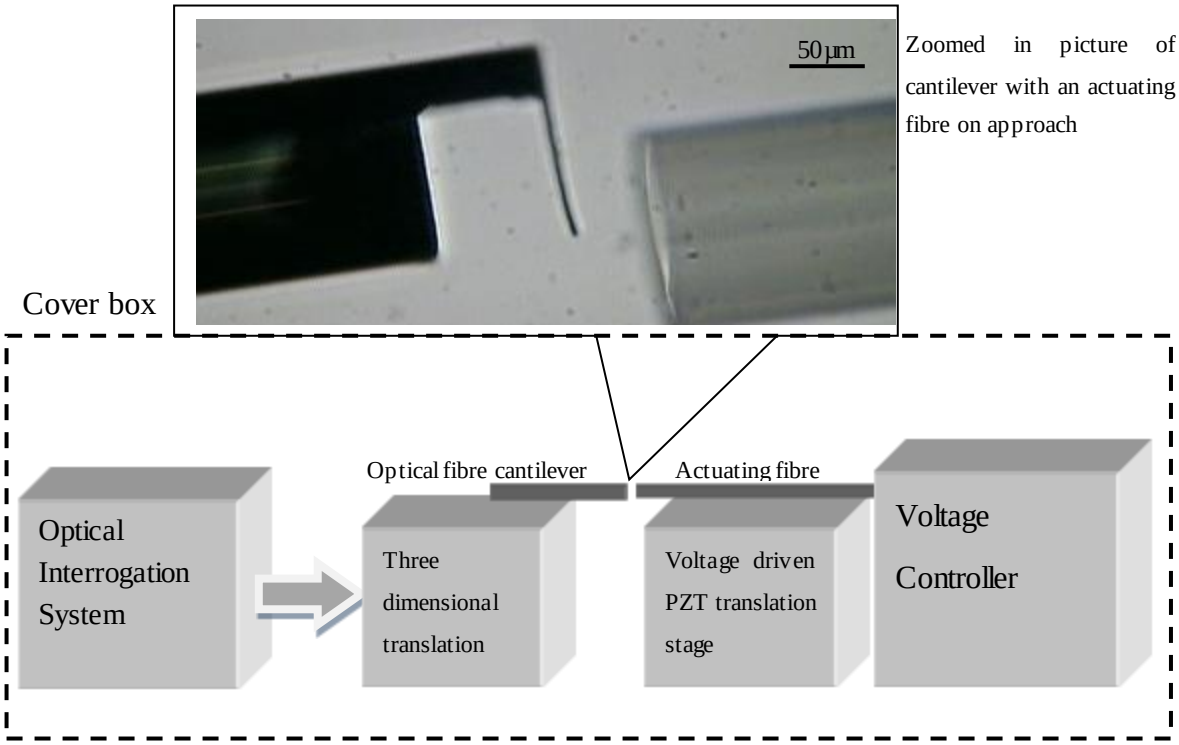

Figure 4.10 Optical fibre cantilever actuation experiment set-up. A cover box is used to isolate the system from ambient environment. Zoomed in part shows microscopy view of an actuating fibre is approaching the optical fibre cantilever from right.

Figure 4.11(a) shows the cantilever deflection over a range of 9000 nm. The maximum residual error of the cavity length (compared with ML10) is around 10 nm and a calculated r.m.s. error is ±8.9 nm, which means our interrogation system is capable of detecting cantilever deflection change up to a few nanometers. A single wavelength laser based interrogation system is used to acquire the dynamic optical signal when

applying a triangular voltage to the piezoelectric driven translation stage. As shown in Figure 4.11(b), the response signals from a single wavelength laser interrogation system is cosinusoidal while the actuating fibre is in contact with the cantilever and displacing it over several fringes, as we would expect.

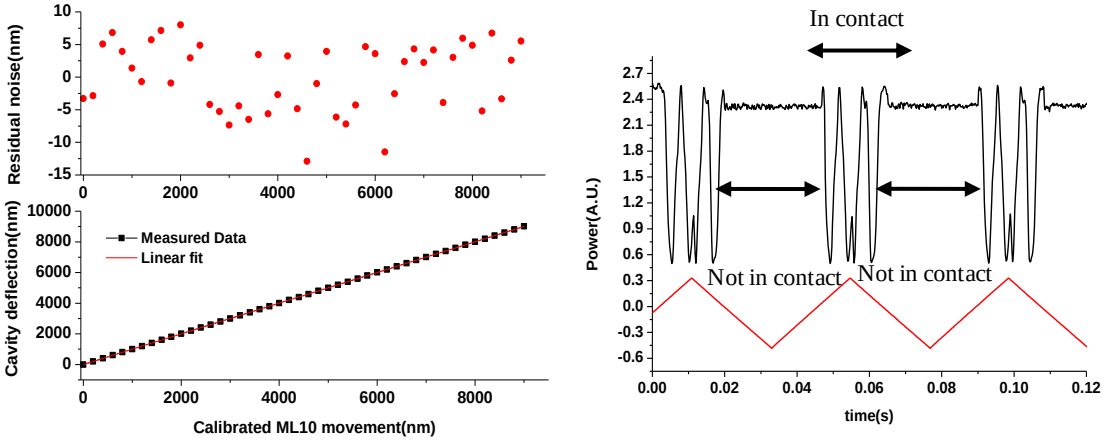

(a) (b)

Figure 4.11 (a) Measured cavity length change by optical fibre cantilever interrogation system versus ML10 with the residual error shown, (b) Dynamic response of micro-machined cantilever: top trace shows return from the cavity monitored at a single wavelength, bottom trace shows the piezoelectric driving voltage signal.

4.3 Optical fibre-top cantilever for temperature sensing

One of the applications for optical fibre-top cantilever is temperature sensing. Although it is well established, it's a useful demonstration of the capability of using an optical fibre cantilever as a temperature sensor.

Similar to the bimetallic effect [4.6], the thermal coefficient of expansion mismatch between the two components of a sandwiched layer can be used to provide displacement as a function of temperature. A fused silica cantilever with a metal layer coated on one surface will generate a tip deflection due to the temperature change. The deflection of the cantilever beam d could be written by the following equation:

$$d = kL^2/2 \tag{4.2}$$

Here k is the curvature of the cantilever bending and L is the cantilever length. By using the equation presented in [4.6], we have:

$$k = \frac{1}{r} = \frac{6b_1b_2E_1E_2t_1t_2(t_1+t_2)(\alpha_1+\alpha_2)\Delta T}{(b_1t_1^2E_1)^2+(b_2t_2^2E_2)^2+2b_1t_1E_1b_2t_2E_2(2t_1^2+3t_1t_2+2t_2^2)} \quad (4.3)$$

Where r is the cantilever bending radius, t_1 and t_2 are the thickness of aluminium coating, b_1 and b_2 are the width of coated area of the cantilever, α_1 and α_2 are thermal expansion coefficient of coating material and substrate, E_1 and E_2 are the Young's Modulus of aluminium and fused silica respectively, and ΔT is the temperature change. Using equation 4.3, cantilever tip deflection can be easily calculated.

During the experiment the machined cantilever is first evaporated with 4 nm chromium (Cr) to aid adhesion and then coated with ~500 nm aluminium. Aluminium is chosen due to its high thermal expansion coefficient, and ease of deposition. It is assumed that the aluminum tends to oxidase to aluminium dioxide (Al_2O_3) in the presence of air with a few nanometers thickness, however, the deflection caused by this additional layer is very small, and can be ignored. For high temperature sensing applications, metals with a higher melting point will be required.

4.3.1 Temperature sensing

After the top surface of a cantilever was functionalized, the machined optical fibre cantilever was placed into a ceramic tube furnace (LENTON-1200) for temperature cycling. The tube was then sealed by filling insulating material in order to keep a stable thermal environment. A thermocouple is employed to monitor the temperature change next to the cantilever as shown in Figure 4.12. The schematic configuration of applying heat to a fibre-top cantilever sensor is shown in Figure 4.13(a). It can be seen that cantilever will bend down due to the different thermal expansion for aluminium and fused silica. The cooling down curve of the furnace from 500 ℃ is also shown in Figure 4.13(b).

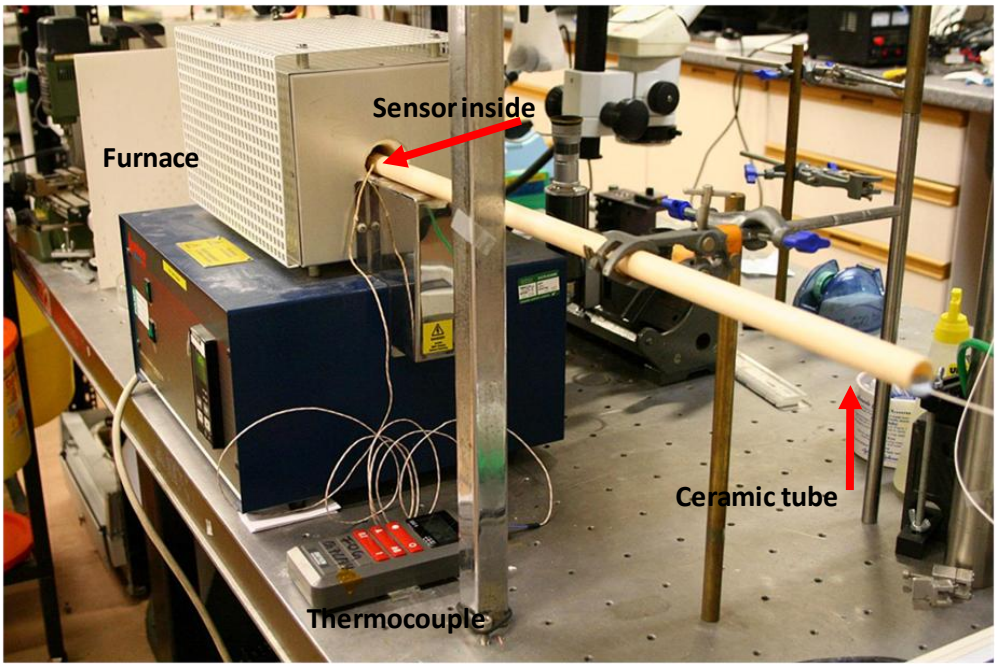

Figure 4.12 Experiment set-up of the optical fibre cantilever temperature sensing system.

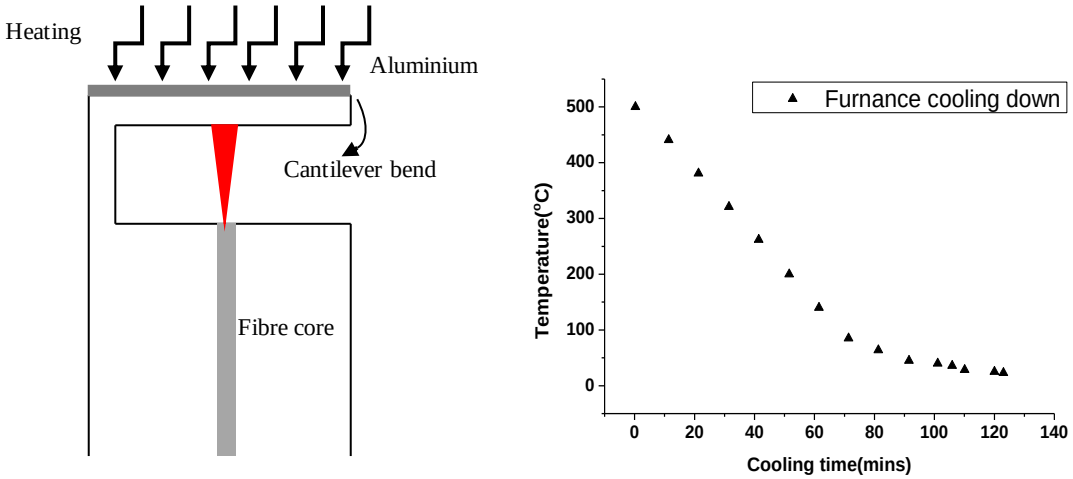

(a) (b)

Figure 4.13 (a) Schematic configuration of fibre-top cantilever temperature sensing. (b) Furnace cooling time vs. temperature change. Furnace is allowed to cool down from 500 ℃. Above 100 ℃ the temperature drops quickly and as temperature goes lower, the cooling process becomes slower.

The furnace is first heated up to 500˚C and then held at this temperature for half an hour to allow uniform temperature distribution to form in the ceramic tube. For each temperature cycle the furnace is switched off and allowed to cool down naturally. The cantilever deflection during cool down period is recorded by the interrogation system

mentioned in Chapter 3. Here we assume that the aluminium coating layer covered the whole fused silica cantilever, the structure is uniformly heated and no other additional forces are applied on the cantilever. The zero deflection position of the cantilever is at room temperature. In our case, all the experiments start at room temperature of 20˚C. We assume the cantilever deflection towards the fused silica side indicates an increase in deflection.

The measured temperature change versus cantilever deflection is plotted in Figure 4.14. The red solid line represents the modelled response based upon the model presented in reference [4.6], whereas the black squares indicates the measured data. When the temperature increases, a compressive surface stress is applied to cantilever due to the thermal expansion difference between Aluminum and fused silica.

We believe that the mismatch between the model and linear fit of measured data is probably due to several reasons: The coating layer may start to delaminate at higher temperature. The fabricated cantilever is not a perfect rectangular beam with uniform thickness, which will change the mechanical characteristic and finally laser micro-machining induced thermal shock [4.7] might produce the micro-cracks inside the cantilever, which will slightly change the Young's modulus of the material. According to Figure 4.14, the slope of linear fitting (dashed line) is 40.2nm/˚C. By using the phase recovered algorithm discussed in Chapter 3, this equals a temperature resolution of 0.08˚C. The thermal-optic coefficient of air is ~10^{-6} K^{-1} and fused silica is 1.55×10^{-5} K^{-1}, in our case, the maximum cavity change due to a change of refractive index of air is tens of nanometers for the 500K temperature range, which can be ignored here.

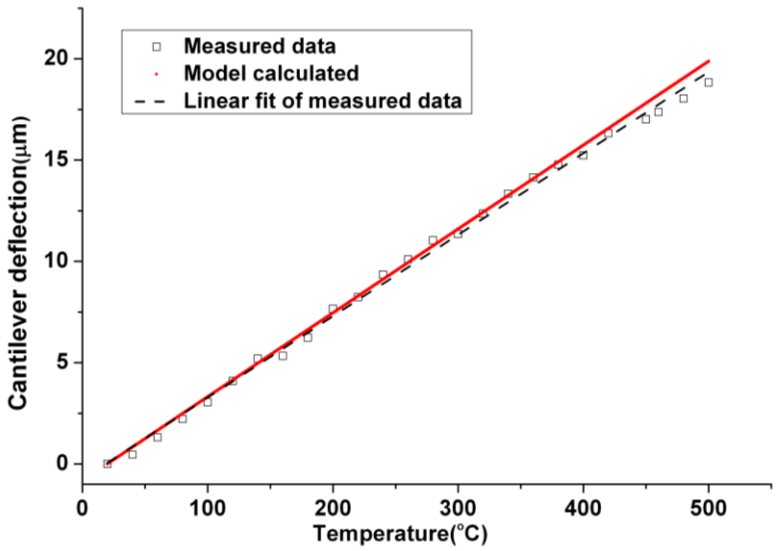

Figure 4.14 Temperature change versus cantilever deflection change. Both the measured and model calculated data are shown.

To further investigate the thermal response of an optical fibre cantilever sensor, extended monitoring was carried out with over 16 hours. The temperature was cycled three times from 500˚C to 100˚C, dwelling for at least 1 hour at these temperatures. Figure 4.15 shows the cantilever deflection variations during the whole cycling process. For each cycling a maximum deflection of ~18 μm is found. When the furnace cooled down to room temperature the cantilever returns to the zero position. By using the phase recovery algorithm discussed in Chapter 3, temperature noise can be further reduced. When held at 100˚C and 500 ˚C, we can see from Figure 4.15 temperature noise and fluctuation is reduced due to the phase recovery algorithm. As seen from the figure, the sensor is capable of reliably measuring temperature up to 500 ˚C.

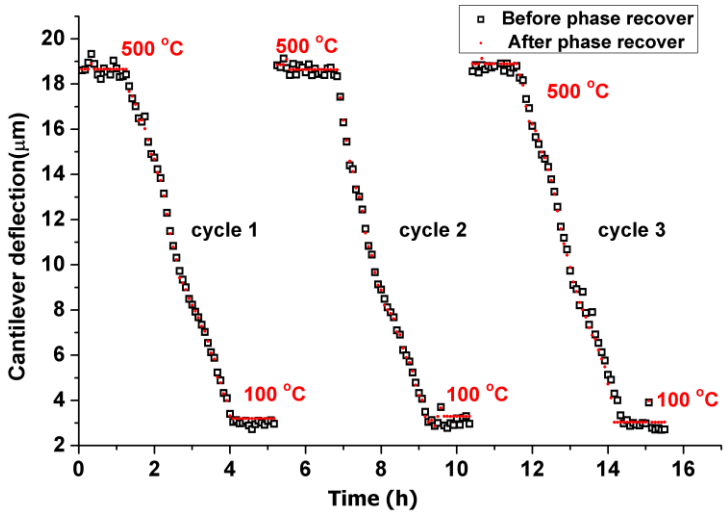

Figure 4.15 Cantilever deflection during extended temperature cycling trials at 500 ℃ and 100 ℃ for three times.

By using a linear fitting from Figure 4.14, we can express the relationship between cantilever deflection and temperature change with the following fitted equation:

$$T = 24.8756L + 18.53 \tag{4.4}$$

Where T is the measured temperature in ˚C and L is the cantilever deflection in micrometers. Using this calibration we plot the measured temperature data from 20˚C to 500˚C in Figure 4.16. From the insert of Figure 4.16, we can see that the maximum temperature error of ±4.8˚C is found at 500˚C and the r.m.s. temperature error calculated by experimental data is ~±1.4˚C over a 500˚C range. Here temperature errors show the temperature repeatability during real measurements, while the temperature resolution of 0.08˚C mentioned above is based on the best case deflection measurement from the fitted data after phase recovery. The temperature error here is bigger than the previous resolution calculated after using phase recover algorithm. We suspect that temperature drift, thermal noise, and vibrations are the main contribution of this error during the practical temperature measurement.

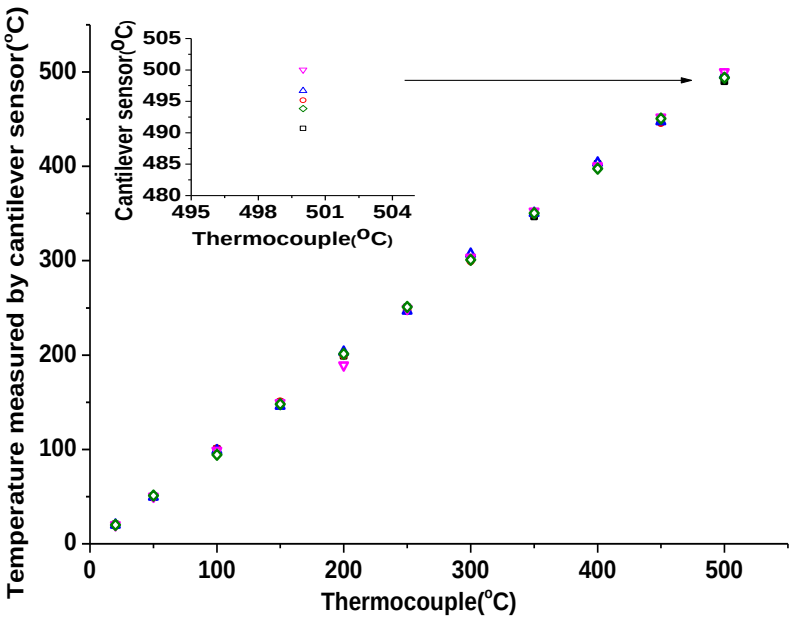

Figure 4.16 Monitored temperature by a thermocouple vs. monitored temperature by an optical fibre-top cantilever sensor. The insert figure shows the temperature spread error at 500 ℃. The error is measured to be ±4.8 ℃.

In this section, micro-cantilevers which were fabricated onto the end of a single mode optical fibre were demonstrated by the combination of ps-laser machining and FIB milling techniques. The potential route for rapid manufacture of such cantilevers with the laser fabrication stage take only a few seconds while the FIB polishing gives us an optical surface finish. In the future, laser machining techniques may offer the potential for low cost mass production. The ability to use this cantilever sensor as a temperature sensor is demonstrated. A temperature resolution of 0.08 ℃ based upon the best case deflection measurement resolution and a sensing range of up to 500 ℃ have been shown. Extended duration temperature stability was also tested to monitor sensors as they were cycled from room temperature to 500 ℃ several times. In this particular test the average temperature r.m.s. error within the whole measurement range is ~±1.4˚C with maximum experimental temperature error is ~±4.8˚C found at 500 ℃. The demonstration of optical fibre cantilever as a temperature sensor proved the reliable sensing capability by deflection measurement interferometrically. This also opens the route of using optical fibre cantilever as a transducer for other applications, such as chemical and biological sensing.

4.4 Optical fibre-top cantilever for pH sensing

4.4.1 Introduction to pH sensing

In some applications such as chemical analysis or the control of biological systems, it is critical to monitor the pH value of the aqueous media [4.8][4.9]. pH is essential in finding the chemical characteristics of a substance and to control chemical reactions. Several techniques are commonly used in order to measure the pH of solutions, mainly based on Ion Sensitive Field Effect Transistor (ISFET) [4.10], magneto elastic [4.11], conductimetricor [4.12] and optical techniques [4.13].

Electrical based techniques do have many advantages：they are cheap, easy to fabricate, accurate and sometimes have large pH detection range. However, these sensing techniques usually need a long response time and sometimes it's difficult to detect very small sample volumes down to ~μL. The other commonly used technique is optical-based pH sensor [4.14] [4.15]. This technique usually involves the use of colorimetric or fluorescent indicators, in which the amplitude of an optical absorbance or a fluorescent signal is measured. These sensor schemes are simple and cost-effective but their main drawback is their robustness, which depends on the absolute signal amplitude (absorbance or fluorescence intensity) and hence they can be influenced by undesired external factors such as excitation light intensity fluctuations, temperature, concentrations of the analyte or the indicator, or even bleaching or leaching of the indicator.

The concept of using micro-cantilevers as highly sensitive chemical and physical sensors was first reported in 1994 [4.16]. To date, physical sensors using micro-cantilevers have been demonstrated by detecting thermal energy, force, magnetic field, and infrared radiation [4.17][4.18][4.19]. Extremely sensitive chemical and biological sensors for analytes including DNA, alcohol, mercury, antigen-antibody binding, and bacteria have also been reported based on micro-cantilever sensors [4.20][4.21][4.22]. Unlike many other types of transducers for chemical sensors, these cantilevers are simple mechanical devices. They are small, typically 0.2-1 μm thick,

20-100 μm wide, and 100-500 μm long, and are connected to an appropriate support for convenient handling. Such devices have seen widespread use. For example, forming a sharp tip onto a micro-cantilever makes it useful as a probe for mapping localized surface topology in AFM.

Micro-cantilevers have already been reported as pH and chemical sensors in recent years. One approach is to use a surface-modified micro-cantilever to detect pH changes. For example, Ji *et al* [4.22] demonstrate a maximum pH sensitivity of 49 nm deflection/pH unit using a silicon dioxide/gold (SiO_2/Au) cantilever. The variation of pH versus cantilever deflection is discussed, but the detailed explanation for surface interaction mechanism on pH activated cantilever is still uncertain. A more widely used method which can make material sensitive to pH variations, is to micro-pattern hydrogels which can sense a pH change and actuate as a transducer. When hydrogels are utilized as sensing micro-structures, their function is improved as the reduced size leads to faster mass transfer and chemomechanical response. As a result, researchers have fabricated a variety of novel sensors based on bio-chemical sensors. Bashir *et al.* [4.23] used swellable hydrogels as a transducer deposited on top of a micro-cantilever and demonstrated the potential as an ultrasensitive pH sensor. Silicon-on-insulator wafers were used to fabricate cantilevers with a polymer consisting of poly (methacrylic acid) (PMMA) patterned using free-radical UV polymerization. The mechanical amplification of polymer swelling as a function of pH change within the dynamic range was obtained with a maximum deflection sensitivity of 1 nm/$5\times10^{-5}\Delta$pH, however the effective measurement range of pH is limited between pH 5.9 to pH 6.5 due to the characteristic of their sensor. VanBlarcom *et al.* demonstrated a biodegradable pH-responsive hydrogel micro-cantilever sensor [4.24]. They created a theoretical hydrogel swelling model to verify the test result of the sensor in a protein-rich solution and 1nm/$5.7\times10^{-5}\Delta$pH sensitivity is achieved for the resulting sensor with a detectable pH range from 5 to 6.5.

In this section, micro-cantilevers machined directly onto the end of standard telecommunication fibres will be employed to detect pH change in a liquid environment. The structure fabricated forms a Fabry-Perot cavity, where measurement of the cavity length allows us to infer the cantilever deflection due to changes in pH. By forming the cantilever onto the end of a fibre allows alignment to the readout system, via the fibre core during the fabrication stage, therefore, no post fabrication mechanical alignment of the sensor is required. The use of optical fibres offers the potential for a miniaturised sensor with electromagnetic immunity, small physical size, and biocompatibility. The interferometric approach to monitor cantilever deflection is significantly more robust than a simple intensity-based sensor set-up [4.25]. Finally, the micro scale nature of the sensor offers potential for rapid responses using a small test volume.

4.4.2 pH sensor fabrication

The fabrication techniques are similar to the fibre-top cantilever temperature sensor discussed previously. The resulting cantilever is ~100μm long, 18μm wide and 8μm thick. It should be noted that due to the scale of the single mode optical fibre and the resolution of the control system, the minimum cantilever thickness machined by ps-laser is down to 7-8μm.

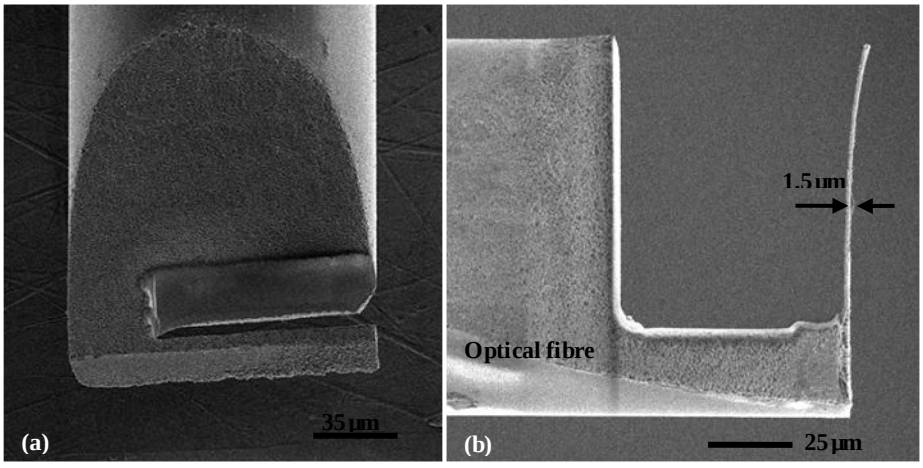

Figure 4.17 Fabricated cantilever onto the end of an optical fibre with SEM view: (a) Before FIB polishing, (b) After FIB polishing. The thickness of the final cantilever is 1.5μm.

After the laser processing is completed, these cantilevers are brought to the FIB chamber for further modification without changing the position on the fibre holder. Using FIB it is possible to achieve cantilever thickness down to ~1.5µm which gives a suitable thickness for pH measurements. An SEM image of the cantilever before and after FIB machining is shown in Figure 4.17. The thickness is measured to be 1.5 µm, which provide higher sensitivity for chemical sensing. To the best of our knowledge, this is the thinnest optical fibre-top cantilevers reported so far.

4.4.3 Experiment and discussion

The basic experiment for the optical fibre cantilever pH measurement system shown in Figure 4.18. The analysis of the interferogram is based upon extracting the free spectral range of the cavity, which is directly related to the cavity length. SM-125 optical interrogator (Micron Optics, USA) is used to demodulate the phase information from the cantilever. This was already discussed in Chapter 3. Figure 4.19 shows the fringes from the machined cantilever. The cavity length calculated by FFT is ~59.3µm in this case.

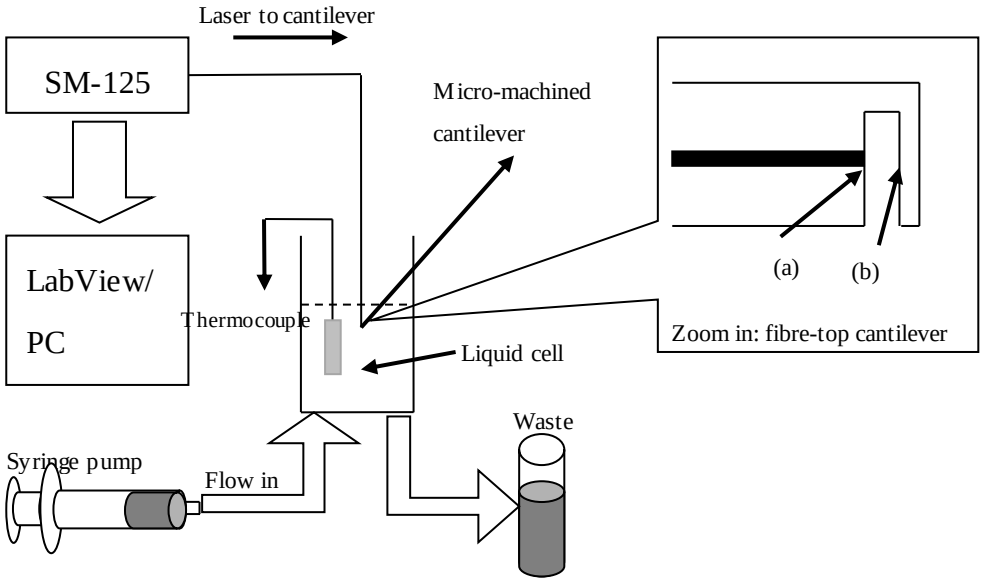

Figure 4.18 Schematic of pH measurement set-up. A fibre-top cantilever is immersed into the liquid cell and a thermocouple monitors the temperature. SM-125 optical interrogator demodulates the cavity length and the deflection of cantilever is calculated by LabView/PC. The zoomed in part shows the two reflecting surfaces which create the FP cavity.

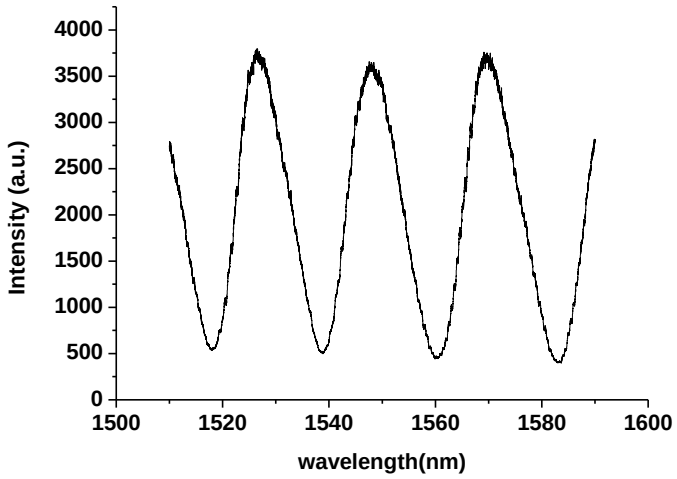

Figure 4.19 Fringes of a laser/FIB machined optical fibre-top cantilever with a cavity length of 59.3μm.

Prior to using the micro-machined cantilever as a pH indicator, it is calibrated with an actuating fibre end to apply a known deflection. The movement of the actuating fibre is controlled by a calibrated piezoelectric translation stage. The process is repeated several times in order to prove the mechanical robustness of this micro-machined cantilever. A ML10 position sensor (Renishaw, plc. UK) is employed to calibrate the sensor with the detailed calibration process discussed in [4.5].

In order to make the cantilever sensitive to pH one side of the cantilever must be 'activated', so that a change in pH results in a different strain on each face of the cantilever. It is this strain differential that causes the cantilever to deflect according to the Stoney equation discussed in Chapter 2. Two layers are investigated in this work (i) Al_2O_3/Au and (ii) MHA/HDT. Both MHA (16-mercapto-hexadecanoic-1-acid) and HDT (1,6-hexanedithiol) were purchased from Sigma-Aldrich.

Before testing the pH sensitivity the background system noise level with the cantilever in a fluid was measured. This is achieved by immersing the cantilever into Phosphate Buffer Solution (PBS) pH 7.0 solutions and monitoring the cantilever position. The experiment was temperature controlled (23˚C ±0.2˚C) and insulated in order to maintain a stable temperature environment. In order to investigate the temperature effect on the cantilever deflection, a fibre-top cantilever is immersed into the water and a thermocouple monitors the ambient temperature changes over 200 minutes. The relative cantilever deflection is acquired every 10 seconds over 200 minutes, with results shown

in Figure 4.20. Here the maximum cantilever deflection fluctuation is around ±12 nm, with an r.m.s. error of ~±6 nm. From this data we conclude that a temperature variation within a degree does not affect the cantilever deflection within the measured noise level.

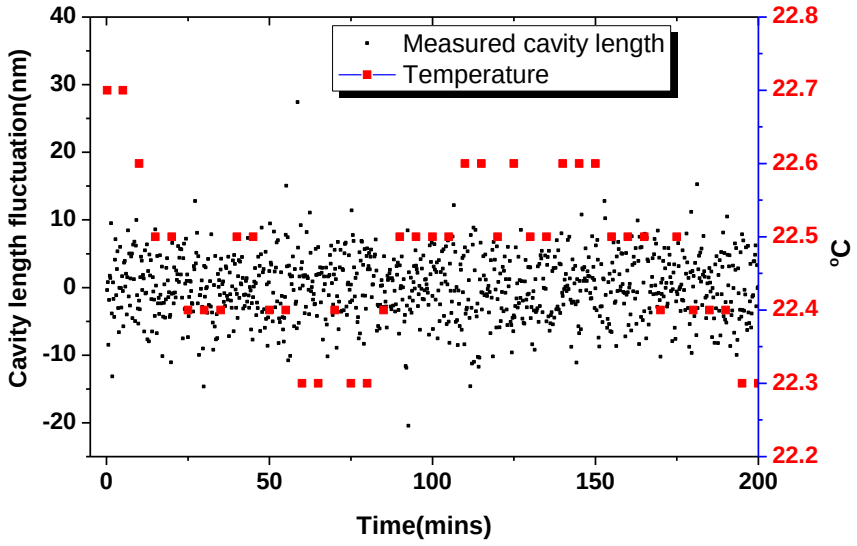

Figure 4.20 Thermal stability of cantilever deflection over 200 minutes. ~20nm cavity length fluctuation is found when temperature changes from 22.3 ℃ to 22.7 ℃.

In order to investigate the effect of flow turbulence upon the cantilever deflection was monitored while gently injecting PBS pH 7.0 solution into the liquid chamber at a constant speed of 50μL/min. The cantilever is initially immersed in PBS pH 7.0 solution and a thermocouple is also placed in the liquid cell to monitor the temperature change. The cavity length and temperature are shown in Figure 4.20. After injection the temperature dropped down rapidly by 0.3˚C then returned back to 23˚C after 40 seconds. The rapid drop of the temperature was due the lower temperature difference between the injected liquid and the ambient temperature. As the liquid flowed outside the liquid cell, the temperature started to return to ambient temperature. An average (r.m.s) cavity fluctuation during this period was found to be 12.8 nm, which was comparable to the system noise level. Therefore by carefully controlling the injection speed, the influence of flow turbulence on the cantilever deflection can be minimised.

For pH measurements the cavity length is measured in reference to the initial cavity length when the sensor is immersed into PBS pH 7.0 (defined as 0 nm). We define 'bending down" as cantilever bending towards the gold coated side while, 'bending up' refers to bend towards the Al_2O_3 side. The experiment is first conducted to test the thermal stability of the micro-machined cantilever with a coating on it in a liquid environment. The whole experiment is carried out at a temperature of 23˚C±0.2˚C, with the interrogation system shown in Figure 4.18. The system is covered with foam and filled with insulating material in order maintain a stable temperature environment. After that, the cantilever is immersed into PBS 7.0 solution and the relative cantilever deflection is acquired every 10 seconds over 200 minutes (Shown in Figure 4.21). It's clear that the maximum cantilever deflection fluctuation is around ±12nm, with an r.m.s. error of approximate ±6nm, which means for temperature variation within a degree, the deflection noise level of cantilever is ~8nm, therefore, small temperature changes of <0.5˚C is within the noise level.

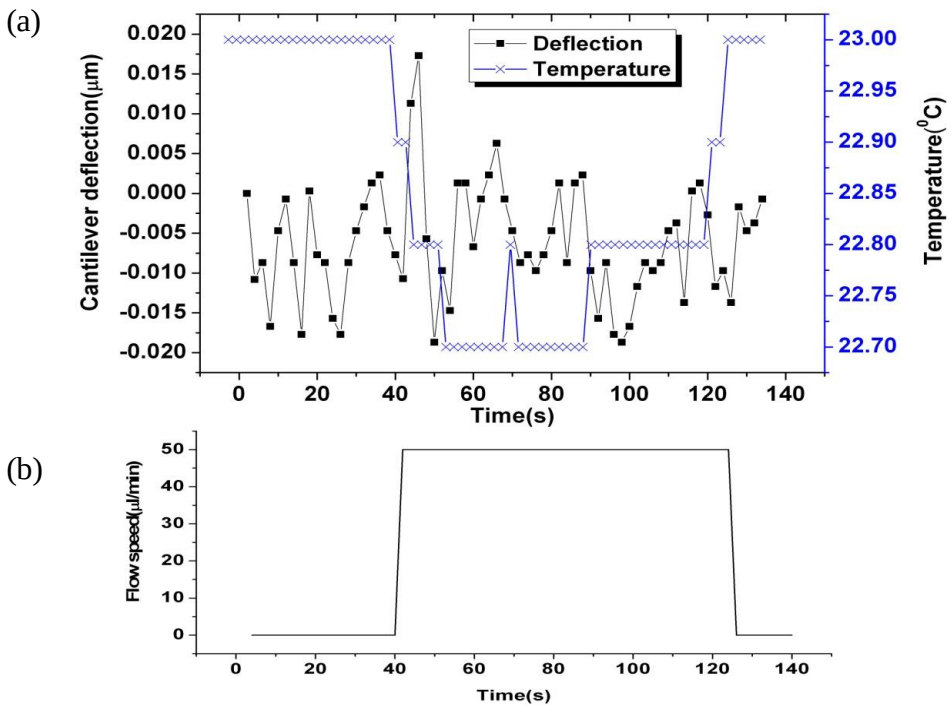

Figure 4.21 Cantilever cavity fluctuation versus temperature change over a measurement time of 140 seconds. (a) Fibre-top cantilever deflection before and after injection of flow. (b) Flow speed versus injection time. Injection starts at 40s and finishes at 125s.

4.4.4 Results and discussion

To measure pH, the cantilever is functionalized with different pH active coating layers. Two different coating layers are selected here. One of them is Al_2O_3/Au, which has shown high sensitivity on a silicon nitride (SiN_3) cantilever [4.26]. The other is called MHA/HDT coating, which proved to be a stable coating layer for pH sensing [4.27].

An Al_2O_3/Au functionalised pH sensor was made by first evaporating 4nm of Cr to the SiO_2 surface and then depositing 20 nm aluminium onto the top side of the cantilever. It was then stored at room temperature overnight until the entire aluminium thin film oxidizes to Al_2O_3. The bottom side of the cantilever is coated with 4 nm of Cr surface and followed by 20 nm of gold (Au) to form as a blocking layer for pH measurement.

pH 4.0 (product No.FB67160) and pH 10.0 (product No. FB67162) buffer solutions were purchased from Fisher Scientific Company. The pH of each buffer solution used between 4 and 10 was formed by varying the proportion and the exact pH value was measured using a commercial pH meter with a resolution of 0.1 pH unit at 23˚C. The concentration of the final solution is controlled at 100mM.

The effect of pH on both Al_2O_3/Au and MHA/HDT functionalized cantilevers was investigated using the experiment set-up shown in Figure 4.18. The experiment was carried out at a temperature of 23˚C±0.2˚C and the final cavity length is determined by FFT algorithm discussed in Chapter 3.

First, the effect of different pH level on an Al_2O_3/Au cantilever was investigated. Aluminum oxide-coated surfaces have been shown to be sensitive to pH e.g., it has been used to modify ISFET gate surfaces [4.28]. A coating of Al_2O_3 will change the influence of pH on cantilever surface stress due to the interaction with H^+, thus generate a bending signal. To reference the zero position of the cantilever, the fresh coated cantilever is first immersed in PBS 7.0 solution and the cavity length is recorded. After that PBS 9.0 solution is injected gently at a constant speed and allows a few minutes for the cantilever to achieve a steady-state deflection, then the cantilever is washed with PBS 7.0 solution and PBS 8.5 solution is injected. The same process is

repeated from PBS 9.0 to PBS 4.0 in steps of 0.5 pH each time followed by another cycle from pH 4.0 to pH 9.0. All PBS solution is measured by an electro pH meter and the temperature is monitored by a thermocouple at 23˚C±0.2˚C. The concentration of each PBS solution is 100mM. The schematic view of Al_2O_3/Au activated cantilever is shown in Figure 4.22(a) and the steady-state deflection of the cantilever is plotted as a function of pH in Figure 4.22(b). At each pH, cantilever deflection reaches an equilibrium position after 1 to 2 minutes. For each cycle, the mean of up to six measurements are used to determine the steady-state cantilever deflection. The deflection response of the Al_2O_3/Au cantilever indicate that when pH>7.0 the surface stress increases, and reaches ~180 nm deflection at pH 9.0 towards Al_2O_3 side. The cantilever bends down towards the Au side when pH<7.0 and reach a maximum deflection around 100 nm. It's also clear that the Al_2O_3 /Au functionalized cantilever is sensitive from pH 7.0 to pH 9.0 and ~100 nm/pH sensitivity is achieved, with the resolution of our system equals to an r.m.s. pH resolution of ~0.1 pH. This sensitivity is unique to the device and enables novel applications such as a pH sensor which can be used in very small volumes down to ~50μL.

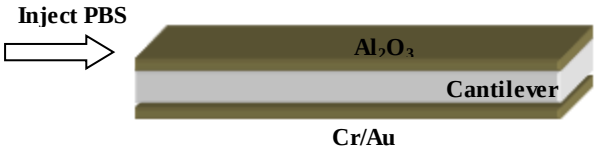

(a)

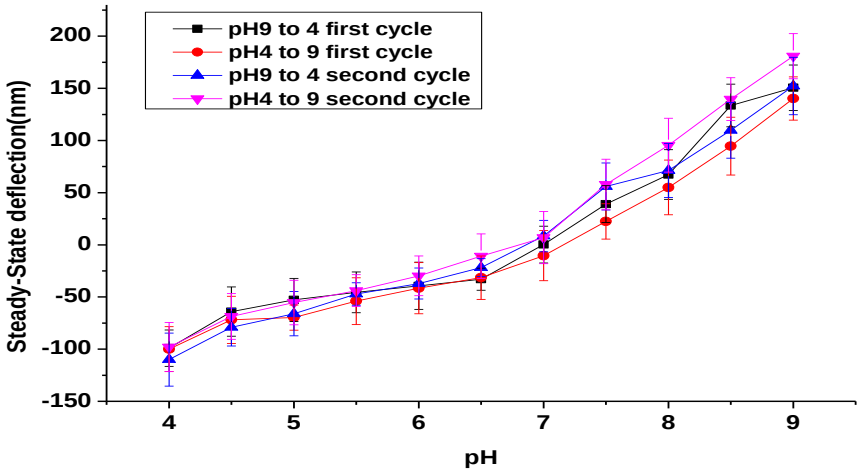

(b)

Figure 4.22 (a) Schematic diagram of Al_2O_3/Au activated cantilever (b) Steady-State cantilever deflection versus pH change. pH is cycled from 4 to 9 and then 9 to 4 for twice.

The Al_2O_3 surface is not suitable for long term use in high or low pH solutions. In low pH solutions, a reaction with the chloride (Cl) ion produces aluminium chloride ($AlCl_3$), while in high pH solution the surface will dissolve into solution due to chemical reactions that produce water soluble product.

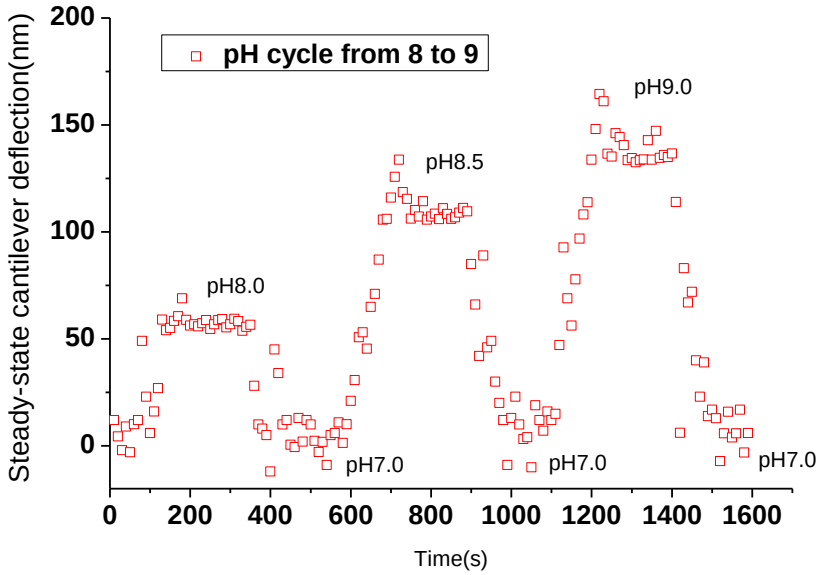

Figure 4.23 Steady-State cantilever deflection versus pH changes when cycling between pH 8.0, pH 8.5, pH 9.0 and pH7.0 respectively.

To further investigate the life time of the micro-machined optical fibre cantilever sensor, a cycling experiment is commenced by alternately injecting PBS 4.0and PBS solution from 8.0 to 9.0 at a 0.5pH interval. The measurement is taken every 10 seconds, and the Steady-State cantilever deflection versus pH is plotted in Figure 4.23. It should be noted that when washing with PBS 7.0 solution, the injected volume should be sufficient to wash away any reactant in the previous solution to ensure a constant solution concentration. From Figure 4.23, it takes ~100s for the sensor to reach steady-state for each pH from 8.0 to 9.0. The noise level when cantilever reaches equilibrium is ~10nm. When washing with PBS 7.0, the cantilever deflection is seen to return to the same position with a noise level around ~15nm. In this way, the sensor is capable of monitor small volume (down to ~50μL) pH change within 1-2 minutes. This opens a new route for rapid pH measurement of small sample volumes.

The life time of the sensor is greatly influenced by the presence of chemical coatings on the surface of the cantilever; hence it's crucial to selecting a robust coating layer which could survive in both low and high pH environments. To further improve the life time of the cantilever pH sensor, a MHA/HDT functionalized cantilever was tested, and this

is expected to extend the life time of sensor. pH 4.0 and pH 10.0 PBS was injected alternatively into the liquid cell with MHA/HDT functionalized cantilever placed inside.

MHA/HDT cantilever was functionalized by Self-Assembled Monolayer (SAM) process [4.29]. A micro-machined optical fibre cantilever with top surface coated with Au was immersed in 10mM MHA solution overnight for SAM process. A gold-alkylthiolate monolayer was then produced in a well-ordered, regularly oriented array. The functionalized cantilever is then washed with Ethanol and blown dry gently using nitrogen. After that, the bottom side of cantilever is coated with Au followed by the similar procedure used earlier in this chapter, in order to compensate the bimetallic effect due to any temperature changes. HDT coated surface will protect the cantilever from any non-specific adsorption, which will affect the surface stress change. The schematic configuration of a MHA/HDT activated sensor is shown in Figure 4.24.

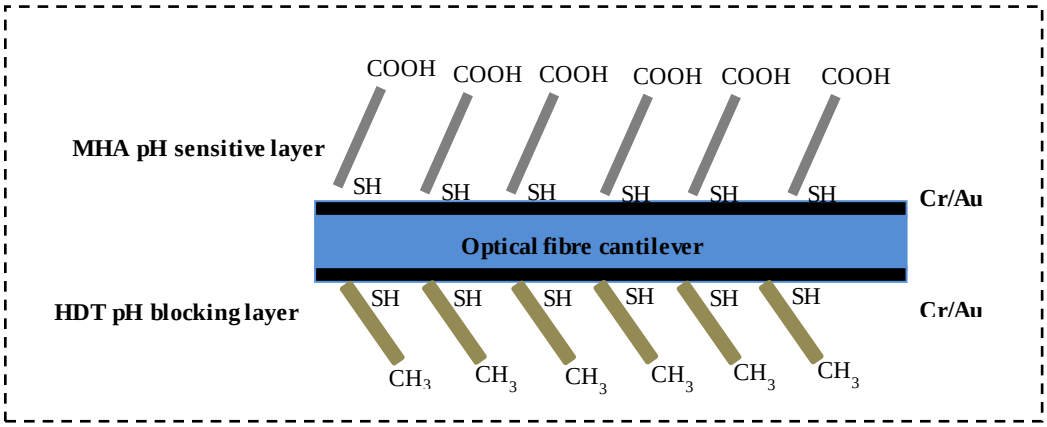

Figure 4.24 Schematic diagram of MHA/HDT activated cantilever. Both sides of cantilever are first coated with Cr/Au then bind to MHA and HDT respectively via SAM process. -COOH is pH sensitive and -CH_3 is pH insensitive.

A cycling experiment by using the same experimental set-up as Al_2O_3/Au cantilever is carried out. The Steady-State cantilever deflection dwells at pH 4.0 and pH 10.0 for four cycles and the results are plotted in Figure 4.25. A maximum cantilever deflection of 90nm is achieved at pH 10.0 while there is hardly any deflection observed at pH 4.0.

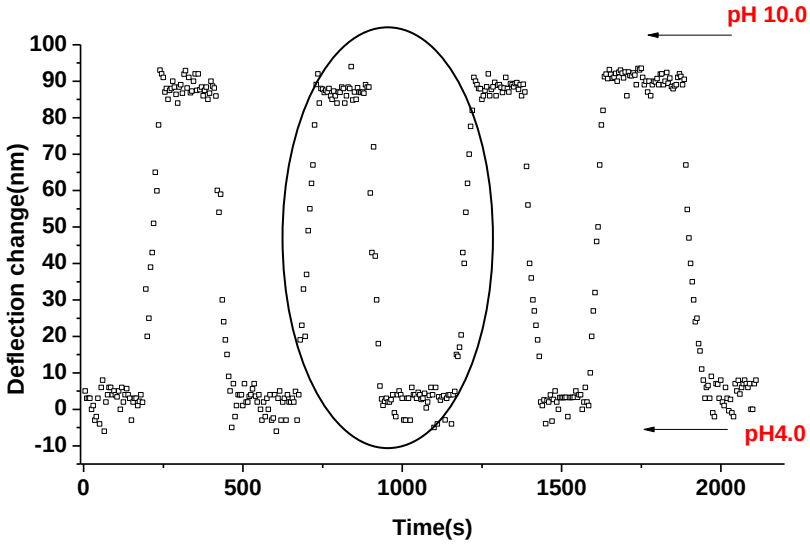

(a)

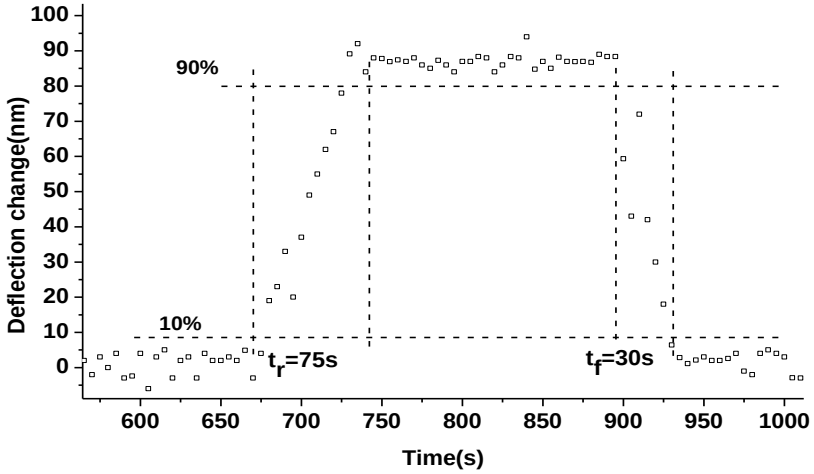

(b)

Figure 4.25 (a) Steady-State cantilever deflection dwells at pH 4.0 and pH 10.0 respectively, (b) Zoomed in image shows the single cycling between pH4.0 and pH10.0. t_r and t_f are the rising time and falling time respectively.

The deflection of the cantilever is due to the sum of all simultaneous surface interactions. These reactions result in a gradual surface stress increase while the pH increases from 4.0 to 10.0. The cantilever deflection change between pH 4.0 and pH10.0 are shown in Figure 4.25. A response time of 75s is found from pH 4.0 to pH 10.0, and 30s when pH is shifted from 10.0 to 4.0.

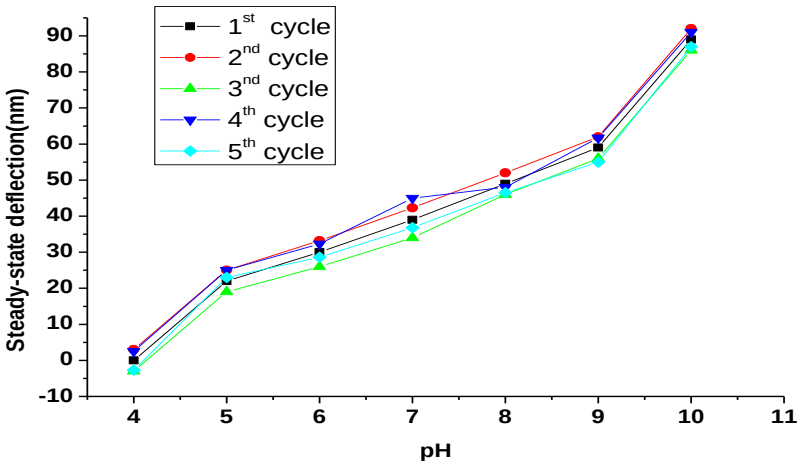

Figure 4.26 Steady-State cantilever deflection versus pH change. pH is cycled from 4 to 10 for five times and a maximum deflection of ~90nm is achieved at pH 10.0. All of the cycles show that when increasing the pH, cantilever deflection increases accordingly.

From Figure 4.26, a maximum cantilever deflection of 90nm is achieved at pH 10.0 while at pH 4.0 the cantilever is around zero deflection, which is different from Al_2O_3/Au activated cantilever. This is due to the different behavior of activated layer coated onto the optical fibre cantilever with hydrogen ion in the solution. In order to investigate the repeatability of the sensor, a cycling experiment is carried out fifth times from pH 4.0 to pH 10.0 in steps of 1.0 pH. A maximum cantilever deflection error of 15 nm is found around pH 4.0, the error at other pH values is around 10 nm. The response shows good linearity between pH 5.0 and pH 9.0 and when the pH is further increased to 10.0, the nonlinear effect starts to appear. It is also clear that the deflection depends on the pH changes of the buffer and the functionality of the –COOH monolayer on the Au surface. The deflection originates from the MHA liquid interface and also depends on the chemical environment of these interfaces. For a MHA functionalized cantilever *pKa* value of ~5 is usually found in solution [4.29]. At pH<5 the majority of carboxy groups is protonated while at pH>5 most of them are likely to deprotonated and become negatively charged, which is in the form of $–COO^-$. Therefore increasing the pH will increase the population of $–COO^-$, this in turn increases the lateral forces in the MHA monolayer generating more surface stress to deflect the cantilever.

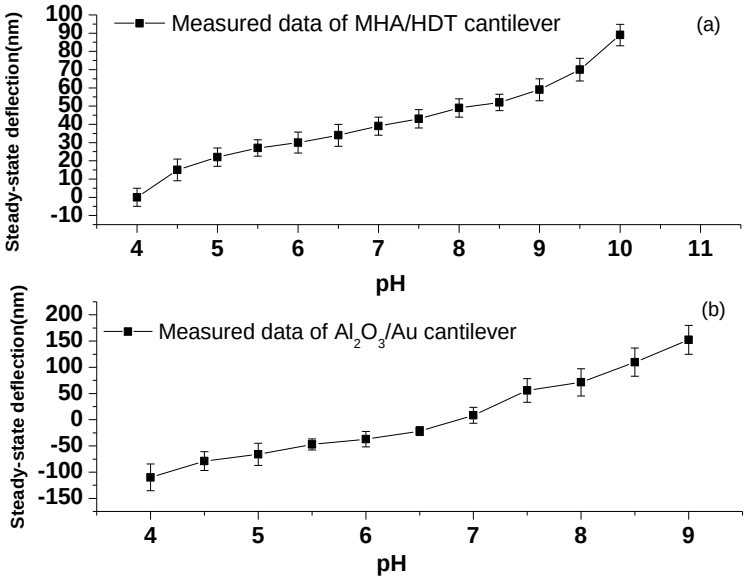

Figure 4.27 Deflection response of optical fibre cantilever as a function of pH for (a) MHA/HDT coated cantilever and (b) Al_2O_3/Au coated cantilever. A maximum cantilever deflection of ~90nm is found at pH 10.0 for MHA/HDT cantilever and~150nm for Al_2O_3/Au cantilever at pH 9.0.

To compare the pH response of the two cantilever pH sensors functionalized with Al_2O_3 or MHA, the cantilever steady-state deflection versus pH change is plotted in Figure 4.27. The data shows that MHA functionalized cantilever is capable of detecting pH over a range of pH 4.0 to 10.0, with an average sensitivity of ~15nm/pH. It can be seen that the overall pH response curve is not linear, but a linear response can be found from pH 5.0 to pH 9.0, which indicates a better region for pH sensing. The same trend has also been found in Al_2O_3 functionalized cantilever with a measurement range from pH4.0 to 9.0 and the average sensitivity is ~60nm/pH, which equals to ~0.1pH resolution. With the increase of pH, the sensitivity tends to increase accordingly. The same trend has also been reported in [4.22] for different function layers.

A micro-cantilever machined onto the end of a standard optical fibre with appropriate coatings applied to sensitise the structure to pH was investigated in this section. A combination of ps-laser and FIB machining techniques make it possible to form cantilever with a dimension of 112μm long 15μm wide and ~1μm thick. The micro-machined cantilever has been demonstrated as a pH sensor. pH variation from 4.0 to 9.0 with a maximum deflection of ~200nm has been found for an Al_2O_3 /Au

functionalized cantilever and pH4.0 to 10.0 with up to 90nm deflection has been found for an MHA/HDT functionalized cantilever. A pH detection time of approximate 2 minutes was found with this micro-machined cantilever sensor for a small sample volume of ~50μL. It should be noted that the sensitivity of the cantilever could be improved by further thinning the cantilever. Future potential application can focus on measurement of pH in harsh environments where conventional pH meters are unsuitable. It may also be possible to extend the measurement range by multiplexing an array of cantilevers where each cantilever is modified for certain pH range.

4.5 Conclusion

In this chapter, optical fibre cantilever fabrication techniques are discussed. This can be achieved by the combination of ps-laser machining and FIB milling technique. The mechanical response of cantilevers was tested for practical sensing. Finally two applications: temperature and pH sensing were demonstrated by using the optical fibre-top cantilever sensors. The results showed the advantages of fibre-top cantilever when measuring different parameters in a space constrained environment. The technique also offers potential for low-cost and mass production manufacturing.

Reference

[4.1] G Gruca, S D Man, M Slaman, J H Rector, and D Iannuzzi, " Ferrule-top micromachined devices: design, fabrication, performance", *Measurement Science and Technology* , vol.21, pp. 094003-094012, 2010.

[4.2] H B Sun and S Kawata, "Two-Photon Laser Precision Microfabrication and Its Applications to Micro-Nano Devices and Systems", *Journal of Lightwave Technology*, vol.21, pp. 624-629, 2003.

[4.3] M Steen, "Laser material Processing", Second edition, Springer, 1998.

[4.4] Chalcogenide-Based Optical Waveguides, University of Cambridge, http://www-cpg.ch.cam.ac.uk/Research/ChalcogenideBasedOpticalWaveguides.php,2014.

[4.5] F Albri, J Li, R R J Maier, W N MacPherson and D P Hand, "Laser machining of sensing components on the end of optical fibres", *Journal of Micromachanics and Microengineering,* vol. 23, pp. 045021-045029, 2013.

[4.6] W H Chu, M Mehregany and R L Mullen, "Analysis of tip deflection and force of a bimetallic cantilever microactuator", *Journal of Micromachanics and Microengineering,* vol. 3, pp.4-7, 1993.

[4.7] D P Hand and P S Russell, "Solitary thermal shock waves and optical damage in optical fibers: the fiber fuse", *Optics Lett*ers, vol.13, pp.767-769, 1988.

[4.8] I Canals, J A Portal, E Bosch and M Roses, "Retention of Ionizable Compounds on HPLC. 4. Mobile-Phase pH Measurement in Methanol/Water Immaculada Canals", *Analyical Chemistry,* vol.72, pp.1802-1809, 2000.

[4.9] W D Huang, S Deb, Y S Seo, S Rao, M Chiao and J C Chiao, "A Passive Radio-Frequency pH-Sensing Tag for Wireless Food-Quality Monitoring", *IEEE Sensors Journal,* vol.12, pp.487-495, 2012.

[4.10] L H Jiao and N Barakat, "Ion-sensitive field effect transistor as a pH sensor", *Journal of Nanoscience and Nanotechnology,* vol.13, pp.1194-1198, 2013.

[4.11] Q Y Cai and C A Grimes, "A remote query magnetoelastic pH sensor", *Sensors and actuators B,* vol.71, pp.112-117, 2000.

[4.12] Y Chen, S C Mun and J Kim, "A wide range conductometric pH sensor made with Titanium dioxide/Multiwall carbon nanotube/Cellulose hybrid nanocomposite", *IEEE Sensors Journal,*vol.13, pp.4157-4162, 2013.

[4.13] J Goicoechea, C R Zamarreno, I R Matıas and F J Arregui, "Optical fiber pH sensors based on layer-by-layer electrostatic self-assembled Neutral Red", *Sensors and actuators B,* vol.132, pp.305-311, 2008.

[4.14] V Misra, H Mishra and H C Joshi, "An optical pH sensor based on excitation energy transfer in Nafion film", *Sensors and actuators B,* vol.82, pp.133-141, 2002.

[4.15] M Z Tian, X J Peng, J L Fan, J Y Wang and S G Sun, "A fluorescent sensor for pH based on rhodamine fluorophore", *Dyes and Pigments,* vol.95, pp.112-115, 2012.

[4.16] T Thundat, R J Warmack, G Y Chen and D P Allison, "Thermal and ambient - induced deflections of scanning force microscope cantilevers", *Applied Physics Letters,* vol.64, pp.2894–2903, 1994.

[4.17] H J Mamin and D Rugar, "Sub-attonewton force detection at millikelvin temperatures", *Applied Physics Letters,* vol.79, pp.3358-3360, 2001.

[4.18] J R Raiteri and H Butt, "Measuring Electrochemically Induce d Surface Stress with an Atomic Force Microscope", *Journal of Physical Chemistry,* vol. 99, pp.15728-15732, 1996.

[4.19] T Thundat, P I Oden and R J Warmack, "Microcantilever sensors", *Microscale Thermophysics Engineering,* vol.1, pp.185-199, 1997.

[4.20] A M Moulin, S J Oshea and M E Welland, "Microcantilever-based Biosensors", *Ultramicroscopy,* vol.82, pp.23-31, 2000.

[4.21] R R Aiteri, M Grattarola, H J Butt and P Skladal, "Micromechanical cantilever-based biosensors", *Sensors and Actuators B,* vol. 79, pp.115-126, 2001.

[4.22] H F Ji, K M Hansen, Z Hu and T Thundat, "Detection of pH variation using modified microcantilever sensors", *Sensors and Actuators B,* vol.72, pp.233-238, 2001.

[4.23] R Bashir, J Z Hilt, O Elibol and A Gupta, "Micromechanical cantilever as an ultrasensitive pH microsensor", *Applied Physics Leters,* vol.81, pp.3091-3093, 2002.

[4.24] VanBlarcom A, D S and N Peppas, "Microcnatilever sensing arrays from biodegradable, pH-responsive hydrogels", *Biomedical Microdevices,* vol.13, pp.829-836, 2011.

[4.25] J Li, F Albri, R R J Maier, W N MacPherson and D P Hand, "Micro-machined optical fibre cantilever as sensor elements", *Proceedings of SPIE,* 842816, Brussels, 2012.

[4.26] R R Aiteri, M Grattarola, H J Butt and P Skladal, "Micromechanical cantilever-based biosensors", *Sensors and Actuators B*, vol.79, pp.115-126, 2001.

[4.27] J Fritz, M K Baller, H P Lang, T Strunz, E Meyer, H J Guntherodt, E Delamarche, Gerber C and J K Gimzewski, "Stress at the Solid-Liquid Interface of Self-Assembled Monolayers on Gold Investigated with a Nanomechanical Sensor", *Langmuir*, vol.16, pp.9694-9696, 2000.

[4.28] C D Fung, P W Cheung and W H Ko, "A generalized theory of an electrolyte-insulator-semiconductor field-effect transistor", *IEEE Trans. Electron Device*, vol.33, pp.8-18, 1986.

[4.29] R G Nuzzo and D L Allara, "Adsorption of bifunctional organic disulfides on gold surfaces", *Journal of American Chemistry Society* , vol.105 , pp.4481-4483, 1983.

Chapter 5

Fibre side cantilever sensor

5.1 Introduction

In this chapter, cantilever structures fabricated onto the side of the fibre, addressed via micro-machined 45° turning mirror, are proposed for sensing applications. For example, this has the capability to measure acceleration where the direction is perpendicular to the direction of the optical fibre. The 45° turning mirror can be aligned to couple the reflected light from the side cantilever back into the fibre core. In this way, the structure offers the possibility of fabricating longer cantilevers thereby achieving higher sensitivity which scales with the cantilever length.

5.2 Fabrication of 45°in-fibre micro-mirror

In this section, fabrication techniques to manufacture the in-fibre 45° mirror for optical fibre side sensing applications are investigated. The ideal 45° mirror should be fabricated with good alignment to the fibre core with an optical quality surface finish for efficient operation. Laser micro-machining techniques can offer fast prototype ability, however, in this case, it is difficult to achieve an optical surface finish of the micro-mirror. The rough surface will lead to optical scatter when light is reflected via the mirror surface. Therefore, it's difficult to monitor the reflected signal due to reduced intensity.

Fabrication techniques which can offer optical quality surface finish and the capability to machine 3D structure with precise control would be desirable. Based on these requirements, FIB milling is used to manufacture the 45° in-fibre mirror. In terms of a $20\,\mu m \times 20\,\mu m$ mirror, the fabrication time of FIB is 1 to 2 hours with the optimised ion beam parameters and <20nm surface finish. Therefore, it offers a suitable fabrication route to manufacture the desired mirror.

5.2.1 *Fabrication process*

The fabrication process of the in-fibre 45˚mirror is described as follows. First of all, the prepared single mode fibre was brought to FIB chamber. The SEM (aligned at 38.0 ºangle relative to the optical fibre side) is available for real-time monitoring during the fabrication process. The acceleration voltage of the FIB was set at 30keV throughout the machining process.

Two approaches to fabricate the in-fibre mirror are developed in this chapter. The first approach is to use bitmap (see Figure 5.1(b)). This work was carried out in collaboration with Dr Jining Su from the department of mechanical engineering at Heriot-Watt University. A rectangular bitmap pattern to ion beam is assigned, and the 3D micro-mirror was fabricated by changing the dwell time at each beam position. The beam diameter and the ion current are 66nm and 3nA in this case. In the scanning process, the pixel spacing was set to half of the beam diameter by assigning a bitmap with 302×302 pixels to a $10 \times 10\ \mu m^2$ milling area. A reflective mirror with 45˚ inclined angle to the fibre core was successfully obtained after 43 scanning passes at a maximum dwell time of 255 µs. The total machining time for the mirror is 80 minutes. The result of this process is shown in Figure 5.1 (a). Figure 5.1 (b) shows the ion dose exposure process when fabricating the reflective mirror.

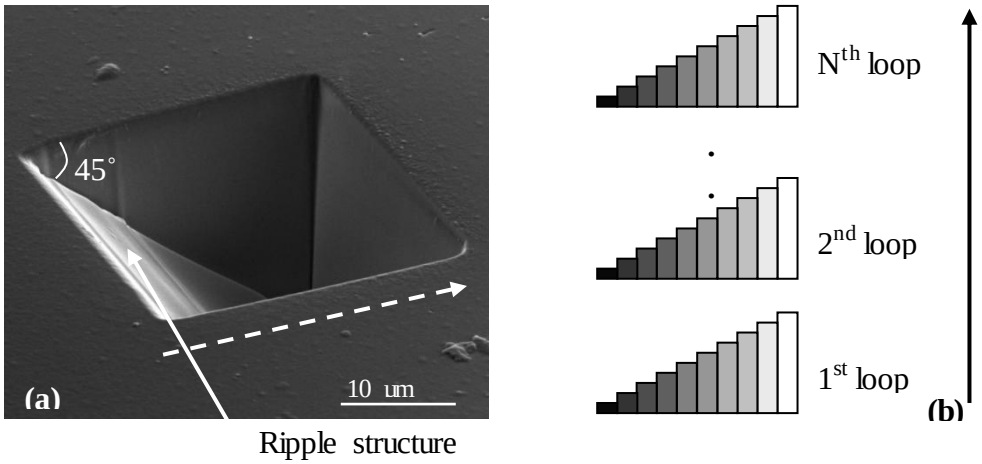

Figure 5.1 The 45˚ reflective mirror carved on top of the fibre (a) and the total exposure dose used for experiments with N exposure loops (b). Rectangles in (b) represent exposure elements corresponding to cross sections along dot-arrow of (a). Vertical arrow in (b) shows exposure order.

Clearly, a 'surface ripple' structure is on the machined mirror surface (Figure 5.1 (a)). This structure will reduce the mirror quality and thus reduce the reflectivity of the mirror surface. The formation of periodically modulated ripples in the picture is said to be caused by off-normal incidence of the ion beam [5.1] produced by ion-bombardment of solid surfaces. Such ripples on the reflective mirror will affect the surface finish, causing beam scattering, therefore, it is necessary to remove them. The wavelength of these ripples typically depends on the ion incident angle; according to Bradley and Harper's theory [5.1] the wavelength approaches infinite when the ion incident angle approaches 90 °to the surface normal, and this means ideally a ripple-free surface can be achieved when the ion incident angle is 90 º.

As a result, an ion beam polishing process is used to remove the ripples on the mirror. Here an ion beam current of 1nA incident along the surface of the reflective mirror is used to polish the surface. In order to compensate for the Gaussian profile of the incident ion beam, the polishing angle was offset by 0.5˚ with respect to the surface of the reflective mirror as shown in Figure 5.2 (a). A layer of platinum was then coated onto the mirror surface to increase the reflectivity of the mirror. The SEM image of the polished mirror is showed in Figure 5.2 (b).

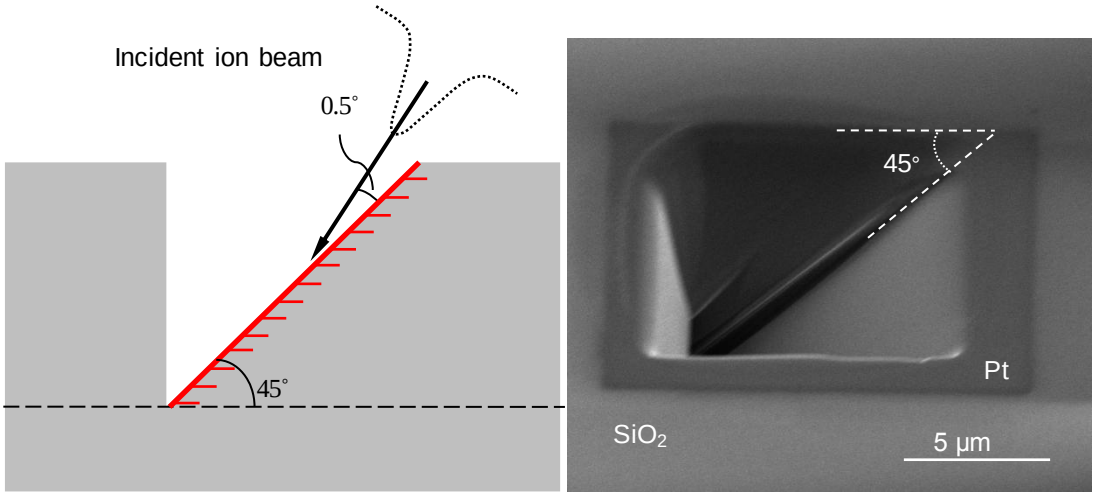

(a) (b)

Figure 5.2 The 45˚ reflective mirror caved at the centre of the optical fibre. (a) A sketch of the ion polishing process; (b) shows SEM images of the 45˚ reflective mirror viewed from 52˚

This approach takes about an hour in total to fabricate the initial mirror structure and approximately another hour to polish the mirror. Although it is expected that overall machining time could be reduced by improving the process and sequence of fabrication steps, currently the total machining time can be ~2 hours, and this has an impact on the time and cost of manufacturing. A fast and straightforward machining technique needs to be developed to reduce the machining time while still maintaining an optical quality surface.

The second approach involves a two-step process as shown in Figure 5.3. First of all, the fibre mount is rotated clockwise to 44˚ aligned with the horizontal level. For the purpose of making a rough cut, a 25µm by 25µm rectangular pattern was assigned to cover the fibre core, and a clear cross section process is used to finish the a cut. The machining time for this step takes only ~12 minutes and the resulting mirror is roughly 42˚~44˚. After this process, the fibre mount is turned 1˚ anti-clockwise for polishing purposes.

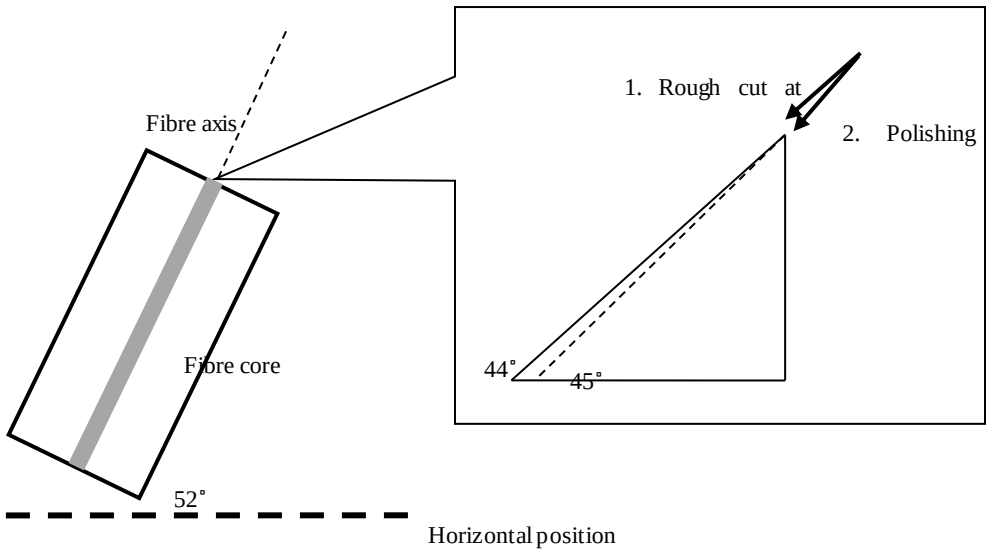

Figure 5.3 Side view of FIB machining of 45˚mirror set-up. The fibre is tilted 52˚ in FIB chamber for FIB machining. The zoomed in part shows the steps used for machining the mirror: a rough cut at 44˚ and then polishing the mirror at 45˚.

Here polishing is carried out where the ion beam is incident along the surface of the reflective mirror with a current of 7nA. Again a layer of platinum can be coated onto the mirror surface via FIB induced deposition to increase the mirror reflectivity. The

machining time of a polished single mirror takes less than half an hour. The SEM images of the final machined mirror are shown in Figure 5.4(b) with the angle accurately measured at 45.0˚. In total, it took ~40minutes to fabricate the mirror. This approach reduced the total machining time to less than an hour and eliminated the ripple structure made by using the bitmap method. The fabrication techniques to make the single mirror in the fibre made it easy to transfer onto a MCF (this will be discussed later in section 5.6), where multi-axes displacement/deflection measurement are possible by combining with the in-fibre 45˚ mirror structure.

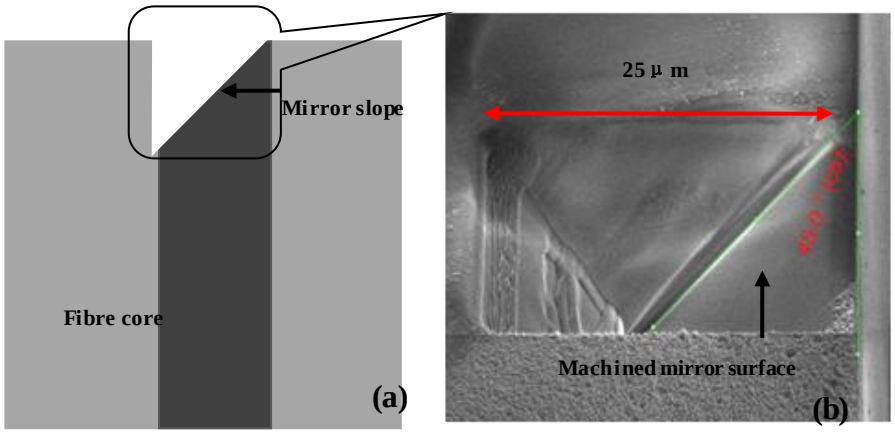

Figure 5.4 FIB machining of in-fibre 45˚ mirror. (a) side view of machined in-fibre 45˚ mirror, (b) SEM angled view of the zoomed in mirror surface. The mirror is measured to be 45˚.

5.3 Analysis of 45˚ mirror

5.3.1 Effect of mirror size

The size of the micro-machined 45˚mirror plays an important role. The initial design of the mirror size was a 10µm by 10µm square pattern which can cover the optical fibre core (8.2 µm), and mode field diameter (9.2 µm for a SMF-28 optical fibre). It seemed obvious that when a BBS was injected into the optical fibre, the reflected optical spectrum by 45˚ in-fibre mirror should be identical to the BBS spectrum, since the light is reflected (via the turning mirror) off the fibre side wall only. However, if any additional reflective surfaces are present this will form an optical cavity and fringes will be observed. Figure 5.5 shows an FIB polished mirror. The red circular line indicates the location of the fibre core area. It can be seen that the machined mirror is not in the

centre of fibre core. In this case, unexpected interference was observed during the experiment and it was found that the optical path length difference calculated by using the FFT algorithm was the same distance between the optical fibre core and the fibre side wall. This indicated the existence of an FP cavity after machining the 45˚ in-fibre mirror.

Several experiments were commenced to find out the origin of the additional reflection, which appeared to be co-located with the mirror. One possibility was the modification of refractive index change induced by FIB milling. Ion beam induced refractive index change was a common phenomenon often found when it interacted with the target material [5.3]. Usually, a Δn of ~0.002 to 0.034 is measured after milling was finished in fibre core. The refractive index change induced by the ion beam can be varied due to the composition of the fibre material. In our case, the reflection between the ion modified fibre core and unmodified cladding is calculated to be ~ 0.014% thus less likely to produce the fringes.

Another experiment trial was also implemented by machining a 45 ˚mirror with a larger size, 25μm by 25μm square and comparing the normalised reflection spectrum with 10μm by 10μm mirror. It was found that during the 10μm by 10μm mirror fabrication process, the location of the mirror can deviate from the centre of fibre core due to the alignment (shown in Figure 5.5). Therefore, to machine a mirror much larger than the full mode diameter can ensure the guided beam in the fibre to be covered by the mirror.

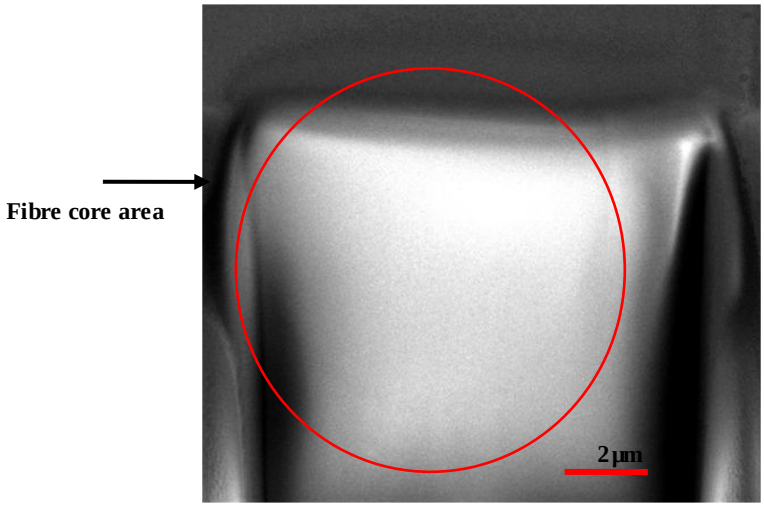

Figure 5.5 SEM view of the FIB micro-machined 45° mirror (10µm by 10µm) off the centre of an optical fibre. Fibre core area is marked with the red circle.

It was clear from Figure 5.6(a) that when the mirror size was increased to 25µm by 25µm square, the interferogram disappeared and a flat spectrum response was found after normalization with respect to the source spectrum. When reducing the mirror size to 20µm by 20µm, fringes started to appear again (shown in Figure 5.6(b)). These experiment results gave us the conclusion that the minimum machined mirror size should be 25µm by 25µm.

It is assumed that when reducing the mirror size to the size of the optical fibre core, the mode diameter at the end of fibre is larger than 9µm for a SMF-28 single mode fibre, and this might cause a fraction of the transmitted light beam directly reflected by the fibre end facet. On the other hand, some of the light is reflected by the 45° mirror and transmits through the cladding and then reflected by the fibre side wall and finally recoupled to the core via the 45°mirror. These two beams interfere with each other and produce a pattern as a function of λ. In addition, there are cases where the mirror doesn't fully cover the fibre core area due to the misalignment between the fibre core and the machined mirror, therefore, will produce a reflected surface on the optical fibre end facet.

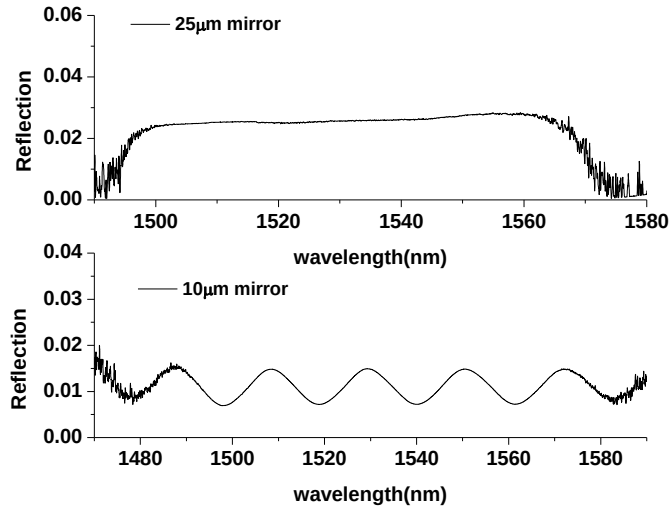

(a)

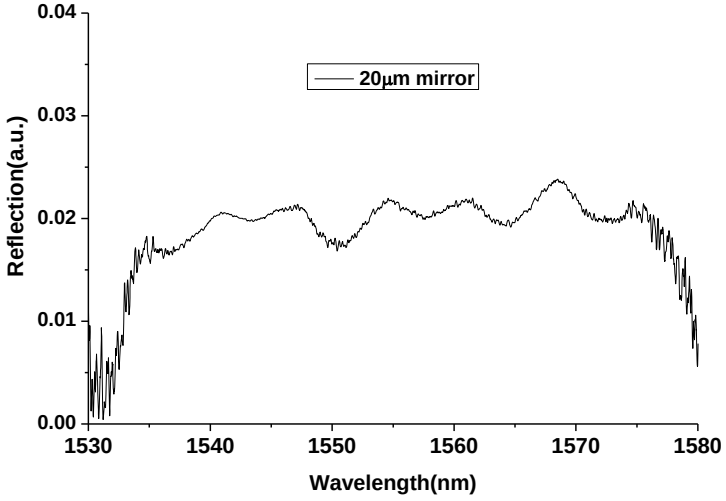

(b)

Figure 5.6 Normalized reflection spectra versus different mirror sizes. (a) Comparison between the reflection seen from a 10μm by 10μm and a 25μm by 25μm square mirror. (b) Reflection spectrum of a medium 20μm by 20μm square mirror.

5.3.2 Modelling of light reflected by the 45˚mirror

It is important to control the machined mirror to be exactly 45˚, as this will affect the amount of reflected power back into the core. The acceptance angle of the SMF-28 single mode optical fibre is 14˚, thus a very small angle deviation from 45˚will lead to significant reflection power loss. It would be helpful to study the relation between the acceptable angle of machined mirror and the intensity of reflected light recoupled back to the fibre core. In this way, the acceptable error range of machined mirror will be

calculated and provide a further guidance for machining and the maximum angle error range for the in-fibre 45˚mirror.

Here, a weakly guiding step-index single-mode fibre is assumed. It is well known that the analytical solution of the fundamental HE_{11} in the single mode fibre can be accurately approximated by a Gaussian distribution of transverse and linear polarized electrical field. It can be assumed that the electrical field in both XZ E_x and YZ plane E_y can be expressed by the following equation:

$$E_x = \left(\frac{4P\sqrt{\mu_0/\varepsilon_0}}{\pi n_2 w_0^2}\right)^{1/2} \exp\left(-\frac{r^2}{w_0^2}\right) e^{i\beta Z} \tag{5.1}$$

$$E_y = \left(\frac{4P\sqrt{\mu_0/\varepsilon_0}}{\pi n_2 w_0^2}\right)^{1/2} \exp\left(-\frac{r^2}{w_0^2}\right) e^{i\beta Z} \tag{5.2}$$

P is the Poynting vector, ε_0 is the dielectric constant in vacuum, μ_0 and is the permeability of vacuum, n_2 is refractive index of the propagation media, w_0 is the beam waist, r is the optical fibre radius and β is propagation constant.

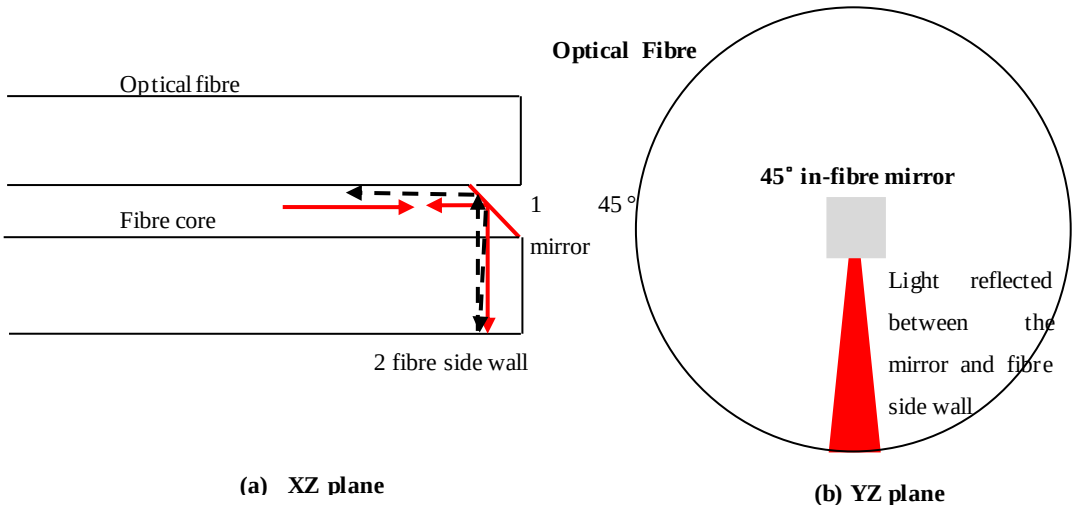

Figure 5.7 Schematic diagram of FIB machined 45˚ in-fibre mirror and light transmission at the mirror surface in the fibre. (a) Side view of an optical fibre with 45 °mirror machined in the centre. 1 is the coated mirror surface and 2 is the coated fibre side wall. The red arrow shows the light transmission while the black arrow represents the light transmission at the mirror surface with a small angle deviation of the mirror. (b) Top view of (a). The black circle is the optical fibre profile while the gray rectangle in the centre represents the 45 ° in-fibre mirror seen from the top of the optical fibre.

Here, partial analytical theory is used to derive the coupling loss of micro-machined 45˚ mirror. A similar model to optical fibre splicing loss analysis [5.5] is used.

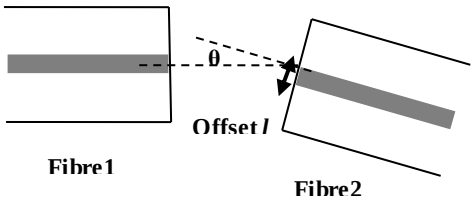

Figure 5.8 Schematic diagram of modelling configuration of the transmission loss between two optical fibres. θ is the angle deviation and a vertical offset l between the two optical fibres is also used for modelling.

The transmitted light can be divided into XZ and YZ planes (shown in Figure 5.7). It is assumed that both the mirror and the optical fibre side wall are coated with platinum (Pt) and have a 90% reflectivity. In XZ plane, light is reflected back by the 45˚ mirror and recoupled into the fibre core. If the mirror is machined to be exactly 45˚, the coupling loss can be calculated by using the Gaussian beam propagation theory. In YZ plane, the curved shape of optical fibre can be considered as an index lens. For a weakly guided mode, the refractive index difference between the fibre core and cladding is very small and is ignored in this analysis. It can be assumed that the light reflected by the fibre wall will be refocused to the centre of optical fibre according to the geometric optics law.

If the machined mirror angle deviates a small fraction from 45˚, then the light transmitted in the fibre will be reflected by the side wall and recoupled back to the optical fibre core, provided that the light is in the acceptance angle of the SMF-28 fibre. In the case of an SMF-28 fibre, N.A. is 0.12 and the acceptable angle θ_c is 7˚. Suppose the offset of recoupled beam from the centre of fibre core is d. For a 0.5˚ deviation, the calculated offset for the recoulped beam is approximately ~1.5μm from the central of fibre core. In this case, coupling loss due to fibre core misalignment must be taken into account. The model for this case can be shown in Figure 5.8. The amount of transmission loss induced by offset of the fibre can be expressed as [5.5] :

$$T = \left(\frac{2w_1 w_2}{w_1^2 + w_2^2} \right)^2 \exp\left(-\frac{2d^2}{w_1^2 + w_2^2} \right) \tag{5.3}$$

d is the light travelling distance between the two optical fibres, w_1 and w_2 are the waist size of Gaussian beam before and after the reflection. In our case, w_1 and w_2 are the same and for an SMF-28 fibre is 9.176μm. Therefore, equation 5.1 can be rewritten as:

$$T = \exp\left(-\frac{d^2}{84.2} \right) \tag{5.4}$$

d is associated with the deviation angle:

$$d = \frac{\sin 2\theta}{\sin(135° - 2\theta)} \times 62.5 \tag{5.5}$$

As can be seen from Figure 5.8(a), the red solid lines refer to the transmission path of injected light beam while the black dash lines represent the transmission direction of the reflected beam as the machined mirror has a θ° deviation from the 45° which means the angle of the recoupled beam to the fibre core needs to be smaller than 3.5°. In YZ plane, all of the light will be reflected back and focussed onto the optical fibre core. Therefore, the total reflectivity in XZ plane can be written as:

$$T = \left(\frac{2w_0 w_2}{w_0^2 + w_2^2} \right)^2 \cdot \exp\left[-\frac{2(\pi n_2 w_0 w_2 2\theta)^2}{(w_0^2 + w_2^2)\lambda^2} \right] \tag{5.6}$$

θ is the deviated angle from machined 45° mirror, n_2 is the refractive index of fibre core which is 1.457 for standard telecommunication fibre with central wavelength of 1550nm, λ is the transmission wavelength, w_0 and w_2 are the waist size of Gaussian beam at the fibre reflection point. In XZ plane, the light beam hits the turning mirror and transmitted to the fibre side wall, at this point the beam waist expanded to w_1. Suppose that the beam waist further expanded to w_2 after recoupling into the fibre core by the turning mirror. Assuming that the mirror is coated with 50nm Pt, and for 1550nm has a reflectivity of ~0.9. The following equation can be used to calculate the beam waist expansion $w(z)$:

$$w(z) = w_0 \sqrt{1 + (\frac{Z}{Z_R})^2} \tag{5.7}$$

Here Z is the distance along the beam from the beam waist, Z_R is the Rayleigh range, which can be calculated by:

$$Z_R = \frac{\pi w_0^2}{\lambda} \tag{5.8}$$

The beam waist of the HE_{11} mode before the reflection at surface 1 is w_0, therefore, from [5.5] the beam waist can be calculated by the following equation:

$$\frac{w_0}{a} = 0.65 + \frac{1.619}{V^{\frac{3}{2}}} + \frac{2.879}{V^6} \tag{5.9}$$

a is the optical fibre core diameter and V is an mode number related with the optical fibre. In our case, the core diameter of a SMF-28 single mode fibre is 8.2μm, therefore, beam waist w_0 is calculated to be 9.176μm, and the Rayleigh range is Z_R=170.57μm. On the other hand, because of the 10% coating loss at reflection surface 1 and 2, the total optical fibre power from the machined mirror coupled back to the fibre core can be expressed as:

$$T' = T_1 T_2 = 0.9 * 0.9 * 0.9 * \frac{4(4Z^2 + \frac{w_0^2}{w_2^2})}{(4Z^2 + \frac{w_0^2 + w_2^2}{w_2^2}) + 4Z^2 \frac{w_0^2}{w_2^2}} \tag{5.10}$$

Take equation (5.10) into account, the total transmission loss versus the machined 45° mirror deviation angle θ is plotted in Figure 5.9. It shows how the mirror angle affects the reflected intensity of light recoupled back to the fibre. In the case of cantilever deflection measurement, at least a 1% of reflection is necessary to achieve an acceptable fringe visibility for sensing; therefore, the angle of 45°in-fibre mirror should be very well controlled to 45°±0.35° to maintain enough reflection power for interrogation.

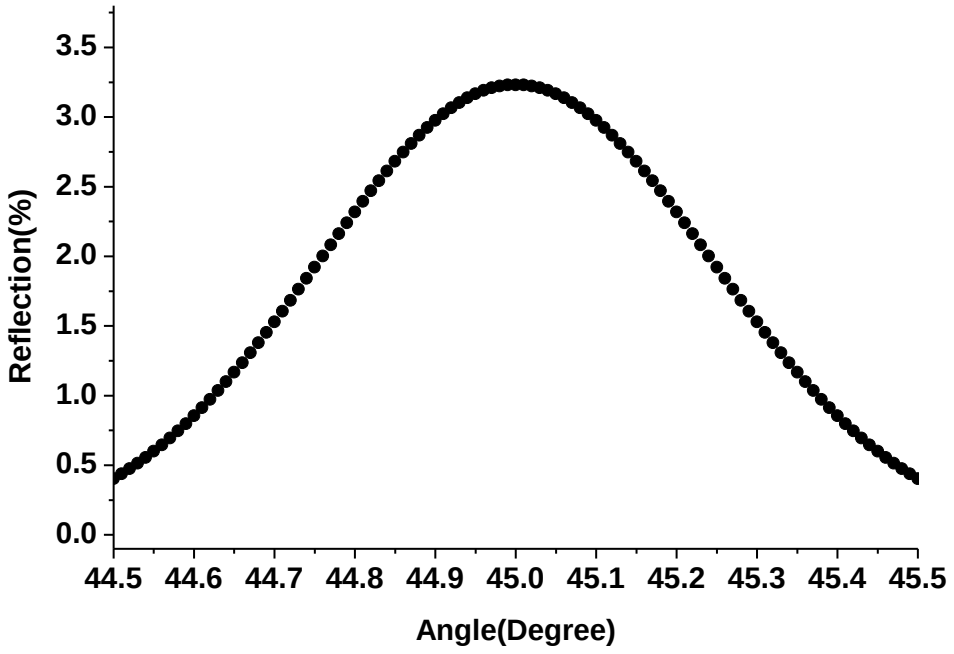

Figure 5.9 Transmission loss modeling results of reflection from the 45° mirror versus the FIB machined mirror angle. The reflection drops quick as the mirror angle deviates from 45°.

To verify the surface quality and the angle of the FIB machined 45° mirror, the whole structure was mounted on a 45° mechanical polishing block with an error of ±0.05°. The optical fibre was first aligned in the mechanical polishing block to ensure there was no angle misalignment and the surface finish was assessed by using a commercial white light interferometer (Zygo New View 5000) as shown in Figure 5.10. A scanning area of 10μm by 10μm was used to study the surface roughness and surface profile of in-fibre 45° mirror. As part of the imaging, the beam from Zygo was blocked by the shape of machined structure, great care must be taken to locate the mirror position and focus the beam onto the mirror surface so that fringes can be seen on the screen.

The surface finish, R_a, of the mirror is measured to be smaller than 20nm, shown in Figure 5.11, and the deviation of the angle in both x and y directions are monitored to be within ~±0.05°. This is not expected to contribute much error for deflection measurement based upon the theoretical modelling. The results give confidence that the machined mirror alignment and surface finish are suitable for producing the beam

steering and reflection for deflection measurement based upon an external optical cavity.

In order to achieve an accurately machined 45˚ mirror, caution needs to be taken for the alignment of the optical fibre before machining. The tip of optical fibre hanging outside of the mount should be less than 0.5mm, since the fibre will start to bend due to its gravity during the machining process. In addition, a good conductivity of optical fibre needs to be maintained during the whole machining process. This is usually done by dipping a fraction of silver painting between the metal block and the fibre. The good conductivity can ensure there was no drift due to charging effect which can lead to the drift of the whole pattern.

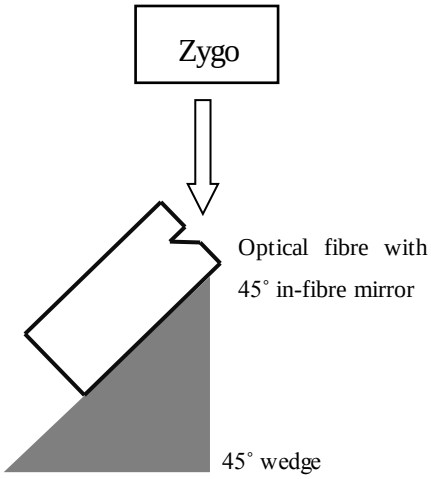

Figure 5.10 Experiment set-up of Zygo measurement.

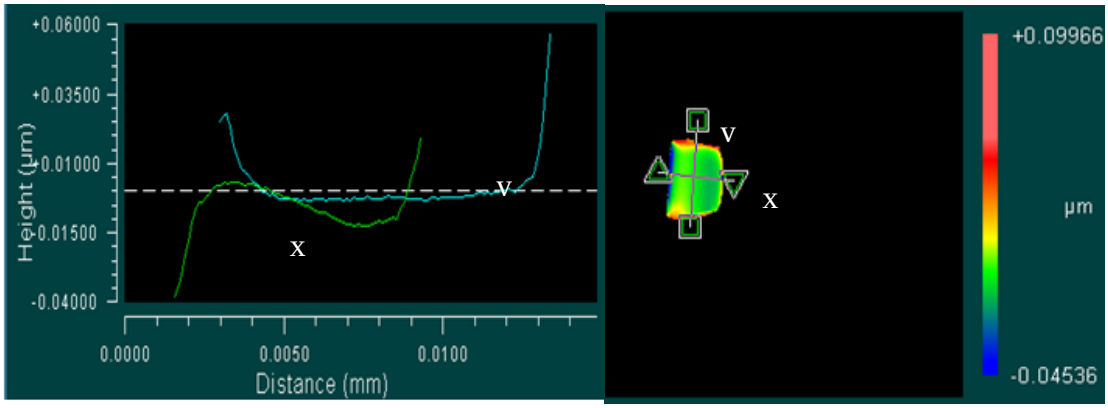

Figure 5.11 Surface measurement results from Zygo white light interferometer.

5.3 Theoretical analysis of acceleration measurement

One of the potential applications of the FIB machined in-fibre mirror is for fabrication of an acceleration sensor. Therefore, it's important to introduce the acceleration theory for cantilever beam before the accelerometer is designed and manufactured.

Based upon mechanics theory [5.6] a simple model for acceleration measurement can be derived. Assume that the optical fibre cantilever is excited by a sinusoidal function with a fixed frequency ω then the acceleration model used for optical fibre cantilever here can be considered as a harmonic excitation model. The excitation force F can be written by:

$$F = F_0 \cos \omega t \tag{5.11}$$

F_0 is the maximum force, t is the time variable. If we consider the damping effect, the damping force F_d can be expressed by the following equation:

$$F_d = -c\dot{x} \tag{5.12}$$

Where the damping constant c is the constant resistance developed per unit velocity. $\dot{x}$ is the velocity. For our cantilever beam resonant analysis by using the model described in Figure 5.12, we have the following equation:

$$\ddot{x} + \frac{c}{m}\dot{x} + \frac{k}{m}x = F(t) \tag{5.13}$$

Where $\ddot{x}$ is the acceleration, m is the mass of the test sample and k is the spring constant. The complete solution for a damped system can be expressed as:

$$x(t) = X_0 e^{-\xi\omega_n t}\cos(\omega_d t - \varphi_0) + X\cos(\omega t - \varphi) \tag{5.14}$$

where ω_n is the resonant frequency of cantilever. ξ is the damping coefficient of the system. X_0 is the amplitude of transient vibration while X is the amplitude of steady-state vibration. From the above equation, we can see that the general solution eventually reduces to a particular solution, which represents the steady-state vibration.

The steady-state motion is present as long as the forcing function exists. The amplitude X and phase of the steady-state vibration φ can be expressed by the following equation:

$$X = \frac{F_0}{[(k - m\omega^2)^2 + \xi^2\omega^2]^{1/2}} \tag{5.15}$$

$$\varphi = \tan^{-1}\left(\frac{\xi\omega}{k - m\omega^2}\right) \tag{5.16}$$

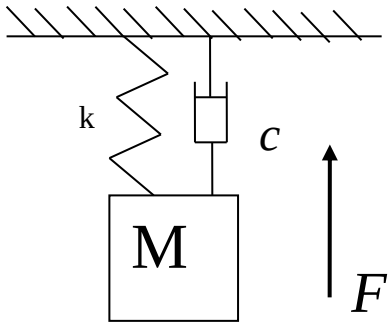

Figure 5.12 Schematic model of a harmonic excitation damping system. A test sample with M mass is vibrate when applying a force *F*.

Suppose we have the following equation:

$$\omega_n = \sqrt{\frac{k}{m}}\delta_{st} = \frac{F_0}{k}r = \frac{\omega}{\omega_n} \tag{5.17}$$

Here, δ_{st} is the amplitude of a undamped system, r is defined as the ratio of the harmonic force frequency over the undamped natural frequency. Then the phase φ can be written as:

$$\varphi = \tan^{-1}\left(\frac{2\xi r}{1 - r^2}\right) \tag{5.18}$$

And the amplitude ratio of the force vibration M can be expressed as:

$$M = \frac{X}{\delta_{st}} = \frac{1}{\sqrt{(1 - r^2)^2 + (2\xi r)^2}} \tag{5.19}$$

From equation (5.19), we can see that any amount of damping reduces the magnification factor. For any specified value of *r*, a higher value of damping reduces the value of *M*. The reduction in *M* in the presence of damping is very significant at or near resonance. In the case of micro-machined optical fibre side cantilever, air force induced damping can be ignored thus a simple model based on Newton's second law can be used.

5.4 Micro-machined optical fibre 2D accelerometer

One of the applications of micro-machining in-fibre mirror is for acceleration measurement. This is demonstrated by machining an optical fibre side cantilever and re-coupling the light via the in-fibre 45˚ turning mirror to the fibre core for interrogation purpose.

5.4.1 *Initial trial*

The initial design is to use ps-laser machining technique to fabricate an "L" shape cantilever onto the end of an optical fibre, as shown in Figure 5.13(a). The end tip of the fibre produced by the L shape will provide mass weight for acceleration to be measured. The thickness of cantilever needs to be machined down to ~1μm to be sensitive to less than 10g (g: gravity constant) acceleration, which is not possible to achieve by ps-laser machining. Thus FIB machining is used to thin the cantilever down to 1μm after a thick cantilever was first machined by ps-laser. However, the machined cantilever was not mechanically stable due to the laser induced fracture inside the cantilever. The free standing part of the cantilever broke off when the thickness of the cantilever is polished down to ~3μm by FIB. We believed that the laser induced cracks inside the optical fibre weaken the mechanical stability of cantilever and this made the cantilever break more easily.

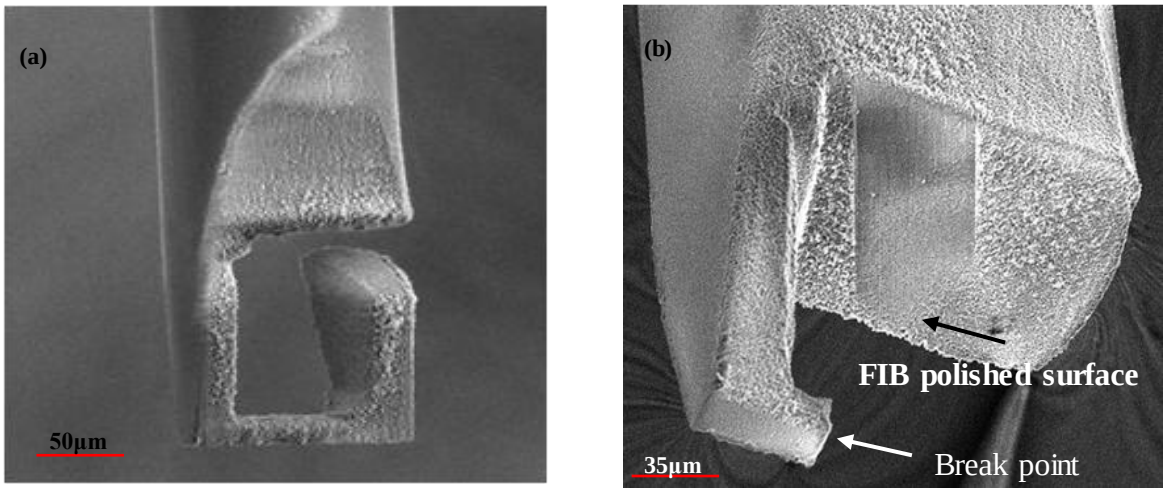

Figure 5.13 SEM view of (a) L shape optical fibre-top cantilever machined by laser/FIB process, (b) Zoomed in view of the broken cantilever when thinning the cantilever surface by using FIB.

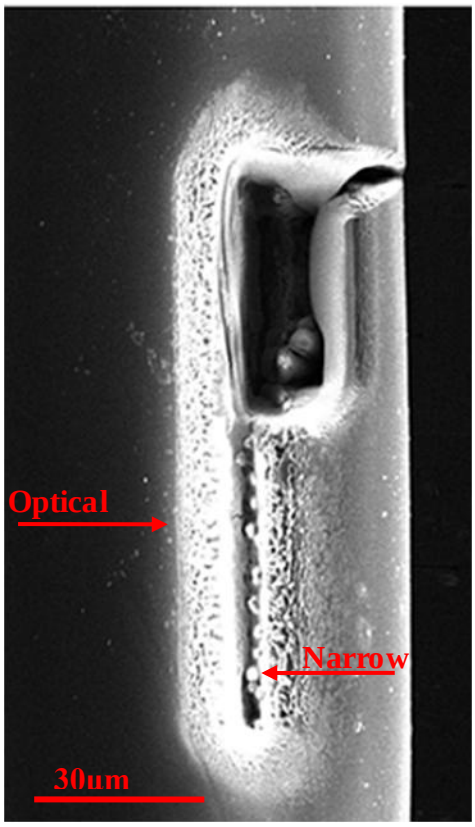

Figure 5.14 SEM view of FIB machined slot into an optical fibre. The machining stops as a result of the narrow slot produced during the machining.

Another trial was made by using direct FIB machining technique to mill a cantilever onto the side of an optical fibre. The use of FIB milling can accurately carve the structure while reduced the crack and damage inside the cantilever, however, it's a time

consuming process in terms of material remove rate. In addition, the machining process stopped at some point because of the narrow gap between the optical fibre and cantilever, which makes it difficult for material to come out into free space, therefore, the material removal rate is reduced accordingly. Figure 5.14 shows an FIB carved slot into an optical fibre with a current of 65nA and a voltage of 30keV. Part of the slot with a width of ~25μm has been successfully machined. On the other hand, the narrower slot with a width of (~10μm) at the bottom of the optical fibre was still connected with each other before the FIB stopped machining. The results show that when the width of the slot becomes narrower, it is difficult for FIB to ablate the material from an optical fibre. In this case, if only a FIB process is used, it would be hard to produce cantilever structure with suitable dimension for sensing within the dimension of a single mode optical fibre.

5.4.2 *Micro-machining of fibre side cantilever*

To address this issue, ps-laser machining techniques and set-up described in Chapter 4 are used to fast prototype a cantilever which can separate the cantilever from the main body of the optical fibre. Figure 5.15 shows the top view of a ps-laser machined cantilever. Due to the profile of laser beam, the cutting edge is tapered [5.7] , however, this can be further modified by FIB milling. The benefit of using laser micro-machining here is rapid initial prototyping of the micro structures and the potential to be scaled up in an automated manufacture process.

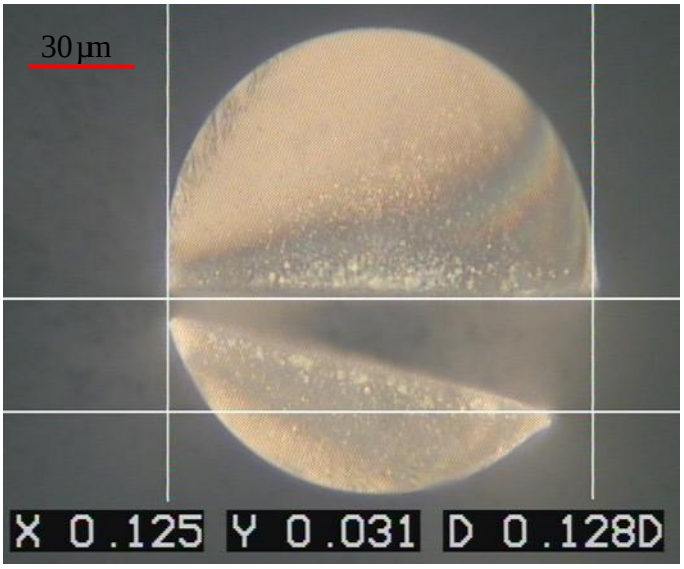

Figure 5.15 Top view of ps-laser machined optical fibre side cantilever on a single mode optical fibre. The big gap at the right side of the optical fibre indicates the laser starting point while the narrow gap at the left side of the optical fibre indicates the laser finishing point.

The cantilever is produced by using ps-laser machining to remove 4 parallel straight lines with a spacing of 5µm along the length of the fibre. This defines the separation between the thicker part of the fibre containing the core, and the thinner cantilever. The average power of laser in this case is usually around 10W, with a repetition rate of 40kHz scanning at 100mm/s (Figure 5.16). Typical dimensions of the resulting cantilever are ~1mm long, 20µm thick and 35 µm wide. Further modification is finished by FIB machining to reduce the thickness of cantilever down to ~7µm. The tip of cantilever surface 1 together with the reflecting surface 2 shown in Figure 5.17 are polished to be an optical surface quality for interference purpose.

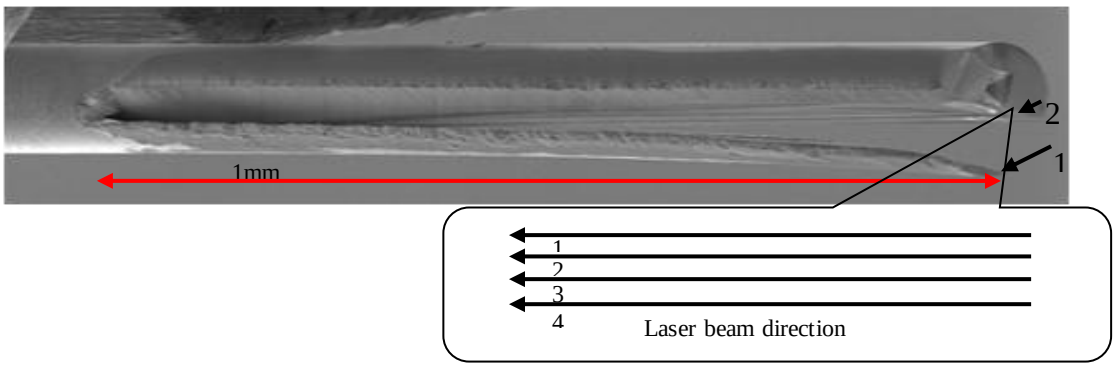

Figure 5.16 SEM view of laser/FIB machined fibre side cantilever. 1 and 2 indicate the two reflection surfaces of an FP cavity. The zoomed in part shows that four straight lines are used to ablate the optical fibre to produce the cantilever. The total cantilever length is measured to be ~1mm.

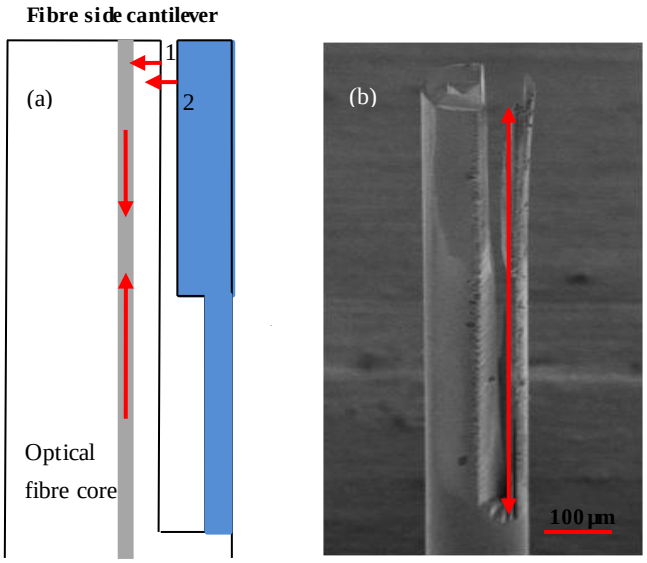

Figure 5.17 Laser/FIB machined optcial fibre side cantilever. (a) Side view of the optical fibre cantilever. The red arrow shows both the incident and the reflected light directions. The blue part at the right side of the optical fibre indicates the cantilever. (b) SEM view of the fabricated cantilever.

To optically monitor the deflection of this cantilever from light guided in the fibre requires a turning mirror. FIB machining is used to produce a 45˚ mirror as discussed in 5.2.1. The polished mirror surface allows light to be coupled from the fibre core to the cantilever and back. The FIB polished surface 1 and 2 created a FP interferometer capable of measuring deflection generated by the cantilever. With this approach, the total machining time of the optical fibre cantilever accelerometer is ~2 hours with optimized ion beam energy parameters.

The key point of successfully modifying a side cantilever by FIB at the desired position is to accurately align the optical fibre before machining. Rotating the fibre 180^{o} is necessary to machine from the opposite side and clear the back end of the tapered shape. This needs accurate alignment of cantilever with respect to the FIB machining direction. Currently mounting the fibre in the correct orientation is managed by a small angle rotational mount manually. It would be more convenient to have an optical fibre holder with at least 5 axis freedoms in the future thus small angle directional misplacement can be accurately positioned.

A suitable dimension of side cantilever for low g (<10g) acceleration should be machined to 1 to 2 mm long, ~5-10μm thick. It would be challenging to fabricate an accelerometer within the size of an optical fibre. The feature size of ps-laser machining is ~±10μm, which means for smaller feature size e.g. reduce the cantilever thickness, an FIB polishing process would be necessary.

The combination of FIB and ps-laser machining techniques addressed the issues of using either single FIB milling or ps-laser machining techniques, and improved the machining efficiency for prototyping micro-elements in a standard single mode fibre with a sub-micron feature size.

5.4.3 *Phase interrogation technique*

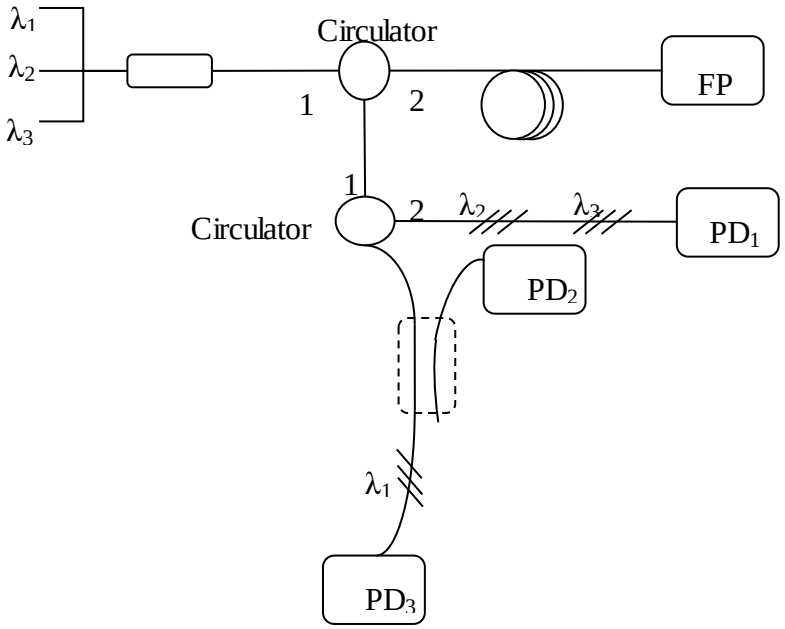

Figure 5.18 Schematic configuration of 3λ laser interrogation system. Each wavelength is interrogated by a PD.

For dynamic acceleration measurements a broadband source and spectrometer is unsuitable due to the low frame rates possible. Therefore a reduced number of wavelengths can be monitored using high speed photodetectors. Such phase interrogation methods have been reported previously [5.8]. The three wavelength technique improves upon single wavelength techniques by reducing phase ambiguities and is useful in applications where rapid changes go beyond one full cycle of the transfer function. Figure 5.18 shows the schematic of the interrogation system. The interrogation units provide optical signal filtering, optical to electrical signal conversion, amplification and output.

For practical use, the FP cantilever sensor can be illuminated with all three laser wavelengths (1532, 1547, and 1563 nm) and the reflected light was filtered by means of fiber Bragg gratings so that the signal for each wavelength can be recorded individually. Each laser source delivered up to 10mW power, sufficient to multiplex up to six sensors by distributing the power via a directional coupler network. The detectors were high-bandwidth InGaAs photodiodes (PD), and their voltage outputs were recorded by a LabView PXI system with up to 10MHz sampling rate.

In our case, as the wavelength shift is much smaller than $\frac{\lambda}{2}$, therefore, only a single wavelength operated at 1532nm is necessary to interrogate the deflection of cantilever under vibration. The wavelength is first tuned to the quadrature point which is called Q point [5.9] (illustrated in Figure 5.19) of the optical fibre accelerometer spectrum. In this region, phase information can be demodulated with a near linear response and highest sensitivity is achieved due to the highest derivative. The Q point of different laser machined cantilevers may vary from each other, thus it's important to first determine the operation point by tuning the wavelength of the laser source.

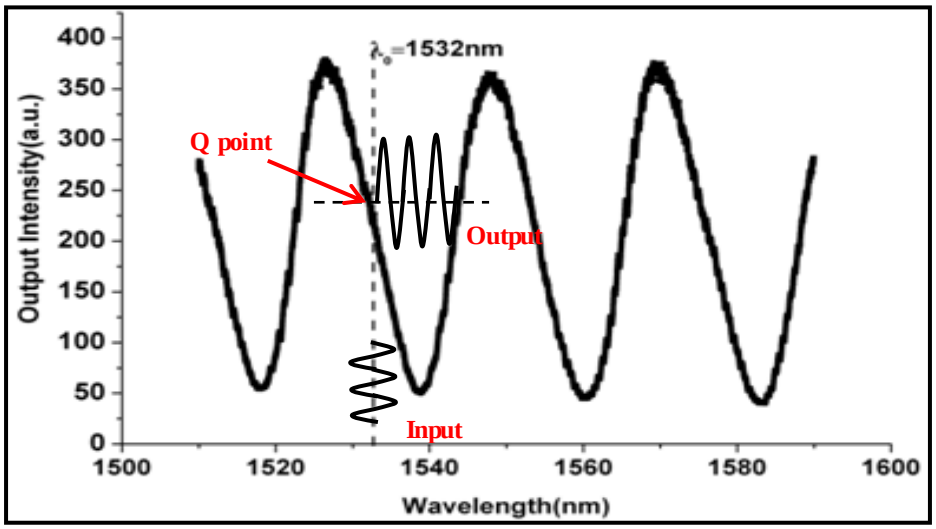

Figure 5.19 Interferogram from an optical fibre cantilever accelerometer, with the laser wavelength operated at 1532nm.

5.4.4 *Acceleration measurement*

The accelerometer is calibrated by rotating the sensor under the influence of gravity. Deflections are recorded for a 360° full turn and repeated several times to set for drift and hysteresis. The measured results of optical fibre rotation angle versus side mounted cantilever deflection are shown in Figure 5.20. As the optical fibre rotation, the side cantilever deflects due to gravity. The relation between the rotation angle and cantilever deflection in theory follows a cosine function. It is clear that a cosine trend is found as the optical fibre is rotated, showing a good match with the theory. From the results, a maximum deflection change of ~45nm/g is achieved when the fibre is rotated

~180 °. The noise level of the laser based interrogation system used here is ~10nm, which means a ~0.2g static acceleration resolution is achieved.

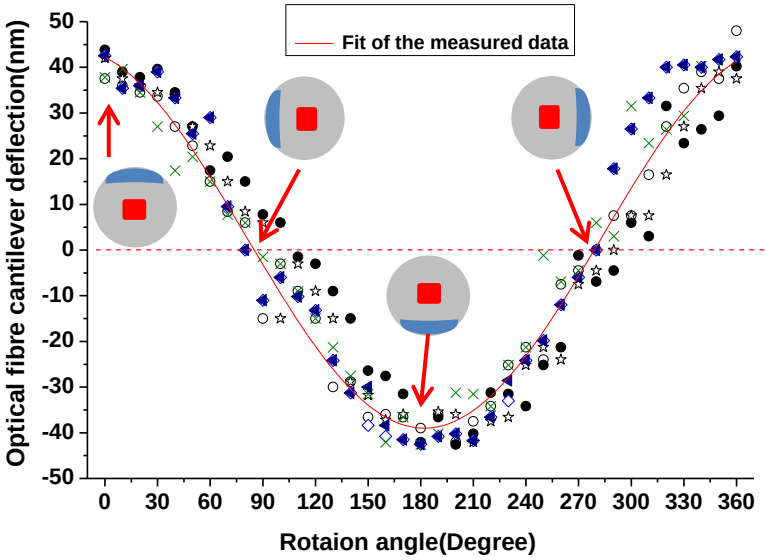

Figure 5.20 Optical fibre side cantilever deflection versus optical fibre rotation angle. The fibre is rotated from 0 °to 360 ° and measured for six times represented by different shape and colour in the figure. The red arrows indicate the four position of side cantilever when rotating at 0 °, 90 °, 270 °and 360 °. The blue region in the fibre (top view) shows the top view of cantilever while the red rectangles in the centre of the optical fibre indicate the 45 °mirror (top view).

In principle the acceleration sensitivity of the optical cantilever sensor depends on the length of machined cantilever. Higher acceleration sensitivity can be achieved by increasing cantilever length up to ~2mm for example or by reducing the thickness via FIB polishing. Thinner cantilever <7µm can be difficult to machine due to the accurate alignment of FIB with respect to the cantilever position, while increasing the cantilever sensitivity will also affect the resonant frequency, and hence the upper operating frequency. Assuming that the cantilevers follow a rectangular beam model, a resonant frequency of ~13kHz for fibre side accelerometer can be calculated. This equals to a sensitivity of ~25nm/g for fibre side accelerometer. The actually sensitivity is ~45nm/g, which is more sensitive than the theoretical calculation. It is expected that during machining, laser/FIB might introduce cracks into the material and change the mechanical property. Furthermore, the geometry of the cantilever will also have an impact on the resultant cantilever.

Dynamic acceleration experiment is carried out by using the experiment set-up shown in Figure 5.21. The response from both micro-machined optical fibre cantilever accelerometer and a B&K 4500 accelerometer (B&K, Denmark) for reference purposes are recorded via a PXI LabView interrogation system. Based on the calibration result of acceleration due to gravity (g) measurement, deflection of side cantilever is transferred to acceleration using Newton's second law.

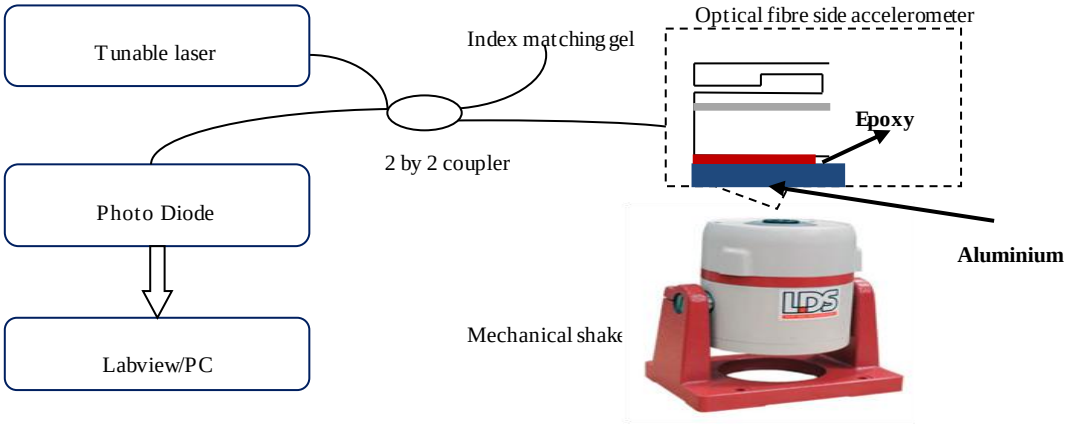

Figure 5.21 Experiment set-up of optical fibre accelerometer for dynamic acceleration measurement.

Then the machined cantilever is glued carefully to an Aluminium plate that is attached to a LDS9400 shaker (Linear Dynamic System LTD, UK). A sinusoidal drive current with controlled amplitude activates the shaker. The acceleration response for both electronic and optical accelerometer is shown in Figure 5.22. The applied acceleration is measured by B&K 4500 electronic accelerometer to be 3.3g at a vibration frequency of 200Hz. Using the calibration results from Figure 5.20, the deflection of optical fibre side cantilever can be converted into acceleration. It can be seen that the optical fibre cantilever can successfully measure the acceleration without any signal distortion, though the noise shown is a little higher than the reference accelerometer. The zoomed in part in Figure 5.22 (b) indicates the noise of a dynamic acceleration measured by optical fibre accelerometer.

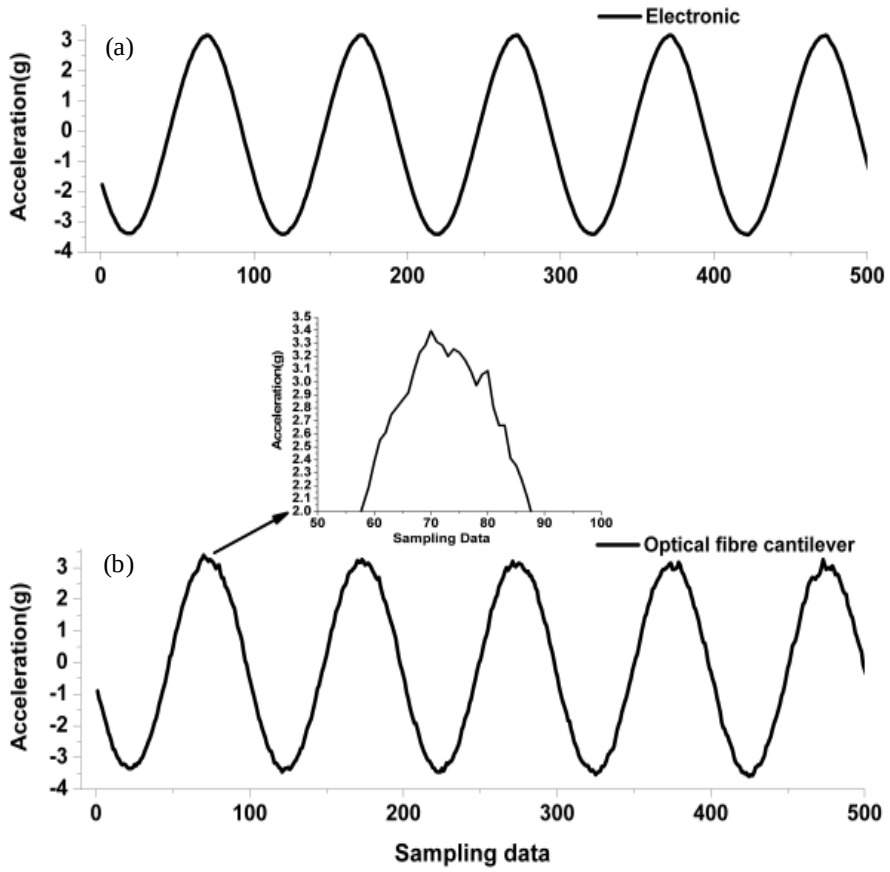

Figure 5.22 Acceleration from fibre cantilever compared with electronic accelerometer. Measured acceleration is 3.3g at 200Hz. (a) Acceleration measured by B&K 4500 electronic accelerometer. (b) Acceleration measured by optical fibre side cantilever.

To test the ability of optical fibre accelerometer to measure different frequencies, the frequency response of the cantilever accelerometer is plotted in Figure 5.23. A linear frequency response is demonstrated from 40Hz to 300Hz. The calculated resonant frequency of the optical fibre accelerometer is ~13kHz, therefore a larger dynamic range up to ~8kHz is expected. It can be seen from Figure 5.23 that from a frequency range of 40Hz to 300Hz, the acceleration response of optical fibre cantilever is nearly linear. The results demonstrated that the laser/FIB machined cantilever can be used for measuring different dynamic accelerations.

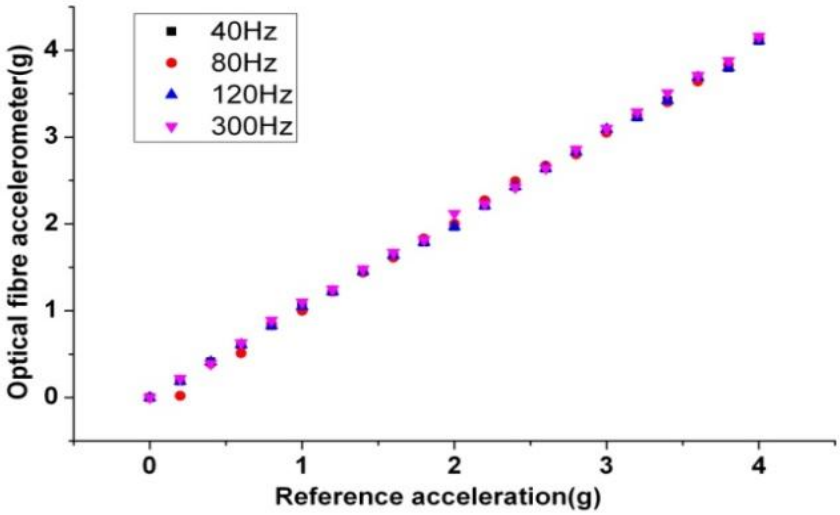

Figure 5.23 Optical fibre accelerometer response at different frequency. x axis shows the peak acceleration of applied signal measured by B&K 4500 electronic accelerometer while y axis is the peak acceleration of applied signal measured by optical fibre accelerometer.

To show that the sensor can measure acceleration in two axis, the acceleration responses of both vibration and cross axis were recorded in Figure 5.24. The vibration frequency of 40Hz is used for testing. The results show the optical fibre cantilever accelerometer measures a significantly higher response in the vibration axis (on-axis) than in the cross axis (off-axis). The minimum crosstalk is calculated to be ~44.6dB at 4g: the maximum acceleration tested.

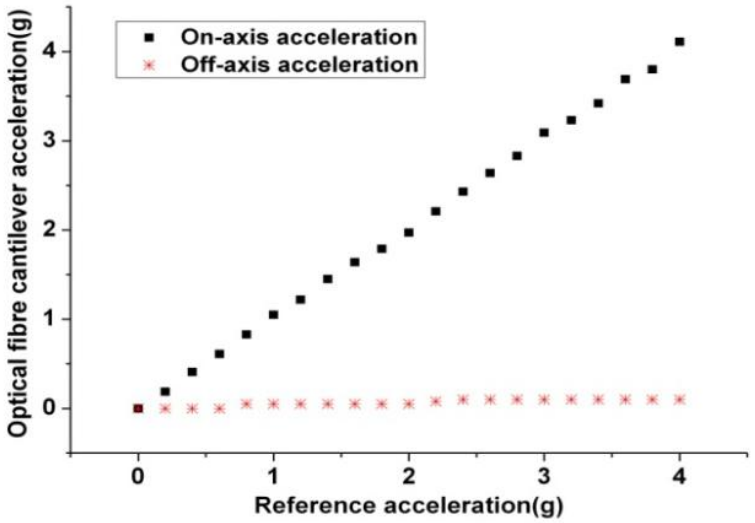

Figure 5.24 On-axis and off-axis response of optical fibre accelerometer at 40Hz. On-axis acceleration means the cantilever vibration direction, while off-axis acceleration indicates the vibration perpendicular to the cantilever vibration direction.

To summarise, an accelerometer with micro-machined cantilevers onto the fibre tip and side of optical fibre are demonstrated. The side cantilever contains an FIB milled 45° mirror into the core of optical fibre. The accelerometer is capable of measuring 2D acceleration with a static resolution of 0.01g from 40Hz to 300Hz. The all silica micro-machined accelerometer provides routes for sensing in harsh and high temperature environments. In addition, by properly designing the dimension of optical fibres, 3D accelerometer can be potentially fabricated on a multi-core optical fibre as a single probe and this will be discussed in the following section.

Experimental results demonstrated that an acceleration resolution of 0.2g within 300 Hz bandwidth is achieved. The micro-machined cantilever accelerometer offers the capability of measuring acceleration in harsh environment with a robust all silica design. In addition, no mechanical alignment is needed during machining process, which combines sensing probe and readout as a single element.

5.5 MCF cantilever sensor for acceleration detection

The major fabrication aim is to machine four 45° mirrors into the cross section of a multi-core-fibre (MCF) for the purpose of multi-axis displacement and acceleration measurement in a space constraint environment.

5.5.1 *Fabrication of 45° mirror in MCF*

The 25µm by 25µm 45° in-fibre mirror is machined using the same approach discussed in 5.2, other than that 4 mirrors are machined onto a single MCF instead. The mirrors are aligned to direct the light torward the nearest external surface. (Shown in Figure 5.25)

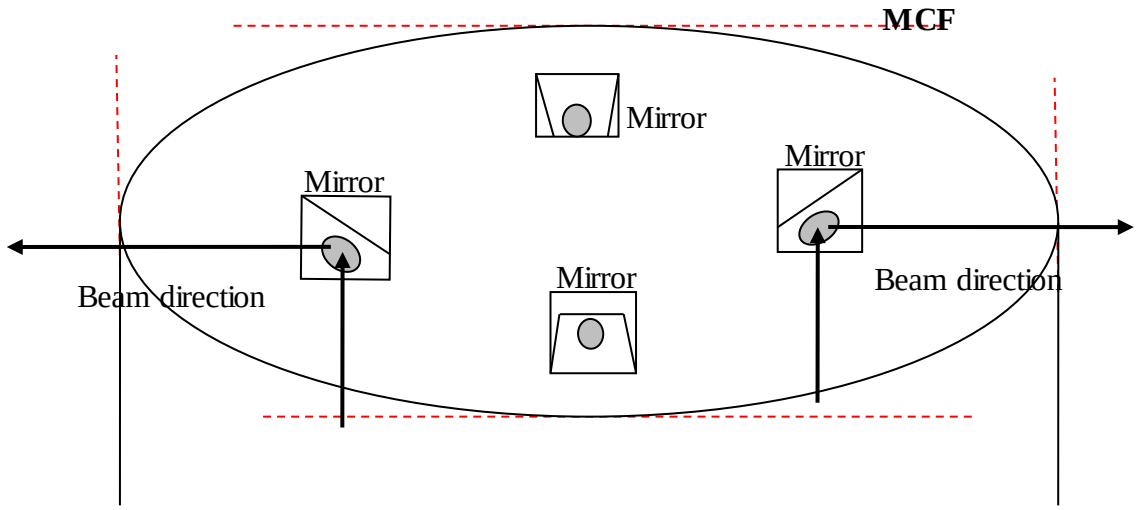

Figure 5.25 Schematic diagram of 45° mirror machined into MCF. The MCF is tilted 52°in FIB chamber in order to show the location of each mirror. The black arrows indicate the direction of light propagating in the fibre.

The MCF was mounted onto an optical fibre holder. The side of the fibres were dotted with silver loaded paint to provide strength of holding with no deformation, as well as adding grounding to negate drift during fabrication. A circle of approximately 100µm diameter by 250nm depth was machined into the cross section of a gold-coated multi-core fibre to locate the fibre core area. If necessary this can be repeated, until the actual location of the four cores on the surface of the cross section were visible. The core positions were carefully measured using SEM (Cross Section), taking angles from the centre of the whole fibre. Having carried out the angle measurement again, the fibre was tilted to zero and carry out angle location measurements to match the FIB presentation during fabrication. Figure 5.26 showed the four fibre core area to locate the mirrors later on.

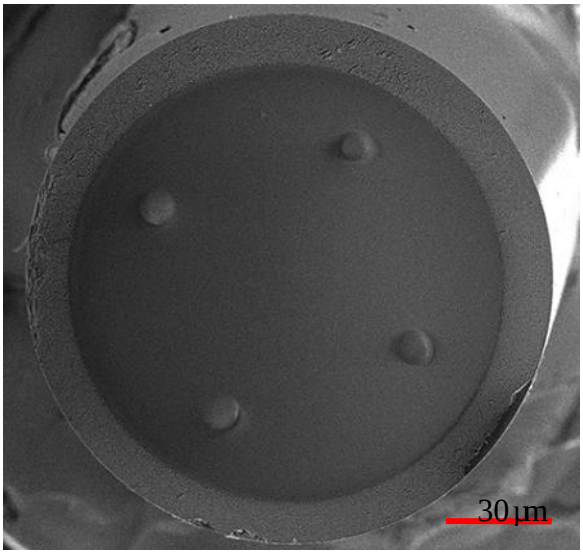

Figure 5.26 SEM view of MCF with 4 core exposed for identification.

In order to locate the centre of core easily after Pt deposition, squares of 30µm diameter by 250nm depth were machined over each core centre to permanently mark each core location and Pt deposition over each square will allow further fabrication with minimal charging.

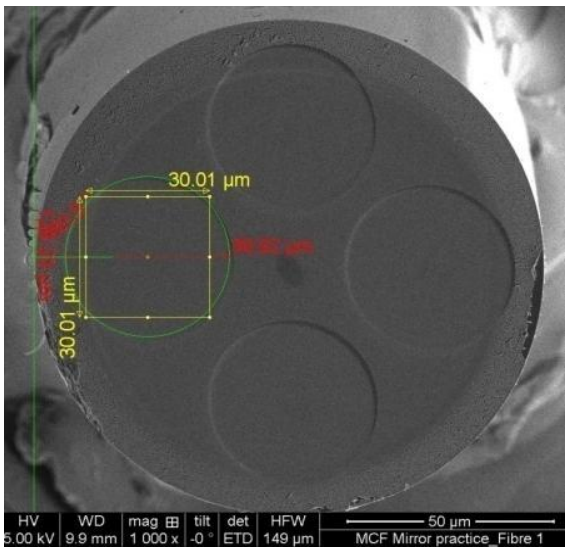

Figure 5.27 SEM view of in-fibre mirrors fabrication process on a MCF. The yellow square measures the dimension of the area used to locate the fibre core area for FIB machining.

Rough 45^{o} mirrors following the same fabrication methods were machined over each core centre position first (shown in Figure 5.27). This ensured that the shallow edge of each mirror is positioned at a 90^{o} angle to its neighbour which will simultaneously

position each parallel to theoretical tangential lines drawn round the fibre circumference. Figure 5.28 shows the SEM view of the MCF during FIB machining. An ion beam scanning pattern is applied onto one of the fibre core by using the same technique developed for 45° mirror machining in section 5.2. A further coating of platinum will be carried out over each rough mirror. For each individual mirror, the fibre has to be rotated by 90°, tilted to 7° and polished to a final finish angle of 45°. The total fabrication time in this case is ~35 minutes for each mirror.

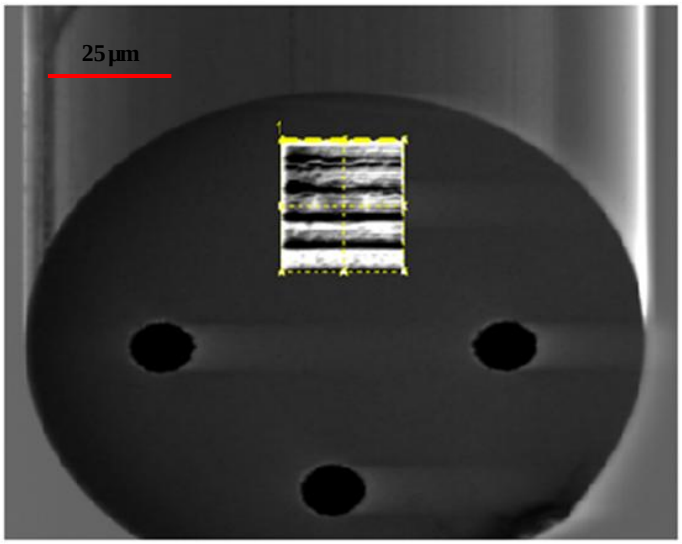

Figure 5.28 SEM view of 45˚ mirrors machining process on MCF. The yellow dash line indicates the machining area on one of the fibre core.

It is found that as much grounding as possible of fibres is very desirable, so the holder has no clamp as such – this tends to flatten and slightly bend fibres – but is designed to be used with (minimal) silver loaded paint as a fixing. This is easily dissolved with acetone to release the fibres after fabrication completion. As the multi-core fibre centre is softer than the rest of the fibre as a whole, unusual features may appear there when machining the 100µm diameter circle. If these features cause problems, it may be necessary to fabricate a "doughnut" shape rather than a circle to avoid machining the centre of the multi-core fibre. Figure 5.29 showed the overview of final machined 45˚ mirror into a MCF. It can be seen from the zoomed in part, the mirror is accurately machined to be 45˚ with a smooth surface finish.

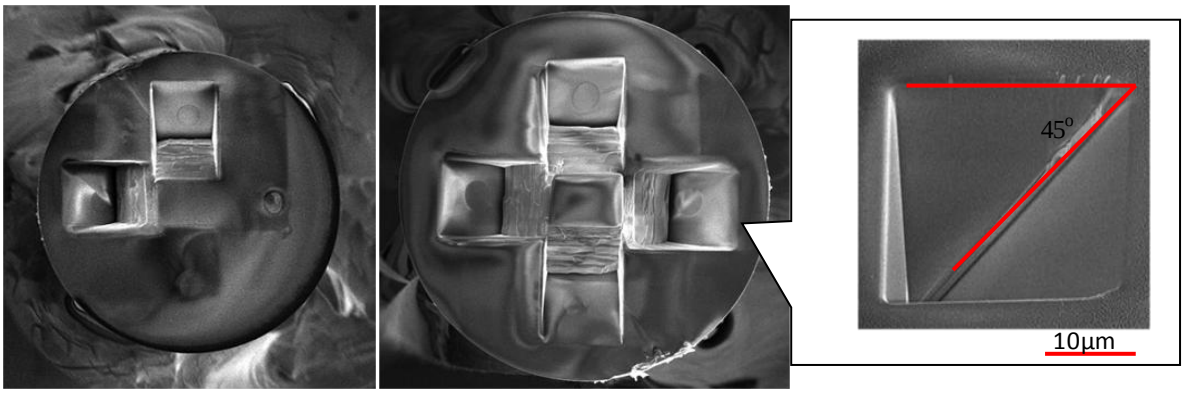

(a) (b) (c)

Figure 5.29 (a) SEM view of FIB fabricated two 45˚ mirrors in a MCF. (b) SEM view of FIB fabricated four 45˚ mirrors in a MCF. (c) SEM view of zoomed in 45˚ mirror from one of the machined mirror in (b).

The size of the mirror is set at 25µm by 25µm, bigger mirror size >25µm is excessive due to the dimension of MCF, particularly after mocking up an image of what it will look like when completed. This will still leave a spare location to use for parameter adjustment and should allow good visualisation of area needed for light transmission in the fibre.

5.5.2 *MCF 3D displacement measurement*

To demonstrate the MCF as a micro-displacement sensor, multicore fibre with 45˚ mirrors machined was mounted onto a 3D piezoelectric driven translation stage with three perpendicular mirrors placed next to the MCF to allow displacement measurement between the fibre and the fixed reference mirrors to be measured. An optical cavity is formed between the fibre sidewall and the fixed mirror (Figure 5.30). The MCF is connected to a MCF fan-out device, which allows 4 cores to be interrogated separately. They are connected to SM125 optical interrogator (Micro Optics) to obtain the cavity interferogram and hence the final cavity length is determined.

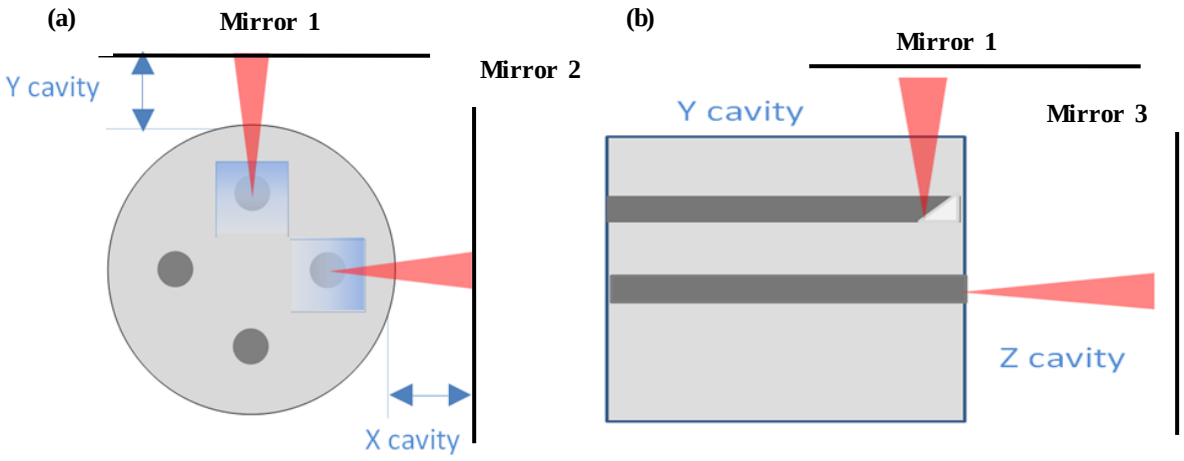

Figure 5.30 Schematic diagram of MCF three-axis displacement sensor. (a) top view of cavities formed between the 45° machined mirror and mirror 1 in Y axis, mirror 2 in X axis respectively. (b) side view of cavities formed between the 45° machined mirror and mirror 1 in Y axis, mirror 3 in Z axis respectively.

The measured interferogram in both X, Y and Z axis are plotted in Figure 5.31(a). The distances calculated by FFT analysis are 352.45μm, 416μm and 1.12mm respectively. Figure 5.31(b) shows the cavity length changes in X, Y and Z axis versus the movement of PZT.

It can be seen from Figure 5.31(c), the calculated minimum r.m.s. residual error when moving the PZT is ~50nm over a measurement range of 250μm. This demonstrates that the MCF probe is capable of measuring displacement in three perpendicular directions simultaneously, which offers possibility of a single probe to provide multi-dimensional measurement in a space constrained environment.

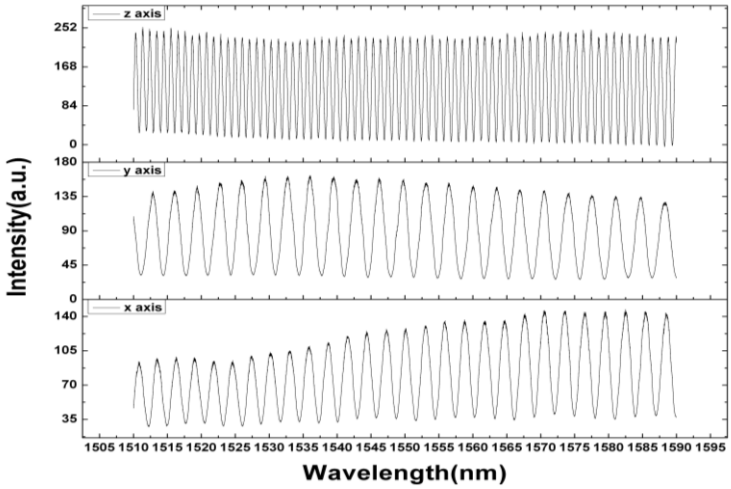

(a)

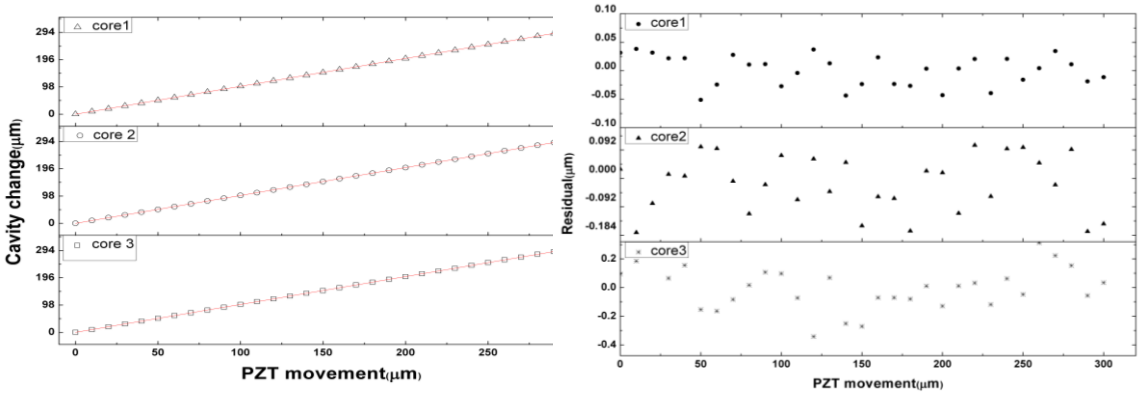

(b) (c)

Figure 5.31 (a) Interferogram obtained between X,Y and Z cavities respectively. (b) Calibrated cavity lengths change for X,Y and Z cavities versus PZT movement. (c) Residual error of cavity lengths change for X, Y and Z cavities respectively.

In this section, 45˚ micro mirrors were successfully fabricated onto the end of an MCF by using focused ion beam machining. These structures offer the potential for having a single probe capable of multiple measurements in a confined measurement volume. Initial experimental results show that the machined structure can be used as a three dimensional position sensor to measure the displacement between the mirror and a surface.

5.5.3 *2D acceleration measurement*

Another application of this micro machined 45˚ mirror on MCF is 2D acceleration measurement. Here the whole fibre forms the cantilever, and is freely suspended inside

a metallic tube. The inner surface of the metallic tube serves as a reflecting surface, allowing the light in the MCF to be reflected by the micro-mirror machined into the MCF.

Before the MCF is encapsulated into the tube, it is necessary to add a proof-of-mass at the tip of MCF to optimise the acceleration range down to <10g for our application. A "glass solder" preform, which has a donut shape, is used as end mass and carefully inserted through the fibre by a 3D translational stage and cured in place by epoxy, shown in Figure 5.32. The outer diameter of the soldering preform is 735µm while the inner diameter is 264µm. The weight is enough to produce the low g acceleration measurement with this particular MCF cantilever dimension. Cavity length fringes between the 45° mirror in MCF and a reflecting tube surface are shown in Figure 5.33.

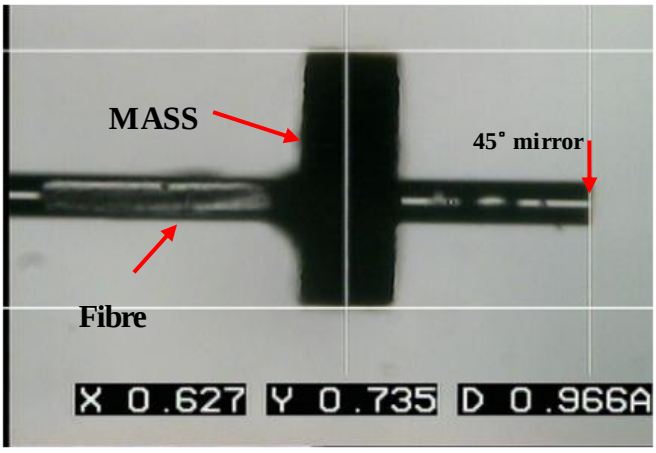

Figure 5.32 Microscopy view of basic structure of a MCF cantilever accelerometer with soldering preform as an end mass.

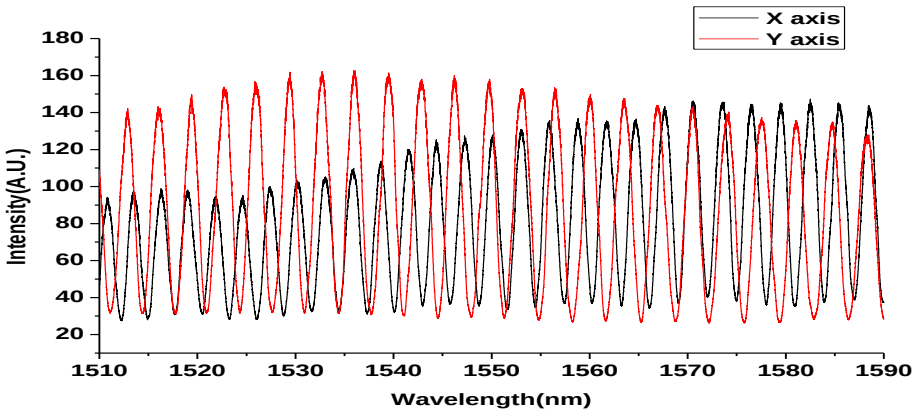

Figure 5.33 Interferogram obtained between a MCF and the reflecting tube surface to form a FP interferometer.

Consider the optical fibre itself is a cantilever. The deflection at the end of optical fibre can be expressed as:

$$x = \frac{A\rho l^4 a}{8EI} \tag{5.20}$$

Where A is the cross-sectional area of the beam, ρ is the mass density, l is the length of the optical fibre, a is the acceleration, E is the Young's modulus and I is second moment of area. For a cylinder shape:

$$I = \frac{\pi d^4}{64} \tag{5.21}$$

Where d is the diameter of the fibre, for the silica fibre employed in this work, ρ=2280kg/m^3, E=59GPa and d=125μm.

The deflection of the optical fibre under acceleration is proportional to l^4, so increasing the cantilever beam length can increase the sensitivity, however, longer cantilever will reduce the frequency detection range and also is not suitable for applications in space constraint environment. The first resonant frequency of a cylindrical cantilever beam can be expressed as:

$$f_1 = \frac{3.52}{2\pi l^2}\sqrt{\frac{EI}{\rho A}} \tag{5.22}$$

Acceleration is measured by using the three wavelength laser interrogation system described in section 5.3 but only one wavelength is used for cantilever acceleration measurement. The frequency response (Magnitude ratio of Output signal divided by input signal) of MCF accelerometer is investigated over a range of 10-6000Hz and plotted in Figure 5.34. It can be seen that below 2000Hz, the amplitude ratio of frequency response is nearly flat. As the vibration frequency increases, the frequency response ratio also increases, which means a nonlinear response happened here. The measured resonant frequency of MCF cantilever accelerometer is around 4200Hz, while the resonant frequency calculated by model is 4380Hz for cantilever with ~6mm length. As the cantilever hinge is glued to the metal tube by epoxy, the real cantilever length taken to calculate the resonant frequency is different from the measured one. Another factor which might cause the error is the alignment between the mirror and the reflected metal surface. The deviation of scatter light can lead to poorer visibility thus increases the deflection error of interrogation system and finally lead to the measured acceleration error.

In the case of low g acceleration measurement with a frequency bandwidth up to 2000Hz, it was possible to tune the resonant frequency and expand the flat response range by optimising the cantilever length and the weight of end mass.

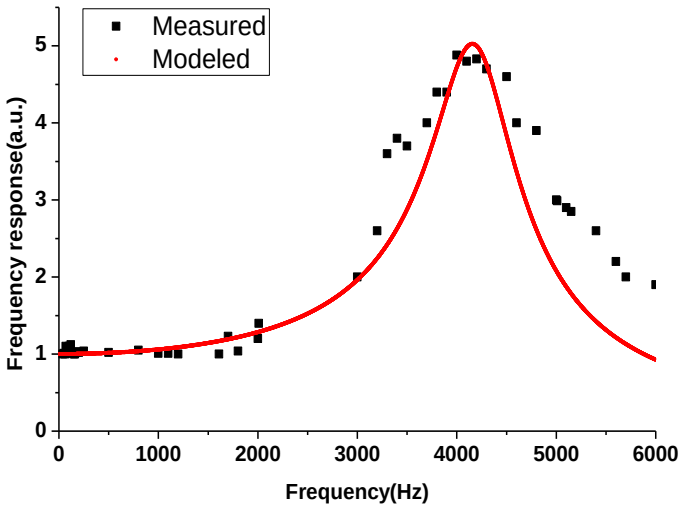

Figure 5.34 Frequency response of a MCF accelerometer versus frequency change. Black square shows the measured acceleration by optical fibre side cantilever while the small red dot is the frequency response from theoretical calculation.

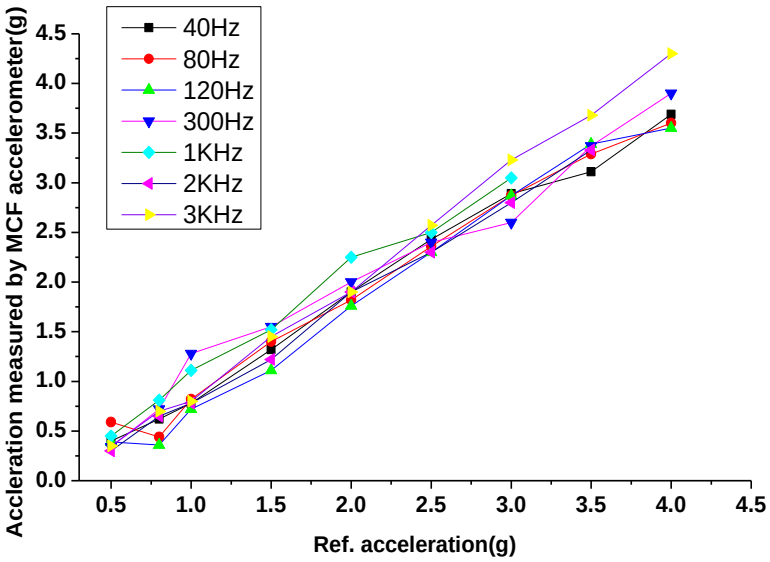

Figure 5.35 Measured acceleration from a MCF accelerometer compared with B&K 4500 electronic accelerometer at different frequencies. The applied acceleration is 3g at a vibration frequency of 60Hz.

Secondly, acceleration responses of MCF optical fibre accelerometer under different vibration frequencies are monitored (as shown in Figure 5.35). The same electronic accelerometer is used as a reference. The acceleration measured by MCF cantilever is close to the applied electronic accelerometer. In low frequency vibration (<2kHz), increase in applied acceleration will lead to a nearly linear response of acceleration

measured by MCF, however, as the frequency increase to 3kHz, acceleration measured by MCF starts to become larger because of the nonlinear effect of frequency response. To reduce this effect, resonant frequency can be tuned to high range by optimising the cantilever length and weight of end mass [5.10].

Two axis acceleration measurements are also demonstrated by mounting the encapsulated MCF accelerometer to the shaker. The vibration axis of the sensor is pre aligned with the vibration axis of the shaker. To show that the sensor can measure acceleration in two axes simultaneously, the vibration and cross axis response of MCF accelerometer were recorded from 0.5g to 6.2g (shown in Figure 5.36). Both on-axis and off-axis acceleration increase as the amplitude of vibration is increased. The figure shows that the MCF accelerometer measures a significantly higher acceleration response in the vibration axis than in the cross-axis. It should be noted here, any rotational misalignment of the sensor will increase the cross-axis response. The minimum crosstalk is calculated to be ~24.1dB at 6.2g: the maximum acceleration tested.

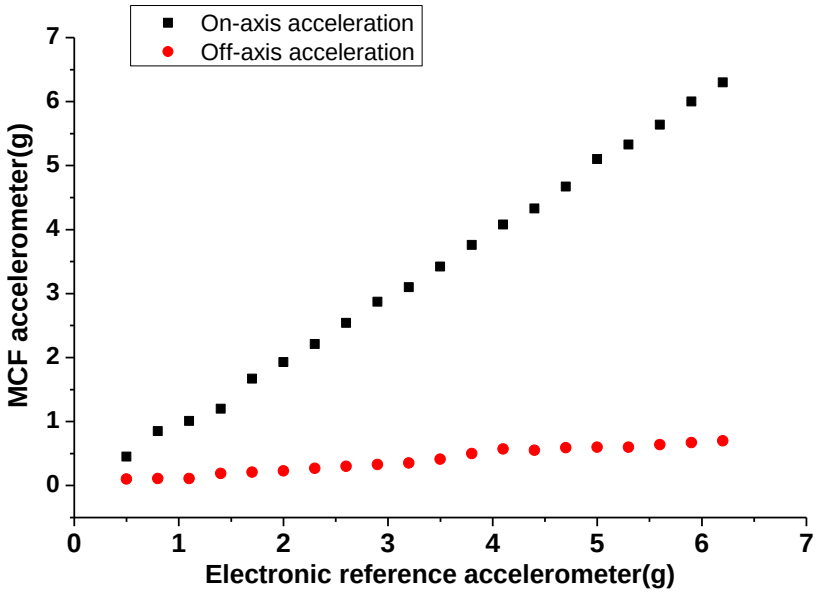

Figure 5.36 On-axis and off-axis accelerations of MCF accelerometer measured at 60Hz.

To further investigate the acceleration response of MCF accelerometer, the sensor is pre-aligned 45° to the vibration axis. Acceleration signals from both X and Y axis are interrogated by the system discussed in 5.5.3 and plotted in Figure 5.37.

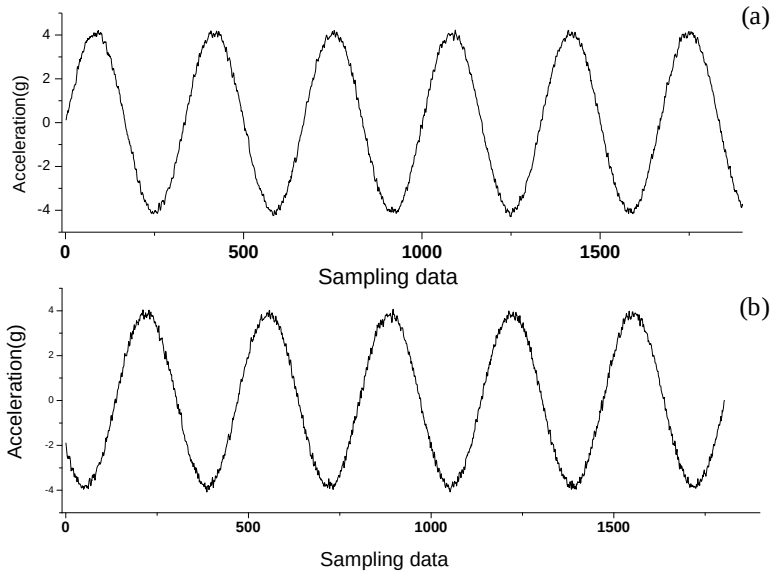

Figure 5.37 Acceleration measured by MCF accelerometer with 45° angle aligned to vibration axis.(a) Acceleration measured in X axis. (b) Acceleration measured in Y axis.

From the figure, it shows that the frequency response of a sinusoidal acceleration at 60Hz with a peak acceleration of 4g. The peak acceleration measured by MCF accelerometer in x axis is 4.1g, while in y axis is 3.92g. Both X and Y axis have an acceleration noise level of ~0.2g.

In this section, an optical fibre cantilever accelerometer is successfully fabricated for two dimensional acceleration measurements. The cantilever sensor consists of 45° mirrors fabricated onto the end of an MCF by using focused ion beam machining and then encapsulating the MCF in a metallic tube. The mirror is accurately aligned with optical fibre core, which avoids issues associated with the alignment of external turning mirror components. A MCF three dimensional displacement sensor is first demonstrated with a displacement resolution of 50nm over a measurement range of 1mm. Further experimental results show that the MCF cantilever can be used as an accelerometer capable of measuring acceleration up to 6g with a linear frequency range

from 10Hz to 2000Hz. The frequency response of the sensor could be adjusted by altering the length of fibre and mass fixed to the end of cantilever which formed the sensing element. The on-axis acceleration is measured to be 10 times higher than cross-axis acceleration.

The MCF cantilever accelerometer offers the potential for having a single probe capable of multiple measurements in a confined measurement volume. The in-fibre micro mirror could also be potentially used for imaging or sensing where the target area is side of the probe. It would be useful if larger diameter MCF is fabricated to allow more space for multi-cantilevers machined in a single MCF. This will offer the route to measure multi-axes acceleration with a single probe. In addition, the all silica feature will make the sensor more robust with harsh environment.

The acceleration range was limited by the shaker used for vibration test. Higher acceleration can be measured if a larger resonant frequency of shaker is used.

5.6 Conclusion

In this chapter, an in-fibre 45° mirror is successfully machined on both single mode and MCFs by FIB milling with optical surface finish. The resulting mirror is demonstrated to be at least 25μm by 25μm to achieve a good reflection spectrum. The characteristic of this micro-machined mirror is evaluated and the angle is verified by white light interferometer to be 45°±0.05°. The in-fibre micro-mirror provides a new route for sensing where the deflection and displacement are parallel to the direction of optical fibres in a harsh and space constrained environment.

Several applications of the 45° micro-mirror are demonstrated: MCF for three-axis displacement measurement, MCF cantilever for two axis acceleration measurements and optical fibre side cantilever for acceleration measurement. We expect that in the future, the in-fibre 45° mirror can be used for sensing in space constrained environment with multiple parameters to be measured.

Reference

[5.1] R M Bradley, and J M E Harper, "Theory of ripple topography induced by ion bombardment", *Journal of Vaccum Science and Technology A*, vol.6, pp.2390-2395, 1988.

[5.2] Y Fu, N K A Bryan, O N Shing and N P Hung, "Influence of the redeposition effect for focused ion beam 3D micromachining in silicon", *The International Journal of Advanced Manufacturing Technology*, vol.16, pp.877-880, 2000.

[5.3] X M Goh, N M Dragomir, D N Jamieson, A Roberts, and D X Belton, "Optical tomographic reconstruction of ion beam induced refractive index changes in silica", *Applied Phycis Letters*, vol.91, pp.181102-181110, 2007.

[5.4] A Yariv, "Optical Electronics", Springer, New York, 1975.

[5.5] D Marcuse, "Loss analysis of single-mode fiber splice", *The Bell System Technical Journal*, vol.56, pp.703-718, 1977.

[5.6] D Kleppner and R Kolenkow, "An Introduction to Mechanics", Second Edition, Cambridge University Press, 2013.

[5.7] F Albri, J Li, R R J Maier, W N MacPherson and D P Hand, "Laser machining of sensing components on the end of optical fibres", *Journal of Micromechanics and Microengineering*, vol. 23, pp.45021-45028, 2013.

[5.8] W N MacPherson, S R Kidd, J S Barton and J D C Jones, "Phase demodulation in optical fibre Fabry-Perot sensors with inexact phase steps", *IEE-Proceeding of Optoelectronics*, vol.144, pp.130-133, 1997.

[5.9] J Y Chen, D J Chen, J X Geng, J Li and H W Cai, "Stabilization of Optical Fabry-Perot Sensor By active feedback control of diode laser", *Sensors & Actuators A. Physics*, vol.148, pp. 376-380, 2008.

[5.10] J Kalenik and R Pajgk, "A cantilever optical-fiber accelerometer," *Sensors and Actuators A* , vol. 65, pp. 350-355, 1998.

Chapter 6

Ferrule-top polymer cantilever sensor for rapid bio-detection

6.1 Introduction

In previous chapters, optical fibre cantilever sensors for physical and chemical application were investigated for temperature/pH sensing, multi-axis displacement and acceleration measurement. In this chapter, the use of polymer film micro-cantilevers on optical fibres for bio-sensing will be investigated. This includes monitoring the binding energy between biotin and streptavidin [6.1] and followed by the rapid food pathogen detection based upon antibody-antigen binding. By functionalizing the cantilever surface with different biomaterials, mechanical bending due to surface stress change can be determined.

The general configuration of a micro-cantilever based biosensor model can be found in Figure 6.1. Frist of all, a thin layer of Cr/Au is coated onto the cantilever surface. Then sensing bioanalyte is functionalized onto one side of the cantilever by a standard SAM process as described in Chapter 4 and blocking analyte is functionalized onto the other side of cantilever for internal control. The binding strength between gold and thiol is so strong that it will form a well ordered thiol-gold bonding. The other end of bio-molecular group is designed to bind with a detection molecule. As a result, surface binding will generate either compressive or tensile stress which is then converted to force on the cantilever surface. The force will go up to an equilibrium position as the binding process proceeds. Hence, by detecting the deflection of this force, the characteristic of the specific analyte can be determined. A typical laser machined cantilever under the SEM is shown in Figure 6.2. The dimension and shape of the cantilever can be varied by adjusting the laser machining parameters.

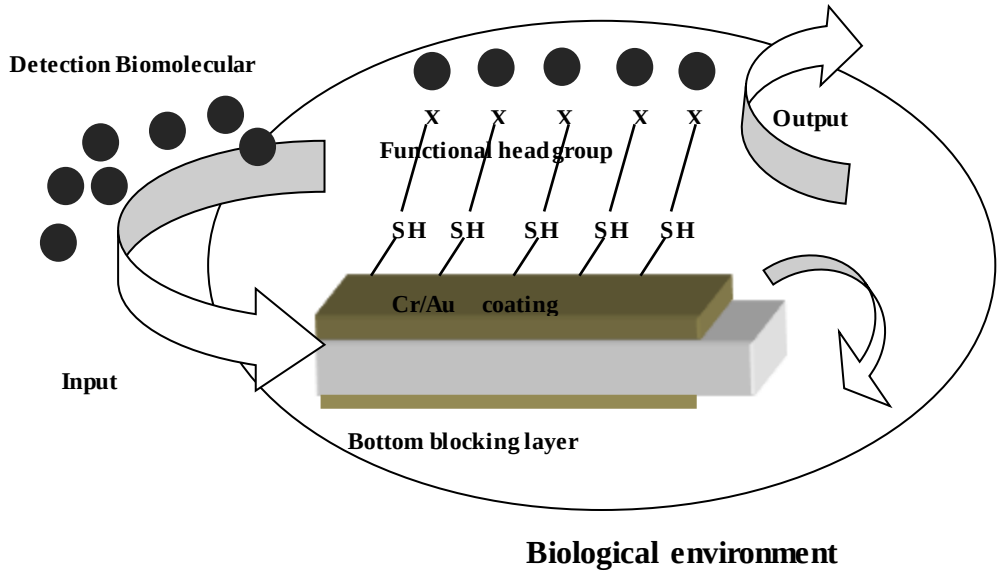

Figure 6.1 General structure of a cantilever based biological sensor model. Cantilever is coated with Cr/Au on both sides. The top side of the cantilever is used for sensing. Here –SH is thiol bond that bounds to Au and –X is the functional head group which interacts with detection biomolecular. The bottom side of the cantilever is usually used as a reference for blocking biological reaction.

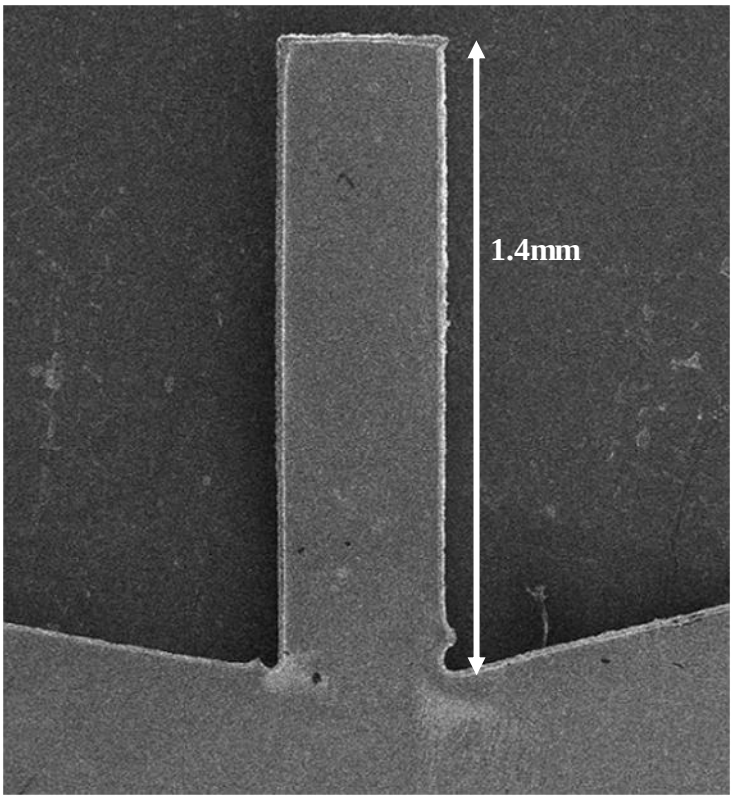

Figure 6.2 Laser micro-machined polyimide cantilever under SEM.

To convert cantilever deflection to bio-molecular binding induced surface stress, adsorption induced differential surface stress between the two sides of the cantilever needs to be calculated by monitoring the cantilever deflection change. Based on Stoney's equation mentioned in Chapter 2, cantilever deflection can be converted to the differential surface stress.

To overcome the drawbacks of the conventional micro-cantilever biosensor, an alternative approach to fabricate a portable ferrule-top cantilever is presented to monitor the biomolecule binding as well as potential application in food pathogen rapid detection. The sensor combines the sensing probe with a standard optical fibre as a delivery device. In this way, the signal can be interrogated using low-cost lamp and spectrometer. A detection limit of streptavidin of 10nM is found with Biotin-HPDP (Pyridyldithiol-activated, sulfhydryl-reactive compound, EZ-Link, Thermo Scientific) functionalized cantilever surface. This was on the same saturation level as previously reported results using optical beam deflection method on a silicon nitride cantilever [6.3]. The saturation time takes only less than 20 minutes at the minimum streptavidin concentration of 10nM.

In this chapter, the use of a ferrule-top cantilever as a biosensor is investigated. Real-time binding process is monitored between biotin and streptavidin and a further application of the sensor for pathogen detection is demonstrated. Furthermore, the effectiveness of cantilever biosensor was also tested, and compared with an ELISA (described in Chapter 2) system.

6.2 Fabrication of ferrule-top biosensors

The initial aim is to fabricate a portable biosensor that can combine the sensing probe and readout as a single element. Here an optical fibre held using a commercial optical fibre ferrule has been used as the support. A polymer cantilever is machined by a ns-laser to the desired dimensions and shapes usually ~1mm long, hundred μm wide and ~20 μm thick. These cantilevers can be bonded to standard fibre optic FC/PC ferrule to form the sensor. In this section, the fabrication techniques of a ferrule-top

cantilever and its applications to monitor biological binding are investigated. This includes biotin-streptavidin binding and a further application in rapid food pathogen detection is discussed.

The fabrication of a ferrule-top cantilever can be divided into several steps (Figure 6.3). First of all, patterning the supporting intermediate layer; second, ns-laser machining of the cantilever; third, functionalization of cantilever surface; forth, laser bonding of cantilever to optical fibre ferrule and finally secure the bonding by epoxy. Each of these steps will be discussed in detail in the following sections.

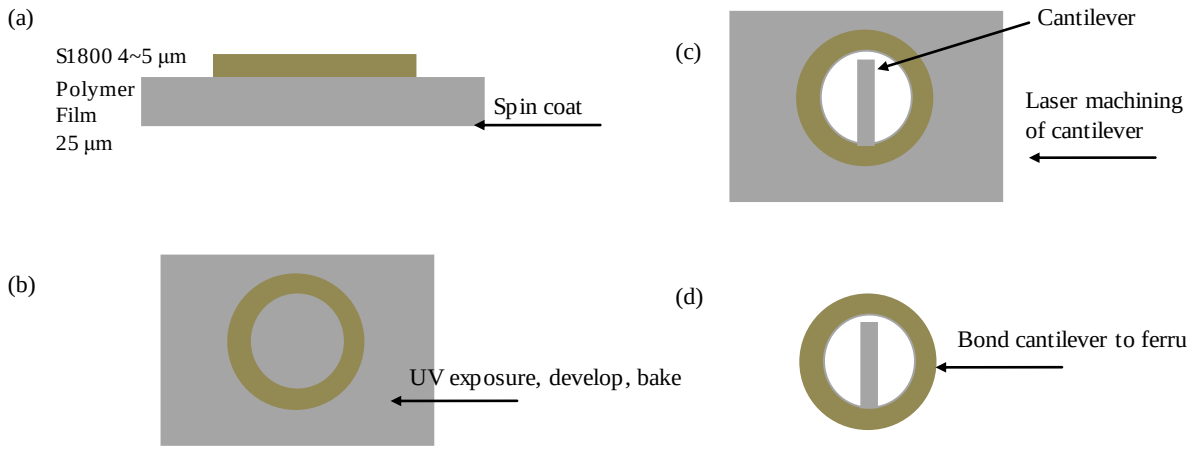

Figure 6.3 Overall fabrication process of ferrule-top biosensor. (a) Side view of spin coated S1800 photoresist on top of 25µm polymer film. (b) Top view of patterned ring after UV exposure, developing and baking process. (c) Laser machining of polymer cantilever. The cantilever is shown with gray colour in the centre of the ring structure. (d) Final cantilever with supporting layer ready for bonding to the optical ferrule.

6.2.1 Introduction to Inazuma laser workstation

A diode-pumped and Q-switched nanosecond Inazuma laser is used for both machining and bonding. The laser head provides 1064nm output and can be doubled to provide a 532nm output. The maximum output of the laser is 35W for Q-switched power in 1064nm and 20W in 532nm. For polymer cantilever machining purpose, a few Watts of laser average power above the ablation threshold is enough to produce a rectangular shape with mm dimension. The pulse repetition rate is adjustable from 15 kHz to 100 kHz.

The laser beam is collimated and focused into the scan head for machining. The stage can travel in vertical direction up to several hundreds of mm. When machining, the sample is clamped onto the stage with a bolt in order to secure its position.

The machining process starts with finding the correct *DOF* and allowing maximum machining efficiency at this point as discussed in Chapter 4. The aim of laser machining is to form to the suitable cantilever shape which matches with the ferrule dimension for bonding process.

6.2.2 Patterning the support structure

The aim of building up a ring structure on top of polymer film is to form the intermediate layer supporting the cantilever. The dimension of the donut shape will fit the standard optical fibre ferrule (Throlabs1550, FC/PC). The polymer film is first cleaned and nitrogen dried as the substrate for spin coat. S1800 photoresist (Microposit Co. Ltd) is poured onto the polymer substrate. Due to the characteristics of this photoresist, only 5µm of S1800 can be spin coating onto the 25µm substrate, therefore, cleaning is crucial as ~µm surface roughness will affect the thickness and flatness of the intermediate supporting layer.

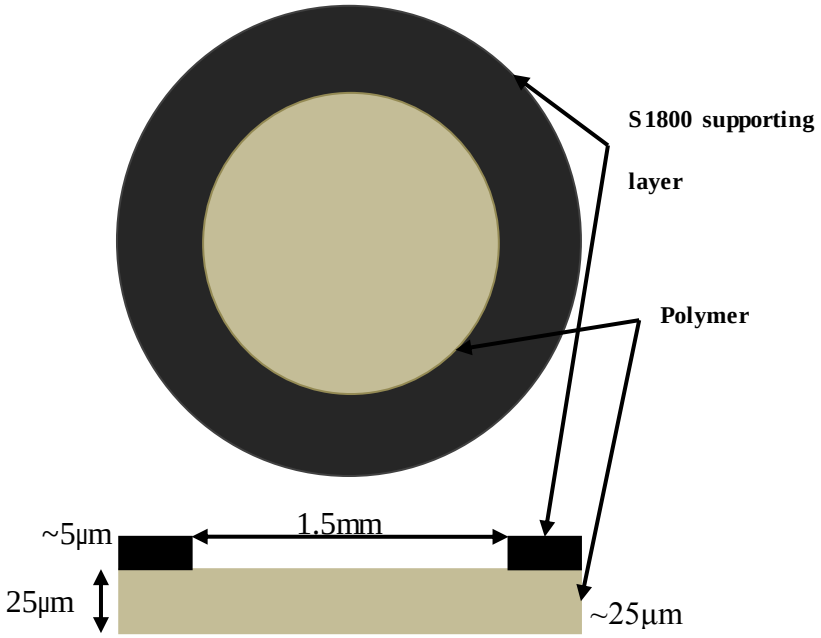

Figure 6.4 Top and side view of patterned structure onto 25µm polyimide film to create a supporting layer of the cantilever. The black ring shows the S1800 photoresist used as a supporting layer while the grey circle indicates the polyimide substrate.

S1800 photoresist was patterned on top of polymer film (Kapton Co. Ltd.) to form circular ring structures by spin coating (shown in Figure 6.4). The polyimide film will form the cantilever after laser processing. S1800 was used as an intermediate supporting layer, providing an nm flat surface for laser bonding between the optical fibre ferrule and polyimide substrate. The patterning steps follow the standard photolithography processes (shown in Figure 6.5), and can easily produce lots of similar patterns simultaneously. The resulting pattern had a maximum depth of 4~5µm determined by the characteristic of S1800. A layer of positive photoresist was first spin coat onto a cleaned 25µm polyimide substrate.

After spin coating, the sample was taken to an oven and baked at 65˚C for 1minute and then 95˚C for 3minutes. This will form a flat S1800 thin layer onto the polymer substrate. Once spin coating was completed, the sample was covered by a photomask and UV exposure at an intensity of 120mJ/cm^2 for 3 minutes. Then the patterned film was developed and baked again to ensure a stable structure. The final pattern is shown in Figure 6.4, where the intermediate photoresist layer is found to be 5µm. The material

characteristic of photoresist is very important to create a good adhesion between the substrate polymer and itself. A number of materials (SU-8, PMMA) have been tried to meet this requirement. However, most of the materials available have poor adhesion to polyimide substrate and can easily come off in a short period of time. S1800 was the only photoresist available to have good adhesion onto polyimide surface based on the trial experiments.

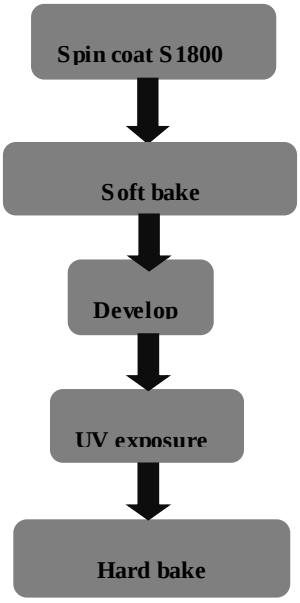

Figure 6.5 Fabrication procedures for preparing the intermediate layer.

The second step is to laser micro-machining cantilever onto the patterned substrate. In order to prepare the sample, the patterned structure is taken to ns-laser machining system and clamped onto a work stage. Optimised laser machining parameters with a repetition rate of 100 kHz, 30 mm/s scanning speed, 10.6W average laser power is used to cut the cantilever. Lower speed and higher laser power produced thermal damage to the machined cantilevers. On the other hand, when increasing the machining speed, the laser was not able to ablate the material. Figure 6.6 shows the cantilever structure after laser processing. The dimension of resulting cantilever is 1.4mm long, ~300μm wide, and 25μm thick. Based on the mechanical characteristic of the cantilever with this dimension, tens of nanometers deflection can be expected from <1N/m surface stress which is a reasonable detection range for most of the micro-cantilever based

biosensors. In this chapter, the fabrication of a single ferrule-top cantilever is discussed, however, demonstrates the potential of mass production.

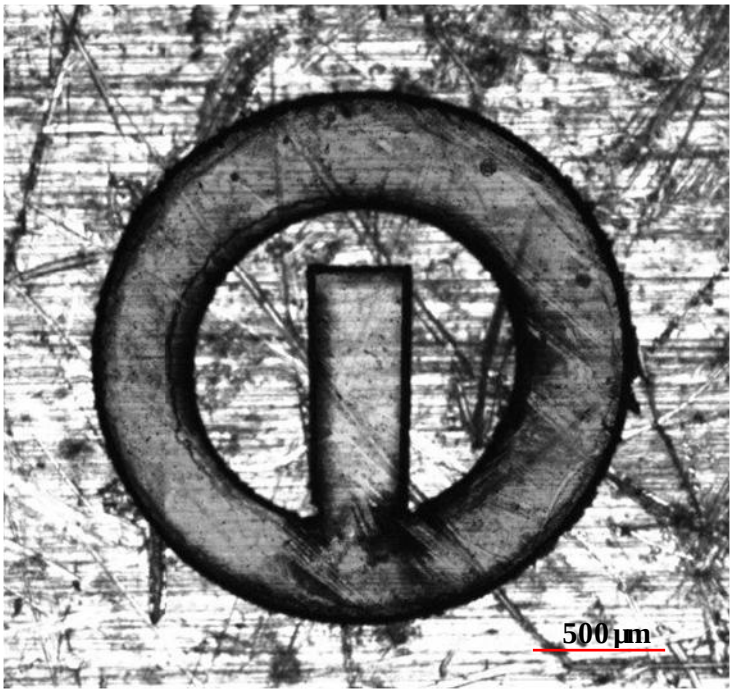

Figure 6.6 Laser machined polymer cantilever viewed under a microscope.

After the cantilever is successfully machined, the surface must be functionalized with different bio-molecules to meet the binding requirement. In terms of different biological applications, cantilever will be either activate or deactivate depending upon the specific analyte. The SAM process is an effective way to bind thiol group (–SH) to a gold coated cantilever surface. The bonding between –SH and gold is so strong that it's possible to develop micro-cantilever sensors functionalized with different biomolecules. The typical procedure normally starts with coating one side of the cantilever with 4nm Cr and then ~20nm Au followed by the SAM process to add activated biomolecules onto the cantilever surface. The other side of cantilever is functionalized with a blocking biomolecule used as an internal reference control. The blocking layer can reduce the error caused by non-specific binding for ferrule-top cantilever biosensor. This is one of the advantages of cantilever based biosensor, since most of other types of biosensor need a second reference sensor to avoid non-specific binding for biological applications. Special care must be taken when dealing with

cantilevers, as it may be contaminated and produce a rough bonding surface, therefore, surface protection and cleaning with nitrogen is necessary to ensure a clean cantilever surface for bonding.

6.2.3 Structure bonding

The bonding process can be divided into two stages. First of all a laser pre-bonding process is used to temporarily attach the cantilever to the ferrule and then post-bonding with epoxy to form a permanent and rugged bond. The combination of pre and post bonding process can provide sufficient bonding strength between the optical fibre ferrule and the polymer cantilever, thus avoid the possibility of epoxy flowing onto the optical fibre facet. The purpose of the bonding is to attach the cantilever structure to the fibre optic FC/PC ferrule firmly. As a result, the sensing probe and readout can be integrated as a single element and both measurement and data transmission can be finished by simply contacting the sensor with the test solution.

The laser pre-bonding process is shown in Figure 6.7. A fibre optic FC/PC ferrule with cantilever structure aligned in position was securely held by an aluminium block. A microscope slide covered the ferrule from the top and was clamped firmly onto the work stage. Using microscope slide allowed the laser beam to be easily transmitted into the bonding resin. The process provided an initial bonding to secure the ferrule-top cantilever sensor and avoid the risk of epoxy adhesive flowing into the cantilever cavity gap. Furthermore, laser bonding is a direct bonding process by fast melting and cooling of the bonding material at a molecular level. Therefore, it's more robust compared with using epoxy.

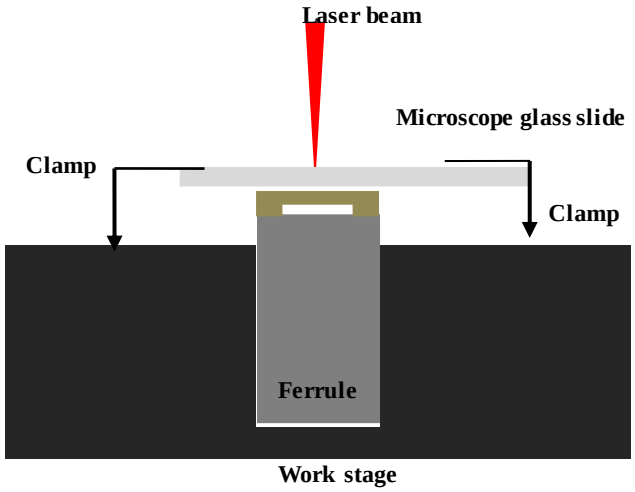

Figure 6.7 Experiment set-up of laser bonding process.

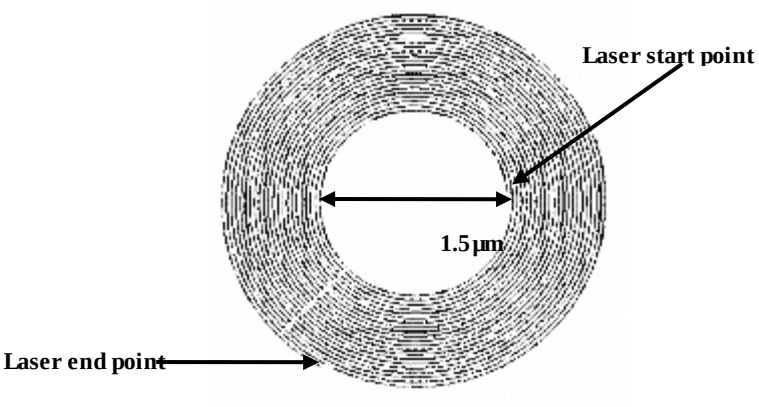

Figure 6.8 Schematic diagram of ns-laser machining pattern used for bonding.

The bonding pattern is programmed by the waver runner software (Utfield Technology) as shown in Figure 6.8. The laser beam with a wavelength of 532nm was started inside the ring pattern and followed the direction of the pattern until it ended at the outside of the ring. An optimal bonding speed of 5mm/s, 100 kHz repetition rate and ~2W of average laser power were used during the experiment to achieve the best bonding strength. A one-step direct bonding process by laser would be ideal, however, the adhesion between the supporting photoresist and the ceramic optical fibre ferrule was not strong enough to provide the bonding strength necessary for sensing application and the sensor has to be further secured by glue applied around the outer circumference of the structure.

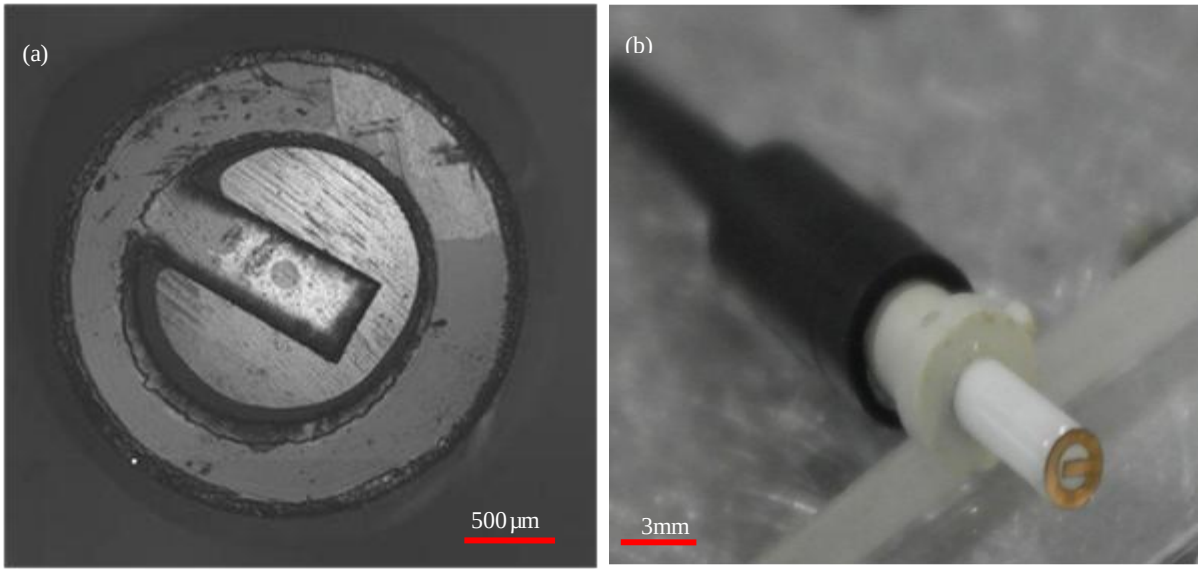

Figure 6.9 (a) Top view of a ferrule-top biosensor under microscope, (b) Fabricated ferrule-top biosensor.

After the laser pre-bonding process, post bonding process by epoxy was used to secure the bonding strength between the ferrule and polymer film. Both machined polyimide cantilever pattern and the optical fibre ferrule were mounted onto the translational stage first. Special care needs to be taken when aligning the centre of ferrule to the tip of the cantilever till fringes can be seen from interrogation system to form a FP cavity. The cavity allows the laser machined cantilever to bend for bio-sensing. By gluing the outside edge of ferrule after the initial laser bonding process, the risk of contamination of the fibre end facet due to the epoxy falling into the gap is avoided.

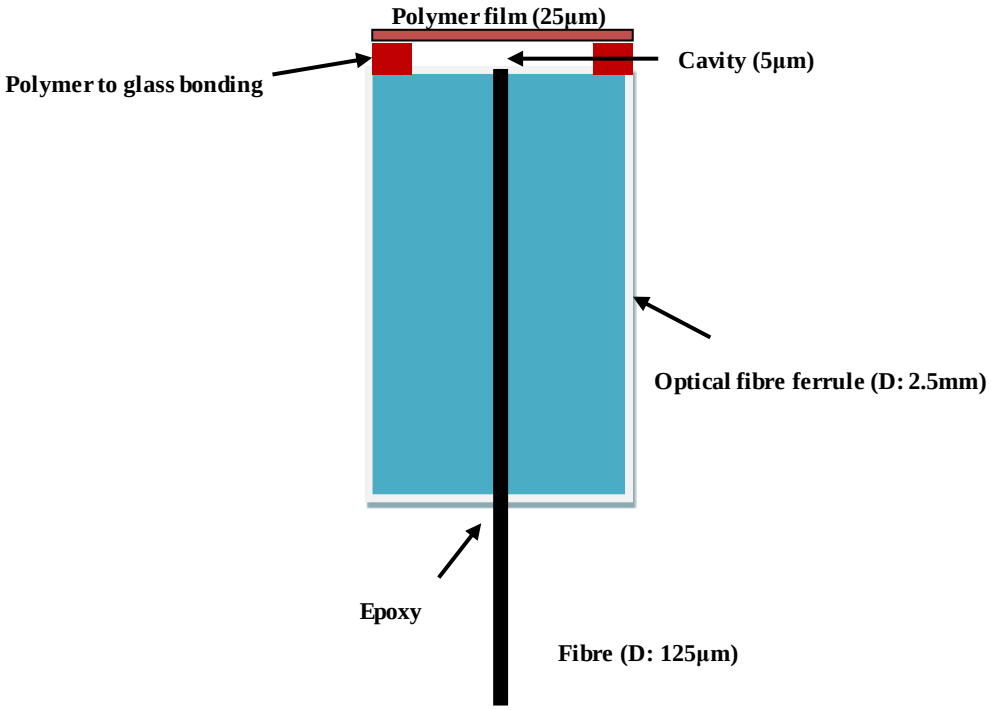

Figure 6.10 Side view of a ferrule-top cantilever biosensor with an optical fibre inserted into the ferrule and glued in place by epoxy.

The side view of a typical ferrule-top cantilever biosensor is shown in Figure 6.10. Interference is formed between the inserted optical fibre end facet and the polymer cantilever. When used for monitoring biological binding due to surface stress changes the cantilever will deflect either upwards or downwards depending upon the particular functionalised coatings and whether they are on the outer or inner surface of the cantilever.

6.3 Syringe pumping system design and biological binding experiment set-up

In order to monitor biotin-streptavidin binding, the reaction is usually observed in a liquid cell at a constant flow. Therefore, it is important to design and manufacture micro-scale fluid pumping system and investigate the behaviour of the fluid at a micro-scale. In the following section, the design of optical fibre cantilever biological sensing system will be discussed. Methods for pumping the solution into the liquid cell and the interaction with micro-cantilever sensor will be investigated.

6.3.1 Liquid cell design

The design of a liquid cell for optical fibre cantilever biosensors is shown in Figure 6.11. The whole block is mounted onto an aluminium base plate, which can be easily attached onto other alignment blocks. Due to the rapid thermal diffusion speed of aluminium, uniform heat dissipation within the whole plate can be quickly achieved. The main body of the reaction cell is made of PTFE, a biocompatible polymer material resistant to the biological solutions under test. A cell is machined into the material, allowing the reaction fluid flow smoothly via the inlet and outlet channels. The volume of the liquid cell is 50μL, enough space for the solution to interact with micro-cantilever surface. A transparent lid seals the reacting cell and ensures a relatively stable environment for biological binding.

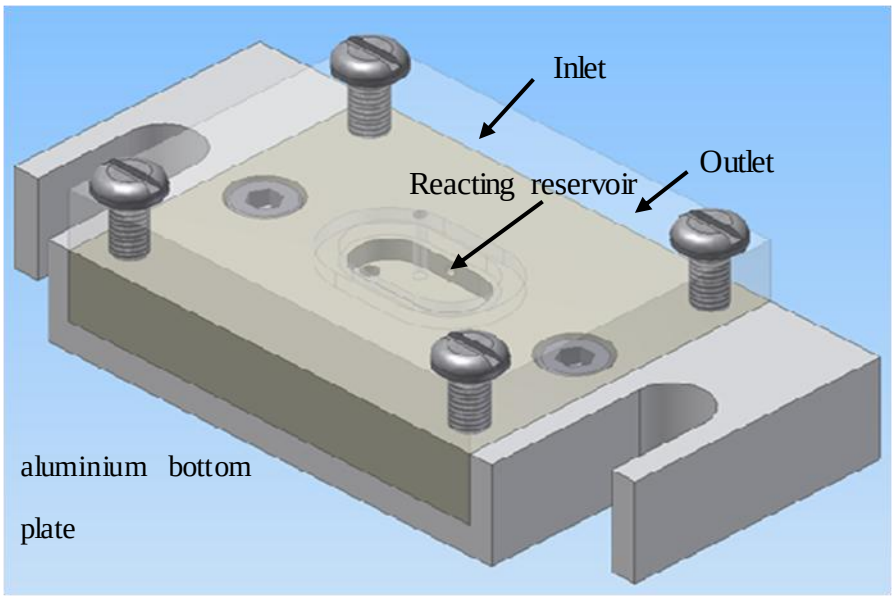

Figure 6.11 Liquid cell design for biological experiments. Ferrule-top cantilever can be dipped into the reacting reservoir from the top.

The design has several advantages. First of all, the size of the whole mount is portable and easy to be removed for other experiments. In addition, the small size of the cell allows biological solution to interact with a micro-cantilever effectively within a small volume. Finally, it's easy to enclose in a temperature controlled environment to minimize the thermal drift of cantilever as well as keep a stable temperature for biological interaction.

6.3.2 Computerised syringe pumping system

Biological reactions usually need a stable environment to keep the reaction going for several hours. In this case, a mechanical pumping system is designed and manufactured which can deliver fluid into the liquid cell at a well-controlled rate and allows the solution to continuously interact with the surface of micro-cantilever sensor. The schematic of system design is shown in Figure 6.12. A syringe with a volume of 10ml is mounted onto a mechanical translation stage. Another block is mounted on top of the translational stage and ensures good contact with the back of syringe. The stage can travel in one axis with a ~μm accuracy. This allows a constant injection fluid speed to pump the solution into the liquid cell. The movement of the translational stage is controlled by a LabView program, and the pumping speed can be optimised via software to minimize the flow turbulence effect on the cantilever deflection.

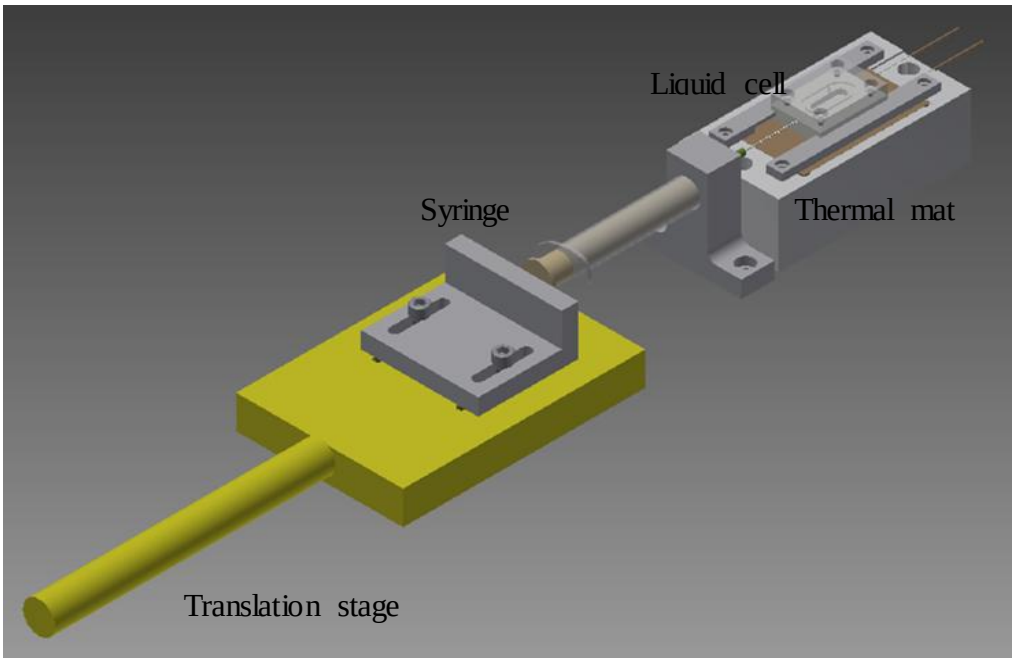

Figure 6.12 Experiment set-up of the syringe pumping system. Solution is injected into the liquid cell via a translation stage pumped syringe.

The tip of the syringe is a needle, which can be inserted into the liquid cell and sealed from the outside. A thermal mat is then attached to the back side of the liquid cell and clamped down to an aluminium block. A temperature controller is employed to control

the temperature with ±0.1˚C accuracy. The cantilever biosensor is then immersed into the liquid cell while the solution is injected into the cell at a slow constant speed.

6.3.3 Experiment set-up

All biological experiments discussed use the same interrogation approach. The experimental set-up for optical fibre cantilever interrogation is shown below, similar to the system described in the previous chapter. Figure 6.13 shows the schematic diagram of a syringe pumping system. The sensor is sealed into a 50μL liquid chamber with a thermocouple placed near the sensor to monitor the chamber temperature and provide feedback to a temperature controller (temperature resolution ±0.1˚C). This allows temperature to be stabilised to ±0.1˚C.

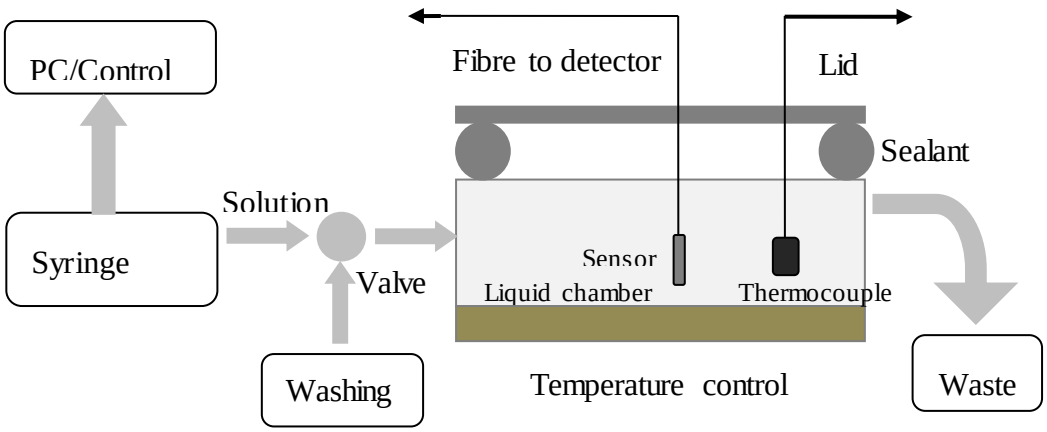

Figure 6.13 Schematic diagram of liquid cell pumping system. Ferrule-top biosensor is immersed into the liquid chamber via a hole though the lid from the top. A thermocouple monitors the temperature in the reaction chamber. An O ring seals the chamber via a plastic lid. The whole liquid cell is temperature controlled by a temperature controller from the bottom. Biological solution is added and an in-let valve can be switched between injecting solution and washing.

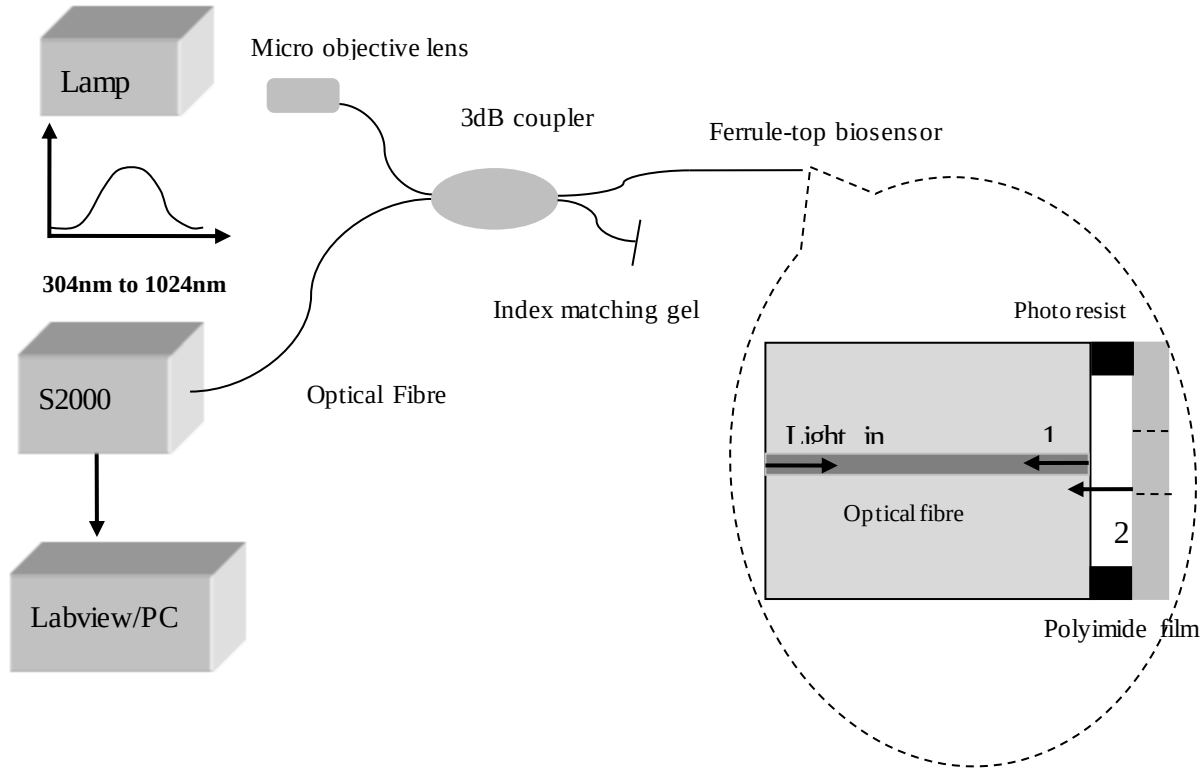

Figure 6.14 Schematic diagram of a ferrule-top biosensor interrogation system. Light from the lamp is coupled into the fibre via a microobjective lens. The reflected light is coupled back via 3dB coupler and processed by S2000 and LabView system. Zoomed in part illustrates the side view of a ferrule-top cantilever. The incident light is reflected by optical fibre end facet 1 and bottom surface of cantilever 2.

In Figure 6.14 the light is coupled to the sensor via a 3dB coupler. A HP780 optical fibre (Thorlab, USA) is inserted into a FC/PC ferrule with an inner diameter of 127μm. The 780nm wavelength region is used due to its higher interrogation phase sensitivity compared with 1550nm. In addition, a high intensity response can be achieved in this wavelength with the light source we used for interrogation. The reflected light is partially reflected at the 1st and 2nd surfaces, whereas 1st refers to fibre end facet and 2nd refers to cantilever surface. When the light is reflected and propagates backwards, these two signals pass through the same fibre coupler and finally, wavelength information is acquired by an S2000 spectrometer. The cavity length L between surface 1and 2 can be calculated by FFT is used to find the frequency peak which determines the cavity length.

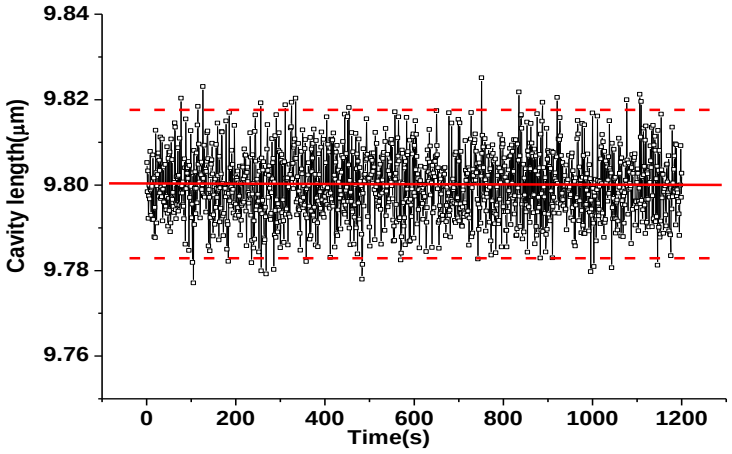

Figure 6.15 Cantilever cavity length versus time

The cavity length over a time of 20mins is recorded and plotted in Figure 6.15. We can see that the maximum cavity length error is ~±25nm and a calculated standard deviation of ±12nm is achieved. The fluctuation is much smaller than reported in previous chapters for cantilever cavity length in a normal air flow environment. We assume that this is because the damping effect is increased in a liquid environment, which makes much more difficult for cantilever to vibrate. On the other hand, the refractive index of solution reduces the visibility of fringes due to the reduction in Fresnel reflectivity. Therefore, the end facet of an optical fibre may require a thin layer of deposited metal to optimise the fringe visibility.

Flow rate and temperature can lead to ambiguous cantilever deflection, and this will affect the overall performance of the sensor. In our case, both sides of cantilever are coated with the same thickness of gold to minimise thermal sensitivity due to differential thermal expansion. The differential coating thickness error for the 15nm range is smaller than 5nm. By using the equation presented in [6.4], temperature induced deflection change is <8nm for 0.5˚C. In this experiment, temperature is controlled within ±0.1˚C, which means the thermal induced deflection is within the noise level. However, the injection of liquid solution can also cause a temporary temperature change and lead to an additional deflection.

To test the effectiveness of liquid flow, solution is injected by syringe pumping at a rate of 2µl/sec into the test chamber. Data in Figure 6.16 inferred that at this rate the monitored cantilever fluctuation is still within the system noise.

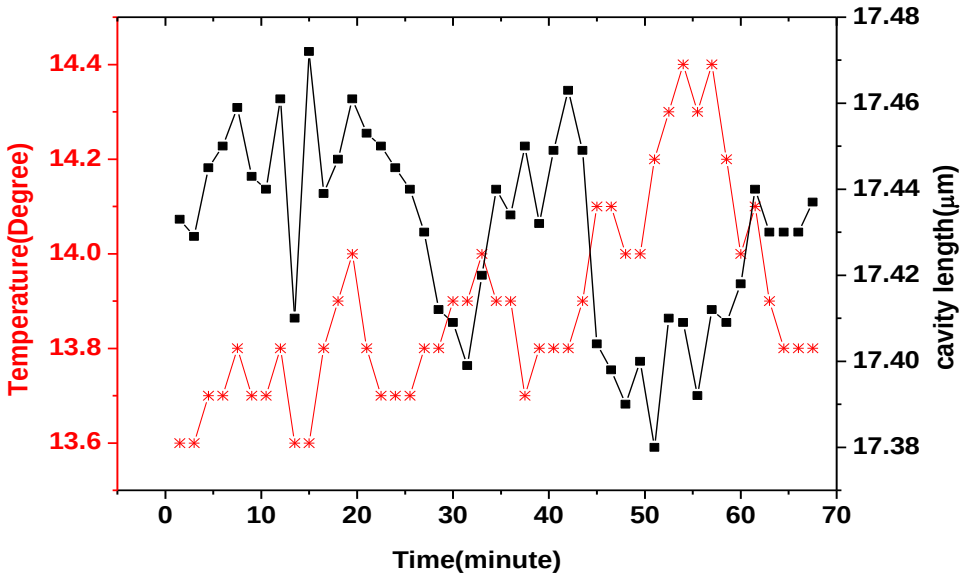

Figure 6.16 Cantilever cavity length change versus temperature change over a measurement period of 70 minutes. The temperature change is shown in red curve while the cavity length change is shown in black curve.

The temperature variation is ~0.8K while the cavity variation is ±40nm with an r.m.s. error of ~28nm. As a result of the low reflectivity produced between the cantilever and the liquid surface, fringes visibility degraded rapidly once the cantilever is immersed in the liquid solution. It is better to inject the liquid at a slow speed and make sure the cantilever is fully immersed into the solution and to avoid bubbles. If any bubbles exist in the fluid, the final interfered signal can be reduced dramatically and multiple cavities can be formed, which will make it difficult to determine the real cavity length. To avoid the bubbles, injection speed needs to be controlled carefully. Usually, lower speed can reduce the vibration effect to the cantilever, however, in this case, it is easier to generate the bubbles. Therefore, a higher injection speed while not causing the cantilever to fluctuate would be necessary (as shown in Chapter 4 for pH sensing).

6.4 Biotin-Streptavidin binding

6.4.1 Introduction to Biotin-Streptavidin interaction

The strong interaction between avidin and biotin was discovered as early as 1941 [6.5]. Avidin is a protein commonly purified from chicken egg white. Biotin is a vitamin found in all cells. Streptavidin is a 60 kDa protein purified from the bacterium *Streptomyces avidinii*. Streptavidin has an extraordinarily high affinity for biotin. One of the most important applications of this binding is the purification or detection of various biomolecules. The strong streptavidin-biotin bond can be used to attach various biomolecules to one another or onto a solid support. Harsh conditions are needed to break the streptavidin-biotin interaction, which often denatures the protein of interest being purified. However, it has been shown that a short incubation (~hours) in water above 70℃ will reversibly break the interaction without denaturing streptavidin, allowing re-use of the streptavidin solid support [6.6].

In this section, the ferrule-top micro-cantilever sensor is designed and fabricated to monitor the surface energy change caused by biotin-streptavidin binding. The use of the sensor opens the route for new drug discovery and disease diagnosis.

6.4.2 Materials preparation

Berger *et al* [6.7] has used this technique to investigate surface stress and kinetics change during SAM processing. This technique is employed here to demonstrate the possibility of using ferrule-top cantilever sensor to monitor surface stress change during SAM process.

The basic SAM functionalization is finished in a fume cupboard environment to allow ventilation during the process. The thiol sample is first weighed via a 4 decimal balance and then dissolved in 100% CH_3CH_2OH solution for SAM processing. The cleaned cantilever is brought to fume cupboard with a small beaker. The SAM process is finished by immersing the cantilever in thiol solution and leaving in a non-oxygen environment for 1-2 hours. The time is sufficient to form a nicely ordered gold-thiol

bond onto the cantilever surface. It is important that during SAM, oxygen is not admitted, since this will seriously reduce the binding between gold and –SH. To avoid the oxygen, the sample can be filled with nitrogen and sealing it afterwards.

To investigate the binding energy during the SAM process, one side of cantilever is functionalized with HDT (hexadecanethiol) and the other side with thiol-PEG (Poly(ethylene glycol) methyl ether thiol) as shown in Figure 6.17. Thiol-PEG is used as a blocking layer to prevent biological reaction on this side of the cantilever. Positive cantilever deflection refers to bend towards the HDT side while negative deflection means bending to thiol-PEG side.

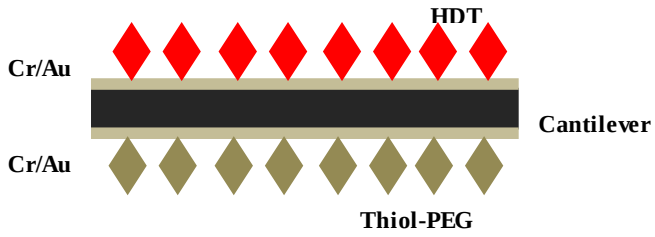

Figure 6.17 Schematic view of functionalized cantilever. Cantilever is first coated with Cr/Au on both sides. HDT and thiol-PEG are functionalized onto top surface and bottom surface of the cantilever respectively.

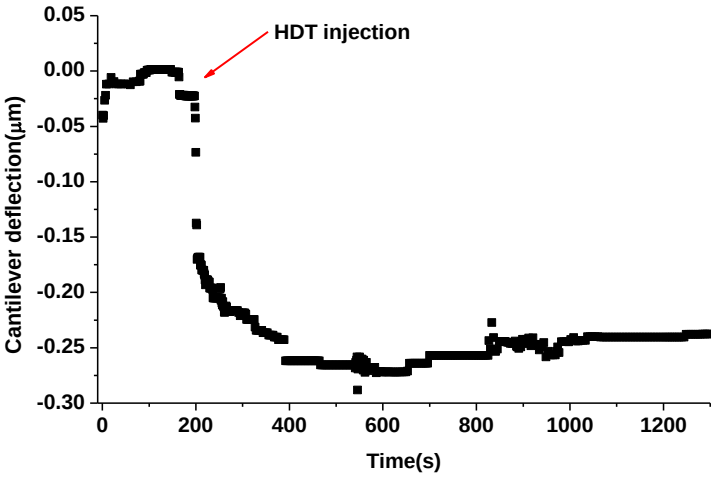

Figure 6.18 Real time monitoring of HDT binding process versus cantilever deflection. HDT is injected at 200 second and the whole process is monitored for ~1000 seconds.

Cantilever deflection derived from the interrogation system in Chapter 4, was measured as a function of time with a HDT concentration of 1mM (shown in Figure 6.18). Internal control was used here, where the other side of cantilever is coated with Cr/Au and functionalized with thiol-PEG. In this case, the injected HDT will only interact with the top Cr/Au surface, while the bottom surface is a blocking layer. The benefit is that both sides are coated with same thickness of Au layer, therefore, deflection due to the bimetallic effect is minimized. Furthermore, the thiol-PEG functionalized side provides a blocking layer that won't react with HDT solution. During the whole experiment, a strong response in cantilever deflection was observed and it saturated 400 seconds after HDT injection. The cantilever bends towards thiol-PEG side corresponding to a compressive surface stress. This indicated that the surface stress on HDT side is larger than the stress on thiol-PEG side.

Based on Stoney's equation (equation 2.8), cantilever deflection can be easily converted to differential surface stress. In our case, the length of the cantilever is 1.4mm, t is 25μm, E is 2.5GPa for polymer, μ is 0.42. From Figure 6.18, the noise level of the system is within ~10nm. This is calculated to be a minimum detectable surface stress of ~4.6mN/m.

The maximum surface stress during this process is calculated to be ~100mN/m, which is in the same level demonstrated in a previous publication [6.7] for thiol chain lengths of 16. The saturation developed on a time scale of ~200s similar to that previously reported for monolayer formation by chemisorption on gold [6.8]. It was clear that after the saturation point, the cantilever deflection almost reached a flat line and no further deflection was found after further injection of HDT. The noise level found in this period was on the same level as before SAM process. It can be inferred that after the saturation, the reaction reaches an equilibrium state, therefore, the differential surface stress.

6.4.3 Experiment and results analysis

To further investigate the binding stress on the cantilever surface, the use of ferrule-top polyimide cantilever to monitor real time binding process between biotin-HPDP and streptavidin is demonstrated. By using the interrogation system mentioned in Chapter 3, the binding process between biotin and streptavidin is monitored and analysed. During the whole experiment, pH is controlled at 7.4 with Phosphate Buffer Solution (PBS) solution. Biotin-HPDP (Thermo Scientific EZ-Link) is pyridyldithiol-activated, sulfhydryl-reactive biotinylation reagent that conjugates via a cleavable disulfide bond to enable use in variety of biological application. One side of the cantilever is functionalized with biotin-HPDP while the other side with thiol-PEG by using the similar SAM process discussed in the previous section. Both sides of cantilever are coated with the same thickness of Cr/Au in order to minimize the temperature induced deflection as we mentioned previously. The aim of thiol-PEG is to block any non-specific binding on the reference side of cantilever. The step is important, since non-specific binding between protein and gold or protein and biotin-HPDP may lead to additional surface stress change, which in turn will contribute additional cantilever deflection. The schematic diagram of functionalized cantilever can be found in Figure 6.19(a). Here we define cantilever bend towards the thiol-PEG side as positive whereas cantilever bend to Streptavidin side as negative.

Figure 6.19(b) showed the real-time cantilever deflection plotted as streptavidin is injected gently to the liquid chamber. The cantilever bends away from biotin functionalized surface. The reaction was rapid after injection of streptavidin.

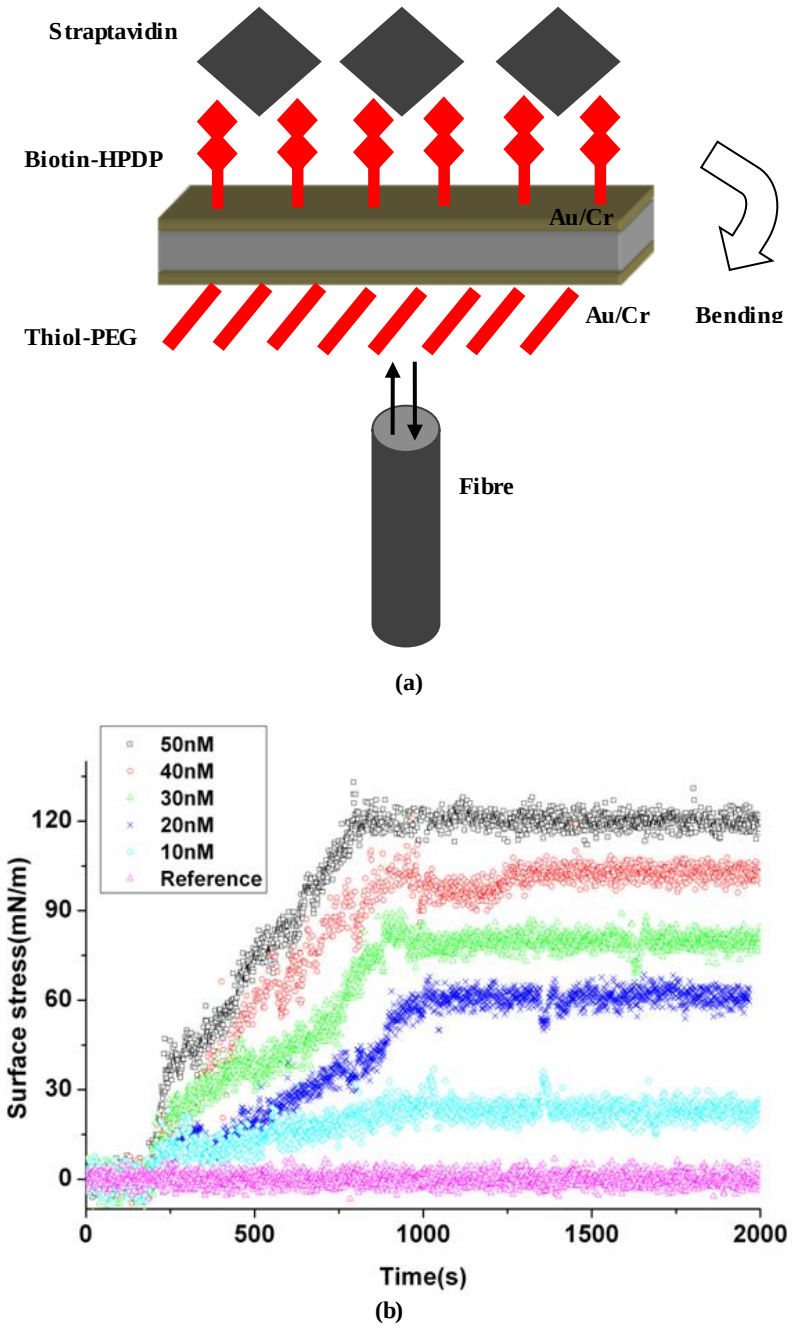

Figure 6.19 (a) Schematic diagram of cantilever structure with biotin-HPDP functionalized onto the top side and thiol-PEG onto the bottom side. (b) Time versus cantilever surface stress change. The response time is roughly ~10 minutes to allow cantilever goes to equilibrium state. With a maximum surface stress ~120mN/m found at 50nM.

Cantilever deflection for streptavidin at a concentration of 10nM, 20nM, 30nM, 40nM and 50nM are monitored. For each case, after injection, the cantilever starts to bend rapidly. A reaction time of approximate 10 minutes was found before the cantilever reaches a steady-state deflection for each case. The minimum binding time of ~10

minutes was found at 50nM concentration. It seemed that the higher the concentration the less time it took to reach the saturation position. This was probably because that as the streptavidin concentration increases then the number of available streptavidin molecules bind to the biotin will increase, thus causing more compressive surface stress. As a result, the differential surface deflection was increased. The cantilever deflection was monitored for another 20 minutes and there was no continuous deflection observed after the saturation. It can be indicated that most of the streptavidin has bonded onto the biotin site and the interaction between each molecule had reached equilibrium, and thus there is no additional differential surface stress applied on the cantilever surface. The sharp edge between the maximum cantilever deflection and the saturation level might due to the differential surface stress change. When the binding reaction reached a balanced point, the surface energy went to equilibrium state, therefore, the deflection fluctuation stayed within the system noise level.

The minimum detectable level of streptavidin is ~10nM, limited by the interrogation resolution. The cantilever deflection of the biosensor at this concentration was just above the noise level of the interrogation system. When reducing the streptavidin concentration, below this level it was hard to detect any deflection.

To test the repeatability, a fresh activated cantilever was used. Under the same experimental condition, cantilever deflection after streptavidin injection versus time was monitored. The deflection was converted by Stoney's equation to the surface stress and plotted in Figure 6.20. After injection of the same concentration of streptavidin, the cantilever started to deflect and reached an equilibrium point in each case. Although the saturation level of cantilever deflection was not the same in each case, the difference between the two is within 15nm based upon the best case we measured. The different saturation may suggest that the geometry of laser micro-machined polymer cantilever is slightly different. Thus the surface stress is not the same for a given deflection by using Stoney's equation. Furthermore, the biological environment and characteristic of streptavidin may also vary, resulting in different surface energy.

The effective reaction time monitored was between 15~20 minutes. This is a reasonable response time for most binding experiments using micro-cantilever transducers as presented in earlier chapters.

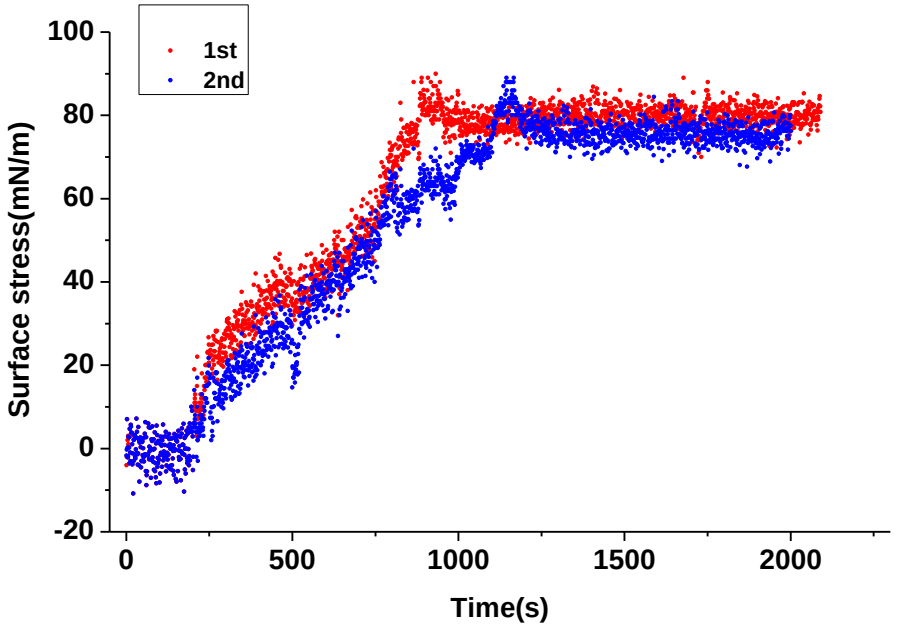

Figure 6.20 Repeat monitoring of surface stress changes versus time at a streptavidin concentration of 30nM.

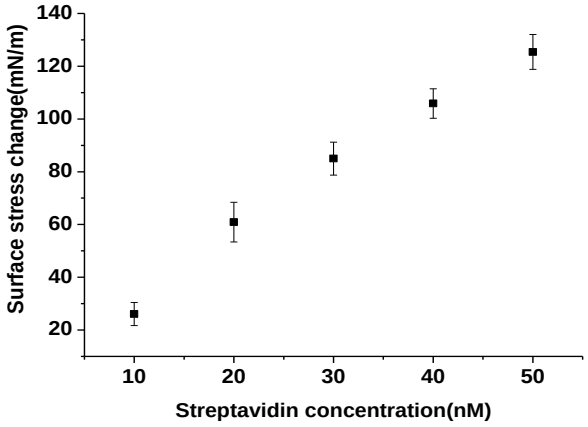

Figure 6.21 Concentration of streptavidin versus cantilever differential surface stress change. When increasing the concentration of streptavidin the surface stress increased accordingly. The minimum detectable surface stress is at 10nM concentration of streptavidin.

The injected streptavidin concentration vs. surface stress change is plotted in Figure 6.21. Starting with the minimum detectable concentration at 10nM and then increasing

to 50nM with 10nM steps. A maximum binding stress of 129.4mN/m between biotin-HPDP and streptavidin was found at a concentration of 50nM. At each concentration, three repeat experiments were carried out in order to identify the saturation level of cantilever deflection. In each case, ~10mN/m surface stress difference was found between each experiment at a fixed concentration. The surface stress increased as the concentration of streptavidin increases, however, at higher concentration, the speed of surface stress change is slower than at lower concentration, and there was a trend for streptavidin to saturate at a higher concentration.

Unlike conventional methods which use a smooth functionalized layer on a gold coated Si/Si_3N_4 cantilever surface, a polyimide cantilever with nanometer surface roughness is used. In this case, the inter-analyte induced deflection will be enhanced [6.9]. The measured stress surface value in our case is therefore larger than the smooth one.

6.4.4 Summary

In this section, a ferrule-top cantilever biosensor was successfully fabricated onto the end of an optical fibre. The sensor combined sensing probe and readout as a single element, thus time-consuming alignment process during use was avoided. The fabrication techniques offer potentially low cost and mass production, which is promising for industrial application.

The use of the ferrule-top polymer cantilever as a biosensor to investigate biotin-streptavidin binding was also demonstrated. A minimum streptavidin detection level of ~10nM was observed. The development of a new generation of micro-cantilever biosensors allowed high sensitivities fast response biological binding with small sample volume and potential offered new route for clinic drug diagnosis.

6.5 Food pathogen detection by micro-cantilever technique

6.5.1 Introduction to traditional methods

The current development of label-free biosensors for new drug discovery, disease diagnostics and the healthcare industry has driven researchers to investigate

miniaturised biosensors that can improve the detection sensitivity and reduce the response time. In this section, a potential application of ferrule-top biosensor as a rapid food pathogen detection device will be investigated and discussed. Different pathogen concentration from 10^4cfu/ml to 10^8cfu/ml (cfu: Colony-Forming Units) are injected into reaction solution and a minimum detectable pathogen concentration of $<10^4$cfu/ml based up on the interrogation system developed in this thesis is demonstrated.

According to the working principles, foodborne pathogen detecting methods can be divided into several main groups, including classical culture methods, bioluminescence, cell counting, immunological methods and nucleic acid-based assays [6.10] etc. These detection methods can be rapid, as the detection time is usually within a day, more convenient (automation), sensitive and specific [6.11].

Traditional food pathogen detection methods are based on particular culture media that can be used to identify, isolate or enumerate viable microorganisms [6.12]. These methods are both qualitative and quantitative; furthermore, they are well established, reliable, sensitive and low cost [6.10]. However, traditional methods usually involve multi-step processes and the preparation is always time-consuming, needing extra labour and special skills [6.13].

A most widely used immunological technique for rapid biodetection is called ELISA (mentioned in Chapter 2), which is based on the specific binding between an antibody and its antigen. An ELISA system basically consists of a primary antibody (also called detection antibody) that was immobilized to a microtitre well, antigen, and a secondary labelled with an enzyme [6.14]. Figure 6.22 below shows four different formats of ELISA. The first one is called direct assay which the antigen is attached to an ELISA well and enzyme is attached to the antigen via primary detection antibody. The second one is indirect assay. In this case, the antigen is attached to an ELISA well and a primary detection antibody bound to the antigen, followed by a labelled secondary detection antibody attached to the primary detection antibody. The third one is called

direct sandwich ELISA which a capture antibody is first attached to an ELISA well and antigen is attached to the capture antibody with a labelled primary detection antibody bind to the antigen. The final one is called indirect sandwich ELISA. The detection processes start by attaching a capture antibody to an ELISA well then bound to an antigen. A labelled secondary detection antibody binds to the antigen via a primary detection antibody. The ELISA technique has played an important role in the area of rapid detection as a well-established method. The detection limitation the ELISA system is usually from 10^3 to 10^5cfu/ml [6.13]. Although the technology is theoretically highly specific binding between antibody and its antigen [6.15], it still need labelling process for detection and this sometimes brings additional error.

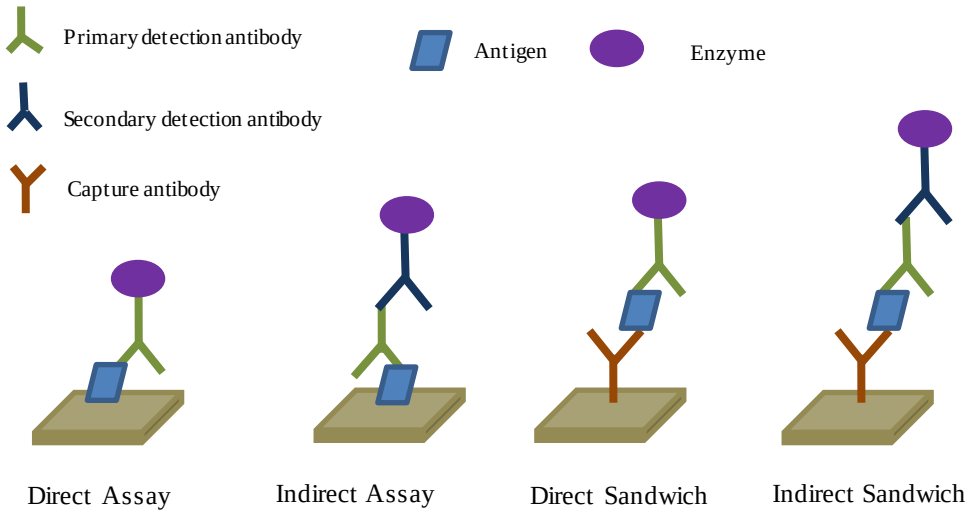

Figure 6.22 Formation of common ELISA detection configuration: Direct Assay, Indirect Assay, Direct Sandwich and Indirect Sandwich.

Polymerase chain reaction (PCR) has been a very popular diagnostic method in the field of pathogen detection over the last 20 years [6.16] and has received much attention because of its potential to be a selective, specific, sensitive and automatic rapid detection method. However, the procedure is often time-consuming, therefore, add the cost to the whole system. With the development of real-time (quantitative) and multiplex PCR [6.17], the method is becoming more cost effective, and powerful, thus is accepted by more and more people.

By transferring surface stress to nanomechanical force, micro-cantilevers based biosensors are capable of monitoring DNA hybridization, conformational changes of DNA [6.18], and antigen-antibody binding in solution [6.19]. Recent experiments using micro-cantilever sensors have demonstrated this label-free approach for pathogen detection with a high sensitivity of 1000cfu/ml pathogen [6.20].

In this section, the ferrule-top cantilever as a practical biosensor will be designed and manufactured for *Listeria innocua* pathogen detection based upon the binding between antibody and antigen. A proof-of-concept experiment collaborated with Dr R Fowler and Miss Y X Zhou in school of life science, Heriot-Watt University has shown the capability of detecting $<10^4$cfu/ml *Listeria innocua* in a buffer solution. Compared with the traditional micro-cantilever, the ferrule-top biosensor can integrate the sensing probe with readout as a single element.

6.5.2 Listeria species and biotinlated antibody

In this thesis, the specific binding of *Listeria innocua* pathogen is investigated. These pathogens can be usually found in food such as fresh and salt water, sewage sludge, and decaying vegetation. Here, a non-pathogenic *L. innocua* strain was used for proof-of-concept binding experiment. Figure 6.23 shows the microscope view of Listeria bacteria with an oil immersion lens on a standard microscope slide. The dimension of the Listeria bacteria is measured to be a few microns, which is much bigger than an antibody (dimension in ~nm).

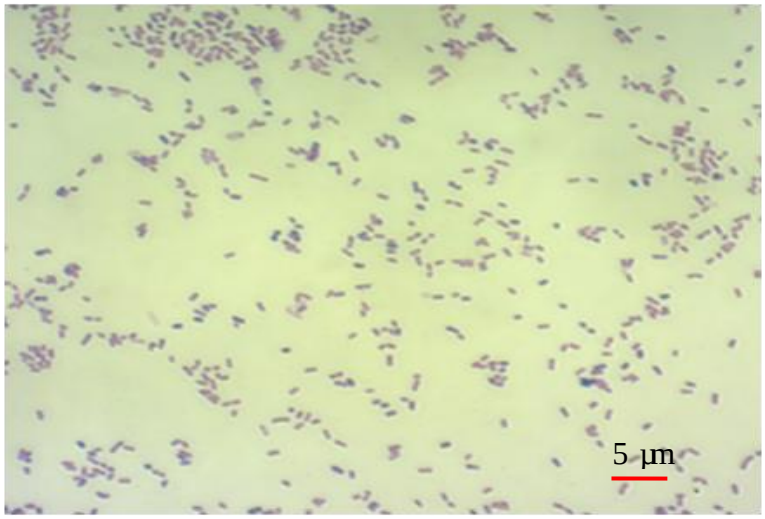

Figure 6.23 Listeria bacteria under microscope with an oil immersion lens.

6.5.3 Materials preparation

Table 6.4 below lists the reagents, media used for the experiment. All the materials are prepared and provided by Miss Y X Zhou, MSc student in the department of life science.

Table 6.4 Reagents, media and broth used for binding experiment

10% Formalin	*1:10 dilution of Formaldehyde Solution*
Blocking Buffer	*1% Bovine Serum Albumin (BSA, Sigma, 1000546947) in TBS*
Coating Buffer	*0.05M Carbonate-Bicarbonate, pH 9.6*
Elution Buffer	*50mM Tris-HCl, 1.4M NaCl*
Phosphate Buffered Saline (PBS)	*Phosphate Buffered Saline (Oxoid, BR0014)*
Sample/conjugate diluent	*1% BSA, 0.5% Tween 20 in TBS*
Stop Solution	*0.18M H_2SO_4*
Tris Buffered Saline (TBS)	*50mM Tris-HCl, 150mM NaCl, pH 7.6*
Wash Solution	*0.5% Tween 20 in TBS*

The *Listeria innocua* strain was purchased from Oxoid. Cultures were established as described by the manufacturer. Biotinylated polyclonal rabbit anti-*L.monocytogenes* antibody (Abcam, product ab20766) and the HRP (horseradish peroxidase) labelled polyclonal rabbit anti-*L. monocytogenes* antibody (Abcam, ab20357) were used as the capture antibody and detection antibody respectively. All media and broth were obtained from Oxoid, and prepared by MSc student Y X Zhou.

The bacterial sample was prepared by inoculated into food sample, adding three *L. innocua* colonies in 5 ml saline and diluting with Maximum Recovery Diluent (MRD) to a series of dilutions down to 10^{-6}. A centrifuged (Micro Centaur, MSE, S99407346) was used to separate bacteria from the solvent.

Cantilevers were first coated with a thin layer of Cr for adhesion and then evaporated with 20nm gold. The selected biotinylated capture antibody was coated onto the cantilevers by self-assembly monolayer process. 100µl of biotinylated capture antibody diluted with coating buffer (0.05M Carbonate-Bicarbonate) was added into a 1.5 ml eppendorf with the gold coated cantilever inside. Then the eppendorf was sealed with parafilm in the fume cupboard and left at room temperature for ~3 hours. After this procedure, the remaining buffer was removed and the cantilever was washed (all wash steps consisted of applying the wash solution 5 times, each was accomplished within 5 minutes along with gentle shaking on a flat surface). Finally, 200µl blocking solution was added into the reaction tube that was incubated at room temperature for ~2 hours, following a cantilever washing process carried out as before.

6.5.4 Pathogen study on functionalized cantilever surface

The purpose of this experiment is to investigate the binding characteristic of biotinylate antibody onto a gold coated polymer cantilever and compare it with the traditional ELISA well. The schematic diagram of an ELISA detection system is shown in Figure 6.24 with all steps finished at room temperature. First of all, biotinylated capture antibody diluted with coating buffer was added into each well and incubated for 1 hour. The ELISA wells were washed following the same washing steps used earlier in this

chapter. After that, blocking solution was added into each well and incubated for 2 hours in order to block the non-specific binding site. The blocking solution was removed and wells were washed. Following the step (2) in Figure 6.24, *L. innocua* suspension was added into the wells with the plate incubated for 1 hour. The bacteria were discarded and wells were washed as before. In step (3) shown in Figure 6.24, 100µl detection antibody labelled with HRP was suspended in conjugate diluent (1:1000 dilution, 1µg/ml) and added into each well then incubated for 1 hour. The remaining detection antibody was removed and wells were washed as before. To detect the specific binding between the detection antibody and captured *L. innocua,* 100µl substrate was added into each well and the plate was incubated for 20 minutes. The reaction was stopped by adding 100 µl stop solution. Optical density of detection antibody was measured using SpectraMax M5 (Molecular Devices, MV02640) by detecting the absorbance of light at 450 nm.

To compare the results with the polymer cantilever, biotinylated capture antibody with different concentrations (0, 4, 10, 20, 50,100µg/ml) were used to coat the wells of 96-well microtitre plate in the coating step. The well that had been incubated with coating buffer was used as a negative control.

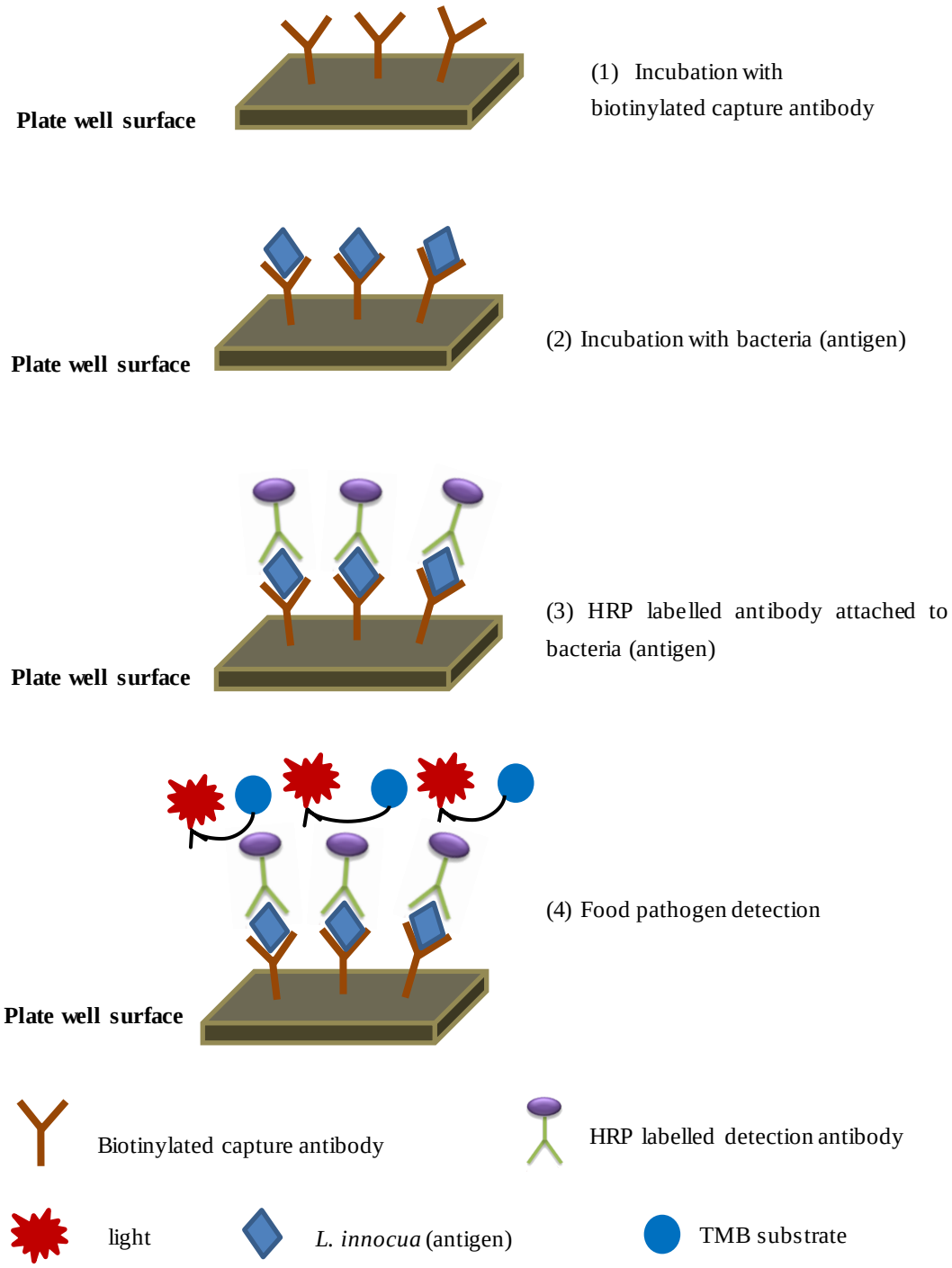

Figure 6.24 Schematic diagram of food pathogen detection by using ELISA system. (1) Biotinylated capture antibody is incubated onto the ELISA well. (2) Bacteria antigen binds to the capture antibody via incubation. (3) HRP labelled antibody binds to bacteria (antigen). (4) *L. innocua* pathogen detection process.

The optical density (Absorbance) change versus the captured antibody concentration in both ELISA system and the cantilever based system was tested and the results are

shown in Figure 6.25. It is obvious that the optical absorbance of ELISA was much higher than that of the cantilevers, especially after the concentration had reached 10μg/ml. This is due to the different surface area between an ELISA plate well and the cantilever. More antibodies are captured by the ELISA surface than a cantilever surface due to the larger surface areas.

The optical absorbance increased as the concentration of the capture antibody increased for an ELISA system and a shape increase was found between the concentration of 4 and 10μg/ml. Then the rising speed slowed above 10μg/ml, which indicated a saturation was about to be achieved due to the binding between antibodies and antigens. On the other hand, the optical absorbance of the cantilever based system reached a peak position with a capture antibody concentration of 10μg/ml. Optical density dropped as the concentration increased over 10μg/ml. It might due to that cantilever has a much smaller surface area (~1mm×~300μm) compared with an ELISA well, therefore, the occupied space between each capture antibody on the cantilever surface are so close to each other that can prevent further chemical reaction between antibodies and pathogens in the solution, reducing the detection sensitivity.

It was also observed that the fluctuation of optical density was quite small between 20 and 100μg/ml for both of the cantilever and ELISA surfaces. The concentration of 4μg/ml was recommended by the manufacturer for this particular antibody, while the results of this experiment suggested that a concentration of 10μg/ml can be more sensitive.

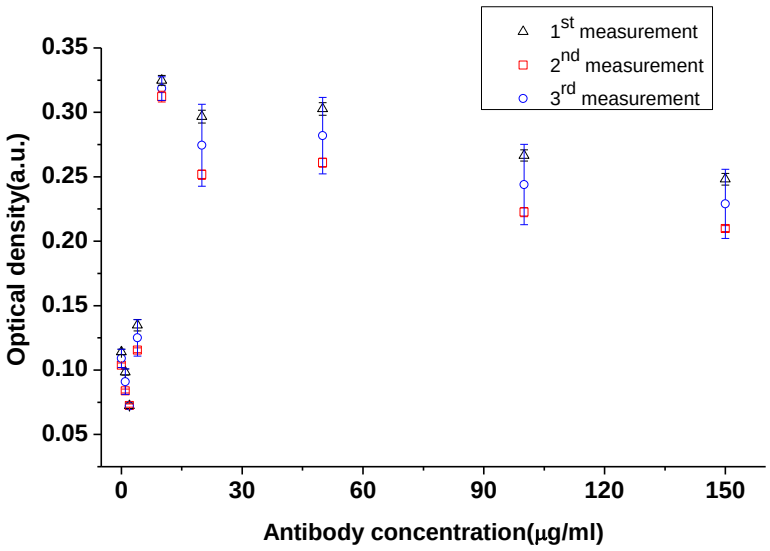

(a)

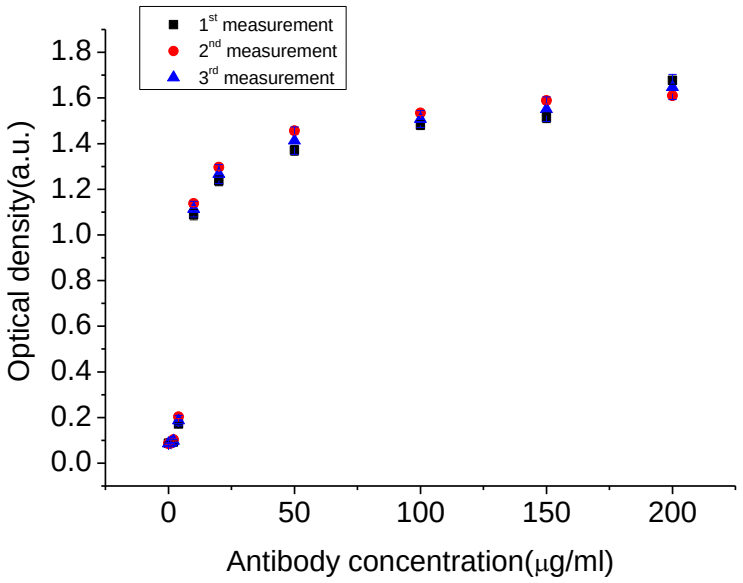

(b)

Figure 6.25 Measurement results of optical density (absorbance) versus the concentration of capture antibody solution for cantilever experiment (a) and ELISA system (b).

6.5.5 Cantilever pathogen detection

To detect pure culture of *L. innocua*, a ferrule-top biosensor coated with capture antibody by self-assembling with 50μg/ml capture antibody solution was placed in the chamber. 50μg/ml concentration rather than 10μg/ml was used because the sensitivity was more stable in this region as can be seen from Figure 6.25(a). A bacterial sample with the concentration of 10^4cfu/ml, which had been fixed with 10% formalin was

tested following the steps described above. The schematic diagram of the functionalized cantilever was shown in Figure 6.26, where the top side of the cantilever was functionalized with active antibody while the back side of the cantilever was functionalized with de-activated antibody to prevent non-specific binding during the experiment. Therefore, specific binding between pathogen and capture antibody will only happen on the top surface of the cantilever.

A ferrule-top biosensor was placed inside a liquid chamber with a volume of around ~50µl in which the deflection of the cantilever was monitored. A blocking buffer was injected into the chamber to ensure the blocking of non-specific binding sites. As the cantilever deflection reached a steady-state after about 10 minutes, the sample with *L. innocua* was injected into the chamber. The deflection cantilever was monitored until another equilibrium position was achieved. The temperature of this experiment was controlled by a commercial available temperature controller with a temperature resolution of ±0.1˚C. The whole experimental set-up is covered with foam and filled with insulation materials to minimise heat dissipation.

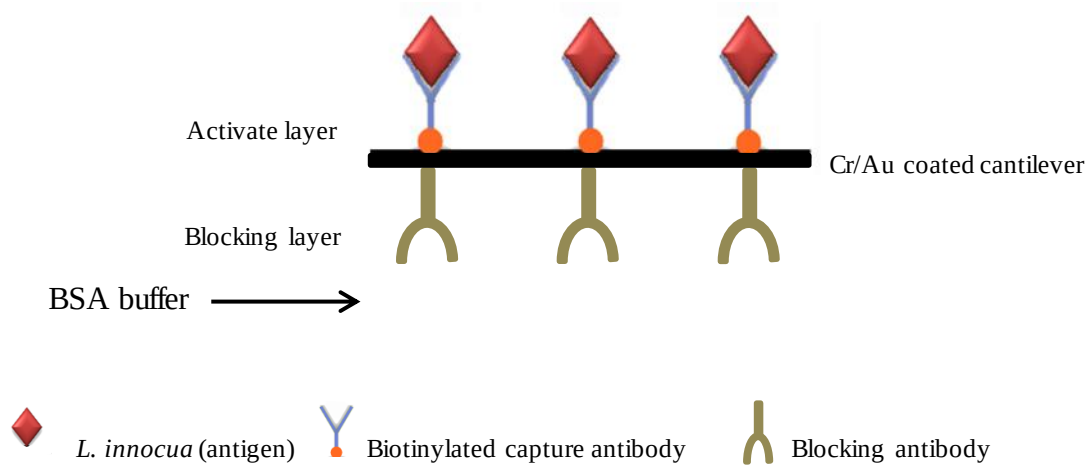

Figure 6.26 Schematic diagram of binding structure for pathogen detection. The cantilever is coated with Cr/Au on both sides. The top side of the cantilever is activated with biotinylated antibody while the bottom side is functionalized with blocking antibody.

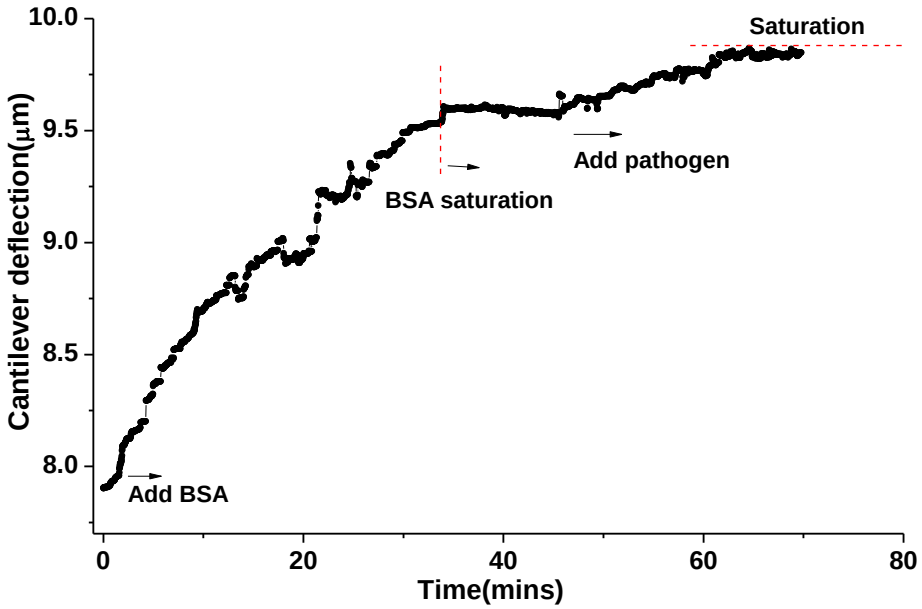

(a)

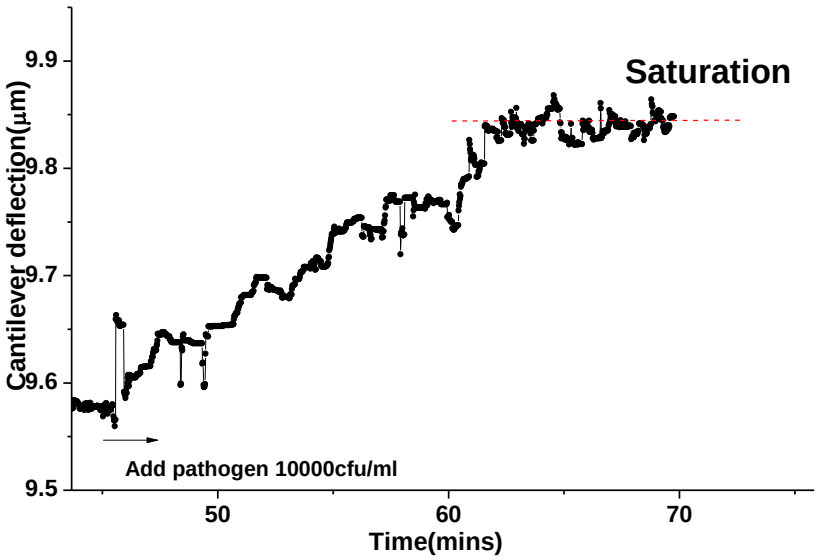

(b)

Figure 6.27 (a) Real time detection of pathogen at a concentration of 10^4cfu/ml versus cantilever deflection. (b) Zoomed in part shows after injection of pathogen. The deflection noise level is ~20nm after saturation.

First of all, BSA was injected gently into the chamber at a constant speed of 10 μL/min. Lower speeds reduced flow turbulence during injection and allowed a stable measurement environment. Due to non-specific binding, the cantilever first bent upwards, which equaled to a compressive surface stress. After about 40 minutes, it stopped bending and started to saturate. To ensure all biotin was blocked by BSA

solution, we kept injecting BSA for another 10 minutes after saturation. After that, pathogen with a concentration of 10^4cfu/ml was injected. It can be seen from the Figure 6.27(a), the cantilever starts to bend again after ~5 minutes and another equilibrium position was achieved within half an hour. During the whole process, surface stress caused by the interaction of biotin-antibody and pathogen binding was ~50mN/m calculated by Stoney's equation.

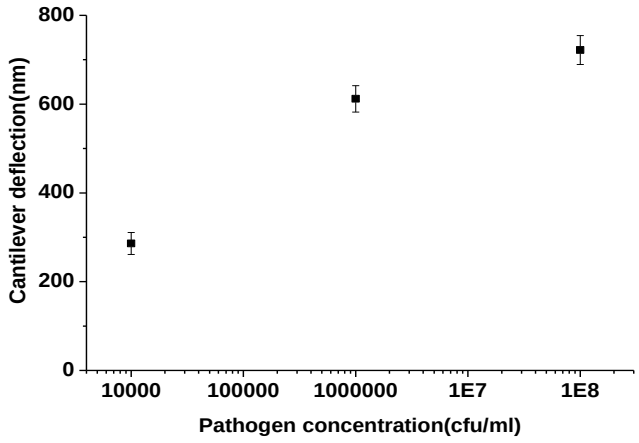

Figure 6.28 Pathogen concentration versus cantilever deflection change at the concentration of 10^4, 10^6, 10^8cfu/ml respectively.

The same experiment was done while increasing the pathogen concentration to 10^6cfu/ml and 10^8cfu/ml. At each pathogen concentration, the cantilever deflection at the equilibrium position was recorded and plotted in Figure 6.28. The fluctuation range after deflection saturation level was used as error bar for each pathogen concentration. It is clear that the maximum cantilever deflection increased as the pathogen concentration increased. At higher pathogen concentration, this trend seemed slow down. The size of pathogen is much larger than antibody which indicates that the interaction between adjacent pathogen will yield repulsive force and generate compressive surface-stress at the top side of sensing cantilever. As a result, cantilever will bend downward.

6.6 Discussion

The main purpose of this chapter is to demonstrate the possibility of using ferrule-top biosensors to monitor biological binding processes. First of all, real time binding between biotin-streptavidin and antibody-antigen was monitored successfully by ferrule-top cantilever sensors. The technique is also useful as a rapid detection method for small volume sample identification. Based on the experiment results, the ferrule-top biosensor had demonstrated a minimum detection concentration of ~10^4cfu/ml pathogen. The resolution of the system is calculated to be ~10^3cfu/ml by using the interrogation system developed in this thesis (discussed in Chapter 3). However, higher sensitivity can be achieved by machining thinner cantilever or using a second reference cantilever to reduce the background noise. Based on the experiment results, the ferrule-top biosensor seemed to be a more rapid detection method than the ELISA technique reported from previous papers. The sensor was capable of detecting the real time binding process between biotinylated antibodies and pathogens in sample after 24 hours incubation (enrichment) within one hour; while on the other hand, the results have to be carried out in approximately one day by using ELISA technique.

The ferrule-top biosensor has a few advantages over the traditional ELISA. First of all, the approach is label-free, therefore, reduces the preparation time for labelling. In addition, the test volume required for the ferrule-top biosensor is smaller compared with an ELISA well and antibody can be functionalized onto the cantilever surface without any capture antibody required in an ELISA detection system. Therefore, the material cost of the system can be greatly reduced. From biological point of view, the mechanical sensitivity of the cantilever might be further improved by optimizing the position/orientation of antibodies bound onto the cantilever surface. As a result, bacteria repel each other more and thus generate more surface stress.

The ferrule-top biosensor has demonstrated the potential to be more sensitive, cheaper and faster compared with the ELISA technique. Furthermore, it can also be applied for simultaneous detection of foodborne pathogens by using cantilever array (each of them

can be coated with different antibodies) for a single measurement to improve the sensitivity. Finally, the sensor can monitor the dynamic process of a biochemical reaction. This will potentially benefit the real time foodborne pathogens detection in the future.

6.7 Conclusion

In this chapter, a ferrule-top cantilever biosensor was successfully fabricated onto the end of a standard optical fibre. The sensor combines sensing probe and readout as a single element, thus there is no involvement with time-consuming alignment process. The fabrication techniques offer potentially low cost and mass production, which is promising for industrial application.

After fabrication, the use of the sensor for biotin-streptavidin binding has been investigated. A minimum detection level of ~10nM of streptavidin was achieved. Furthermore, the use of the cantilever biosensor for food pathogen detection has been demonstrated. Food pathogen level of 10^4cfu/ml was successfully detected in real-time within 30 minutes, with a sample volume of ~50μL. The demonstration of the ferrule-top cantilever allows the development of a new generation of micro-cantilever biosensors with even higher sensitivities (10^4cfu/ml) based upon the resolution of our interrogation system developed in this thesis. The ferrule-top cantilever biosensor will also open the new route to transfer micro-cantilever based sensor to the clinic with a potentially low-cost fabrication process.

Reference

[6.1] P C Weber, D H Ohlendorf, J J Wendoloski and F R Salemme, "Structural origins of high-affinity biotin binding to streptavidin", *Science*, vol.243, pp.85-88 , 1989.

[6.2] K M Hansen and T Thundat, "Microcantilever biosensors", *Methods*, vol.37, pp.57-64, 2005.

[6.3] W M Shu, E D Laue and A A Seshia, "Investigation of biotin–streptavidin binding interactions using microcantilever sensors", *Biosensors and Bioelectronics,* vol.22, pp.2003–2009, 2007.

[6.4] W H Chu, M Mehregany and R L Mullen, " Analysis of tip deflection and force of a bimetallic cantilever microactuator", *Journal of Micromechanics and Microengineering,* vol. 3, pp.4-7, 1993.

[6.5] P Gygy, C S Rose, R E Eakin, E E Snell and R J Williams, "Egg-white injury as the result of nonabsorption or inactivation of biotin", *Science,* vol.93, pp.477-478, 1941.

[6.6] A Holmberg, A Blomstergren, O Nord, M Lukacs, J Lundeberg and M Uhlén "The biotin-streptavidin interaction can be reversibly broken using water at elevated temperatures", *Electrophoresist*, vol.26, pp.501-510, 2005.

[6.7] R Berger, E Delamarche, H P Lang, C Gerber, J K Gimzewski, E Meyer and H J Guntherodt, "Surface Stress in the Self-Assembly of Alkanethiols on Gold", *Science* , vol.276, pp.2021-2024, 1997.

[6.8] R C Thomas, L Sun, and R M Crooks, "Real-Time Measurements of the Gas-Phase Adsorption of n-Alkyl thiol Mono- and Multilayers on Gold", *Langmuir,* vol.7, pp.620-622, 1991.

[6.9] N V Lavrik, M J Sepaniak, and P G Datskos, "Cantilever transducers as a platform for chemical and biological sensors", *Review of Scientific Instrument,* vol.75, pp.2229-2243, 2004.

[6.10] E Boer and R R Beumer, "Methodology for detection and typing of foodborne microorganisms", *International Journal of Food Microbiology,* vol. 50, pp.119-130, 1999.

[6.11] P Feng, "Bacteriological Analytical Manual", 8th Edition, Revision A, 1998.

[6.12] F Ricci, G Volpe, L Micheli and G Palleschi, "A review on novel developments and application of immunosensors in food analysis", *Analytica Chimica Acta,* vol.605, pp.111-129, 2007.

[6.13] P K Mandal, A K Biswas, K Choi and U K Pal, " Methods for rapid detection of foodborne pathogens: an overview", *American Journal of Food Technology,* vol.6, pp.87-102, 2011.

[6.14] S Jadhav, M Bhave and E A Palombo, "Methods used for the detection and subtyping of *Listeria monocytogenes*", *Journal of Microbiological Methods,* vol.88, pp.327-341, 2012.

[6.15] A M Sewell, D W Warburton, A Boville, E F Daley and K Mullen, "The development of an efficient and rapid enzyme linked fluorescent assay method for the detection of Listeria spp. from foods", *International Journal of Food Microbiology,* vol.8, pp.123-129, 2003.

[6.16] O Lazcka, F J D Campo and F X Muñoz, "Pathogen detection: A perspective of traditional methods and biosensors", *Biosensors and Bioelectronics,* vol.22, pp.1205-1217, 2006.

[6.17] S Jadhav, M Bhave and E A Palombo, "Methods used for the detection and subtyping of *Listeria monocytogenes*", *Journal of Microbiological Methods,* vol.88, pp.327-341, 2012.

[6.18] W M Shu, D S Liu, M Watari, C K Riener, T Strunz, M E Welland, S Balasubramanian, and R A McKendry, "DNA Molecular Motor Driven Micromechanical Cantilever Arrays", *Journal of American Chemistry Society,* vol.127, pp.17054-17060, 2005.

[6.19] G H Wu, R H Datar, K M Hansen, T Thundat, R J Cote and A Majumdar, "Bioassay of prostate-specific antigen (PSA) using microcantilevers", *Nature Biotechnology* , vol.19, pp.856-860, 2001.

[6.20] H Sharma and R Mutharasan, "Rapid and sensitive immunodetection of Listeria monocytogenes in milk using a novel piezoelectric cantilever sensor", *Biosensors and Bioelectronics,* vol.45, pp.158-162, 2013.

Chapter 7

Optical probe for prostate stiffness detection

In this thesis a technique that can demodulate cantilever deflection with nm resolution has been demonstrated. Both cantilever design and fabrication onto the end and side of a single mode fibre have been investigated. The demonstrated results show the potential of using optical fibre probes in confined spaces. These techniques can be applied to a wide range of applications. As an example of this an interferometric sensor probe that includes a 45˚ polished optical fibre as a key component of the sensor is developed for prostate tissue stiffness measurement. The sensor can offer a much higher sensitivity and resolution with a reduced sensor size compared with devices based upon electrical sensing technology.

7.1 Introduction to prostate stiffness detection

Prostate cancer (PCa) is the most commonly diagnosed cancer in men 0. Like most cancer treatment, early diagnosis increases the survival rate of the patient. Diagnosis of PCa is carried out using four main methods: digital rectal examination (DRE); a prostate-specific antigen (PSA) blood test 0; prostate biopsy, and trans-rectal ultrasound (TRUS) [7.3]. DRE is a convenient but subjective test, where the prostate is palpated using the fingertip. Palpation reveals if the prostate is enlarged, and may also reveal the presence of harder nodules which are indicative of cancer. DRE is highly subjective, and depends strongly on the skill and experience of the medic performing the examination 0. In addition, DRE may only have higher levels of accuracy when PCa is at a more advanced stage, which limits its utility as a tool for early stage PCa detection. A blood test to identify high levels of prostate-specific antigen (PSA) may also be used for diagnosis. Unfortunately the use of the PSA test has been subject to a high rate of false-positive results, leading to unnecessary surgery 0. In addition, some types of cancer may not cause the production of PSA, which further reduces the reliability of the test. If PCa is suspected using either of the recently described

diagnostic methods, a prostate biopsy may be carried out. In this procedure, needles are inserted into the prostate via the perineum and core samples of the gland are removed for analysis. The samples are assessed using the Gleason Grade for tissue quality 0 and following these tests, a patient may be recommended for surgery.

TRUS and TRSE (trans-rectal sonoelastography) are also used to diagnose the extent of PCa and other prostate nodules. In a TRUS examination, a probe is inserted into the rectum which images the prostate via its posterior surface. TRSE adds the measurement of tissue stiffness to the B-mode image captured using TRUS. In most TRSE probes, an inflatable cuff is attached to the protective sheath over the probe. The cuff is inflated and deflated, usually by hand, to compress and release the tissue around the probe. The changes in the image between compression cycles are processed to produce a map of (usually relative) stiffness of the tissue in the prostate.

A key problem with these four common diagnostic methods is low sensitivity and specificity. DRE is unlikely to be able to distinguish small nodules of potentially malignant cancer. In addition, biopsy may miss cancerous regions of the gland altogether, leading to a misleading assessment of the type of cancer present. Failures in these diagnostic tools mean that some men undergo unnecessary prostate surgery.

Inadequacies in the current diagnostic tools for PCa diagnosis have led to the development of a dynamic instrumented palpation (DIP) device to measure prostate stiffness and diagnose PCa type based on the mechanical properties of the tissue. A DIP device palpates the prostate gland at a controlled frequency and allows the dynamic and static behaviour of the tissue to be measured. This allows the measurement of the shear modulus and Young's modulus of the prostate gland, both of which can be used to distinguish different types of PCa and other benign disease.

A DIP device made in this way can be inserted rectally and used to palpate the anterior surface of the prostate gland in a similar manner to current DRE practice. The advantage of the device over DRE is that an absolute measurement of stiffness is given

that can be compared to other measurements of prostate stiffness and used to diagnose more accurately the presence of PCa or other prostate disease such as benign prostate hyperplasia (BPH).

A key requirement for a DIP-based device that can be used *in vivo* to replace DRE is to reduce the risk to the patient. Using an optical fibre based measurement approach will enhance the safety of such a device due to the EMI free operation process. In addition to the conventional electrical gauge, which limits the size and spatial resolution of the device, optical fibre sensor approach has prospect to greatly reduce the probe dimensions.

In this section, a fibre optic diaphragm sensor (the "photonic finger" or "p-finger") is designed and manufactured to evaluate the relative stiffness of simulated prostate tissue. A DIP device was developed with a flexible membrane that is inflated and deflated at a controlled frequency. The device was tested on a model prostate gland with a unilateral stiff inclusion simulating advanced PCa with Dr Steven Hammer and Dr Will Shu at Institute of Mechanical, Energy and Process Engineering, Heriot-Watt University. The relative stiffness of the two sides of the model prostate gland was evaluated by comparing the change in dynamic response of the membrane when it is pressed on sites with and without the simulated PCa tumour.

7.2 Fabrication of the sensor

The fabrication of the sensor can be divided into two steps: forming the body of the sensor from laser cut acrylic layers, and inserting and aligning the optical fibre FP diaphragm sensor.

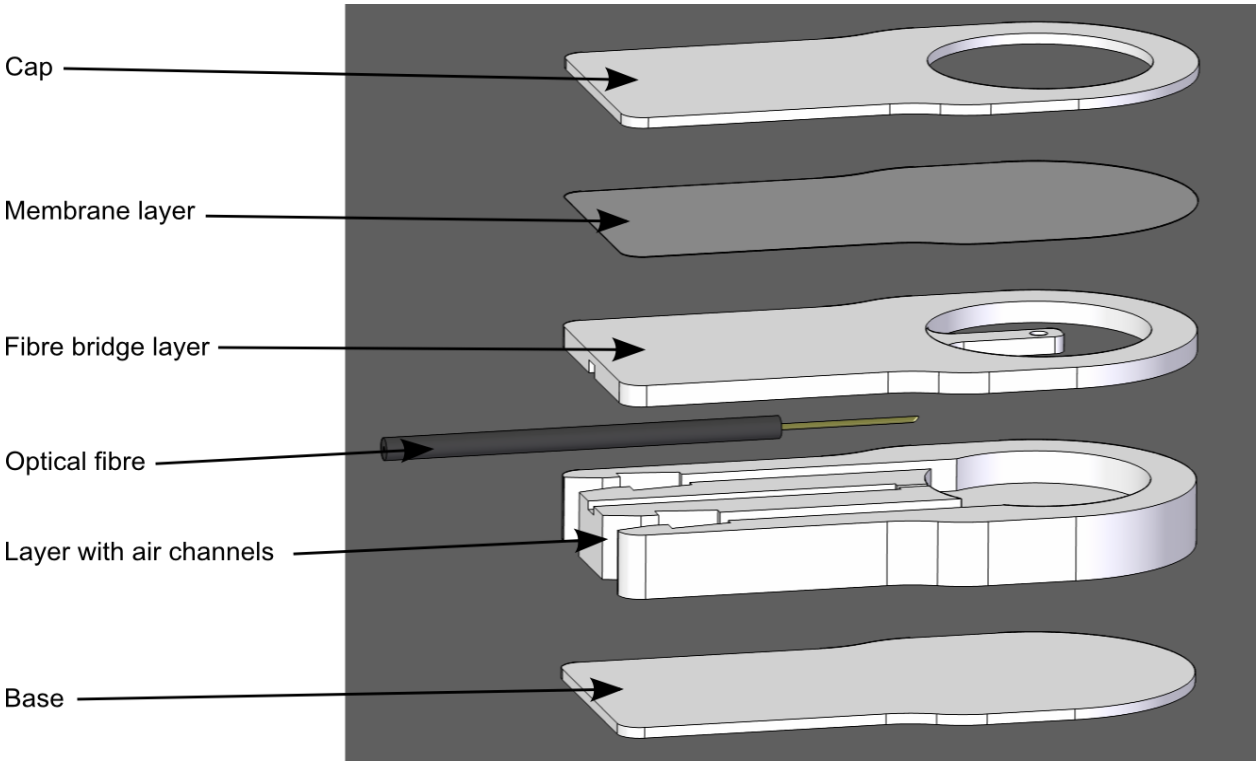

Figure 7.1 An exploded view of the sensor. The air supply tubing and fittings have been omitted for clarity.

The body of the sensor was fabricated from layers of laser-cut acrylic which were held together with contact adhesive (Figure 7.1). The dimensions of the device were 27mm long by 14 mm wide by 5 mm deep. The main layer (labelled the air channel layer in Figure 7.1) of the device was formed from 3 mm thick acrylic sheet. The membrane was held in place by adhesive attached to the cap and the air channel layer, and expands through the 10mm diameter hole in the cap. Cut-outs for bayonet tube connections were formed in the air channel layer. The tube connections were fixed in place using epoxy cement. The air channel layer also has a support channel sized to fit the cladding of the bare optical fibre. The layer above this has a "bridge" with a hole which is aligned with the centre of the membrane. The bridge supports the optical fibre and provides a guide for its insertion and alignment with the membrane centroid. Silicon tubing was fitted on to the tube connections and then used to attach to 1.6mm outer diameter PTFE tubing. The tubing was attached to a syringe which was manually actuated to inflate and deflate the membrane. The system was leak checked before measurement to avoid spurious motion of the membrane due to leakage.

A SMF28 optical fibre was mechanically polished to 45˚ (Figure 7.2) and then inserted to the bridge. By carefully aligning the position of the fibre and monitoring the interferogram, an FP interferometer is formed between the 45˚ fibre tip and membrane. The membrane was formed from a 50 μm thick silicone-based clear plastic film. The optical fibre was placed below the centre of the membrane in a support channel. The centreline of the optical fibre was placed 0.9 mm below the lower surface of the membrane when at rest.

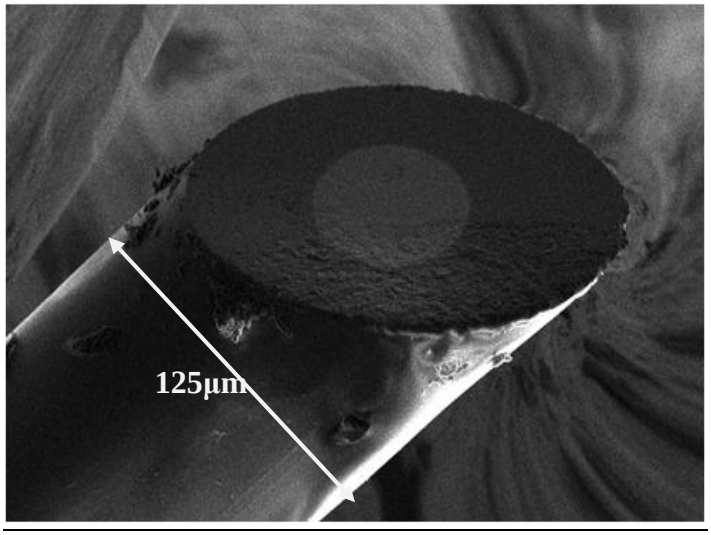

Figure 7.2 45˚mechanical polished single mode optical fibre. The centre part of the fibre is coated with silver.

The optical fibre was bonded into place with cyanoacrylate adhesive after clear fringes are observed indicating good alignment between the fibre and diaphragm.

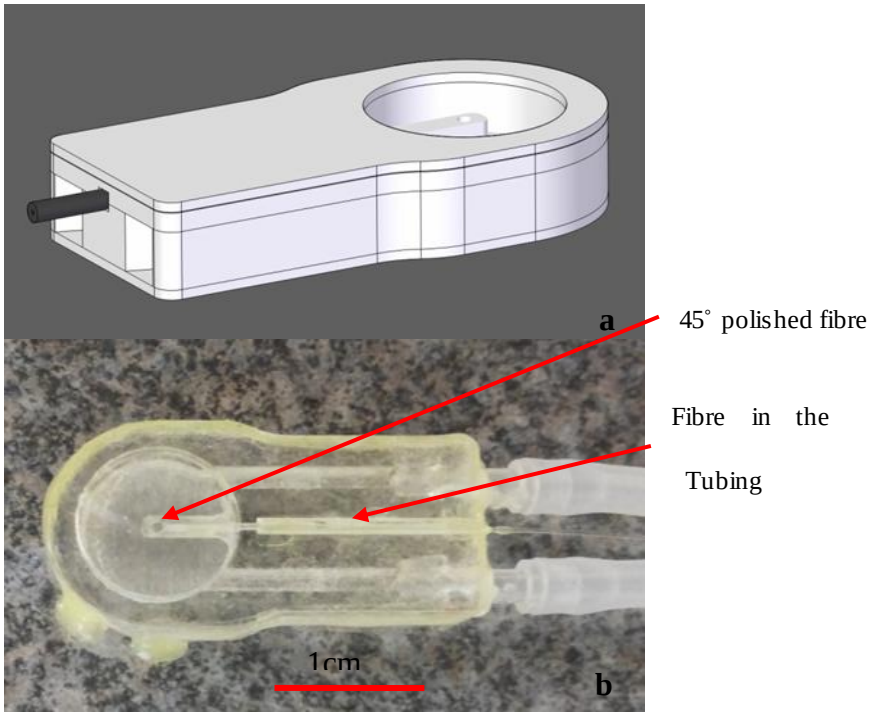

Figure 7.3 A CAD rendering of the sensor (a) and a fabricated sample sensor with optical fibre aligned in the centre of the diaphragm(b).

The optical fibre was bonded into place with cyanoacrylate adhesive after clear (high visibility) fringes are observed in the reflection spectrum. The final sensor assembly is shown in Figure 7.3 (b).

7.3 Sensor principle

The 45˚ polished fibre is employed to allow light to be reflected from the diaphragm, as shown in Figure 7.4. An external FP interferometer is established between the diaphragm and fibre side wall. The 45˚ polished mirror is coated with silver to maximise its reflectivity. The fringes of the diaphragm sensor are shown in Figure 7.5. From this data the cavity length is calculated to be 721µm.

As the diaphragm touches the prostate tissue, stiffness can be converted to the deflection of the diaphragm, thus the monitored cavity length will change accordingly. The cavity length is calculated using the approach described in Chapter 3.

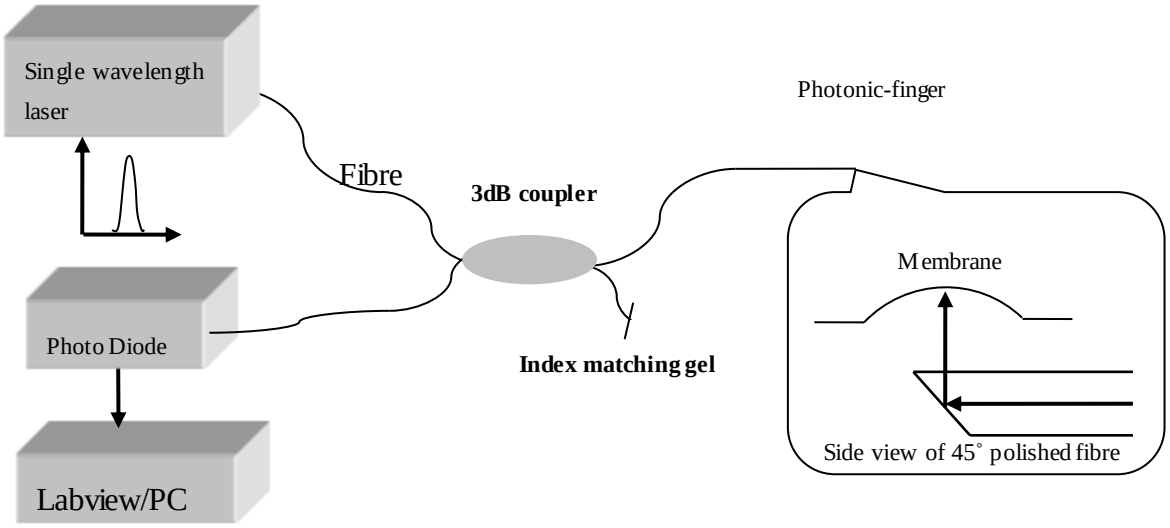

Figure 7.4 Schematic diagram of Photonic-finger interrogation system. The zoomed in part shows the interferometry is create between the 45° polished fibre and the membrane surface.

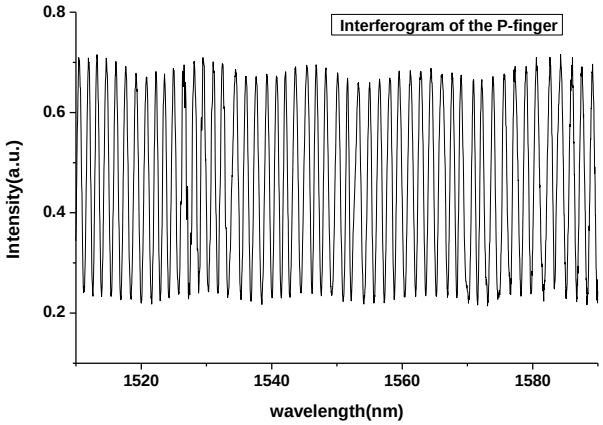

Figure 7.5 A monitored interferogram of the designed P-finger sensor.

The static cavity length fluctuation over 1.5 hours is shown in Figure 7.6 where the calculated r.m.s. error for cavity fluctuation is ±386nm. This larger fluctuation (compared with static cantilevers) is to be expected given the much larger size of the membrane, and may also be susceptible to vibration of the front part of the 45° polished fibre which is only partly supported by the sensor structure. A small vibration of the fibre will lead to the deflection of the tip and causing a measured cavity length change. In addition, thermal induced noise will affect the small deformation of glued hinge which will also add to the cavity length fluctuation. However, the measurement error here is already much smaller compared with an electrical gauge which is usually to be

~ μm. This demonstrates that the sensor is capable of measuring a large dynamic range while maintaining a high spatial resolution, and has the potential to be miniaturised further.

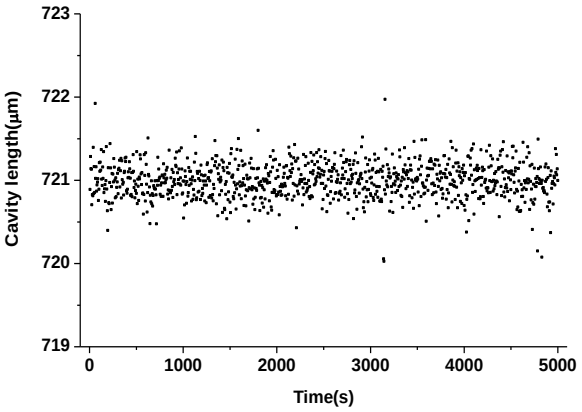

Figure 7.6 Cavity length fluctuations over 90 minutes.

7.4 Experimental results and discussion

7.4.1 Sensor calibration

Calibration aims to test the static performance of sensor under different back pressure. In this way, air leakage can be identified and the deflection of the membrane can be calibrated. For a clamped circular diaphragm with small deflection (less than half of the diaphragm thickness), the peak deflection can be expressed as 0:

$$y_p = \frac{3(1-\mu^2)a^4}{8nEh^3} \tag{7.1}$$

where y_p is the deflection at the central point, μ is Poisson's ratio, E is Young's modulus, n is the refractive index of the air here, a is the radius of diaphragm, and h is the thickness of the diaphragm.

The sensor calibration set-up is shown in Figure 7.7, where a water manometer is used for pressure calibration. One end of the U tube manometer is open to the air while the other end is connected with tubing to the outlet of the sensor. The inlet of the sensor is connected with a syringe by a plastic tube. An optical interrogator SM-125 (Micro

Optics) is used to acquire the reflection spectrum from the sensor and a LabView program is employed to demodulate the wavelength information to cavity length. This can be converted to peak diaphragm deflection by equation 7.1.

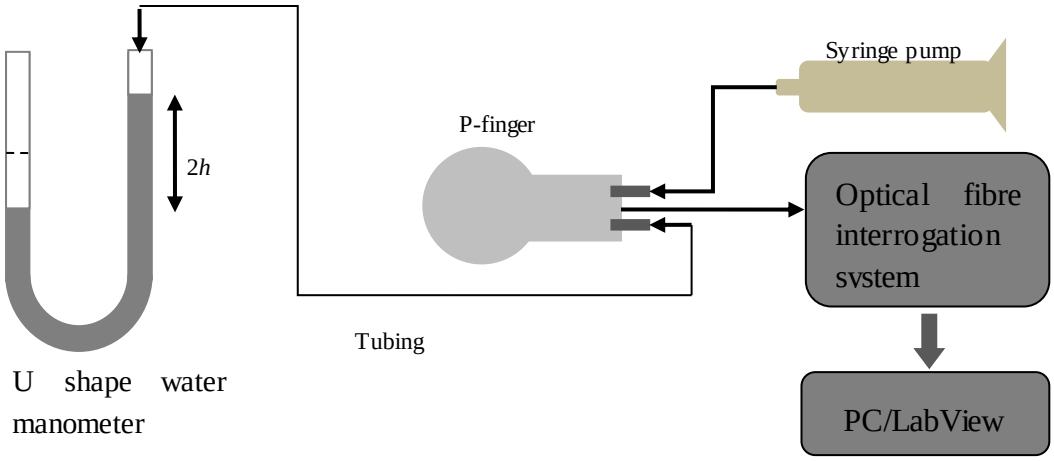

Figure 7.7 Sensor calibration set-up

The pressure inside the membrane actuated by the syringe makes the membrane deflect and this displaces the level of the water in the U-tube. The difference in water height in the manometer is proportional to the pressure difference. By measuring the difference in height, the differential pressure can be calculated. The demodulated peak deflection of the membrane was plotted against the pressure difference between the atmosphere pressure and the syringe pumping pressure in Figure 7.8. Differential pressures between 200 and 900 Pa were monitored. Both a forward cycle with increasing pressure and a reverse cycle with decreasing pressure were tested.

It can be seen from Figure 7.8 that the cycling is nearly linear which matches with theoretical prediction. However, the small deviation from the theoretical line is possibly due to the material characteristic of the diaphragm, or imperfections in the mounting arrangement resulting in deviation from the ideal response.

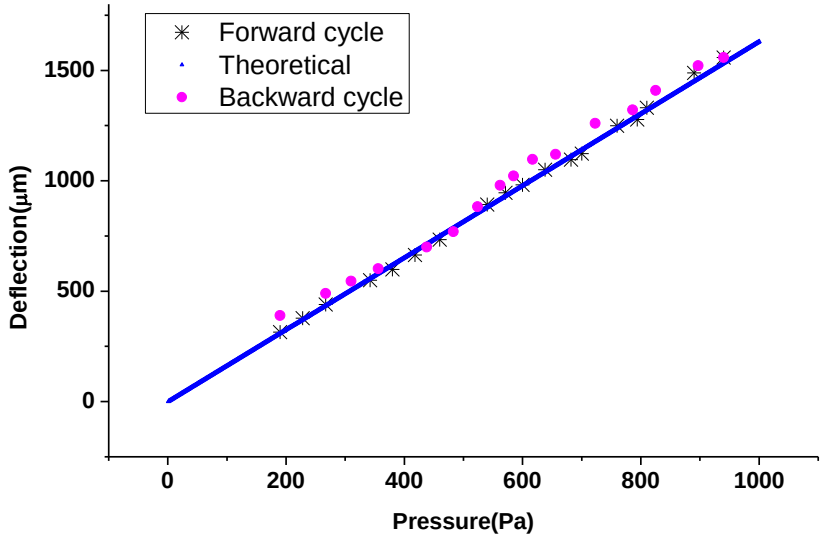

Figure 7.8 The static cycling response of the membrane sensor. Both a forward cycling from low pressure to high pressure and a backward cycling from high pressure to low pressure are carried out.

It can be also seen that a large deflection range of up to 1000 μm with a nearly linear response is achieved under static pressure excitation. Both the forward and backward cycling show that the sensor can operate in a large deflection range while maintaining a linear response. The measured r.m.s. error is <1 μm over a 1000 μm measurement range and it's difficult to be plotted in Figure 7.8.

7.4.2 Dynamic cycling

The aim of dynamic measurement is to test the mechanical response from the simulated prostate tissue by applying a compressive dynamic strain to the sample. This is achieved by modulating the peak deflection of the membrane with a sinusoidal excitation and measuring its response. In the case of dynamic measurement, the sensor operates at a fixed cavity length and a small fraction of deflection excited by the pumping pressure will be detected. A schematic diagram of the dynamic measurement apparatus is shown in Figure 7.9. The P-finger sensor is mounted on top of a three-axis translation stage and the test prostate sample is fixed onto a base plate. The inlet of the sensor is connected to a syringe pumping, which can modulate the pressure inside the sensor dynamically. A single wavelength laser interrogation system is employed here to read out the signals.

A tunable laser based interrogation system is employed for dynamic measurement, with the wavelength selected to be near the quadrature point (the same operation point as used in Chapter 5 for acceleration measurement). The reflected light was then detected by a photo-diode and a LabView PXI A/D platform with a sampling rate of 10MHz and an A/D converter with 12-bit resolution was employed for data acquisition and analysis. In this test the change in pressure are deliberately very small therefore it is sufficient to use one wavelength to interrogate the cavity length and extract the deflection from the measured intensity.

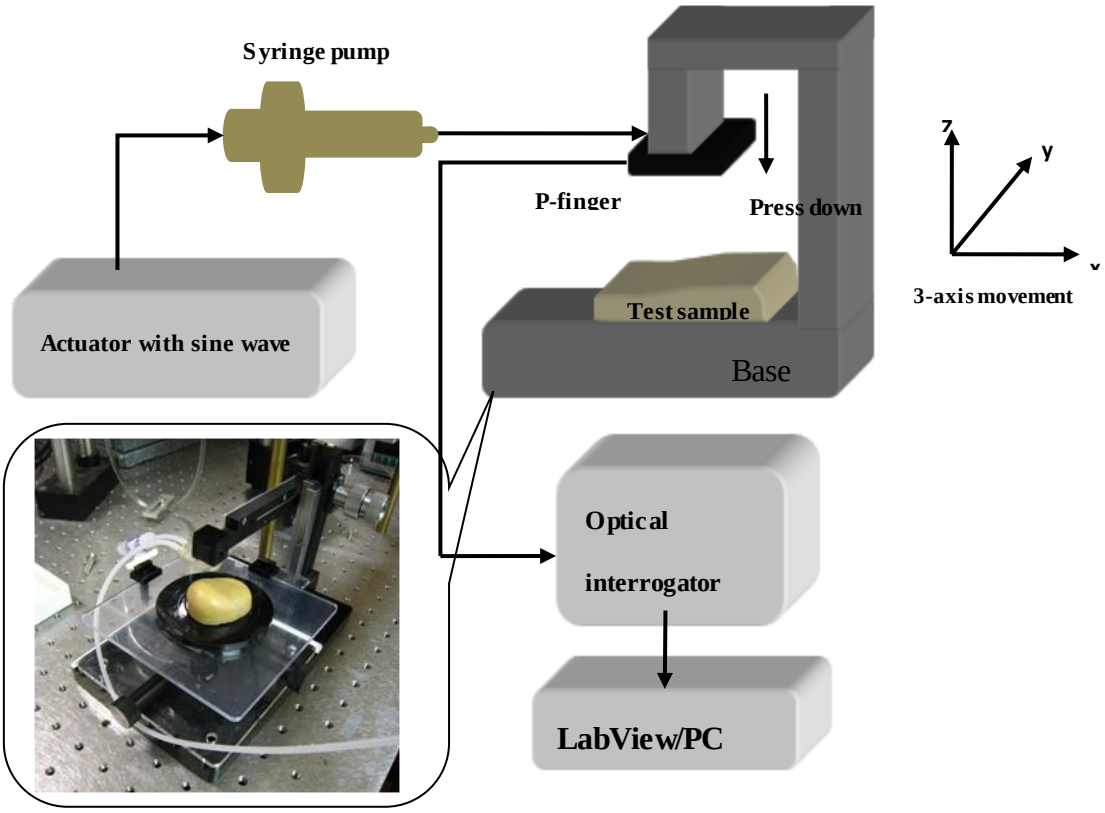

Figure 7.9 Experimental set-up of dynamic test. Zoomed in section showed the rea image of a P-finger sensor attached to the top of the translation stage with a test prostate model set on the based plate. The sensor is connected to a syringe pump to give an actuated signal.

Since the change in pressure is very small, the measured membrane deflection will also be very small. The relation between the deflection change and the interfered fringe change in spectrum domain can be expressed by:

$$\frac{\Delta\lambda}{\lambda} = \frac{\Delta d}{d} \tag{7.2}$$

λ is the laser operation wavelength, d is the absolute cavity length (which here refers to the distance between the polished fibre and the membrane), Δd is the pressure induced deflection change, and $\Delta\lambda$ is the deflection induced fringe shift. In our case, λ is 1532nm, d is ~731 μm, and Δd is normally <1 μm. The deflection induced fringe shift is <2.1nm which is within the linear range of the spectrum if the laser operates near the quadrature point.

In the tests, the model prostate gland is mounted on a three axis linear stage. The sensor is mounted on top of the stage and pressed down to contact the sample. Before measurement begins, the zero pressure position for the membrane must be calibrated. This is achieved by gently pushing the device so the membrane just contacts the surface of the model prostate gland (available from Dr Steven Hammer), and then carefully adjusting the vertical position of the sensor until the output signal from the interrogation system is stable. This ensures that the cavity length between the centre of the membrane and the 45°polished fibre has not changed and there was no additional pressure applied on the sample.

The pressure inside the membrane chamber is dynamically actuated with a sinusoidal pressure wave using a syringe pump. 5Hz, 15Hz and 20Hz sinusoidal signals were used to actuate the syringe pump, thus modulating the deflection of the membrane. Previous work 0 has suggested that actuation frequencies in this range produce a large response from prostate tissue. The reflected deflection after the membrane contacts the model prostate gland is monitored using the tunable laser interrogation system.

Changes in the amplitude and phase relationship of the applied air pressure and measured membrane deflection signals are related to the stiffness of the material being measured. The amplitude of the deflection signal is reduced as the membrane touches the prostate model and will be plotted in the following section. The size of the reduction in deflection is related to the stiffness of the material being touched. In

addition, when the prostate model is touched by the membrane, a phase shift occurs between the applied air pressure and the displacement of the membrane. The phase shift is related to the shear modulus of the material.

7.4.3 Prostate model stiffness test

A typical response of the excited sine signal before and after touching the simulated PCa tissue is shown in Figure 7.10. The response before and after touching the simulated healthy tissue is shown in Figure 7.11.

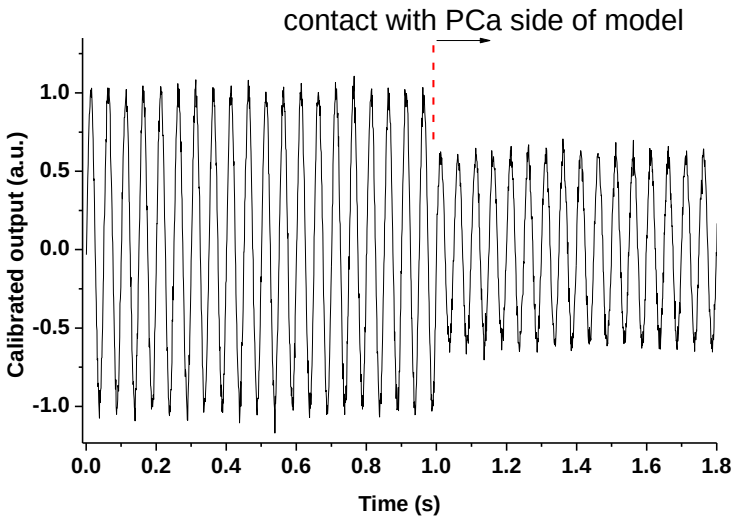

Figure 7.10 The intensity change in the dynamic deflection of the membrane before and after touching the side of the model prostate gland with PCa.

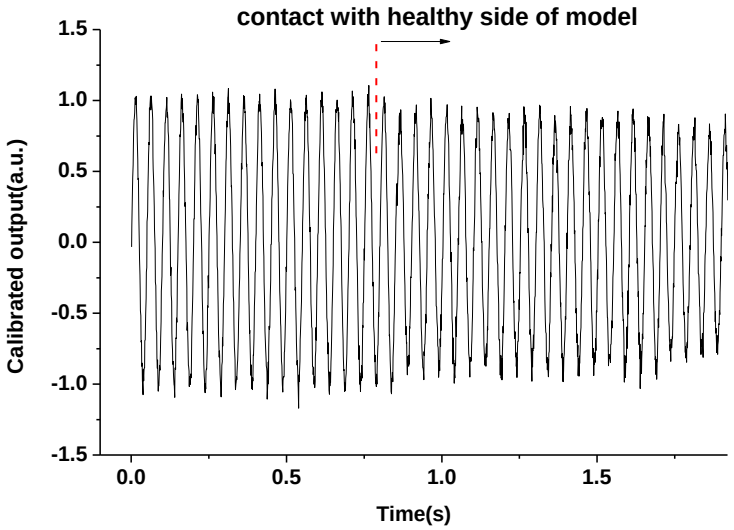

Figure 7.11 The intensity change in the dynamic deflection of the membrane before and after touching the healthy side of the model prostate gland.

On touching the PCa side of the model prostate gland (Figure 7.10), a larger reduction in the amplitude of the measured displacement is observed than when touching the healthy side (Figure 7.11). The larger reduction is due to the increased stiffness of the PCa region of the model, which increases the stiffness of the membrane and PCa region combination, thus reducing the ability of the air supply to inflate the membrane to its unloaded peak displacement.

The dynamic behaviour of different materials may be distinguished using two parameters. The first parameter, amplitude ratio (*AR*), is defined as:

$$AR = \frac{A_{air}}{A_{tissue}} \tag{7.3}$$

Where A_{air} is the membrane deflection in air and A_{tissue} is the membrane deflection in contact with the tissue. Air pressure is measured in Pa and membrane displacement is measured in μm. This is related to the elastic behaviour of the material. The second parameter is the tangent of the phase difference θ between the displacement waveform before and after contacting the tissue and is expressed as $\tan(\theta)$, which is related to the shear modulus of the material. The *AR* and phase difference were calculated from

a 5 seconds portion of the loaded signals. For each measurement, the sensor was held in place on the prostate model and actuated. The dynamic behaviour of real biological materials can vary with the frequency of the applied loading. To test the ability of the probe to distinguish PCa from healthy tissue at different frequencies, it was used to dynamically load the model at 5, 15 and 20Hz. Three positions on each side of the model were chosen, and measurements of membrane displacement at each frequency were made at each position. To distinguish between PCa and healthy tissue, *AR* was plotted against $\tan(\theta)$ as shown in Figure 7.12. Two regions of data emerge, showing a cluster of PCa measurements with low $\tan(\theta)$ and high *AR*, and a cluster of healthy tissue measurements showing high $\tan(\theta)$and low *AR*. In terms of PCa tissue model, it is clear that the most of the data with different actuating frequencies have lower tanθ between 0.17 to 0.23, however, the same measurement results for healthy tissue model have larger spread region. The results indicate that a healthy tissue model contains more elastic component than a PCa tissue model thus a higher tanθ is often found. In terms of amplitude ration, the PCa tissue usually has higher number compared with a healthy one. This is probably due to that PCa tissue is harder and after in contact with P-finger sensor, it might be more difficult to deflect the membrane.

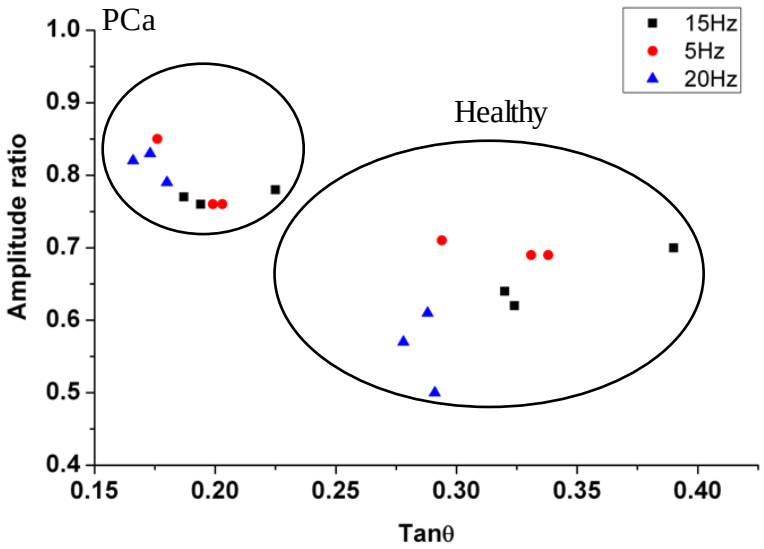

Figure 7.12 PCa may be distinguished from healthy tissue in the prostate model at different actuation frequencies. The plot of amplitude ratio against the tan of the phase difference between the excitation signal and the measured displacement shows distinct clusters of PCa and healthy results.

One limitation of this pilot study is the realism of the reference prostate model used. The model is made from a silicon elastomer molded into a realistic prostate shape. The PCa tumor is made from what appears to be cast polystyrene, which exhibits a weak viscoelastic response. The material composition of a real prostate with PCa is more complex and usually less stiff than in this model. However, the model is designed primarily as a training aid with a long shelf life, meaning that stable materials suitable for long-term use were used in its construction. Further investigation on real prostate tissue would be required to demonstrate the value of the sensor as an aid to diagnosis of PCa.

7.5 Summary and future work

An optical dynamic instrumented palpation sensor for the measurement of tissue stiffness was developed in this section. The sensor consists of a dynamically actuated membrane with a polished optical fibre underneath. A FP interferometer is created between the side of the fibre and the inner surface of the membrane, which gave a displacement r.m.s. accuracy of ±386 nm. The sensor was used to measure the stiffness of a model prostate gland with unilateral prostate cancer, and was able to distinguish simulated prostate cancer from healthy tissue. The relationship between the amplitudes and the phase relationship of the displacement and actuation waveforms were used to distinguish each tissue type.

Reference

[7.1] D M Parkin, F Bray, J Ferlay, and P Pisani, " Global Cancer Statistics", CA *Cancer Journal Clinical*, vol. 55, pp.74-108, 2005.

[7.2] U H Stenman, J Leinonen, W M Zhang and P Finne, "Prostate specific antigen", *Seminars in Cancer Biology* , vol. 9, pp.83-93, 1999.

[7.3] T Loch, I Leuschner, C Genberg, K W Jacobsen, F Küppers, E Yfantis, M Evans, V Tsarev and M Stöckle, "Artificial neural network analysis (ANNA) of prostatic transrectal ultrasound", *The Prostate* , vol. 39, pp.198–204, 1999.

[7.4] L A Baumgart, G J Gerling and E J Bass, "Characterizing the range of simulated prostate abnormalities palpable by digital rectal examination" , *Cancer Epidemiol,* vol. 34, pp. 79-84, 2010.

[7.5] S R Gambert, "Screening for prostate cancer", *Internatinal. Urology and Nephrology,* vol. 33, pp. 249-257, 2001.

[7.6] D F Gleason, " Histologic grading of prostate cancer: A perspective", *Human Pathology,* vol. 23, pp. 273-279, 1992.

[7.7] Y C Fung, "Biomechanics: Mechanical Properties of Living Tissues", Springer, 1993.

[7.8] J Li, F Albri, J N Sun, M M Miliar, R R J Maier, D P Hand, and W N MacPherson, "Fabricating optical fibre-top cantilevers for temperature sensing", *Measurement Science and Technology,* vol. 25, pp.035206-035214, 2014.

[7.9] Y Z Zhu, and A B Wang, "Miniature Fiber-Optic Pressure Sensor," *IEEE Photonics Technology Letters,* vol.17, pp.447-449, 2005.

[7.10] S Phipps, T H Yang, S McNeill, F Habib and R Reuben, "The relationship between prostatic tissue morphology and mechanical properties: in vitro studies", *Proceedings of British Prostate Group Autumn Meeting*, 2003.

Chapter 8

Conclusion and future work

8.1 Introduction

The work presented in this thesis was concerned with fabrication and interrogation techniques for optical fibre based cantilever sensor and its application for the measurement of biological binding, temperature sensing, pH sensing and acceleration measurement. The experimental work will be briefly summarised and an assessment of the conclusions will be presented. Finally, the continuity of current work will be pointed out and discussed.

8.2 Summary of the thesis

Chapter 2 presented a review of fabrication and interrogation techniques of micro-cantilever sensors. Both electronic and optical approaches to fabricate the cantilever structure were discussed. These approaches are well established, however, they are either prone to EMI or are too bulky to be used for some practical applications. Therefore optical fibre cantilever sensors are proposed as a possible solution. Relevant conventional fabrication and interrogation techniques were reviewed first and then compared with the approach developed and investigated in this PhD thesis.

In Chapter 3, FPI theory was introduced, which is essential to understand the operation principle of optical fibre cantilever interrogation system. We demonstrated the basic experimental set-up for a standard optical fibre cantilever interrogation system and FFT algorithm used to determine the cavity length which is essential for cantilever bending measurements. The system can offer potential robust and low cost solutions for industrial applications. The measured system r.m.s. error calibrated by Reinishaw ML10 position sensor (accuracy ~1nm) is around ±15nm and after using a phase recovery algorithm, this error can be further reduced to ~2 nm in a stable environment.

Chapter 4 explored the design and manufacturing techniques for optical fibre-top cantilever sensors. The use of optical fibres offers a route to miniaturise the sensor

configuration and allow real-time bending measurement of micro-cantilevers in order to enable various sensing applications. In this chapter, two major applications of optical fibre cantilever sensors are investigated: temperature and pH sensing. The results show the advantages of a fibre-top cantilever combining the sensing and interrogation as a single element in a constrained measurement area, which was presented at Photon-12, Durham [8.1]. The experimental work for pH sensing is ready for submission to Journal of Smart materials and Structures.

Chapter 5 discussed a sensor based upon a cantilever located at the side of an optical fibre, where a 45˚ turning mirror was machined by FIB into the fibre end, coupling the light back into the fibre core. In this way, displacement [8.2] or vibration perpendicular to the direction of the optical fibre can be measured. In addition, the structure allows longer cantilevers with increased sensitivity. Low g multi-axes acceleration measurement with micro-machined optical fibre side cantilever sensor has been demonstrated. The majority of the work has been prepared to submit to Optics Express.

Chapter 6 explored the use of ferrule-top cantilevers as a biosensor [8.3]. The binding process between biotin-streptavidin was investigated in real time and further application of the sensor for pathogen detection was demonstrated. Furthermore, the effectiveness of cantilevers were also tested, and compared with an ELISA system. The ferrule-top cantilever probe opens the new route for label-free, rapid and portable sensing platform with potentially low-cost fabrication process.

Chapter 7 presented an optical probe for prostate stiffness measurement. The designed sensor offered much more sensitivity and specificity when measuring the modelled prostate comparing with an electrical gauge. The technique developed here has opened new route for accurate and reliable measurement for prostate diagnose in the future. The majority of this work has been submitted to Sensor and Actuator A for reviewing.

8.3 Future work

8.3.1 Improvement of interrogation system

In the thesis, we explored optical interrogation systems using a broadband light source and detected using a spectrometer (Ocean Optics S2000) to offer appropriate cantilever deflection sensitivity. The recovered deflection resolution using phase recovery algorithm was found to be 2-3nm, approaching the resolution limitation of S2000 (~0.45nm). Higher resolution can be achieved by using more accurate spectrometer or optical spectrum analyser, but this will increase the whole cost of the system. Other possible solution may use reference cantilevers to minimise the background noise to improve the sensitivity of the system.

8.3.2 Fabrication MCF cantilever

Based on the experience in the use of novel multi-core optical fibres [8.4] in our group, optical fibre-top cantilevers have been successfully fabricated onto a MCF, which offers new measurement capabilities. A single system may have one measurement cantilever and a reference cantilever to compensate for temperature changes. A multi-cantilever sensor can be activated to detect several different species using a single fibre probe. The use of MCF in this application is novel and a highly speculative area of research. A successful outcome has been demonstrated by a 2-cantilever single fibre sensor with a MCF. Future work will be focused on the 3-axes measurement with a single MCF for space constraint environment.

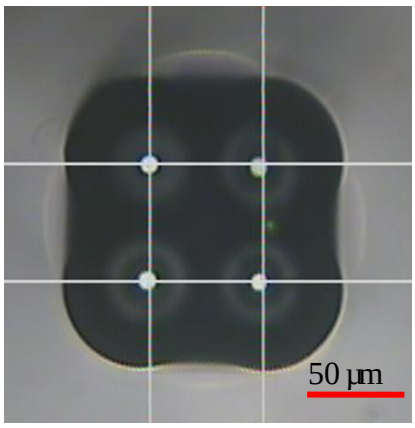

Figure 8.1 A 4-core MCF fibre viewed by a microscope.

In order to accomplish small scale and highly sensitive biological measurement application, new fibre structure with a larger diameter or multi-cores is necessary to allow the manufacturing of longer cantilever beam onto the fibre. Cantilever arrays can also be designed and manufactured. Some of them can be used as a reference to minimise the background noise. With the current optical fibre fabrication technology, these special optical fibre cantilever sensors will become useful tools to monitor biological binding processes which potentially can be used as biomarkers. With high sensitivity, it is also possible to use silica cantilevers machined directly onto an optical fibre for fast and low concentration food pathogen detection.

8.3.3 Optical fibre P-finger for prostate diagnose

Based on the mechanical polished 45° fibre and interferometer data analysis, optical P-finger sensor which is used to diagnose prostate tissue was explored in this thesis. The device was tested on a model prostate gland with a unilateral stiff inclusion simulating severe Prostate Cancer. In this work, the optical fibre has replaced the traditional electrical gauge based up on the experiment data in Chapter 5, made measurement safer and improved sensitivity. A proof-of-concept experiment has demonstrated the capability of the sensor for prostate stiffness measurement; however, the spatial resolution of the sensor is still not high enough for clinic trials with a single point sensor. From the clinical point of view, spatial resolutions of <0.5mm with full degree multi-point gauges are necessary to give an overall measurement of the tissue. In this case, a diagnostic approach combining this with an ultrasonic probe will be advantageous for a comprehensive assessment of prostate tissue. We believe that future work will focused on reduction of the sensor size for multi-point measurements, which will in turn improve the diagnostic resolution and reduce pain during the clinical examination.

8.3.4 Label free bio-sensor for milk pathogen fast detection

In this thesis, L. *innocua* in a food sample was detected by ferrule-top cantilever. Future work will be focused on applying the sensor for simultaneous detection of

foodborne pathogens, which can be achieved by using a cantilever array (each one of them is coated with different antibodies) in a single test. With a higher specialty antibody, we might be able to monitor even lower pathogen concentrations as a result of the specific binding between the antibody and pathogen. Due to the unavailability of the antibody, we are not able to conduct this experiment, however, based on the present result, we would expect a lower detection limit of ~10^3cfu/ml pathogen concentration. A potential useful design instead of using ferrule-top cantilever sensor is to fabricate a cantilever directly onto a polymer fibre. Due to the low Young's modulus and larger diameters of polymer fibres, it is possible to manufacture high sensitivity cantilevers to measure biological binding in real time.

8.4 Conclusions

The initial aim of the project was to explore the fabrication and interrogation technologies and use of micro-cantilever sensors fabricated onto the end of optical fibres. The design and demonstration of the sensor addresses the issues with conventional AFM techniques, in which bulky optical beam detection systems are unsuitable for *in-vivo* measurements. The use of optical fibres offers a route to miniaturise the sensor configuration to allow bending measurement of micro-cantilevers in real-time enabling bio-sensing applications in space constrained environments. Based on this, fibre-top cantilevers have been successfully fabricated by ps-laser/FIB machined techniques with a further demonstration for temperature and pH sensing. Another design with machined cantilever on the side of an optical fibre was also proposed to increase the sensitivity. This demonstrated the potential for multi-axes acceleration measurements down to ~ 0.2g with a single optical fibre in a space constrained environment.

Other designs based on the concept of optical fibre cantilever sensors have extended the application range to biotin-streptavidin binding and real time food pathogen monitoring. These demonstrations allow optical fibre cantilever sensors to monitor real-time biological binding with fast response times and small detection volume. Therefore, in

the long-term, we expect portable touch-and-tell devices combined with optical fibres in the healthcare industry to increase in popularity.

Reference

[8.1] J Li, F Albri, R R J Maier, W N MacPherson, and D P Hand, "Optical fibre cantilever sensors fabricated using ps-laser machining", *Photon-12*, Durham, UK, 3-6 September, 2012. (accepted for poster presentation)

[8.2] J Li, J N Sun, M M Miliar, J M Ritchie, X Luo, R R J Maier, D P Hand, and W N MacPherson, "Focussed ion beam machining of an in-fibre 45° mirror for fibre end sensors", *Proceeding of SPIE 8794, Fifth European Workshop on Optical Fibre Sensors*, vol.8794, pp.847904 , 20 May 2013.(accepted for poster presentation)

[8.3] J Li, Y X Zhou, R Folwer, R R J Maier, D P Hand and W N MacPherson, "Optical fibre cantilever sensor for biological application", *Proceedings of 23rd international conference on Optical Fibre Sensing*, vol.9157, 2 June, Santander, Spain, 2014. (accepted for poster presentation)

[8.4] M J Gander, D Macrae, E A C Galliot, R McBride, J D C Jones, P M Blanchard, J G Burnett and A H Greenaway, "Two-axis bend measurement using multicore optical fibre," *Optical Communication*, vol.182, pp.115-121, 2000.